Karlsruher Institut für Technologie

Charge Asymmetry Measurements in Top Quark Pair Production at $\sqrt{s} = 8\,\text{TeV}$ with the CMS Experiment

Zur Erlangung des akademischen Grades eines
DOKTORS DER NATURWISSENSCHAFTEN
von der Fakultät für Physik des
Karlsruher Institut für Technologie (KIT)

genehmigte

DISSERTATION

von

Dipl.-Phys. Frank Roscher
aus Ettlingen

Mündliche Prüfung: 13. November 2015

Referent: Prof. Dr. Th. Müller
Institut für Experimentelle Kernphysik

Korreferent: Prof. Dr. U. Husemann
Institut für Experimentelle Kernphysik

Introduction

With the start of operation of the Large Hadron Collider (LHC) at CERN in 2010, the field of high energy physics may have entered a new era of discoveries. Providing the most energetic proton-proton collisions that have ever been produced under laboratory conditions, this particle accelerator has opened a new window for research on the basic building blocks of our existence. Giant detectors like the Compact Muon Solenoid (CMS) experiment have been constructed around the interaction points to detect the particles that are produced in the collisions, and a busy field of physics data analysis endeavors to find even smallest deviations from the expectations within the vast amounts of collected data. Humanity's current understanding of the corresponding physics processes is represented by the standard model (SM) of particle physics, which originally was developed during the 1960s and has been confirmed in its predictions in the years since then.

Among the variety of elementary particles described by the SM, the top quark is the one with the highest mass; it thus is of special importance, having influence on a variety of established or newly theorized phenomena occurring at high energies.

The dominant production mode for top quarks at the LHC is the production of top quark-antiquark pairs via the strong interaction. This can occur either via gluon-gluon fusion or through the annihilation of a light quark-antiquark pair in the initial state; in the latter case there is an inherent particle-antiparticle asymmetry of the process, which in part can be conserved during the interaction. It then manifests as an asymmetry in the behavior of the produced top quarks and top antiquarks; this effect is called the *charge asymmetry of top quark pair production*. With a positive charge asymmetry, as it is predicted in the SM, the lower average momentum of the initial state antiquarks at the LHC would result in an excess of top antiquarks detected in the central parts of the detector; correspondingly, an excess of top quarks is predicted for the detector regions that are closer to the beam pipe.

The charge asymmetry started to attract significant interest from the high energy physics community when first measurements by the Tevatron experiments showed significant discrepancies when compared to the standard model predictions. As the charge asymmetry is a quantity that could be affected by many possible extensions of the standard model, this has been seen as a possible indication of new physics processes. Over time both the Tevatron measurements and the SM predictions have been refined, and the discrepancies have become smaller as a result; nevertheless, measurements of this effect at the LHC are needed to arrive at a more conclusive judgment on the possible influence of new physics on the

observable.

In this thesis a variety of measurements of the charge asymmetry at the LHC has been performed. Aside from an inclusive measurement of the overall asymmetry, carefully tuned measurements of the charge asymmetry as a function of secondary variables are presented. The secondary variables in question are the invariant mass, the transverse momentum, and the absolute rapidity of the top quark pair, each of which is sensitive to a different aspect of the charge asymmetry.

In addition to the measurements that determine the values of the observables in the full phase space of top quark pair production, for the first time at the LHC additional results are provided for a restricted, *fiducial* phase space. The measurements for this phase space are less reliant on SM assumptions in the measurement procedure, yielding results that remain correct even under the distorting influences of new physics processes.

Using the full CMS proton-proton collision dataset of 2012, corresponding to an integrated luminosity of $19.7\,\mathrm{fb}^{-1}$, the measurements of this thesis can help to constrain the size of possible new physics processes affecting the charge asymmetry.

The thesis is structured in the following way:

Chapter 1 offers a general introduction to top quark physics and the charge asymmetry, and it summarizes the earlier experimental findings related to this effect.

An overview over the LHC accelerator complex, the CMS experiment, and the technical foundations of the data acquisition is given in Chapter 2.

In Chapter 3 the simulation of collision events is discussed, followed by a description of the reconstruction steps needed to transform the measured electrical signals into information on the produced particles.

Chapter 4 starts by describing the modeling of the physical processes that are most relevant for the analysis; this is done with a focus on the properties important for the event selection, which is the second major topic of this chapter. The selection is designed to extract the $\mathrm{t\bar{t}}$ events from the background contributions. Additionally, Chapter 4 also includes an estimation of the process normalizations based on a template fit to the selected data, as well as the definition of the reduced phase space that is used for the fiducial measurements.

Chapter 5, finally, concerns itself with the main steps and the results of the charge asymmetry measurements. It discusses the reconstruction of the top quark pair system, the background subtraction, the applied corrections of the reconstructed distributions via a regularized unfolding procedure, and lastly the individual systematic uncertainties and how they are estimated.

Contents

1 Theoretical Foundation and Experimental Status

The *standard model* (SM) of particle physics [1–10] is a quantum field theory that stands as the established model of the elementary particles and their interactions. Conceived between 1960 and 1970, it not only explained the experimental results of the time but also predicted the existence of a multitude of particles that afterwards were discovered by experiments: The charm quark in 1974 [11, 12], the bottom quark in 1977 [13], the top quark in 1995 [14, 15], the tau neutrino in 2000 [16], and the Higgs Boson in 2012 [17, 18].

Despite these accomplishments of the model, various observations and theoretical considerations remain that demonstrate that the SM is incomplete. For example, it does not incorporate gravity, non-zero neutrino masses, or viable candidates for the explanation of the concepts of dark energy and dark matter [19, 20]. Such shortcomings continue to motivate particle physicists to devise new models and extensions of the standard model, and to verify or falsify their predictions using appropriate experiments.

Within this thesis it is not possible to give a detailed introduction into the extensive theoretical framework of the SM. Instead an overview over the topics most pertinent to the analysis is provided.

In Section 1.1 a concise overview of the theory of Quantum Chromodynamics is given, which is the foundation for the description of both top quark pair production in particular and the dominant interactions at hadron colliders in general. Section 1.2 goes on to describe the production and decay modes of top quarks at the LHC, whereas Section 1.3 introduces the charge asymmetry in top quark pair production as well as its dependence on other kinematic variables and the influence of possible extensions of the standard model on this effect.

1.1 Quantum Chromodynamics

Quantum Chromodynamics (QCD) is the theory that describes color-charged particles and their interactions via the *strong force* within the SM. It is a renormalizable gauge theory corresponding to the unitary group $SU(3)$, with the quark matter fields being represented by color triplets. The short overview of QCD given in this section is adapted from reference [21].

The Lagrangian density of QCD is given by

$$\mathcal{L}_{\mathrm{QCD}} = -\frac{1}{4}\sum_{A=1}^{8} F^A_{\mu\nu}F^{A\mu\nu} + \sum_{j=1}^{n_f}\bar{q}_j(i\not{D} - m_j)q_j\,, \tag{1.1}$$

wherein $F^A_{\mu\nu}$ represents the gluon field strength tensor, and q_j are quark fields of differing flavors j with masses denoted by m_j. The number of flavors n_f equals six in the SM. Furthermore, $\not{D}$ is a shorthand for $\not{D} = D_\mu\gamma^\mu$, where γ^μ represents the Dirac matrices and D_μ is the covariant derivative:

$$D_\mu = \partial_\mu - ie_s\sum_A t^A g^A_\mu\,, \tag{1.2}$$

with the eight gluon fields g^A_μ, the $SU(3)$ group generators t^A acting on the triplet representation of the quarks, and the gauge coupling e_s, which in analogy to quantum electrodynamics is defined as $\alpha_\mathrm{s} = e_s^2/(4\pi)$.

Introducing the antisymmetric structure constants of $SU(3)$, C_{ABC}, which characterize the commutation relations of the generators $[t^A, t^B] = iC_{ABC}t^C$, the gluon field strength tensor can be defined as

$$F^A_{\mu\nu} = \partial_\mu g^A_\nu - \partial_\nu g^A_\mu - e_s C_{ABC} g^B_\mu g^C_\nu\,. \tag{1.3}$$

The last term of Equation (1.3) occurs only in non-Abelian theories; it results in a self-coupling of the gauge bosons, which takes the form of 3-gluon and 4-gluon interaction vertices. The remaining interactions in QCD are represented by the second term of Equation (1.1), which due to the covariant derivative describes a gluon-quark-antiquark vertex for quarks of the same flavor.

Despite the seeming simplicity of this description, QCD exhibits a comparatively rich phenomenology. Two of the most important effects are *asymptotic freedom* and *confinement*. Both relate to the fact that the effective coupling of the strong force increases as color-charged particles are separated spacially or, equivalently, as the momentum transfer Q^2 of their interactions decreases. While the term "asymptotic freedom" refers to the asymptotically vanishing interaction that can be observed for close particles or high momentum transfers, confinement describes the strong interaction that occurs when color-charged particles are separated: For longer distances the interaction potential becomes high enough to lead to the creation of new $q\bar{q}$ pairs from the vacuum. At sufficient energies this process happens repeatedly, resulting in collimated particle streams called *jets*.

The so-called *running coupling*, i. e. the dependence of the coupling strength α_s on the momentum transfer Q^2, has the side-effect of causing the perturbative approach to QCD calculations to break down for low values of Q^2. This necessitates different approaches to the calculations and generally reduces the accuracy of predictions related to QCD effects.

1.2 Top Quark Physics

Predicted in 1973 as part of a third fermion generation that represented a possible explanation for the CP violation in K meson decays [22], the top quark was discovered in 1995 by the CDF [14] and DØ [15] experiments at the Tevatron.

The top quark is the heaviest particle in the standard model, with a recent combination of measurements at both the Tevatron and the LHC yielding a mass of $173.34 \pm 0.76\,\mathrm{GeV}$[1] [23].

Because of this high mass the top quark plays a significant role in the production of Higgs bosons as well as in the decay of some hypothetical new particles, for example Kaluza-Klein excitations of the gluon [24]; similarly, the precise value of its mass has been important in determining the question of vacuum stability in the standard model [25, 26]. The universe is found to be in a meta-stable state if there is no influence of new physics beyond the standard model.

A second effect of the high top quark mass is a large decay width of about 2 GeV [27] and consequently a very short lifetime on the order of $5 \cdot 10^{-25}$ s. The top quark thus decays before any hadronization can take place, allowing experimental physicists to study a quasi-free quark. Additionally, the spin information of the top quark is passed on to its decay products, allowing for polarization studies to be conducted.

General overviews of top quark physics can be found in references [28] and [29].

1.2.1 Production of Top Quarks

The predominant production modes of top quarks at hadron colliders can be subdivided into two groups.

There is the production of *single top quarks* via processes involving the electroweak interaction, which has been observed for the first time at the Tevatron in 2009 [30, 31]. These processes involve a vertex in which a W boson couples to a top quark and a bottom quark; they thus most prominently allow the measurement of the $|V_{\mathrm{tb}}|$ element of the CKM matrix, which summarizes the information on the strengths of flavor-changing weak decays.

The other production mode, which is more relevant for this thesis, is *top quark pair production*. Though electroweak processes producing pairs of top quarks and top antiquarks do exist, their contribution is much smaller than that of the dominant processes involving the strong interaction. The higher coupling strength of the strong interaction also is the reason why top quark pair production occurs more frequently at the LHC than the production of single top quarks – despite the higher requirements on the center-of-mass energy of the collision. Figure 1.2 shows the leading-order Feynman diagrams contributing to top quark pair production.

It is of some importance that a further subdivision into two smaller groups of processes can be done: These are *quark-antiquark annihilation* processes and *gluon-fusion* processes involving the interaction of two gluons in the initial state.

[1] Natural units with $c = 1$ are used throughout this thesis.

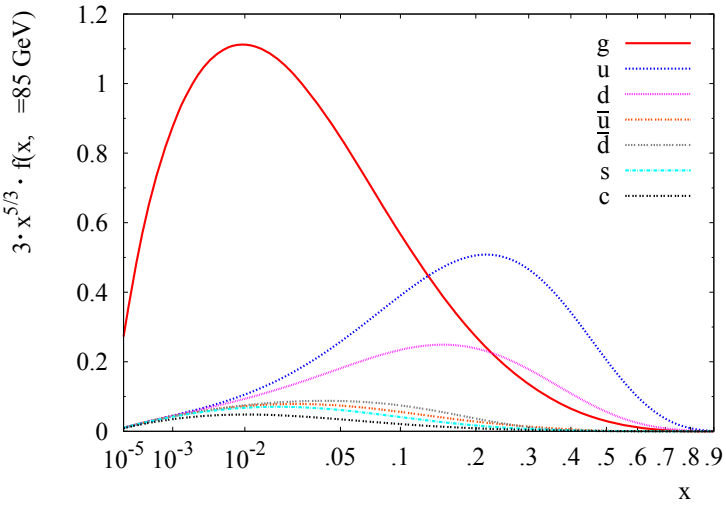

Figure 1.1: The CT10 PDF set [32] for protons, evaluated at a scale of $\mu = 85\,\mathrm{GeV}$; adapted from reference [33]. The variable x denotes the Bjorken scale variable, i. e. the momentum fraction of the given particle relative to the proton.

At the Tevatron quark-antiquark annihilation was the dominant effect, but at the LHC the process is much less common because there are no valence antiquarks in proton-proton collisions. Thus at a collision energy of 8 TeV at the LHC gluon-fusion processes make up about 85% of all top quark pair production.

Due to how the energy is distributed inside the proton, described by *parton distribution functions* (PDFs), the fraction of gluon-fusion processes will become even larger for the increased beam energies in later runs of the LHC. Figure 1.1 shows an evaluation of a PDF set for protons; it can be seen that gluons dominate the part of the distribution that corresponds to lower momentum fractions x relative to the proton. As the overall energy of the protons increases, lower values of x increase in importance for $\mathrm{t\bar{t}}$ production.

The predicted $\mathrm{t\bar{t}}$ production cross section at a center-of-mass energy of 8 TeV and assuming a top-quark mass $m_\mathrm{t} = 172.3\,\mathrm{GeV}$ is

$$\sigma(\mathrm{pp} \to \mathrm{t\bar{t}}) = 247.74^{+6.26+11.47}_{-8.45-11.47}\mathrm{pb}\,, \tag{1.4}$$

with the first uncertainty referring to independent variations of the factorization and renormalization scales, and the second one being associated to variations in the PDFs and α_s. The calculation has been performed using the Top++2.0 program [34].

1.2.2 Decay of Top Quarks

While in principle a decay of the top quark into W boson and either a strange or down quark is possible, these decays are suppressed by the small corresponding elements of the CKM matrix $|V_\mathrm{ts}|$ and $|V_\mathrm{td}|$. Because of this the top quark decays almost exclusively into a W boson and a bottom quark.

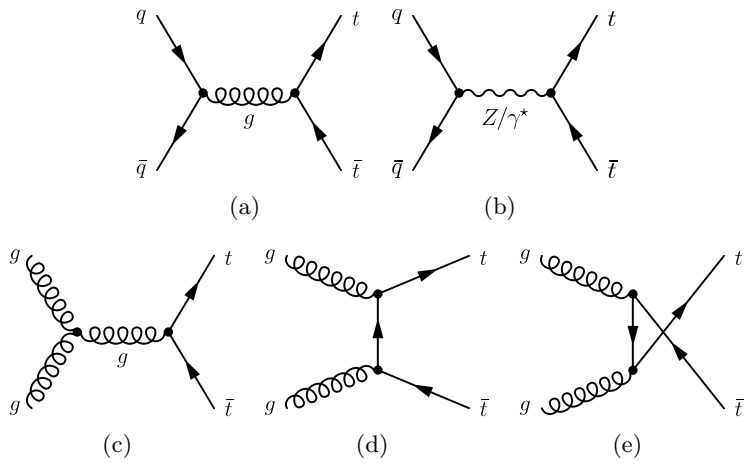

Figure 1.2: Leading-order Feynman diagrams of top quark pair production in proton-proton collisions: Quark-antiquark annihilation both via the strong interaction (a) and via electroweak interactions (b), as well as gluon-gluon fusion processes in (c), (d) and (e).

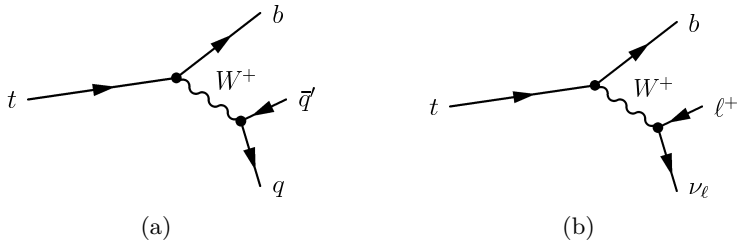

Figure 1.3: Feynman diagrams for the top quark decaying into a b quark and a W boson. The W boson decays either hadronically into a quark q and an antiquark $\bar{q}'$ of different flavor (a) or leptonically into a charged lepton and the corresponding neutrino (b).

The W boson, in turn, decays to particles corresponding to a doublet of the weak isospin: Either into a quark-antiquark pair (*hadronic decay*) or into a charged lepton and the associated neutrino (*leptonic decay*). Taking these two decay modes into account, the complete decay of the top quark is illustrated in Figure 1.3. The hadronic decay occurs roughly twice as often as the leptonic decay; this is because the coupling is the same for both modes, but the number of combinations of possible decay products differs: In the leptonic decay, particles corresponding to each of the three lepton generations can be produced, while in the hadronic decay there are two possible quark generations (the third generation being too massive due to the top quark) that additionally can carry three different color charges.

The two different decay modes of the W boson lead to three different decay modes of top quark pairs:

All-hadronic: Both W bosons decay to $q\bar{q}'$.
Semileptonic: One W boson decays leptonically, the other decays hadronically.
Dileptonic: Both W bosons decay to $\ell\nu_\ell$.

While many precise analyses of LHC data have been performed using the dileptonic decay channel, the semileptonic mode is generally considered to be the most powerful channel. This is because it exhibits both a high branching fraction of about 30% and a comparatively clean signature, allowing for both a good reconstruction of the top quark pair and a significant suppression of background processes. It should be noted, however, that in most analyses the semileptonic decay involving τ leptons is not taken into account, as the reconstruction of tauons is significantly more complicated and less precise than that of the other charged leptons. This is also true for the analysis presented in this thesis; it is performed in the combined electron+jets and muon+jets channels. Hereafter the commonly used term *lepton+jets channel* is used to refer to this combination.

1.3 The Charge Asymmetry of Top Quark Pair Production

The charge asymmetry of top quark pair production [35,36] is an effect that results in different kinematic distributions for top quarks as opposed to top antiquarks. First predicted in 1998 [35] to occur in the standard model production of top quark pairs, it was recognized to lead to observables that can be sensitive to the effects of various possible extensions of the standard model. The effect became the center of a lot of attention in the high-energy physics community when measurements of related observables at the Tevatron (e. g. [37, 38]) indicated inclusive charge asymmetries that were larger than the ones predicted by the standard model by about two standard deviations, with some of the differential measurements even yielding deviations of up to three standard deviations.

In the standard model the effect occurs only at next-to-leading order and beyond; because of this the standard model asymmetry is comparatively modest in size and thus sensitive to new physics contributions. As a charge asymmetry cannot occur in charge-symmetric initial states, only quark-antiquark annihilation processes can contribute, whereas the dominant gluon-fusion process at the LHC does not have a charge asymmetry.

Examples of the most important Feynman diagrams in the SM are given in Figure 1.4. While the interference of Born and box diagrams gives a positive contribution to the charge asymmetry, there is an additional negative contribution from the interference of initial state radiation (ISR) and final state radiation (FSR) diagrams. The different signs of these contributions can be understood conceptually [39, 40] by examining the properties of the color flow: Due to the s-channel exchange of gluons, which are color octets, there is a preference for the color charge to flow from the incoming quark to the top quark and from the incoming antiquark to the top antiquark. If the momenta of these associated quarks differ significantly the color charge undergoes a strong acceleration, leading

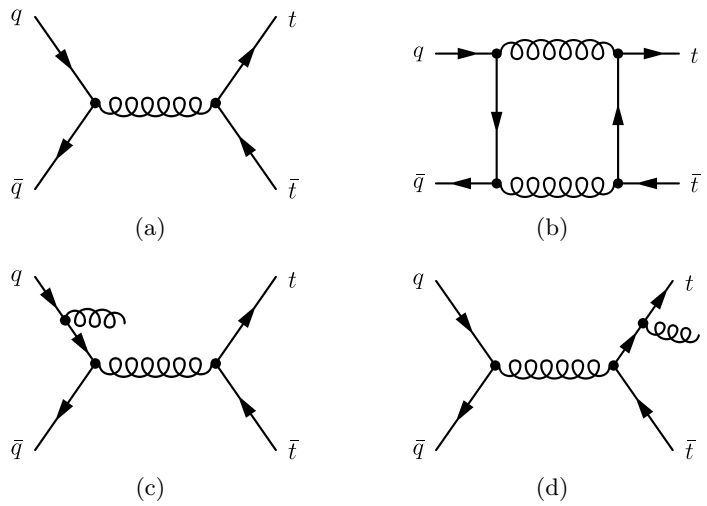

Figure 1.4: Example diagrams for the processes resulting in the standard model charge asymmetry at next-to-leading order. Contributions arise from the interference between Born diagram (a) and box diagram (b) as well as from the interference of initial state radiation (c) and final state radiation (d) diagrams.

to the radiation of gluons. Thus the processes involving radiation of real gluons tend to have a higher proportion of backwards production of the top quarks. This relation is illustrated in Figure 1.5.

In addition to the diagrams discussed above, the electroweak annihilation of quark-antiquark pairs as well as electroweak radiative corrections also have an influence on the overall effect, but this can be considered to be a small correction. Figure 1.6 shows some examples of the corresponding Feynman diagrams.

A positive charge asymmetry, as predicted by the standard model, results in a positive correlation between the momenta of the quark in the initial state and the top quark in the final state; correspondingly, it also induces a positive correlation between the antiquark of the initial state and the top antiquark of the final state.

1.3.1 Observables Probing the Charge Asymmetry

The charge asymmetry is generally measured using the *rapidities* or *pseudorapidities* of the produced top quarks and antiquarks.

The *rapidity* of a particle along a direction z, usually chosen to be along one of the beam revolution directions at the collision point, is defined as

$$y := \frac{1}{2} \ln \left(\frac{E + p_z}{E - p_z} \right) , \tag{1.5}$$

wherein E signifies the particle's energy and p_z signifies the momentum component that is parallel to the chosen direction z.

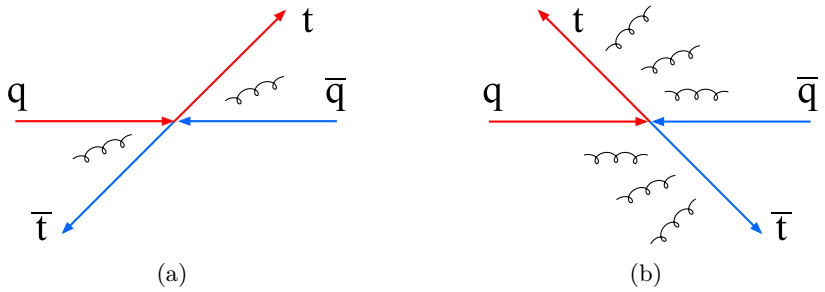

Figure 1.5: Illustration of the relation between top quark pair production in the SM and the radiation of gluons, adapted from [39]. While forward production of top quarks relative to the incoming quarks (a) entails only little gluon radiation, the high acceleration of the color charges required for backwards production (b) causes an increased amount of radiation.

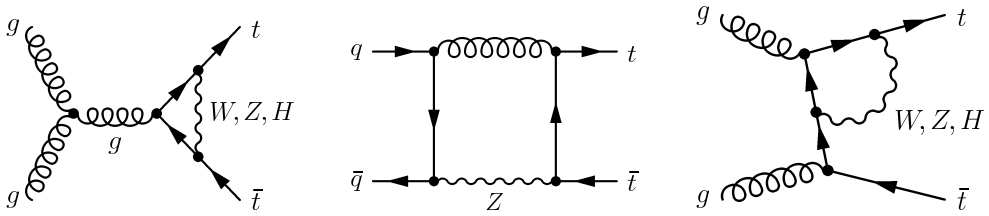

Figure 1.6: Example Feynman diagrams for the electroweak corrections to $t\bar{t}$ production.

The *pseudorapidity* similarly is defined as

$$\eta := \frac{1}{2} \ln \left(\frac{|\vec{p}| + p_z}{|\vec{p}| - p_z} \right) . \tag{1.6}$$

The main advantage of this variable in comparison to the rapidity is that no full measurement of the particle's energy is needed; in fact, it has a direct correspondence with the angle θ between the z direction and the momentum vector $\vec{p}$ of the particle in the laboratory system:

$$\eta = -\ln \left(\tan \frac{\theta}{2} \right) . \tag{1.7}$$

For massless particles rapidity and pseudorapidity are equivalent. The rapidity has been chosen as the base variable for the charge asymmetry measurement in this thesis. It represents a more familiar quantity to physicists outside the field of experimental particle physics, and it has the advantage that rapidity differences are invariant under Lorentz boosts along the z direction. Previous analyses [41] have shown that the measurement resolution is not worsened significantly when compared to a measurement using the pseudorapidity as base variable.

Though the charge asymmetry will generally affect the rapidity distributions of top quarks and antiquarks, the exact manifestation of this difference depends on the experimental setup; this is illustrated in Figure 1.7. Thus the sensitive variables that are constructed to measure the charge asymmetry also need to be chosen differently for the proton-antiproton collisions at the Tevatron and the proton-proton collisions at the LHC [42].

At the Tevatron both quarks and antiquarks occur as valence quarks of the colliding protons and antiprotons, respectively; since the directions of the momenta of the colliding hadrons are known as well, the directions of the colliding quarks and antiquarks are known for the vast majority of collision events. This allows the definition of a forward direction in such a way that a positive charge asymmetry results in a larger number of top quarks than top antiquarks in the forward direction. Consequently the charge asymmetry under such conditions is often called the *forward-backward asymmetry*, and it can be measured using a sensitive variable that is calculated as the difference of the rapidities of the produced top quarks and antiquarks:

$$\Delta y := y_{\mathrm{t}} - y_{\bar{\mathrm{t}}} \tag{1.8}$$

In proton-proton collisions like at the LHC, however, the experimental setup is charge symmetric. While the quarks of the initial state usually are valence quarks, antiquarks can only occur as sea quarks. It is not easily detectable which of the protons of a given collision contributed the quark and which one contributed the antiquark. For this reason a different sensitive variable is chosen for such experiments, exploiting the different average momentum fractions of valence quarks and sea quarks. In the presence of a charge asymmetry the different momenta of

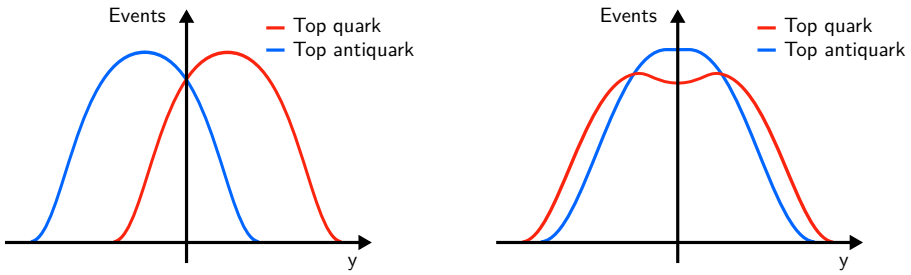

(a) (b)

Figure 1.7: Illustration of the effect of the charge asymmetry on rapidity distributions. The impact for proton-antiproton collisions, like those at the Tevatron, is shown in (a). The charge asymmetry manifests itself as a forward-backward asymmetry, with the top quark generally being emitted in the direction of the incoming proton and the top antiquark emitted in the direction of the incoming antiproton. In proton-proton collisions, like those at the LHC, the same effect results in a central-peripheral asymmetry of the rapidity distributions (b). For the purposes of this explanation both figures show an exaggeration of the qualities of the real distributions.

the initial-state quarks along the z direction result in different absolute rapidities of the produced top quarks. For a positive charge asymmetry one thus expects a wider rapidity distribution for top quarks than for top antiquarks, as illustrated in Figure 1.7(b). In order to measure this manifestation of the charge asymmetry the sensitive variable is constructed as the difference between the absolute values of the top quark rapidities:

$$\Delta|y| := |y_{\mathrm{t}}| - |y_{\bar{\mathrm{t}}}| \tag{1.9}$$

After the choice of a sensitive variable the charge asymmetry for the given experimental setup can be defined as

$$A_{\mathrm{C}} := \frac{N^{+} - N^{-}}{N^{+} + N^{-}}\,, \tag{1.10}$$

wherein N^{+} and N^{-} are the numbers of events with positive and negative signs of the sensitive variable. This is the definition of the charge asymmetry that is used for the remainder of this thesis.

1.3.2 Predictions and Measurements of the Charge Asymmetry

Standard model predictions for the charge asymmetry vary slightly depending on the specific methods used to calculate them, and depending on the amount of electroweak corrections that are considered. As the results of this analysis are compared to calculations at next-to-leading order (NLO), their peculiarities are of some importance to this thesis.

The term *next-to-leading order* in this context refers to the order of perturbation theory in QCD. As the charge asymmetry does not occur at leading order of QCD, such an NLO calculation actually represents the leading order calculation of the charge asymmetry; this can lead to some confusion when the different terminologies are not separated carefully. In this thesis all further references to the calculation precision indicate the order of QCD perturbation theory.

Charge asymmetry calculations at NLO involve the ratio of an asymmetric cross section in the numerator and an overall cross section in the denominator [36]. There is some disagreement among theoretical physicists on whether the so-called *expanded* scheme or the *unexpanded* one is a more correct way to calculate this ratio. In the expanded scheme, which is used for the predictions shown in Section 5.7, the ratio is consistently Taylor-expanded in powers of the couplings. As a result, the comparatively small leading-order cross section is used for the denominator. In the unexpanded scheme, on the other hand, the full NLO cross section is used for the denominator. This is the scheme that the results of NLO event generators (see Section 3.1.1) are based on; because of this the predicted asymmetries of the simulated samples are significantly smaller than those of the theoretical calculations.

The difference between the two schemes is not usually quoted as an uncertainty of the predictions, with the expanded result being considered more correct by the most visible theorists in this field [36, 43]. Instead, it is generally variations of the renormalization scales that dominate the quoted uncertainties.

The most precise predictions [44] for the standard model forward-backward asymmetry at the Tevatron are performed at approximate next-to-next-to-next-to-leading order (aN^{3}LO) and yield an inclusive asymmetry of $(10.0 \pm 0.6)\%$; they build on the full NNLO calculations performed in reference [45], which yield a value of $(9.5 \pm 0.7)\%$.

The LHC charge asymmetry at a center-of-mass energy of 8 TeV, as it is measured in this thesis, is calculated at next-to-leading order [43] to be $(1.11 \pm 0.04)\%$. A different prediction using less common calculation techniques [46] has been performed at next-to-next-to-leading order (N^{2}LO) precision and yields a result of $(1.03^{+0.01}_{-0.00})\%$. The smaller asymmetries when compared to the Tevatron are caused by a much higher fraction of the symmetric gluon-fusion processes and by the necessity of a different significant variable for the definition of the asymmetry.

The first measurement of the charge asymmetry in hadron collisions was performed in 2007 by the CDF collaboration [47], yielding a result of $A_C^{\text{Tev}} = (24 \pm 14)\%$. The most current measurements of the Tevatron use all data that was collected in the lifetime of this accelerator; the reported results are

$$A_C^{\text{Tev}} = (16.4 \pm 4.5)\%$$

by the CDF collaboration [48] and

$$A_C^{\text{Tev}} = (10.6 \pm 3.0)\%$$

by the DØ collaboration [49]. In contrast to earlier findings, which sparked the original interest in the charge asymmetry, these inclusive measurements of the asymmetry do not provide a significant hint for effects beyond the standard model.

The first measurement of the charge asymmetry at the LHC was implemented by the CMS collaboration using the sensitive variable $\Delta|\eta|$ and gave a result of $A_{\mathrm{C}}^{\Delta|\eta|} = (6 \pm 14)\%$ [42]. The uncertainties of this measurement, though, were too large to draw a conclusion on the presence or absence of new physics. The standard model asymmetry using this sensitive variable at a center-of-mass energy of 7 TeV is calculated to take a value of $A_{\mathrm{C}}^{\Delta|\eta|,\mathrm{SM}} = (1.3 \pm 0.11)\%$.

Later analyses switched to $\Delta|y|$ as sensitive variable and gave results of

$$A_{\mathrm{C}} = (0.4 \pm 1.0 \pm 1.1)\%$$

at CMS [50] and, about a year later, of

$$A_{\mathrm{C}} = (0.6 \pm 1.0)\%$$

at ATLAS [51]. A combination of these two measurements was performed [52] and yielded

$$A_{\mathrm{C}} = (0.5 \pm 0.7 \pm 0.6)\% \,.$$

These values need to be compared to a standard model prediction [43] of $A_{\mathrm{C}}^{\mathrm{SM}} = (1.23 \pm 0.05)\%$. Neither result shows a significant deviation from the prediction, and in contrast to the measurements performed at the Tevatron the measured asymmetries are slightly smaller than the predicted values.

For historical context it needs to be kept in mind that these LHC results were published at a time when there still was a considerable discrepancy between the measured and predicted values at the Tevatron. Though the contributions of new physics do not necessarily affect the charge asymmetries at the LHC and at the Tevatron in the same way, as is explained in more detail in Section 1.3.4, the measurements were generally seen as an indication that the Tevatron results did not have an origin in physics beyond the standard model.

1.3.3 Differential Charge Asymmetries

Even though measurements of the inclusive charge asymmetry have converged with the theoretical predictions, measurements of the asymmetry as a function of other kinematic variables remain of considerable interest as a way of enhancing the asymmetry and providing improved precision in the search for deviations from the standard model prediction. Various theoretical publications [39, 43, 53–55] have explored the potential of different *secondary variables* for such differential measurements of the charge asymmetry.

The *secondary variables* chosen for the measurements in this thesis are the invariant mass, the transverse momentum, and the absolute value of the rapidity of the top quark pair. A simulation of the dependence of the standard model charge

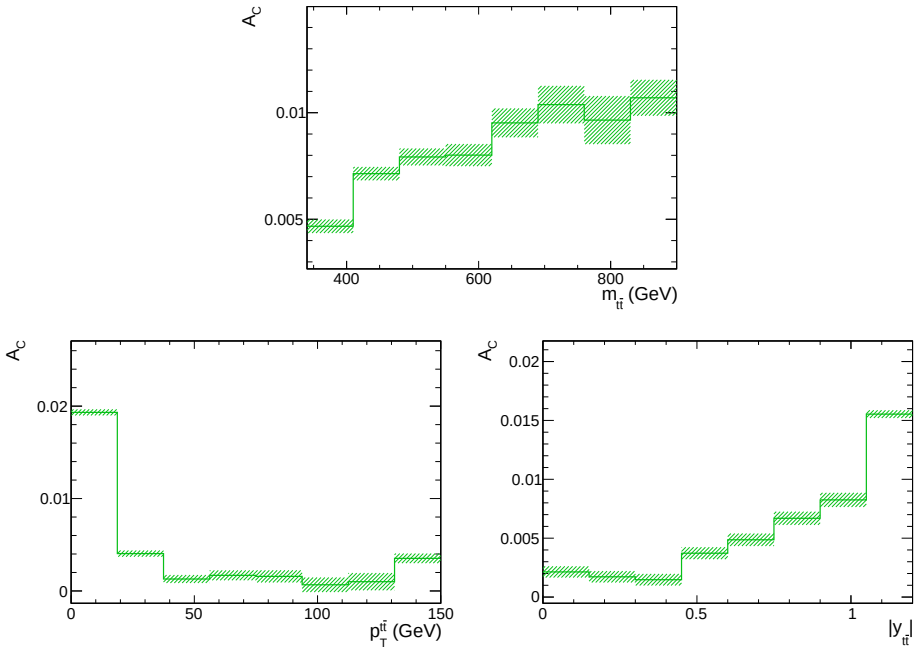

Figure 1.8: POWHEG [56, 57] simulation of the charge asymmetry and its dependence on the secondary variables $m_{t\bar{t}}$, $p_T^{t\bar{t}}$ and $|y_{t\bar{t}}|$ in the standard model. POWHEG does not normalize its calculation in the same way as the most prominent theoretical calculations, and electroweak corrections are neglected; nevertheless, an approximation of the NLO calculations can be obtained by multiplying the shown values by a factor of 1.5 [53].

asymmetry on these variables can be found in Figure 1.8. The following paragraphs explain these distributions and the motivation for measuring differentially as a function of the given variables.

Invariant mass $m_{t\bar{t}}$

Proposed extensions to the standard model that affect the charge asymmetry generally introduce new particles that occur as mediators in top quark pair production processes; see also Section 1.3.4. The effect of many such particles would be more pronounced at high energies and thus at high values of $m_{t\bar{t}}$, making this the most important variable for the detection or exclusion of new physics.

Even in the absence of new physics contributions the charge asymmetry increases for high values of $m_{t\bar{t}}$ because the asymmetric $q\bar{q}$ initial state is enriched [43]; however, this is not of particular interest for the analysis.

Transverse momentum $p_T^{t\bar{t}}$

As explained in Section 1.3 the value of the standard model charge asymmetry at next-to-leading order is determined by a positive contribution from Born and

box diagrams as well as a negative contribution from diagrams involving real gluon emission. The transverse momentum (p_{T}) of the top quark pair allows to distinguish between these two contributions because non-zero values of $p_{\mathrm{T}}^{\mathrm{t\bar{t}}}$ occur only due to the real gluon emission. Thus at low values of $p_{\mathrm{T}}^{\mathrm{t\bar{t}}}$ the positive contribution is enhanced, while small negative asymmetries are expected at high values of $p_{\mathrm{T}}^{\mathrm{t\bar{t}}}$. Measurements as a function of this variable can also help to shed light on the nature of possible new physics contributions; $\mathrm{t\bar{t}}$ production via a color octet shows the relation to gluon radiation indicated above, while production via a color singlet [39] does not.

Rapidity $|y_{\mathrm{t\bar{t}}}|$

A suppression of the dominant but symmetric gluon-fusion process is a good way of enriching the charge asymmetry without relying on any specific model. Because the average momentum fractions of valence quarks and sea quarks in the protons are very different the partonic center of mass and by extension also the top quark pair system are often boosted along the beam axis for quark-antiquark-annihilation processes. Gluon-fusion processes on the other hand tend to not have such asymmetric momenta in the initial state. A discrimination thus is possible by measuring as a function of the absolute value of the rapidity of top quark pair system $|y_{\mathrm{t\bar{t}}}|$. The asymmetric production processes are enriched at high values of this variable.

Just like inclusive measurements of the charge asymmetry, differential measurements as well were pioneered by the Tevatron collaborations. The most current measurements by the CDF collaboration [48] find departures from the standard model predictions corresponding to 2.8 and 2.4 standard deviations for the differential measurements as functions of $|\Delta y|$ and $m_{\mathrm{t\bar{t}}}$, respectively. Just like in the inclusive measurements these deviations point towards larger asymmetries than predicted by the standard model. The DØ collaboration [49] provides similar measurements that do not point toward such a marked increase in comparison to the predictions.

Previous measurements by the CMS [50] and ATLAS [51] collaborations at a collision energy of 7 TeV have not indicated any deviations from the behavior predicted by the standard model.

1.3.4 Theories Beyond the Standard Model (BSM)

Due to the temporary high interest in the charge asymmetry theorists have been studying a variety of models that extend the standard model and introduce new contributions to top quark pair production, affecting the charge asymmetry. More detailed overviews over such models can be found in references [55, 58–61].

The necessity of a significant modification of the standard model asymmetry to accommodate the CDF results means that the most interesting models have been those introducing new tree-level physics; generally, each of the models introduces a new particle that can mediate in the process $q\bar{q} \to t\bar{t}$.

However, the breadth of plausible models is reduced by measurements of quantities other than the charge asymmetry – most notably by resonance searches in the invariant mass spectrum of top quark pair production, and by measurements of the overall cross section of this process. The models generally have several ways to accommodate the conditions imposed by those measurements. One option is a very large width or a very high energy of the predicted resonance, as the cross-section measurements are less sensitive to such models. With these seemingly simple solutions, though, it is often not possible to attain a high enough contribution to the asymmetry. The model could, however, also involve a cancellation of the contributions to the cross section: There may be a cancellation of the quadratic contribution with the term describing the interference with the standard model, or it may be the forward and backward components of the asymmetric terms themselves that balance each other in the inclusive cross section. In the latter case the quadratic term is also required to be small.

Either way, it is established [62] that the absence of large contributions to the overall cross section means that large asymmetries cannot be explained easily without a significant interference between the new physics contribution and the contribution of the standard model.

Some of the proposed new particles are listed in the following, summarizing some of the information provided in references [58] and [63].

- A color-octet vector boson G [64] exchanged in the s-channel and interfering with the diagrams involving the gluon in its stead. The G could, for example, appear as the lightest Kaluza-Klein excitation of the gluon in models involving additional dimensions [65]. Often this boson is seen as the most promising potential explanation of the Tevatron measurements. In the case of disappearing vector couplings it is referred to as an *axigluon*; the measurements of this thesis are compared to an effective field theory describing the effects of such a particle.

- A color-singlet charged vector boson W' [66], as the result of a left-right extension of the SM gauge group. The W' would couple to right-handed quarks and give a t-channel contribution to the process $d\bar{d} \to t\bar{t}$. The available data disfavor this model strongly.

- A color-singlet neutral vector boson Z' [67]. A Z' could occur as the gauge boson of a local flavor symmetry, and it would have the most interesting effect on the charge asymmetry if it occurred in the t-channel and had flavor-changing couplings to top quarks and up quarks. Like the W', however, it is not favored by the available data.

- A Higgs-like scalar isodoublet ϕ [68], exchanged in the t-channel, would be able to achieve reasonably large asymmetries with comparatively small couplings. The required flavor-changing couplings could be justified with flavor symmetries.
- A scalar color-triplet ω or color-sextet Ω [69], exchanged in the u-channel. Such particles occur as part of the scalar sector of many Grand Unified models.
- A right-handed sbottom quark coupling to right-handed down and top quarks [63], as it occurs in the R-parity violating minimal supersymmetric standard model. Such a particle is disfavored strongly by the most recent LHC measurements of the charge asymmetry, one of them being the analysis documented in this thesis.

Figure 1.9 illustrates the effects of various extensions of the standard model on the asymmetries measured at the Tevatron and at the LHC. Depending on the model the measurements at the two colliders can be influenced differently, owing to the different collision energies and the different frequencies of processes in proton-proton collisions and proton-antiproton collisions – most importantly, there is a higher fraction of $u\bar{u}$ initial states in proton-antiproton collisions [70]. As a result measurements of the charge asymmetries at the LHC and at the Tevatron can be considered to provide complementary information; for example, a W' consistent with the temporary high measurements at the Tevatron of an additional asymmetry contribution of 12% would have resulted, as can be read from Figure 1.9, in a very high asymmetry contribution of about 6% at the LHC – allowing for an exclusion of this model even with the early measurements of the charge asymmetry at the LHC.

The additional benefit differential measurements can provide in the context of new physics contributions is demonstrated in Figure 1.10, which shows how the charge asymmetry contributions from various light color-octet models vary differently as functions of $m_{t\bar{t}}$. Similarly, the measurement as a function of $p_{\mathrm{T}}^{t\bar{t}}$ could reveal differences [39] between the s-channel contributions of color singlets and color octets, since only color octets show the relation between asymmetry and radiation that has been described for the SM gluon case in Section 1.3.

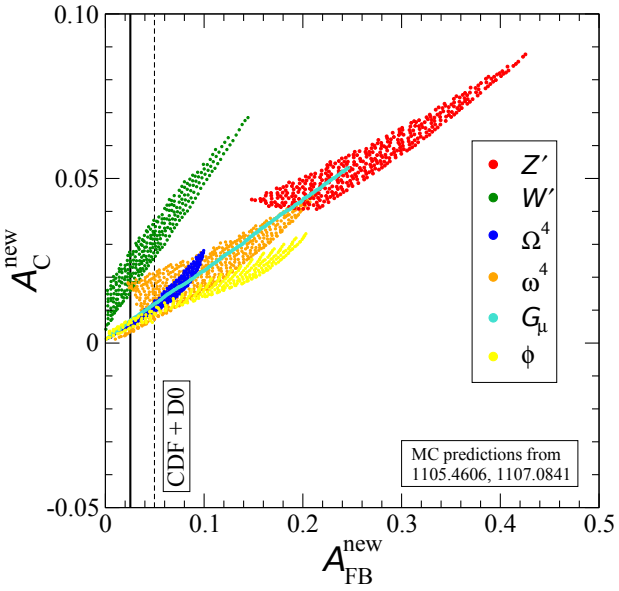

Figure 1.9: Comparison of BSM theory predictions for enhancements of the charge asymmetry with the most current measurements performed at the Tevatron, adapted from reference [55]. The horizontal axis shows the Tevatron charge asymmetry, whereas the vertical axis gives the value for the LHC charge asymmetry at $\sqrt{s} = 7\,\text{TeV}$. The measurement results are indicated with a solid line for the central value and a dashed line for the uncertainties. The combined Tevatron result has been calculated as a weighted average of the CDF and DØ results, and the standard model prediction has been subtracted.

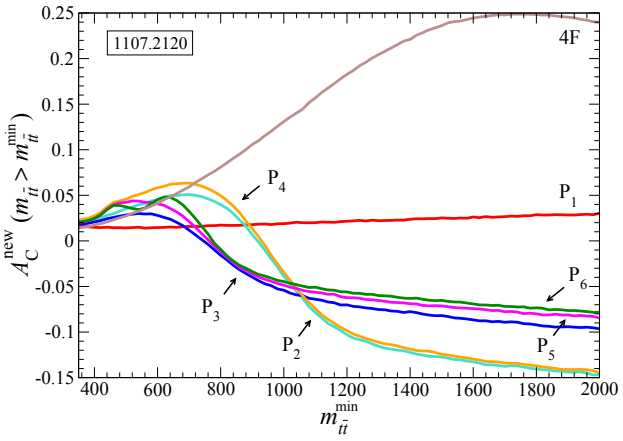

Figure 1.10: Behavior of contributions to the charge asymmetry from various models [71] introducing new color octets G_μ below the TeV scale, taken from reference [55]. The contribution is given as function of a lower cut on the invariant mass of the top quark pair. P1 to P6 refer to light gluon models, whereas 4F signifies a heavy gluon model. The individual models differ both in the number of predicted gluons and in parameters such as the masses, couplings and width parameters. It can be seen that measurements of the charge asymmetry as a function of $m_{t\bar{t}}$ have the potential to discriminate between different models.

2 The CMS Detector and the LHC

This analysis uses data collected by the Compact Muon Solenoid (CMS) detector [72, 73] at the Large Hadron Collider (LHC) [74] in the accelerator complex of the European Organization for Nuclear Research (CERN) near Geneva in Switzerland. The following sections give an overview of both the accelerator ring and the CMS detector, focusing on the parts that were most important for the collection of the data used in this thesis. Similarly, this chapter specifically restricts itself to describing the conditions of the 8 TeV operation of proton-proton collisions in the year 2012.

2.1 The Large Hadron Collider

The LHC is a proton-proton collider, constructed between the years 1998 and 2008, that at the time of writing has been able to provide the most powerful controlled particle collision events ever performed by mankind. It also represents the largest machine that has ever been built.

An overview of the CERN accelerator complex and the LHC can be found in Figure 2.1. The LHC has been constructed in an approximately circular tunnel with a circumference of 26.7 km, roughly 100 m below ground, that originally had been built for the Large Electron Positron Collider (LEP), which operated in the years between 1989 and 2000. The maximal energy of the colliding particles is limited by the strength of the magnetic fields keeping them on their trajectory. In the LHC 1232 superconducting dipole magnets establishing a magnetic field of up to 8.33 T have been installed; an additional total of 392 quadrupole magnets are used to focus the beams. Imperfections of the resulting magnetic fields are reduced by a variety of sextupole, octupole and decapole magnets. The magnets and associated cooling systems are shared for the two beam pipes, which achieves a higher efficiency than a full duplication of all subsystems.

The ring of the accelerator tunnel is not perfectly circular but consists of eight arcs that are interspersed with eight straight sections. Though beam crossings could be induced within each of the straight sections, leading to eight possible collision points called P1 to P8, detectors have only been installed at four of these points; this is illustrated in Figure 2.2. Each of those four points is home to one of the major LHC detectors:

ATLAS (A Toroidal LHC Apparatus) [77] at P1 and *CMS* (Compact Muon Solenoid) [72, 73] at P5 are general purpose detectors for proton-proton collisions. After they had achieved the primary goal of discovering the Higgs boson, their goals have shifted to measurements of the Higgs boson properties and to searches

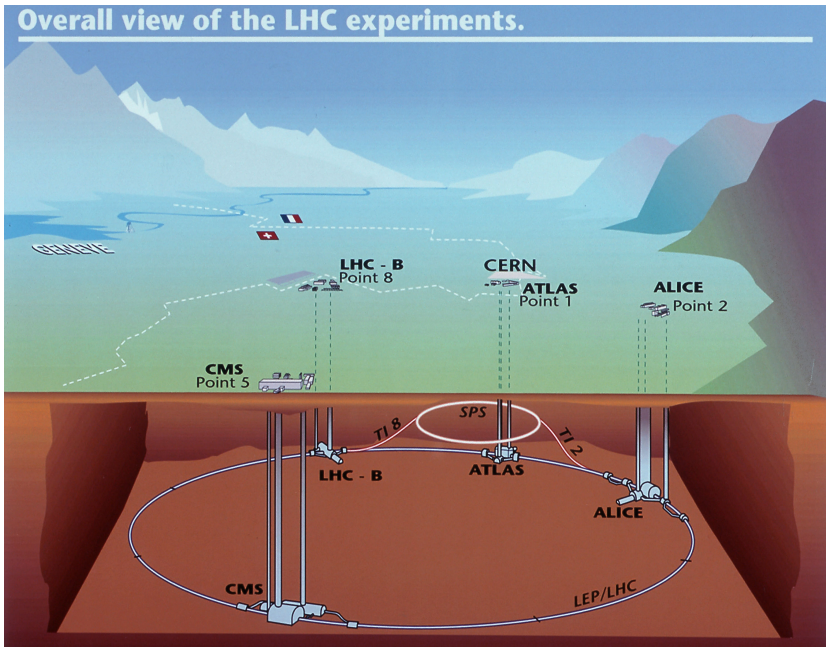

Figure 2.1: Illustration of the location of the LHC accelerator complex at CERN and the associated experiments [75].

for additional Higgs bosons, super-symmetry, and other physics beyond the SM. It is the CMS detector that has provided the data analyzed in this thesis.

The *ALICE* (A Large Ion Collider Experiment) detector [78] at P2 is used to analyze lead-ion collisions and to study the phenomenology of high matter densities like the quark-gluon-plasma. Finally, the *LHCb* experiment [79] at P8 performs precision measurements in the fields of B hadrons and CP violation.

Figure 2.2 also illustrates the different stages of preacceleration of the protons before their insertion into the main accelerator ring of the LHC. They are generated in a duoplasmatron by accelerating electrons in an electrical field and letting them collide with the molecules of hydrogen gas, separating the atom cores from their associated electrons. The resulting proton bunches are focused and accelerated to 750 keV in a radio frequency quadrupole (RFQ) [80]. The next acceleration stages are the LINAC2 [81] and the Proton Synchroton Booster (PSB) [82], accelerating them to 50 MeV and 1.4 GeV, respectively, followed by the Proton Synchrotron (PS) [83] and the Super Proton Synchrotron (SPS) [84], which achieve energies of 26 GeV and 450 GeV. From the SPS the protons are injected into the main ring of the LHC, which accelerates them to the run-dependent final energy of up to 7 TeV. For this injection the protons are separated into two beams that travel the main accelerator ring in opposite directions, allowing for collision energies of up to 14 TeV. Due to technical issues, however, the first two data-taking periods of the LHC have operated at collision energies of only 7 and 8 TeV, respectively.

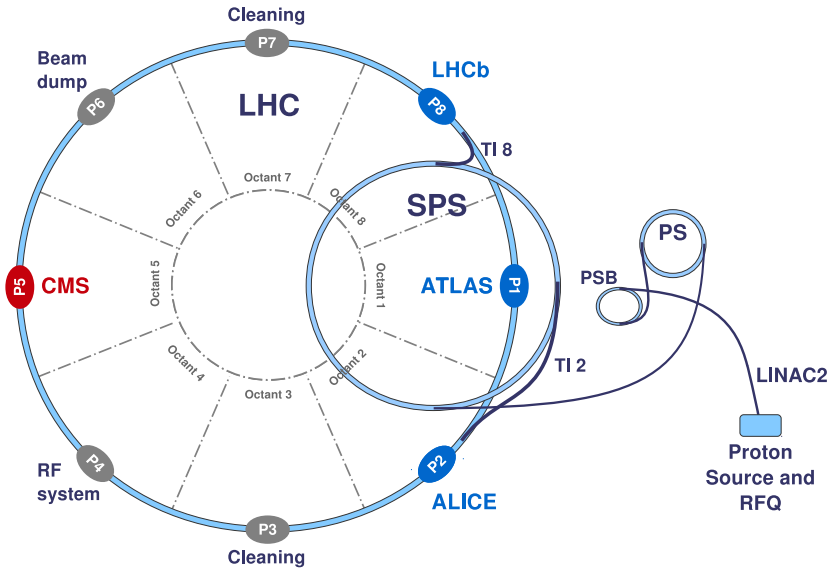

Figure 2.2: Overview over the acceleration chain and the components of the main accelerator ring at CERN [76]. After being produced in the proton source the protons undergo consecutive acceleration steps in the RFQ, the LINAC2, the PSB, the PS and the SPS. The bunches then are injected into the main ring using the transfer lines TI 2 and TI 8, which lead the protons to different directions of revolution. The main ring consists of eight octants, each of which houses one possible collision point P1 to P8 within a short straight section. For the operation of the LHC particle detectors have been installed at four of these eight collision points.

With the goal of producing a high number of interactions of specific processes, the interaction rate $\dot{N}$ corresponding to a specific process in the particle collisions is an important quantity for an accelerator. It is calculated as product of the *cross section* of the process and the *instantaneous luminosity* of the accelerator, which is a machine parameter describing the particle beam configuration. It can be calculated as

$$L = fn\frac{N_a N_b}{4\pi\sigma_x\sigma_y}\,, \tag{2.1}$$

with the revolution frequency f, the number of bunches per beam n, the particle multiplicities in the colliding bunches N_a and N_b, and the widths of Gaussian-shaped transverse distributions of the bunches $\sigma_{\mathrm{x,y}}$.

The *integrated luminosity* results by integrating the instantaneous luminosity over time; it can be used as a measure of the total number of collisions provided by the accelerator in a given time frame. Figure 2.3 displays the evolution of the integrated luminosity at the LHC for the proton-proton collisions of 2012. It also shows the integrated luminosity of data that has successfully been recorded by the CMS experiment; this value tends to be slightly lower due to detector deadtime and temporary downtimes of the data acquisition systems.

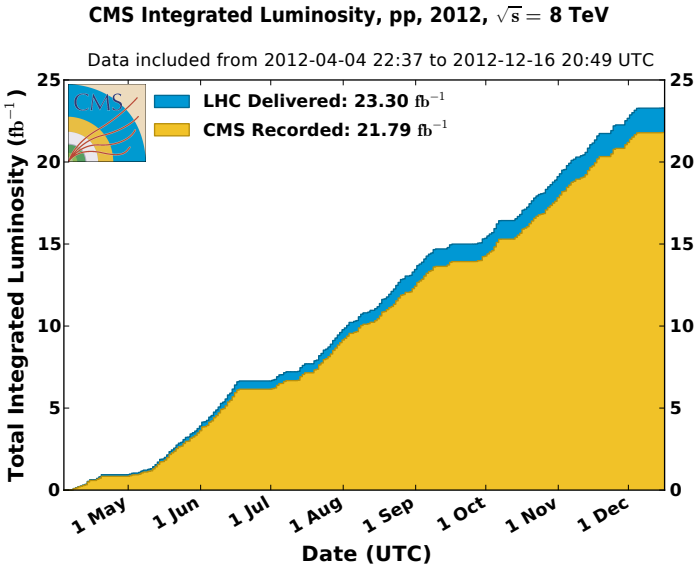

Figure 2.3: Development of the total integrated luminosity in the proton-proton operation at the LHC at a center-of-mass energy of 8 TeV in 2012 [85]. The orange area corresponds to the data successfully recorded by CMS, while the blue band denotes the additional integrated luminosity delivered by LHC but not recorded by CMS. The complete dataset of 2012 is used in this thesis.

2.2 The Compact Muon Solenoid Detector

As introduced above, the CMS [72, 73] detector is one of two general-purpose detectors at the LHC. It is situated under ground at Point 5, near the French village of Cessy. With a weight of 12 500 t it is the heaviest of the detectors at the LHC, even though at a length of 21.6 m and a diameter of 14.6 m it is more compact than the competing ATLAS detector.

CMS has been built as a layered structure around the beam pipe, which is illustrated in Figure 2.4. From the inside to the outside it consists of the tracking system, the electromagnetic and hadron calorimeters, a superconducting solenoid, and the muon system, which is embedded into the iron return yoke of the magnet. The solenoid creates a homogeneous magnetic field of 3.8 T parallel to the beam axis, which allows the measurement of electrically charged particles' momenta and of the signs of their charges by bending the trajectories they take through the detector in a way that depends on those quantities. The other subsystems are introduced in more detail in dedicated subsections.

As the design goals of the CMS detector very prominently included searches for Higgs bosons and supersymmetric particles, there was the need for a precise identification of photons and isolated charged leptons, and for a good reconstruction of the missing transverse energy of an event. Consequently the detector has been fitted with both a tracking system and electromagnetic calorimeters that are very precise, and the hadron calorimeters have been built to allow for a wide geometric

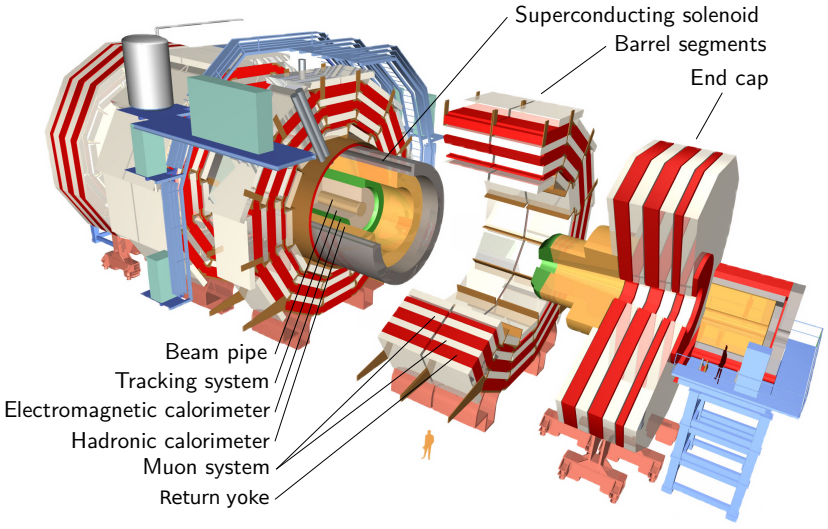

Figure 2.4: Schematic overview of the components of the CMS detector, adapted from references [76, 86]. In a layered structure the beam pipe is encased by the tracking system, the electromagnetic and hadron calorimeters, the superconducting solenoid, and the muon system, which is embedded in the iron return yoke. The hermetic enclosure of the beam pipe is achieved by supplementing the barrel segments with two endcap disks aimed at particles with trajectories that have small angles relative to the beam pipe.

coverage.

When describing the detector geometry of CMS a coordinate system with origin in the center of the detector is used. In this coordinate system the x-axis points towards the center of the accelerator ring, the y-axis points upwards, and the z-axis is chosen to be along the direction of the beam in such a way that the resulting coordinate system is right-handed. The polar and azimuthal angles θ and ϕ are the angles relative to the z-axis and the x-axis, respectively. The pseudorapidity, finally, is given by

$$\eta = -\ln\left(\tan\frac{\theta}{2}\right) . \tag{2.2}$$

Some further information on this angular variable can be found in Section 1.3.1.

2.2.1 Tracking System

The tracking system of CMS [87, 88] is the part of the detector that is closest to the beam pipe. Using semiconductor detector elements it measures the tracks of charged particles that travel through it.

This yields several essential benefits to analyses: By extrapolating the measured tracks back into the beam pipe the particles can be associated to the main interaction vertex or to vertices belonging to additional collisions (see Section 3.1). Similarly, as is described in Section 3.2.7, if the particles belonging to a given jet

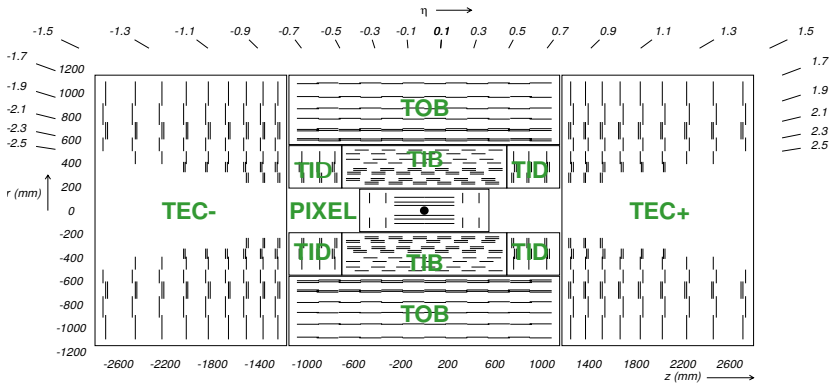

Figure 2.5: Schematic overview of the longitudinal structure of the CMS tracking system [72]. The interaction point is indicated as a black dot in the center. It is surrounded by silicon pixel detectors on the inside and silicon strip detectors on the outside. The barrel part consists of the Tracker Inner Barrel (TIB) and the Tracker Outer Barrel (TOB), whereas the endcap discs are made up of the Tracker Inner Discs (TID) and the Tracker End Caps (TEC). While single lines indicate normal detector modules, each double line represents a stereo module.

can be traced to an origin outside the interaction vertex, the jet can be identified as belonging to a bottom-flavored quark. Finally, the tracks of charged particles are curved due to the magnetic field of 3.8 T established by the solenoid; a measurement of this curvature allows a determination of both the charge and the momentum of the particle.

A technical drawing of the composition of the tracking system is shown in Figure 2.5. Consisting of both barrel and endcap components, it has an overall length of 5.8 m and a diameter of 2.5 m, and it covers a pseudorapidity range of $|\eta| < 2.5$. The innermost components are built using silicon pixel elements, while all outer components are made up of silicon strip elements. Though it is not shown in the diagram, the tracker is equipped with insulation and a cooling system, ensuring a safe operating temperature.

The elements of the silicon pixel detector cover an active area of one square meter, with each pixel being sized $100 \times 150\,\mu\text{m}^2$. This provides a resolution of 10 µm in r-ϕ and 15 µm in z for each of the measured points.

The silicon strip detector is not built as homogeneously. The readout pitch in the barrel varies from 62.5 µm to 125 µm, and the single point resolution in r-ϕ varies between 23 and 53 µm. The end caps are built using readout pitches between 67.7 µm and 102 µm and allow for measurements with a resolution of 30 µm in z-ϕ. Both the barrel and the endcap components of the silicon strip detector employ so-called *stereo modules* to allow for the measurement of the respective missing third coordinates of the vertices. In these modules each strip is paired with another that is rotated with regard to the first one. This yields resolutions ranging from 230 µm to 530 µm for the missing coordinates, using readout pitches between 100 µm and 250 µm.

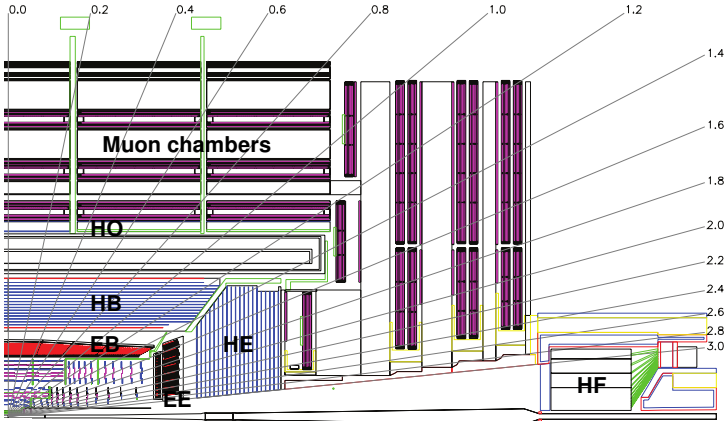

Figure 2.6: Positioning of the calorimeters and the muon system [73]. Only a quarter of the detector is shown. The tracker system, indicated in the lower left, is encased by the Electromagnetic Barrel (EB) and the Hadron Barrel (HB) calorimeters along the r-axis and by the Electromagnetic Endcap (EE) and the Hadron Endcap (HE) calorimeters along the direction of the beam pipe. The solenoid is placed in even further distance from the beam pipe than the HB, followed by the Hadron Outer (HO) calorimeter and finally the muon system, which is embedded into the iron return yoke of the magnet. In the forward direction the Hadron Forward (HF) calorimeter represents the outermost component of the calorimetry system. Different values of the pseudorapidity are indicated by thin lines originating at the collision point.

2.2.2 Calorimetry System

The main calorimetry system consists of two layers, both of which enclose the tracking system; an illustration for the positioning of these and some further detector components can be found in Figure 2.6. On the inner side there is the Electromagnetic Calorimeter (ECAL) [89, 90], which in turn is enclosed by the Hadron Calorimeter (HCAL) [91]. The ECAL is designed to detect electromagnetically interacting particles like photons, electrons and other charged particles, whereas the HCAL focuses on hadrons, which interact with the detector via the strong force and usually are not stopped by the ECAL.

The calorimetry system is important not only for the measurement of the particles that can be detected explicitly, but also for the determination of the overall balance of the transverse momentum in a collision event. This balance yields some information on those particles that cannot be detected, like neutrinos or various hypothesized particles in theories beyond the standard model.

A statistical description of the energy disposition of electrically charged particles traversing the detector material is given by

$$E(x) = E_0 \cdot \exp\left(-\frac{x}{X_0}\right), \tag{2.3}$$

wherein $E(x)$ is the energy of the particle after traversing a distance x in the material, E_0 is the initial energy, and X_0 is the *radiation length*, which is defined as the distance after which the particle energy has been reduced to $\frac{E_0}{e}$. In the case of hadrons the same formula can be used, but the *hadron interaction length* λ_I takes the place of the radiation length. Because of their direct relation to the physical absorption processes these two lengths X_0 and λ_I are employed as units for the specification of the amounts of absorbing material in specific parts of the detector.

Electromagnetic Calorimeter

The ECAL [89, 90] is built using lead tungstate ($PbWO_4$) crystals; they not only serve as *absorbers* but also fulfill the tasks of a *scintillator*. The interaction of particles with absorber material results in particle showers consisting of many secondary particles. While traversing a scintillator, on the other hand, the particles emit photons that can be detected and converted into an electrical signal that is roughly proportional to the energy of the original particle.

Having a single material perform both functions allows for a better energy resolution than that achieved by designs using two different materials. Lead tungstate has a density of $8.28\,\mathrm{g/cm^3}$ and a radiation length of $X_0 = 0.89\,\mathrm{cm}$, and as required for a scintillator it is transparent to visible light. It was chosen in part because of the high speed of its scintillating behavior: About 80% of the light of a given excitation is emitted within 25 ns, which corresponds to the design bunch crossing time.

The main components of the ECAL are the Electromagnetic Barrel (EB) consisting of 61,200 lead tungstate crystals, and the two Electromagnetic Endcaps (EE) located at $|z| = 314\,\mathrm{cm}$ and consisting of 10,764 crystals each. A schematic overview of the ECAL can be found in Figure 2.7. In the barrel the crystals are arranged as parts of larger *supermodules* including additional instrumentation, whereas in the endcaps they are arranged as *supercrystals* of 36 crystals each. Within each endcap the supercrystals are contained within two semicircular aluminum structures called *Dees*.

The crystals have lengths of 230 mm and 220 mm in the barrel and endcap regions, respectively, which corresponds to roughly 25 radiation lengths. While in the EB the detection of photons is performed by silicon avalanche photodiodes, the higher radiation doses in the EE would result in too high leakage currents using this technology; for this reason vacuum phototriodes are used instead.

In addition to the lead tungstate crystals the endcaps are fitted with *preshower detectors* consisting of lead absorbers and silicon detector layers, which provide a better angular resolution than the lead tungstate crystals. This allows for a better discrimination between single photons and neutral pions that decay to two photons with small angular separation.

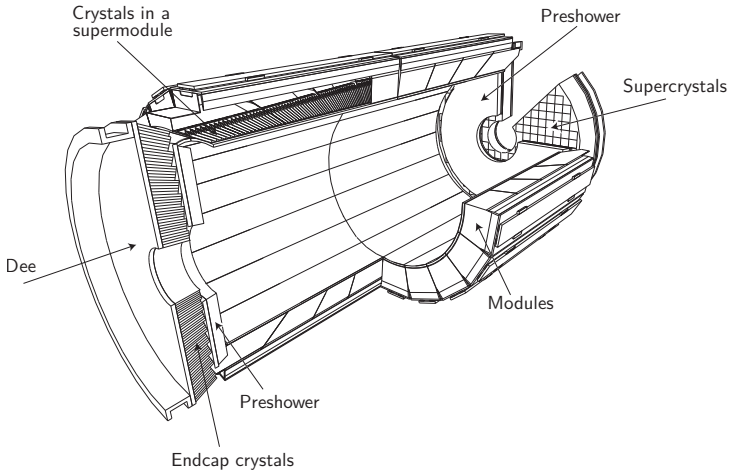

Figure 2.7: Schematic overview of the electromagnetic calorimetry system of CMS [73].

Hadron Calorimeter

In contrast to the ECAL the HCAL [91] is built according to a *sampling structure*. This means that the absorber and the scintillator are different materials, and the calorimeter itself consists of alternating layers corresponding to these two materials. Brass is used as the main absorber material, which is non-magnetic, has a comparatively high density $\rho = 8.53\,\mathrm{g/cm^3}$, and thus also has a short interaction length of $\lambda_I = 16.42\,\mathrm{cm}$. Plastic scintillator materials have been chosen for the optical system of the HCAL.

The HCAL consists of the Hadron Barrel (HB), Hadron Outer (HO), Hadron Endcap (HE), and Hadron Forward (HF) subdetectors; their arrangement can be seen in Figure 2.6 on page 29. The HB and HO cover $|\eta| < 1.3$, whereas the endcaps extend from $|\eta| = 1.3$ to $|\eta| = 3.0$ and the HF has a range of $3.0 < |\eta| < 5.3$. While the HB corresponds to a radiation length of only $5.82 \cdot \lambda_I$, both HE and HF correspond to approximately $10 \cdot \lambda_I$.

The HO is located outside the magnetic coil; the motivation for this subdetector lies in the fact that the HB, located within the coil, is not large enough to contain the hadronic showers completely. Being located outside the magnetic coil means that the solenoid acts as additional absorber material to the HO, extending its thickness to more than 10 hadron interaction lengths.

In the HF a different detection method is used than in the other parts of the hadron calorimetry; it employs copper as absorber material and relies on *quartz fiber calorimetry*. in this technique Čerenkov light is generated by particles traversing the quartz fibers faster than the speed of light in the material. The Čerenkov light then is detected using photomultipliers. Advantages of this technique lie in the high speed of the detection process, which lies on a scale much smaller than the design bunch crossing time of 25 ns, and in the insensitivity to neutrons, which have very large fluxes in the HF.

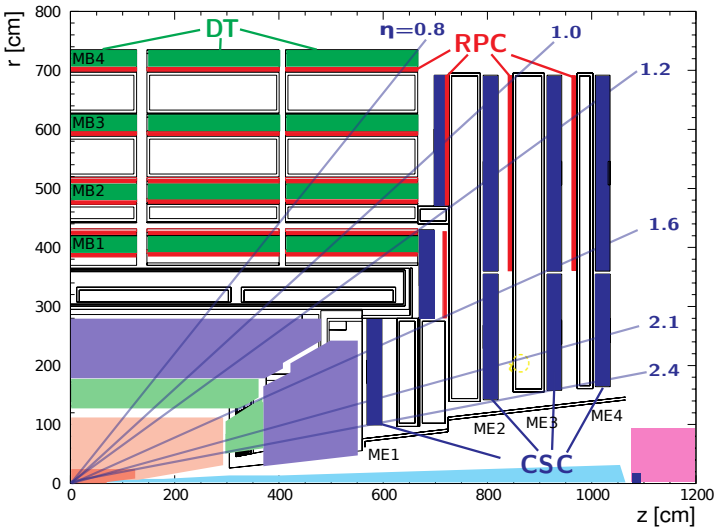

Figure 2.8: Illustration of the composition of the CMS muon system in one quarter of the detector [72]. While the four barrel muon stations MB 1 to MB 4 rely on Drift Tubes (DT), the four endcap muon stations ME 1 to ME 4 utilize Cathode Strip Chambers (CSC). Additionally both types of stations are equipped with Resistive Plate Chambers (RPC), which operate faster than the other used detection technologies.

2.2.3 Muon System

The muon system [92], built into the magnetic return yoke and thus immersed in a magnetic field of 2 T, makes up the outermost layer of the detector. It detects particles that pass through all other detector layers. As the name indicates the vast majority of these particles are muons, which due to their high mass have comparatively small energy losses via bremsstrahlung in the calorimetry systems. Muons occur in many of the most interesting processes of the standard model and of BSM models; their importance and the special care taken in the design of this subsystem is reflected even in the name that was chosen for CMS as a whole.

There are three components making up the muon system, as is illustrated in Figure 2.8:

The Drift Tube (DT) system covers $|\eta| < 1.2$, where the particle flux is comparatively low. With a gas mixture of 85% Ar and 15% CO_2 and a transverse length of 21 mm for the individual drift cells, the drift times in this subsystem are on the order of 380 ns.

The Resistive Plate Chamber (RPC) system covers $|\eta| < 1.6$ and consists of gaseous parallel-plate chambers made from phenolic resin. It provides additional timing information and compensates for the slow detection processes in the other muon subsystems, enabling track building at the trigger level.

The Cathode Strip Chambers (CSC) system in the endcap, finally, extends

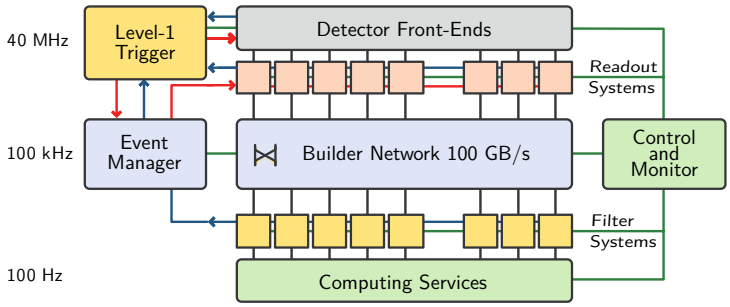

Figure 2.9: Architecture of the CMS data acquisition system [73]. In a first step the data rate is reduced from up to 40 MHz to about 100 kHz by the L1 Trigger; the readout systems are activated only for those events passing this first step. In the builder network a parallel processing of the event fragments is performed and the information is passed on to the HLT filter system. There reconstruction algorithms are applied and the decision whether to store the event is made, achieving a further reduction of the event rate to less than 400 Hz. The whole process is managed and supervised by the control and monitor system.

closer to the beam pipe than the other two subsystems, covering $0.9 < |\eta| < 2.4$. It consists of multiwire proportional chambers, covering roughly 5000 m^2 and using about 2.5 million wires. The individual stations of both the CSC and RPC systems are separated by the iron disks of the flux return yoke.

2.2.4 Trigger System

The large bunch crossing rate of up to 40 MHz at the LHC, coupled with the high amount of subdetector information and the fact that there usually are several simultaneous collisions per crossing, results in an almost unparalleled data rate of the detector readouts. Using present-day technology it is effectively impossible to store this amount of data in its entirety, and techniques need to be employed to reduce the data to a more manageable subset while discarding as little useful information as possible. This is the purpose of the trigger system, which performs a quick analysis of the detector information for each event and discards those events that are not deemed to be of interest.

The first part of the trigger system is the Level-1 (L1) Trigger [93], which is performed on custom-designed and programmable electronics and reduces the data rate to about 0.1 MHz. It operates on special primitive trigger objects provided by the calorimetry and muons systems, which means that a full readout of the detector data can be delayed until after this trigger has made its decision on the retention of an event. In a second step the High-Level Trigger (HLT) [94] further reduces the rate to under 400 Hz. It is implemented in software, using a custom version of the CMS analysis software, and runs on a dedicated computing cluster.

The combination of the electronic devices and computing cluster resources used for the trigger system is referred to as the *Data Acquisition* (DAQ) system. Its composition is illustrated in Figure 2.9.

2.2.5 Computing Infrastructure

The LHC computing grid [95] has been built to decentralize the infrastructure that is needed to process and store both the data and the simulated samples that are used as tools for analyses of the data. It has been designed as a hierarchical structure, with the different levels of the hierarchy serving slightly different purposes.

Historically a single Tier-0 center has operated directly at CERN, close to the DAQ. In recent times, though, it has been supplemented by a second center in Hungary. The Tier-0 performs the *prompt reconstruction* of the raw data provided by the DAQ, transforming the so-called RAW dataset containing detector data into the RECO datasets containing reconstructed hits and high-level physics objects. Each of the datasets held at the Tier-0 is transferred to at least one Tier-1 site, which serves as a backup and eases further distribution of the data.

Currently there are seven Tier-1 computer centers associated with CMS, with one of them being stationed at the Karlsruhe Institute of Technology. The Tier-1 sites perform further processing of the RECO datasets, reducing the amount of data that is needed per event to about 100 kb. The resulting *Analysis Object Data* (AOD) datasets contain only high-level physics objects and some ancillary information on the event. Aside from this processing task the Tier-1 centers also serve as data stores for datasets in various stages of processing, as indicated above.

The final tier of the centrally coordinated computing resources is represented by about 160 Tier-2 centers, of which about 50 are associated with CMS. They act as regional data storage and processing providers for both the needs of the CMS collaboration as a whole and specifically the individual analysis groups stationed in the vicinity of the center.

3 Simulation and Reconstruction of Collision Events

Collision events at the LHC typically result in the creation of a large number of particles, which cause an even larger number of energy depositions in the detector material. The corresponding electrical signals in the various detector components need to be processed by algorithms specifically designed to reconstruct the tracks and energies of the detected particles and, in a second step, to reconstruct the original particles that had been part of the hard scattering process.

In general this reconstructed information does not allow a definite identification of the process that took place in any given event; only statistical statements can be made about the data. For this purpose the data are compared to simulations of the involved interactions that have been subjected to the same algorithms as the data events themselves. These simulations are commonly produced using *Monte Carlo* (MC) methods, which allow to calculate approximations of complicated multi-dimensional integrals by performing a random sampling of the parameter space according to given probability distributions. As the simulated samples undergo the same reconstruction procedures as the data, they allow not only a direct comparison to the data, but they also provide the possibility of optimizing the measurement method while having access to the true *parton-level* values of the simulation. Similarly, the simulations can also be used to derive the corrections that need to be applied to the reconstructed data in order to obtain distributions of parton-level quantities.

The first section of this chapter summarizes the steps needed for the generation of simulated events, as well as the programs that have been used to generate the samples used in this thesis. The second section gives an overview over the reconstruction algorithms that are applied to both data and simulation; it also details some essential corrections that are applied to the samples.

3.1 Generation of Simulated Events

The generation of simulated events is separated into several different steps, as is indicated by Figure 3.1. This factorization is performed mainly because the non-perturbativity of the strong interaction at low energy scales, introduced in Section 1.1, requires dedicated approaches for the description of the composition of the proton as well as for the modeling of gluon splitting and soft or collinear gluon

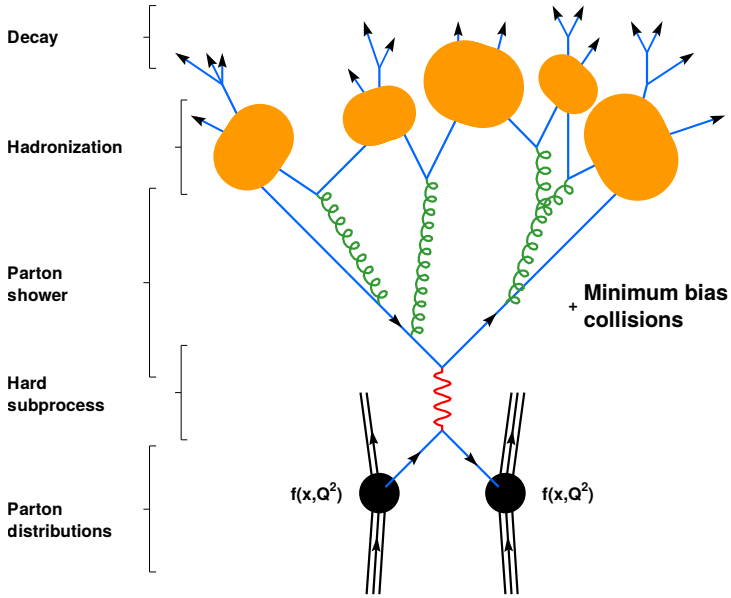

Figure 3.1: Schematic overview of the Monte Carlo event generation stages, adapted from [96].

radiation processes. For the hard scattering, however, the perturbative approach provides the best precision.

Parton distribution functions describe the energy distributions of the quarks and gluons within the colliding protons. They are used as input for the initial state configurations of the first calculation step, which simulates only the *hard scattering* processes. For reasons of computational complexity this stage can only encompass a limited number of radiated particles; any additional, generally softer radiation is added in a second step, the so-called *parton shower*. The *hadronization* stage recombines the color-charged particles produced in earlier event generation phases into color-neutral hadrons. Afterwards the *decays* of any remaining short-lived particles are simulated. Finally, a simulation of the particle interactions with the detector and the resulting signal data need to be performed.

The steps summarized above are complemented by a modeling of the effects caused by the proton remnants and the simultaneous detection of multiple collision events.

Hard Scattering

The hard scattering is calculated using perturbation theory, with calculations for the individual transition amplitudes being represented by Feynman diagrams. These diagrams are part of a formalism for the comparatively complicated integrals that are involved in the calculations. The frequencies and energy distributions of the initial particles for the collision processes are given by the PDFs of the protons.

This simulation step also incorporates the decays of very short-lived particles

that have been produced at this early stage, for example the top quarks and W bosons. Only their decay products are subject to the later steps of the event generation.

As explained in Section 1.1, the perturbative approach requires the strong coupling constant α_s to be small and thus to lead to a quick convergence of the perturbation series. This is the case for interactions with a high momentum transfer Q^2, which consequently is a prerequisite for a process to be treated as part of the hard scattering step.

Parton Shower

The second step, often performed by a different program than the first, simulates soft gluon radiation off the color charges. Such radiation effects, however, can also be part of the first simulation step. This ambiguity of how a given radiation should be simulated and how to ensure the sum of both steps yields the right amount of radiation has led to several different so-called *matching schemes* for the two steps. Some additional information on this topic can be found in Section 3.1.1.

The parton shower uses comparatively simple models for the low-energy interactions of QCD; gluon radiation is described by using the DGLAP QCD evolution equation [97–99] for the branchings, which allows to calculate the radiation probabilities at low energies and small angles using the more precisely understood behavior at higher energies. The models are tuned to the results of appropriate measurements; various different tunes exist, and new tunes are developed as new measurements are taken.

The radiated particles themselves are generated in an ordered cascade, moving backward in time for ISR and forward for FSR. The shower evolution parameter that is used to represent time for the ordering varies among the different implementations, with the most common approaches being a decreasing order in the radiation energy or in the angle of the radiation. To avoid singularities for soft and collinear radiation effects, a cut-off parameter is introduced that typically is defined to be on the order of 1 GeV. The actual calculations of the branchings employ the so-called *Sudakov form factors* [100], which represent the probability of *not* observing a branching within a given range of the shower evolution parameter.

In addition to the considerations detailed above, the simulation of ISR also needs to take into account what kind of radiation effects are already modeled as part of the PDFs themselves; this depends on the scale at which the PDFs are evaluated.

Hadronization and Decay

As the energies of the interactions decrease even further, QCD confinement becomes the dominant effect. The produced color-charged particles cannot permanently exist as free particles and thus recombine into color-neutral hadrons.

This hadronization is described by phenomenological models that, just like the parton shower models, need to be tuned to measurement results.

One important example of such a hadronization model is the *Lund string model* [101]. It models the interactions of two color-singlet particles using the concept of color-flux tubes that are spanned between the particles. The energy of the tubes is depleted by repeatedly creating new quark-antiquark pairs from them, breaking the tubes in the process and introducing new ones in their stead.

The most prominent alternative approach is the *cluster hadronization model* [102, 103], which is of lesser importance for this thesis. Here as a first step any gluons are split non-perturbatively into quark-antiquark pairs. Clusters are formed on the basis of color-singlet combinations of the particles; decays of these clusters are then calculated according to the density of states with appropriate quantum numbers.

After the hadronization process a large number of baryons and mesons have been generated. Many of them have small lifetimes and decay before interacting with the detector; these decays are simulated at the end of this phase. They are performed based on the known branching ratios for the decays of the individual particles, as they can be found in reference [27] and earlier issues of the same publication.

Underlying Event and Pileup

The term *underlying event* refers to effects related to the proton remnants of the collisions. These include multiple interactions of the partons, as well as color connections between the remnants and final-state particles, which affect the hadronization process.

Pileup events, on the other hand, are additional collisions within the same bunch crossing (*in-time* pileup) or in bunch crossings directly before or after the one of the considered event (*out-of-time* pileup). The particles produced in these additional collisions result in detector readouts that are intermixed with the ones of the more interesting collisions; in the case of the out-of-time pileup this happens because the limited temporal resolution of the detector systems does not allow for a full separation. A multitude of strategies is employed to reduce the impact of pileup events on the measurements; they are discussed together with the corresponding parts of the general event processing in later sections of this thesis.

Pileup events predominantly are made up of those processes that occur most often at hadron colliders, i. e. low-energy QCD $2 \to 2$ scattering processes. As these are the events that dominate any dataset that is taken without specific selection criteria, they are also called *minimum bias events*.

In general the average number of pileup events is a function of the luminosity of the collider. The dataset analyzed in this thesis contains an average of about 20 pileup interactions per event; the actual frequency distribution can be seen in Figure 3.2.

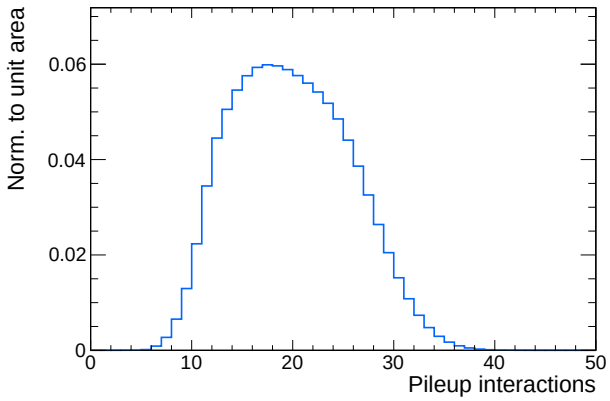

Figure 3.2: Pileup distribution in the analyzed dataset; the distribution has been calculated using the tools described in reference [104].

3.1.1 Event Generators

The simulation steps described above are performed by programs called *event generators*. Many of these programs specialize on a specific subset of the steps, though some implement the full event generation chain.

Among the matrix element generators simulating the hard scattering process, two classes of generators need to be distinguished.

Generators like MadGraph/MadEvent [105–108] and Alpgen [109] only calculate processes at leading order; additional radiation can, however, be simulated by separately calculating the leading order matrix elements of the given process with specific numbers of additional radiated particles. This necessitates the *merging* of the individual subprocesses with different jet multiplicities, for which the CKKW [110, 111] and MLM [112] schemes have found widespread adoption. The leading-order approach in principle allows for a very precise modeling of the radiated particles, but effects due to loop diagrams or diagram interference – like the interference causing the charge asymmetry in the SM – are not modeled correctly.

The inclusion of such effects is the advantage of next-to-leading order generators like Powheg [57] and MC@NLO [113, 114]. They typically do not, however, support the modeling of additional jets as described for the leading-order generators. Taking $t\bar{t}$ production as an example, a single additional radiated particle is simulated as part of the NLO matrix element, but all further radiation needs to be supplied by the parton shower. Only recently this limitation has been lifted as generators using the *FxFx* procedure [115,116] for the merging of NLO calculations have been developed; however, no suitable samples generated using this method were available for this analysis.

The parton shower and the hadronization are most commonly simulated using either Pythia [117] or HERWIG [103]. These programs additionally also provide leading-order matrix element generation for 2→2 processes and thus can simulate pileup events. However, for the hard interactions of signal and background processes usually one of the more specialized programs detailed above is used instead.

Several techniques exist for the matching of matrix element generation and parton shower. For LO generators this is done in the context of the CKKW and MLM schemes that are also used for the merging, whereas NLO calculations are usually matched using the Powheg method [56, 118] or the MC@NLO matching scheme [113, 114]. Some information on the latter two techniques can be found below in the descriptions of the associated generators.

In the following the event generators most relevant to this thesis are described.

Powheg

The program package Powheg Box [57], commonly referred to as Powheg, is a matrix element generator providing NLO event generation. Interfaced to Pythia for the calculation of parton shower and hadronization, Powheg version 1.0 provides the main signal sample of this analysis.

The matching to the parton shower is performed using the eponymous Powheg method [56, 118]. In this method the matrix element generator always produces the hardest radiation of the event. The parton shower, operating afterward, is restricted to producing only softer radiation. This procedure has the advantages of being comparatively easy to implement and of being able to perform the matching without relying on the introduction of events with negative weights, which complicate the statistical analysis and can lead to non-physical results in regions of low statistical power. It has been found, though, that the method yields mismodeling in some phase space regions [119], which is the main point of criticism leveled at it.

MC@NLO

Just like Powheg, MC@NLO is a matrix element generator for calculations at NLO. However, it employs the MC@NLO matching scheme [113,114], wherein the matrix element generator includes explicit corrections to remove the contributions to the cross-section calculation that later would be added a second time by the parton shower generator. This has the disadvantage of needing an explicit implementation for every combination of matrix element generator and parton shower simulation, and it results in the introduction of a significant number of negatively weighted events.

Due to the unavailability of suitable simulated samples, MC@NLO is not used for the analysis in this thesis; it is described only to provide context for the matching scheme implemented in Powheg.

MadGraph

MadEvent [106] is a leading-order event generator that relies on MadGraph [105, 107, 108] to calculate the amplitudes for a given process along with mappings for the integration over the phase space. The combination of these programs is commonly referred to as just MadGraph. The samples that are used in this thesis have been generated using version 5.1.3.30.

The MLM scheme [112] for matching and merging is employed for the MadGraph samples used in this thesis. It relies on a clustering of the generated particles after the parton shower, and it rejects all generated events in which the clusters do not satisfy specific criteria that depend on the original number of generated partons in the hard matrix element. A more detailed explanation of this scheme can be found in reference [112].

Pythia

Pythia [117], though able to perform the full event generation including the hard scattering by itself for some processes, is most commonly used for the modeling of the parton shower, hadronization, and particle decays, as well as the underlying event and pileup interactions. In accordance with that the simulated samples used in this thesis also rely on Pythia, version 6.426, for the simulation of those steps. Only the decays of τ leptons constitute an exception; they are simulated using version 27.121.5 of the dedicated Tauola [120] package.

Though it supports several ways of simulating the parton shower and the hadronization, Pythia by default calculates p_{T}-ordered showers and hadronization according to the Lund string model [101].

HERWIG

HERWIG [103] fulfills a role that is very similar to the one of Pythia. In contrast to Pythia, however, it uses angular-ordered showers, and it employs a cluster model for the hadronization. For this reason a sample generated using HERWIG, version 6.520, is used in this thesis for a determination of the systematic uncertainty in the effects simulated by Pythia.

3.1.2 Detector Simulation

The MC generators detailed above by themselves only simulate the behavior of particles in a vacuum. To attain a comparability of simulation and data, a simulation of the interactions with the detector material and the magnetic field needs to be performed. This simulation relies on an intricate model of the CMS detector and encompasses physical effects like ionization, multiple scattering, bremsstrahlung and electromagnetic and hadronic showering. It also simulates the readout systems of the detector, allowing the simulation to calculate the same sort of information that is used for the analysis of the data.

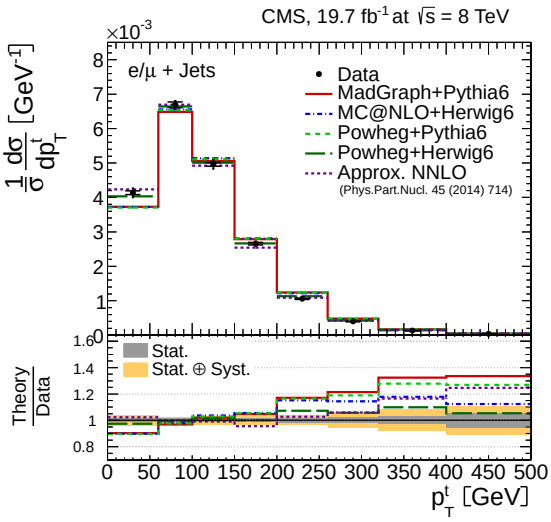

Figure 3.3: Mismodeling of the top quark p_T spectrum as observed by a different CMS analysis [123].

The full detector simulation used for the generation of the main samples of this thesis is based on the GEANT4 [121] toolkit. Some samples used for the estimation of systematic uncertainties instead are generated using the *CMS Fast Simulation* (FASTSIM) package [122], which allows for event production rates that are faster by a factor on the order of 100, but cannot achieve the same level of precision as the GEANT4-based simulation.

3.1.3 Top Quark p_T-Reweighting

Differential cross-section measurements in top quark pair production at CMS [123] have shown that the transverse momenta of the top quarks in $t\bar{t}$ production on average are larger than those simulated by the combination of POWHEG or MADGRAPH and PYTHIA. This finding agrees with the low-p_T results of theoretical calculations for these variables [124]. One of these measurement results is shown in Figure 3.3.

To account for this, the affected simulated samples are reweighted according to a prescription derived from the measurements described above. Each event is weighted with a factor

$$w = \sqrt{f_t \cdot f_{\bar{t}}}\,, \tag{3.1}$$

wherein the two factors f_i for t and $\bar{t}$ are calculated from the generator p_T of the respective top quarks:

$$f_i = \exp\left(0.156 - 0.00137 \cdot \frac{p_{T,i}}{\text{GeV}}\right) \tag{3.2}$$

As the origin of the mismodeling is not yet fully understood, an additional systematic uncertainty is assigned. This is described in Section 5.6.2.

3.2 Reconstruction of Events

The *reconstruction* of the collision events concerns itself with all tasks that are necessary to translate the electrical signals that are generated in the detector into information on the particles that caused these signals. These algorithms can be applied on data just as well as on the results of the detector simulation in the simulated samples. Almost everything that is needed for the reconstruction of CMS events is collected within the CMS software CMSSW [72].

The most common reconstruction method for analyses of 8 TeV data collected at CMS has been the so-called *Particle Flow* (PF) reconstruction [125–127]. Compared to simpler algorithms it has the advantage of combining information from all detector systems in an effort to measure the kinematic properties of each particle separately. It starts out by fitting the measurements of the tracking system, calculating trajectories of the electrically charged particles traversing it. In a second step the trajectories are associated to energy deposits in the calorimetry and muon systems, which help to determine the identity of the particle. Depending on which kind of particle it is identified as, different algorithms are used to calculate the particle four-momentum from the available detector information. Calorimeter deposits that are not associated to tracks are used to reconstruct photons and neutral hadrons. As a result the PF produces a list of reconstructed electrons, muons, photons, and both charged and neutral hadrons.

In a final reconstruction step jets can then be reconstructed from the PF candidates using a clustering algorithm.

3.2.1 Reconstruction of Tracks

In the ideal case the trajectories of charged particles within the magnetic field established by the solenoid have the shapes of helix sections. Due to interactions with the detector material there are deviations from those ideal trajectories. It should be noted, however, that these same interactions are also what creates energy deposits – so-called *hits* – in the detector, which are essential for the detection and reconstruction of the particles.

The calculation of a trajectory from the individual hits [128] is performed using six passes of the *Combinatorial Track Finder* (CTF) [129], which in turn relies on iterative applications of a *Kalman Filter* (KF) track finder [130]. Each pass of the CTF uses slightly different parameters to allow for the reconstruction of different classes of tracks; if a found track satisfies the quality criteria of a given pass, the associated hits are excluded from consideration for the subsequent passes.

As a first step a *seed* for the track finding is selected; in the first two phases, for example, a group of three or two hits in the pixel detector is combined with an additional assumption of the particle originating in the beam spot. Using this basic building block the KF can build a first estimate of the track and iteratively extrapolate it outward to find additional hits that can be associated to it, improving its precision. The extrapolation accounts for the influence of the magnetic field and for the possibility of energy loss and scattering of the particle.

If two trajectory candidates share a certain fraction of their hits, typically of the order of 20% relative to the track with fewer hits, only the track with a larger total number of hits is kept. Should they have the same number of hits, only the candidate with a lower χ^2 value in the fit to the hits is retained.

After all hits of a candidate track have been found, a new fit to those hits is performed, avoiding biases of the original track finding stage such as the beam spot constraint. Finally, the result of this fit iterating from the inside to the outside of the detector is used as the input for a smoothing stage that iterates from the outside to the inside, yielding the best estimate of the track parameters for all points.

The track reconstruction also encompasses a variety of quality criteria that must be passed for a track to be kept. One important example of such a criterion is a limit on the maximum number of detector layers that contain no associated hits even though the track passes through them. Others are related, for example, to the reduced χ^2 of the fit or to the significances of the determined impact parameters.

3.2.2 Reconstruction of Interaction Vertices

A determination of the location of the vertices where particles originate within a given event is important for several reasons, among them an increased precision of the track fitting and a suppression of the contributions from pileup events, which have their origins in vertices different from the one of the main collision.

The reconstruction of such *primary vertices* consists of two steps: In the *vertex finding*, sets of tracks are built that the vertex candidates can be created from. In the *vertex fitting*, on the other hand, the vertex parameters for a given group of tracks are determined using a χ^2 minimization. The tracks that are used for these steps need to satisfy several quality criteria to be considered at all: They need to have at least 2 hits in the pixel detector and 7 hits in the silicon strip detector, and the χ^2 of the track fit divided by its number of degrees of freedom (the *reduced* χ^2) must not be larger than 5.0.

The primary vertex that corresponds to the largest sum of squared track p_{T} values is the one that is used for the later parts of the event reconstruction and for the global track fits.

3.2.3 Reconstruction of Electron Candidates

Electrons generate hits in the tracking system and deplete their energy into the electromagnetic calorimeter, where due to their high ratio of electric charge over mass they radiate highly energetic bremsstrahlung and thus initiate an electromagnetic shower. Electron candidates can thus be reconstructed using information from the tracking system and the ECAL [131]. The track fitting is seeded with superclusters of energy deposits larger than 1 GeV; the use of superclusters is motivated by the helicity of the tracks causing the emission of bremsstrahlung and thus a spread of the signal along the ϕ-direction. The fit itself

is performed using a Gaussian sum filter [132, 133], which considers the nonlinear effects due to the bremsstrahlung losses.

To avoid the misidentification of charged hadrons and other particles as electrons, some criteria [131] are imposed that, for example, limit the fraction of energy that may be deposited in the HCAL, or that require a good agreement between the pseudorapidities of the supercluster and of the extrapolated track.

3.2.4 Reconstruction of Muon Candidates

Being charged particles, muons cause hits in the tracking system. However, their lower charge-to-mass ratio as compared to electrons results in strongly reduced amounts of bremsstrahlung radiation in the calorimetry systems. They thus deposit a significant part of their energy in the muon system, which only rarely are reached by other charged particles and serve as a good way of identifying muons.

Within the CMS collaboration there are two established ways of reconstructing muons [72, 134], leading to objects called either *tracker muons* or *global muons*.

Tracker muons are reconstructed from the inside out by starting with tracks from the tracking subsystem, which are extrapolated to find associated hits in the muon system that allow an identification as a muon track. This approach is preferable for muons with very low energies ($p_\mathrm{T} \lesssim 5\,\mathrm{GeV}$) as they only rarely give rise to hits in more than one muon station.

Global muons represent the more accurate approach for higher muon energies. Tracks are generated both starting from the tracker as well as starting from muon chamber deposits. The global muon reconstruction extrapolates these into a common region and tries to find matching tracks. When a matching has been found the hits of the tracks are combined in a KF fit to reconstruct the global muon track.

Similar to what is done for electrons, additional criteria can be imposed on the muon candidates to suppress misidentifications of other particles. One important example of a source of misidentified muons are *punch-through hadrons*, which are highly energetic hadrons that are able to reach the muon chambers. These particles, however, also leave significant energy deposits in the ECAL and the HCAL, which can be used to discriminate them from muons.

3.2.5 Reconstruction of Photons and Hadrons

After the removal of electron and muon candidates identified via the methods described above, the remaining tracks and energy deposits are considered to find candidates for photons and hadrons.

In a first step the tracks are linked to deposits in the ECAL and HCAL that they come close to. The next steps of the reconstruction then depend on the difference between the momentum estimate derived from the track and the energy estimate calculated from the calorimetry:

If the calorimetry estimate yields a smaller value or a value that is compatible to the momentum estimate, the reconstruction treats this candidate as a charged hadron. In the case of significant differences between the two estimates only the more reliable track momentum is used to calculate the momentum and energy of the particle. Lacking more specific information, this is done using the assumption that the mass of the particle is that of a charged pion. In those cases where the two estimates are compatible, however, a calculation using both information sources is performed; the additional information from the calorimetry subsystems yields improvements for candidates where the tracker-based estimate is less precise, i. e. for particles with large particle energies and pseudorapidities.

Candidates for photons and neutral hadrons are reconstructed if the calorimetry indicates significantly larger energies than the track momenta, as the latter are sensitive only to charged particles and an energy excess in the calorimetry thus is likely to be due to neutral particles. Because it has been found that only 3% of the ECAL energy of a jet is deposited by neutral hadrons, whereas 25% of the deposits are caused by photons, the reconstruction intentionally is biased to find a larger number of photons. It should be noted, however, that within jets the photons themselves typically arise from the decay of neutral pions. If the excess of the calorimetry-based estimate over the tracker-based estimate is smaller than the ECAL deposition as a whole, only a photon candidate is reconstructed. If on the other hand the excess is larger, indicating significant energy depositions in the HCAL, a hadron candidate is reconstructed in addition.

Finally, the remaining clusters in the ECAL and HCAL that could not be linked to tracks are used to reconstruct further candidates for photons and neutral hadrons.

3.2.6 Reconstruction of Jets

As introduced in Section 1.1, the production of highly-energetic color-charged particles in the collisions leads to the production of jets that consist of large numbers of hadrons and their respective decay products. To gain information on the original partons, the jets need to be identified and reconstructed from the individual particles using a *clustering algorithm*.

Clustering Algorithms

An algorithm needs to fulfill two important criteria to be a valid choice for jet clustering: The criterion of *infrared safety* means that the result of the jet clustering needs to be stable in the presence of additional low-energy radiation. Contributions of this kind occur due to the emission of soft gluons, and detector noise can be indistinguishable from such effects, as well. *Collinear safety* similarly requires the jet clustering result to remain stable when a single particle's momentum is redistributed to several particles of low angular separation. Physical processes

necessitating such a criterion are low-angle gluon radiation and gluon splitting, which are common effects in the parton shower.

The main class of clustering algorithms that are used in modern high-energy physics consists of the *sequential recombination algorithms*. Compared to other algorithms that perform a geometric clustering using cones, they have the advantage of fulfilling both infrared safety and collinear safety, and they are easier to incorporate into theoretical calculations. It is also possible to implement the sequential algorithms in such a way that their computational cost is comparatively low – though not necessarily lower than that of cone algorithms.

In sequential recombination algorithms the particle candidates are combined iteratively depending on pair-wise distance metrics $d_{i,j}$ that are defined as

$$d_{i,j} = \min\left(p_{\mathrm{T},i}^{2n}, p_{\mathrm{T},j}^{2n}\right) \cdot \frac{\Delta_{i,j}^2}{D^2} \,. \tag{3.3}$$

In this equation $\Delta_{i,j}$ indicates the distance of the objects in the η-ϕ plane, D is a resolution parameter that determines the size of the final clusters, and n is a parameter that differs between different algorithms of this class, adjusting how the distance metric is calculated.

For each iteration of the algorithm the pair of objects with the smallest value of $d_{i,j}$ is merged into one object. The merging process ends when the smallest distance $d_{k,\,\mathrm{beam}}$ between an object k and the beam, defined as

$$d_{k,\,\mathrm{beam}} = p_{\mathrm{T},k}^{2n} \,, \tag{3.4}$$

is smaller than all other distance metrics $d_{i,j}$.

As indicated above, the individual algorithms of this class differ in the value used for the parameter n. The k_t algorithm [135] uses $n = +1$, whereas the Cambridge-Aachen algorithm [136, 137], which often is used for the analysis of strongly boosted topologies, uses $n = 0$. Finally, the anti-k_t algorithm [138] uses $n = -1$; it is the default algorithm for jet reconstruction within CMS, and it is the algorithm used for the jet clustering in the samples used for this thesis.

Due to the use of a negative value for n, the clustering of the anti-k_t algorithm tends to be centered on high-p_{T} candidates, which incorporate other nearby candidates before those can form low-energy clusters of significant sizes among themselves. The jet formed from a given high-p_{T} candidate tends to be conical as long as there are no competing high-p_{T} candidates within a range of $2D$. Otherwise the jet shapes are clipped depending on the transverse momenta of the associated candidates. This is illustrated in Figure 3.4.

Aside from clustering the PF candidates to reconstruct jets for experimental measurements, it is also possible and useful to apply the clustering algorithms to particles representing the truth information of an event generator. Jets that are built from the generated stable particles that are present after the hadronization

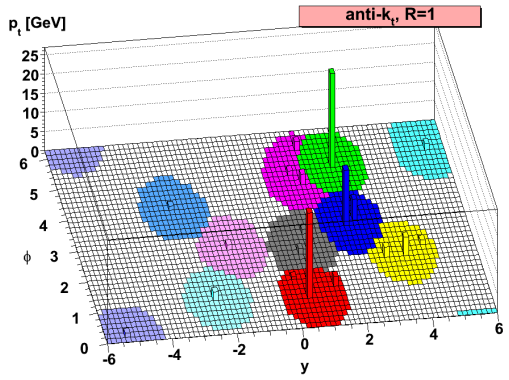

Figure 3.4: Illustration of the clustering behavior of the anti-k_t algorithm using a resolution parameter of $D = 1$ [138].

simulation are called *generator jets*. They are commonly used for resolution studies, and within the context of this thesis they are used for the clean definition of a reduced phase space of $t\bar{t}$ production that corresponds to the events that can be measured in the analysis; c. f. Section 4.5.

Jet Energy Corrections

The transverse momentum derived from the clustered particles of the jet, which is used to determine the transverse momentum of the originating particle, needs to be calibrated to account for several distorting effects of the measurement. For this purpose *Jet Energy Corrections* (JEC) [139] are applied to the jets, consisting of several consecutive correction steps called *levels*. Following common use only the first three of these levels are applied in the processing of the samples used in this thesis; they perform corrections for pileup, detector noise and instrumental response differences:

Level 1: The so-called *offset* correction compensates for the average energy contributions from pileup and detector noise.

Level 2: *Relative* corrections are applied depending on the jet η to account for uninstrumented detector regions and the non-compensating behavior of the calorimeters, i. e. for the response differences between those parts of a shower that are electromagnetic and those that are not. The jet response in regions close to the beam pipe is equalized to the one that is obtained for $|\eta| < 1.3$.

Level 3: The *absolute* correction recalibrates the jet energy as a function of the measured transverse momentum itself.

The less commonly used levels 4 to 7 provide additional, more specific corrections, accounting for example for calibration differences between different parton flavors, or for effects due to the underlying event.

In addition to the corrections described above, which are applied equally to events from data and simulation, there is a residual correction for data-to-simulation differences in the corrections of Level 2 and Level 3; it is applied on data only.

Jet Energy Resolution Correction

Measurements of the transverse-momentum imbalance in dijet events [140] show that the p_{T} resolutions of reconstructed jets are worse in data than in the simulation; this needs to be corrected for in the simulated samples. Table 3.1 contains the measured resolution ratios that are used for this correction.

As a prerequisite for the correction, a matching between the generator jets and the reconstructed jets is performed. Then the overall four-vector of the reconstructed jet is multiplied with a correction factor; this factor is calculated in such way that the p_{T} difference of the matched jets is modified by the right η-dependent correction factors, as given in Table 3.1

Table 3.1: Ratios of the jet p_{T} resolutions in data and simulation, depending on the η of the reconstructed jet [140].

$\lvert\eta\rvert$ range	σ(Data)/σ(Sim.)
0.0 - 0.5	1.079
0.5 - 1.1	1.099
1.1 - 1.7	1.121
1.7 - 2.3	1.208
2.3 - 5.0	1.254

3.2.7 b Tagging

The term *b tagging* refers to the process of identifying which jets originated from b quarks, which is done by analyzing the properties of the reconstructed jets themselves. It is an essential technique for many analyses; in the context of top quark pair production, its importance stems from the fact that top quarks decay to b quarks in almost 100% of cases, as explained in Section 1.2.2. Because of this a separation of b quarks and lighter quarks helps with both background suppression and event interpretation.

One of the characteristic geometric properties of b jets is illustrated in Figure 3.5. After being produced the b quarks form B hadrons, which decay via the weak interaction. Since the relevant CKM matrix element $V_{\mathrm{cb}} \approx 0.041$ is small, they thus have a comparatively long lifetime of $\tau_{\mathrm{B}} \approx 1.6\,\mathrm{ps}$. This results in flight distances on the order of $c\tau_{\mathrm{B}} \approx 480\,\mu\mathrm{m}$ and reaching up to several millimeters. The tracks of the decay products thus can be measured to converge at a secondary vertex that is displaced from the original interaction vertex by an impact parameter d_0, which is a behavior that is less commonly found in jets belonging to lighter quarks.

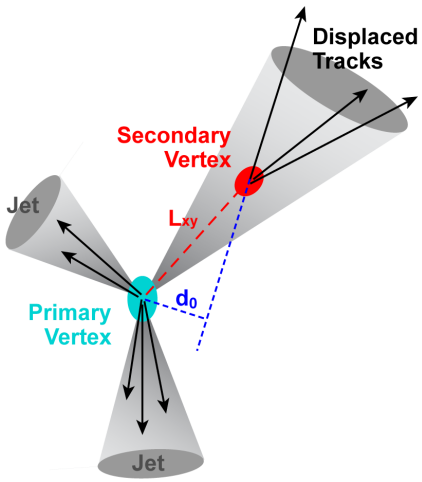

Figure 3.5: Illustration of the secondary vertex of a b jet, adopted from reference [141]. The b quark fragments into a B hadron, which has a comparatively long lifetime. Its decay products thus result in a jet with tracks that do not point to the primary vertex of the hard interaction but are displaced by an impact parameter. The impact parameter for one of the tracks is indicated as d_0. Often the displaced tracks can also be used to reconstruct the secondary vertex and its distance L_{xy} from the primary vertex.

Another useful quantity is the invariant mass of the reconstructed secondary vertex: Due to the rest mass of the b quark being significantly larger than that of any other particle originating jets, the reconstructed invariant masses of b jets also tend to be higher than those of light jets.

A multitude of b tagging algorithms has been invented; see reference [142] for an overview of some of the algorithms implemented in CMSSW. The algorithm used in this thesis is called *Combined Secondary Vertex* (CSV) [142]. Its discriminator is based predominantly on the reconstruction of a secondary vertex, as explained above, but it also considers additional track-based variables to provide separation power even when no secondary vertex can be found.

Typical performance figures to judge the power of a tagging algorithm are the tagging efficiency of b jets and the mistag rate of jets from lighter quarks. There is a trade-off between these two characteristic numbers, which can be adjusted by choosing different threshold values for the b tag discriminator; this is illustrated in Figure 3.6. For each tagging algorithm several working points are defined that correspond to a given mistag rate and the associated discriminator value. The advantage of using such a predefined working point is the possibility of relying on the results of dedicated efficiency studies.

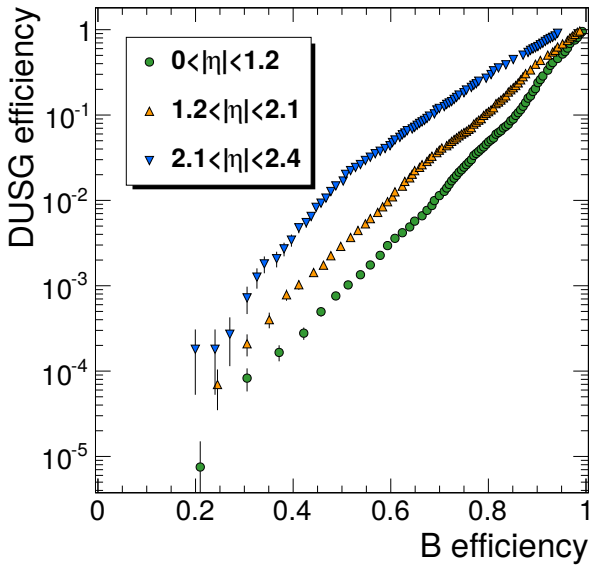

Figure 3.6: Efficiencies of light quarks and gluons (DUSG) and mistag rates of b quarks for the CSV b tagging algorithm at different pseudorapidities, as obtained in simulations [143].

3.2.8 Missing Transverse Energy

The collisions at the LHC can lead to the production of some particles that interact too weakly to be detected by the experiments. In the SM this applies to neutrinos, which are frequently produced in the decays of W bosons. Some of the superpartner particles introduced by supersymmetric theories, if they existed, would also show this behavior.

The measurement of the *missing transverse energy* ($\vec{E}_{\mathrm{T}}^{\mathrm{miss}}$) [125–127] allows to regain some of the information corresponding to such particles. Because the transverse momentum component of the initial state of the collisions is known and negligibly small, any imbalance of the transverse momentum of the final state is caused either by the measurement resolution or by undetectable particles.

In the PF approach that is used for this analysis, the uncorrected $\vec{E}_{\mathrm{T}}^{\mathrm{miss}}$ is defined as the negative vectorial sum of the transverse momenta of the reconstructed PF particles. It is corrected for by a propagation of the energy differences $\Delta\vec{E}_{\mathrm{prop}}$ that are introduced via the jet energy resolution correction and via Level 2 and Level 3 of the JEC (c. f. Section 3.2.6). The corrected missing transverse energy thus can be defined as

$$\vec{E}_{\mathrm{T}}^{\mathrm{miss}} = -\sum_{n=1}^{N} \vec{p}_{\mathrm{T},i} + \Delta\vec{E}_{\mathrm{prop}}\,. \tag{3.5}$$

4 Process Modeling and Event Selection

Though the operation of CMS entails the detection of an enormous number of collision events, generally only a minuscule fraction of the events corresponds to processes that are of interest for a given physical analysis. Figure 4.1 illustrates the orders of magnitude differences between the total collision cross section and the cross sections of specific processes.

For this reason it is necessary to design and implement event selections that can reduce the number of events from background processes while selecting a large fraction of the signal events. To understand which of the many possible selection criteria promise to provide the most benefit, it is necessary to understand the topology and the kinematics of the respective processes. Studies can be performed on simulated samples to optimize the selection criteria and to estimate the resulting yields of the contributing processes.

In the data taken during 2012 only one in 400 million collision events exhibited top quark pair production, which is the process that is studied in this thesis. The selection described in this chapter manages to extract from this dataset a sample that has a signal-to-background ratio of 80%.

The first section of this chapter introduces both the characteristics and the modeling of the signal and background processes of this analysis, as well as the data samples that are analyzed. The second section then details the actual selection criteria that are applied. Afterwards the data-driven modeling of the QCD multijet process is explained, followed by the fitting procedure used to extract an estimation of the different process yields from data. In the last section a generator-level selection is described, which is used to define a reduced phase space that can be measured with smaller model-dependence than it is the case for the full phase space of $t\bar{t}$ production.

4.1 Modeling of Signal and Background Events

4.1.1 Signal Process

As introduced in Section 1.2.2, this analysis centers on the semileptonic decay channel of top quark pairs, commonly referred to as the lepton+jets channel. The advantage of this decay channel lies in a good compromise between a clear signature, allowing a good reconstruction of the $t\bar{t}$ system and a significant reduction of background processes, and a high branching ratio.

Figure 4.2 shows a typical leading-order Feynman diagram of $t\bar{t}$ production and the ensuing top quark decay in this channel. The characteristic features are a

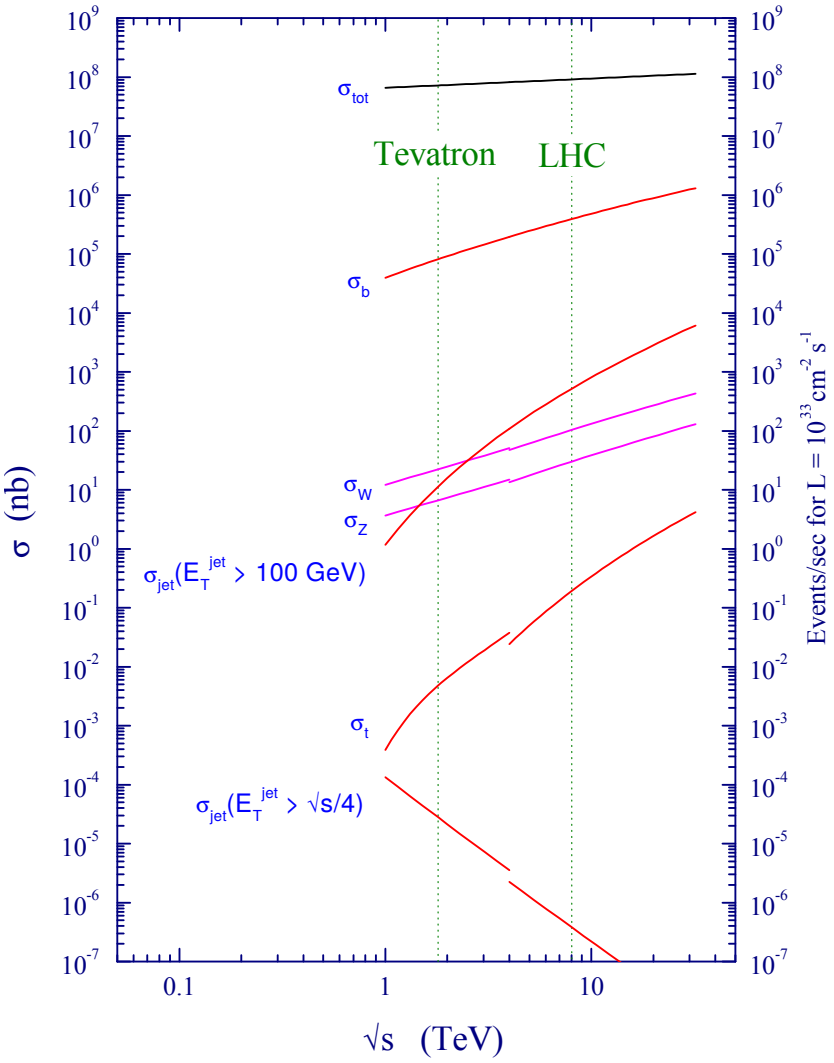

Figure 4.1: Predicted cross sections of some processes as functions of the center-of-mass energy $\sqrt{s}$, adapted from [144]. While for $\sqrt{s} < 4\,\text{TeV}$ the cross sections in proton-antiproton collisions are depicted, for $\sqrt{s} > 4\,\text{TeV}$ those in proton-proton collisions are shown. The dashed green lines indicate the center-of-mass energy of the Tevatron, $\sqrt{s} = 1.96\,\text{TeV}$, and the LHC center-of-mass energy in 2012 operation, $\sqrt{s} = 8\,\text{TeV}$. It can be seen that even at $\sqrt{s} = 8\,\text{TeV}$ the total inelastic proton-proton cross section, shown in black, is about nine orders of magnitude larger than the cross section of top quark production σ_t.

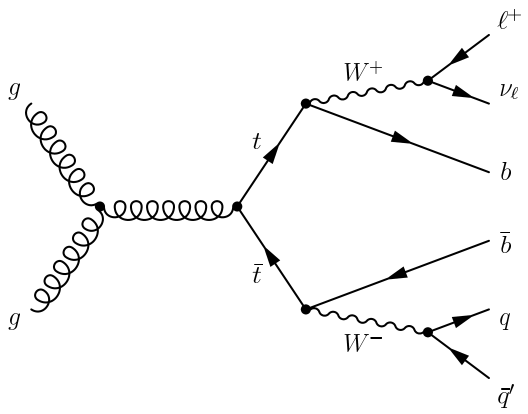

Figure 4.2: Example Feynman diagram of a $t\bar{t}$ event in the lepton+jets decay channel. Each of the top quarks decays into a b quark and a W boson. One W boson further decays into a charged lepton and the associated neutrino, whereas the other one decays into two quarks of different flavors.

charged lepton with high transverse momentum, two b jets that are produced in the decays of the top quarks, and two additional, lighter jets originating from the hadronically decaying W boson. Additionally, the production of a neutrino leads to some missing transverse momentum, but this fact is not used as part of the event selection.

Despite the name *lepton+jets channel*, only those decays are considered in which the charged lepton is either an electron or a muon. The tauon+jets channel is more complicated to handle and has a significantly worse reconstruction resolution, which is why it generally is considered only in analyses dedicated to this specific channel.

The main event generator used for the simulation of $t\bar{t}$ events in this thesis is Powheg. Being an NLO generator, it does simulate charge asymmetric effects in top quark pair production. However, to match theoretical calculations its predictions need to be enlarged by a factor of about 1.5 [53], as it lacks electroweak corrections and uses the unexpanded calculation scheme (c. f. Section 1.3.2). A second restriction is that it is only able to simulate the radiation of a single additional gluon; this introduces a significant reliance on the parton shower generator to correctly simulate any further radiation effects. The nominal sample relies on Pythia using the tune *Z2** for this task.

The CT10 PDF set [32] is used for the simulation of this process, and the top quark mass is set to $m_\mathrm{t} = 172.5\,\mathrm{GeV}$.

4.1.2 Background Processes

Even though the selection is optimized to select $t\bar{t}$ events, a significant fraction of the selected events corresponds to background processes. They pass the selection either because they do have the same signature as the lepton+jets channel or

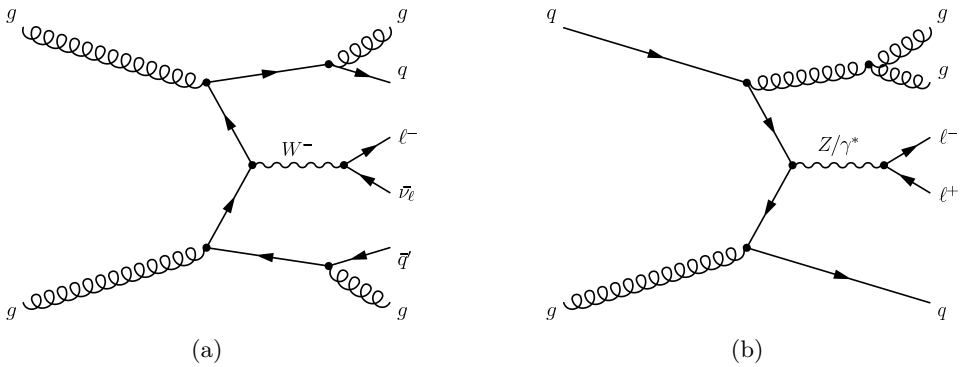

Figure 4.3: Examples of Feynman diagrams of W boson (a) and Drell-Yan (b) production in association with additional jets. As jets from gluons and quarks cannot be distinguished well on reconstruction level, W+jets production shows a signature similar to the one of the signal. The Drell-Yan+jets process similarly can appear like the signal if one of the leptons is not detected or is misreconstructed as a jet.

because misreconstructions of the physical objects cause them to appear as if the signature particles had been produced.

The production of W bosons, the Drell-Yan process, and single top quark production all frequently involve the production of highly energetic charged leptons. The required number of additional jets can be produced in higher-order diagrams of these processes.

Conversely, multijet events resulting from the strong interaction, hereafter referred to as *QCD multijet* processes, frequently involve a sufficient number of jets. However, it is significantly less likely for them to also produce the highly-energetic lepton of the lepton+jets signature.

W+Jets and Z/γ^*+Jets

Figure 4.3(a) demonstrates how the production of a W boson in association with additional radiation can have the same signature as $t\bar{t}$ production if the boson decays leptonically. Despite the low fraction of events with the necessary amounts of radiation and the requirement of b jets to be detected, this process constitutes the dominant background of the lepton+jets channel due to its high cross section.

The Drell-Yan [145] process with associated jet production, which encompasses the production of leptons via Z bosons or virtual photons as well as their interference, is a significantly less important background process. This is because it entails the production of two charged leptons instead of only one, as illustrated in Figure 4.3(b). Unless one of the leptons leaves the detector undetected or is misidentified as a jet, this allows to discriminate against the process in the event selection.

The simulated samples for these processes were generated by MadGraph

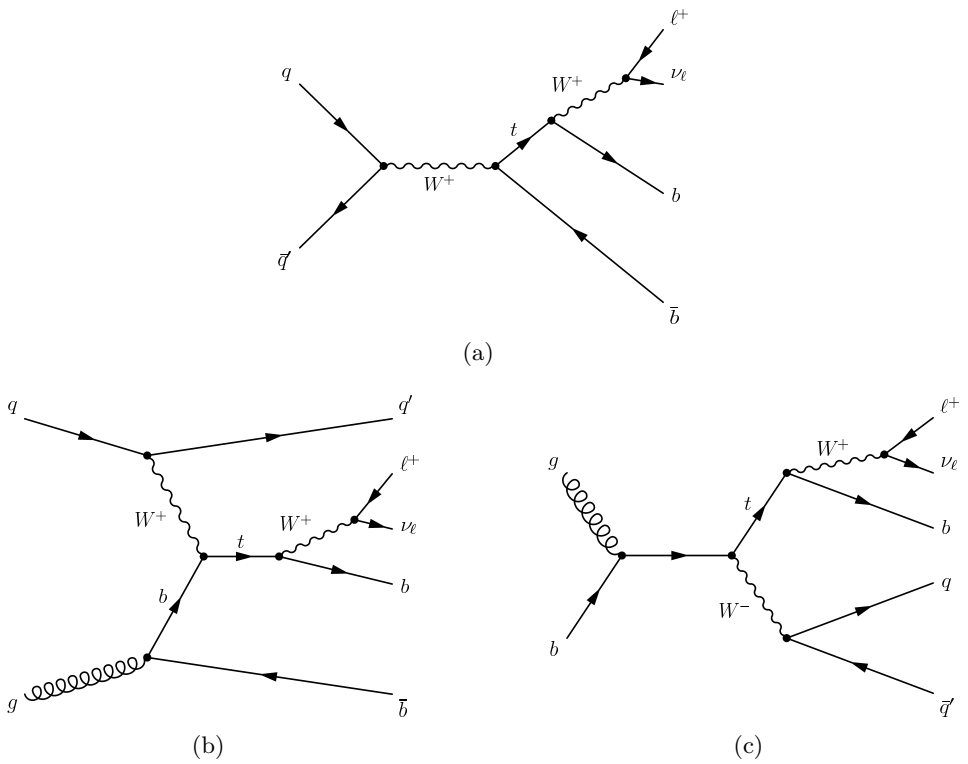

Figure 4.4: Examples of Feynman diagrams for the electroweak production of single top quarks. The *s*-channel is shown in (a), the *t*-channel in (b) and the tW-channel in (c). These processes can appear like the signal process if additional radiation occurs.

interfaced to Pythia. The sample for the Drell-Yan+jets process has been generated with the requirement of the produced lepton pair having a larger invariant mass than 50 GeV, allowing to maximize the amount of useful events achievable with the available computing resources. Because of the resulting dominance of the production via Z bosons this sample hereafter is referred to simply as *Z+jets*; this is in keeping with common terminology.

Single Top Quark Production

There are three different production channels for single top quarks: The *s*- and *t*-channels, which are named after the corresponding Mandelstam variables of the virtual W boson, and the tW-channel, which refers to the associated production of a top quark and a W boson. Figure 4.4 shows examples for the corresponding Feynman diagrams.

In the presence of additional hard radiation single top quark production can display signatures that are almost or completely indistinguishable from that of $t\bar{t}$ events in the lepton+jets channel. Due to the small overall cross section it nevertheless represents only a subdominant background contribution.

Just like the simulated signal events the samples for this process have been generated using POWHEG interfaced to PYTHIA, with a top quark mass of $m_t = 172.5\,\text{GeV}$. Due to the s-channel signature being less similar to $t\bar{t}$ production than the others, it constitutes an insignificant background contribution and is not taken into account within the analysis procedure.

QCD Multijet Processes

QCD multijet processes have a very high total cross section; this leads to them being an important background contribution even though only a very small fraction of the events can pass the event selection. The final states of this process group, as the name indicates, are dominated by quarks and gluons leading to jets. Some of the Feynman diagrams most relevant to this analysis are shown in Figure 4.5.

Due to the high number of jets in this process group the charged lepton is the less commonly produced part of the signal signature. However, even in the absence of a highly-energetic lepton events may be selected if one of the resulting jets is misidentified as a lepton. Alternatively, actual highly-energetic leptons can be produced as part of the weak decay of heavy baryons or mesons in the jets, as illustrated in Figure 4.5(a), or as part of photon conversions, as is shown in Figure 4.5(c). Some of the diagrams of this process class involve the production of B mesons and thus of real b jets, though wrongful tagging is also an important possibility of fulfilling the signal signature criterion on the detection of b jets. Similarly, the misreconstruction of individual physical objects due to imperfections of the detector can also result in the selection of otherwise inconspicuous events.

The low fraction of QCD multijet events that can pass the event selection poses a significant challenge to the simulation techniques. Typically only a very small number of the simulated events remains in the signal region, impairing the usefulness of the simulated samples. Consequently, within this analysis no such samples are used for the QCD multijet process. Instead a template is constructed from a sideband region in data; this is described in more detail in Section 4.3. Nevertheless some simulated samples have been used to extract illustrative predictions for the event yields of QCD multijet events in the selected data samples. Because the values are not used for the actual analysis, details on those samples are omitted in this thesis.

4.1.3 Simulated Samples

The simulated samples used in this thesis have been generated as part of the *Summer12* production campaign of the CMS collaboration. Table 4.1 summarizes the samples, the respective numbers of produced events, and the effective cross sections that are assumed for the corresponding processes.

The cross section of $t\bar{t}$ production has been determined at full next-to-next-to-leading order (NNLO) [146], whereas the single top quark production cross sections have been determined at approximate NNLO [124]. Both the cross sections of the Drell-Yan process and the production of W bosons in association with any

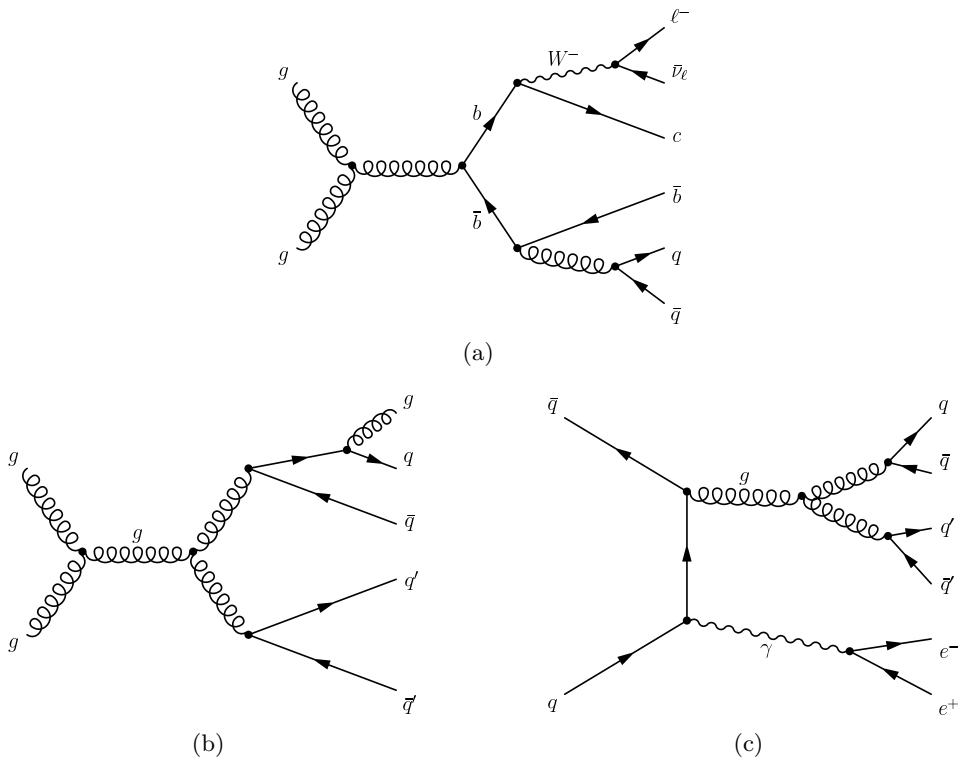

Figure 4.5: Examples of Feynman diagrams for QCD multijet processes. In (a) the production of a $b\bar{b}$ pair via the strong interaction is shown, including some radiative and decay processes that allow the process to approximate the signal signature. It needs to be noted that this diagram is only illustrative, as the b quarks generally hadronize before they decay. In (b) an event containing only quarks and gluons in the final state is depicted, which can appear to have the signal signature if one of the jets is misidentified as a lepton. The radiation of a real photon in association with additional jets is shown in (c). The photon converts into a charged lepton pair; the additional atomic nucleus that is required to absorb the recoil in the case of a real photon is omitted here.

Table 4.1: Overview of the most important simulated samples, with the numbers of generated events N_{prod} and the effective cross sections σ_{eff}.

Process	Generator / Decay Channel	σ_{eff} (pb)	N_{prod}
$\mathrm{t\bar{t}}$	POWHEG + PYTHIA	245.8	21 664 781
	POWHEG + HERWIG	"	21 745 199
	MADGRAPH + PYTHIA:	"	
	hadronic decay		10 525 470
	semilept. decay		36 625 589
	dileptonic decay		12 107 145
W+jets	$\mathrm{W} \to \mathrm{l}\nu$, all parton mult.	36 703	76 031 791
W+2jets	$\mathrm{W} \to \mathrm{l}\nu$	1750	34 017 243
W+3jets	$\mathrm{W} \to \mathrm{l}\nu$	519	15 505 398
W+4jets	$\mathrm{W} \to \mathrm{l}\nu$	214	13 373 510
Z/γ^*+jets	$\mathrm{Z}/\gamma^* \to \mathrm{ll}$, $m_{\mathrm{ll}} > 50\,\mathrm{GeV}$	3531	30 411 164
single top (t-channel, t)	inclusive	56.4	3 754 602
single top (t-channel, $\bar{\mathrm{t}}$)	inclusive	30.7	1 933 353
single top (tW-channel, t)	inclusive	11.1	497 302
single top (tW-channel, $\bar{\mathrm{t}}$)	inclusive	11.1	492 812

number of jets have been calculated [147] at full NNLO by members of the CMS collaboration using the software FEWZ [148], version 3.1.

In those cases where a process is split into several simulated samples, such as the different multiplicity samples of W+jets production and the different channels of single top quark production, the individual samples are renormalized and combined according to the shown cross sections before entering any other step of the analysis.

4.1.4 Data Samples

In this thesis data are analyzed that correspond to the full proton-proton collision dataset recorded by CMS in 2012. As explained in Section 2.2.4, only those events are recorded that pass one of the selections (*menus*) implemented as part of the trigger system. The outputs of trigger menus with similar criteria are collected into *primary datasets* to allow analyses to reduce the number of events that need to be processed as part of the event selection implemented outside the trigger system. The primary datasets used for this analysis are the *SingleMu* and *SingleElectron* datasets, which have undergone the reprocessing campaign of January 22nd, 2013. They contain the output of various trigger menus that require at least one highly-energetic electron or muon to be reconstructed by the trigger. Similarly, the triggers used for this analysis are defined only by criteria on the charged lepton; they are called "HLT_Ele27_WP80" and "HLT_IsoMu24_eta2p1". Equivalent implementations of these triggers are also applied on the simulated events to maintain comparability.

As the names indicate, these triggers require either an electron with $p_{\mathrm{T}} > 27\,\mathrm{GeV}$ or a muon with $p_{\mathrm{T}} > 24\,\mathrm{GeV}$ and lying within a range of $|\eta| < 2.1$. Both triggers

also include isolation criteria, i. e. they impose a maximum energy deposition in the detector that is allowed in the vicinity of the lepton candidate. These criteria help to discriminate against misreconstructed jets and against actual leptons that are produced within the jets.

The data selected are corrected for some known distorting effects. This is done by filtering events that show the corresponding phenomena, following the recommendations within the CMS collaboration [149]. One of these corrections, for example, filters events suffering from anomalous noise introduced by the photo multipliers in the hadron calorimeter [150]. Some other filters remove events in which the tracking algorithm has failed, or in which faulty EE supercrystal signals are detected. All of these filters remove an insignificantly small fraction of the events and can be assumed to not have a noteworthy effect on the physical quantities that are measured as part of this thesis.

4.2 Selection Criteria

This section concerns itself with the different criteria that are implemented as part of the event selection to reduce the amount of background contributions in the data sample. It starts with an introduction of the identification criteria for the individual physical objects that can be measured. After a rundown of the selection criteria, descriptions of some reweighting procedures are given; they are applied to the simulated events to correct for known modeling deficiencies in the selection efficiencies and in the pileup distributions. Finally, the results of the event selection are summarized.

4.2.1 Definitions of Physical Objects

Relative Isolation

One prerequisite quantity that is used for the definitions of the charged lepton candidates is the *relative isolation*. Additional energy depositions close to the trajectory of the lepton are considered to be a hint for additional particles that have been produced close to it. While in the signal process the lepton originates from W boson decays and generally is not accompanied by other particles, the leptons that are produced in the decays of hadrons of QCD multijet interactions, for example, are not as isolated. The relative isolation for electrons (muons) thus is defined as the sum of energy contributions in a cone with radius $\Delta R = 0.3\,(0.4)$ in η-ϕ-space, divided by the lepton p_{T}:

$$I^{\ell}_{\mathrm{rel}} = \frac{E_{\mathrm{CH}} + \max\left(0,\ E_{\gamma+\mathrm{NH}} - \rho \cdot \mathrm{A}_{\mathrm{eff}}(\eta)\right)}{p^{\ell}_{\mathrm{T}}}\,, \tag{4.1}$$

wherein E_{CH} is the energy deposited by charged hadrons and $E_{\gamma+\mathrm{NH}}$ is the estimated energy of neutral hadrons and photons. The definition as used here encom-

passes an area-based correction for pileup effects proportional to the transverse-momentum density of the event ρ, which is determined using k_t jets with a resolution parameter of 0.6. In this correction, A_{eff} is the effective area of the lepton as determined in data [151, 152]. For muons it is given as a function of the η of the muon candidate itself, whereas in the case of electron candidates it is a function of the corresponding supercluster η.

It should be noted that this definition of the relative isolation counter-intuitively entails lower values for more well-isolated leptons.

Electron Definition

For an electron candidate to be accepted as such by the event selection it needs to lie within $|\eta| < 2.5$ and have a transverse energy of at least 30 GeV. Candidates are rejected if their supercluster is within the transition regions between endcap and barrel of the ECAL, parametrized as $1.4442 < |\eta_{\text{sc}}| < 1.5660$. The relative isolation needs to be smaller than 0.1 for the candidate to be accepted.

Further criteria are performed as part of a multivariate electron identification [153], which combines various variables related to calorimetry and tracking parameters, but also transverse momentum and η of the electron. The resulting discriminant is required to be larger than 0.9.

The electron definition also encompasses a conversion rejection [154] aimed at identifying electrons that are created in the conversion of a real photon instead of as part of the hard interaction. To this end, a track-based photon conversion reconstruction with a vertex fit is performed. For an electron candidate to be rejected, an associated conversion candidate needs to pass several criteria:
No hit may be registered before the reconstructed vertex. The χ^2 value of the vertex candidate fit is used to calculate the probability of randomly observing an even larger value, based on the χ^2 distribution with the appropriate number of degrees of freedom; this probability is required to take a value larger than 10^{-6}. And finally, the projection of the distance vector between the reconstructed conversion vertex and the primary vertex onto the direction of the reconstructed momentum needs to be longer than 2 cm. This is motivated by the conversions happening at the earliest due to the beam pipe at around 3 cm, with the photon being assumed to have originated in the primary vertex.

Muon Definition

Muon candidates are required to have $|\eta| < 2.1$, $p_{\text{T}} > 26$ GeV, and a relative isolation smaller than 0.12. They need to be reconstructed successfully both as tracker muons and as global muons; see Section 3.2.4 for an explanation of these definitions. The reduced χ^2 of the global fit has to be smaller than 10 and the number of tracker hits has to be larger than 5. The longitudinal position of the muon track at its closest approach to the beam line is required to lie within 0.5 cm of the longitudinal position of the primary vertex. Furthermore, the global-muon track fit needs to contain at least one muon chamber hit, there must be muon

segments in at least two muon stations, and the track must contain at least one pixel hit.

Jet Definition

The jets that are reconstructed from PF objects for this analysis use the anti-k_t algorithm with a resolution parameter $D = 0.5$; details on the jet clustering can be found in Section 3.2.6. They have to lie within $|\eta| < 2.5$ and are required to have $p_{\mathrm{T}} > 30\,\mathrm{GeV}$. For this it should be kept in mind that the transverse momenta of the reconstructed jets are modified using the jet energy and jet resolution corrections described in Section 3.2.6.

Some additional jet identification criteria are applied to reduce the probability of electrons, photons, or calorimeter noise being misidentified as jets. The jets are required to have at least two constituents, and none of their fractions of neutral hadron, neutral electromagnetic, or charged electromagnetic energy contributions are allowed to be larger than 0.99. Furthermore, there needs to be at least one charged hadron that is reconstructed as part of the jet.

4.2.2 Selection Steps

The selection criteria outlined in this section are applied equally to the simulated samples and the data samples.

Primary Vertex Criterion

The event needs to have a *good primary vertex*, which is defined as a primary vertex for which the weighted sum of the tracks used in its reconstruction is larger than 4, and which lies close enough to the nominal interaction point; the latter requirement is defined in cylindrical coordinates as $|z| < 24\,\mathrm{cm}$ and $r < 2\,\mathrm{cm}$.

Lepton Selection

Exactly one isolated lepton, as defined in Section 4.2.1, is required to be reconstructed in the event.

Second-Lepton Veto

To reduce the contributions from the Z+jets background process and the dileptonic decay channel of $\mathrm{t\bar{t}}$ production, events are discarded if a second lepton is reconstructed. In order to achieve a good rejection rate the lepton identification criteria are loosened for this selection step. Loosely defined electrons need to have $p_{\mathrm{T}} > 20\,\mathrm{GeV}$, $|\eta| < 2.5$, a relative isolation that is smaller than 0.15, and a multivariate identification discriminant that is larger than 0.5. Loosely defined muons similarly must have $p_{\mathrm{T}} > 20\,\mathrm{GeV}$, $|\eta| < 2.5$ and a relative isolation that is smaller than 0.15. The many additional requirements enforced in the nominal muon identification are not required to be passed by loosely defined muons.

Jet Selection

The event is rejected if the number of reconstructed jets, as defined in Section 4.2.1, is smaller than four. As most processes do not entail the production of such a large number of highly energetic jets, this is a very important selection step for the reduction of the background processes.

b Tagging Requirement

Generally two b jets result from the decay of the two top quarks of $t\bar{t}$ production. Since not many processes produce b jets as part of their most common signatures, a requirement on the number of identified b jets is very useful to reduce background contributions.

In order to pass the selection an event needs to contain at least one jet, according to the definition in Section 4.2.1, that has been tagged using the medium working point of the CSV tagging algorithm [142]; c. f. Section 3.2.7 for details on this algorithm and the general concept of b tagging. The medium working point corresponds to a discriminator value of 0.679 and a tagging efficiency of about 70% for b jets. Consequently, in about 50% of $t\bar{t}$ events at least one of the b jets remains untagged. To retain a high signal efficiency the selection thus does not require both b jets to be found.

4.2.3 Corrections on Simulated Events

After the event selection additional corrections are applied to the simulated samples to account for known discrepancies between the data and the simulation.

b Tagging Scale Factors

The performance figures for the tagging of simulated jets do not agree perfectly with those of jets in data [155]. To account for this, scale factors are derived from the corresponding measurements and used to perform a reweighting [156] of the simulated samples.

This reweighting procedure operates independently of the information about jets having been tagged in the reconstructed event. Instead all possible combinations c of tagged and untagged jets are considered to calculate the weight, discarding only those combinations that would not satisfy the b tagging requirement of at least one tagged jet. For each combination the probabilities of observing this tagging behavior in data and in simulation are calculated as

$$P_{c,\text{Simulation}} = \prod_{i=\text{tagged jets}} \epsilon_i \prod_{j=\text{untagged jets}} (1 - \epsilon_j) \tag{4.2}$$

and

$$P_{c,\text{Data}} = \prod_{i=\text{tagged jets}} s_i\epsilon_i \prod_{j=\text{untagged jets}} (1 - s_j\epsilon_j)\,, \tag{4.3}$$

using the tagging efficiencies ϵ of the given jets in simulation, and the associated scale factors s, which describe the data-simulation differences. Both the efficiencies and the scale factors depend on the flavor of the given simulated jet, as well as on its p_{T} and η.

Sums over all considered combinations are performed for the two probabilities given above, and finally the event weight is calculated as the ratio of these sums:

$$w = \frac{\sum_c P_{c,\mathrm{Data}}}{\sum_c P_{c,\mathrm{Simulation}}} \,. \tag{4.4}$$

Lepton Selection Efficiency

Event weights need to be applied to the simulation to compensate for differing lepton selection efficiencies between data and simulation, with effects stemming from the tracking performance as well as trigger, isolation and general identification criteria. These scale factors, determined in tag-and-probe studies, depend on the flavor as well as the p_{T} and η of the selected lepton; they are documented in references [157, 158].

Pileup Reweighting

The simulated samples were generated at a time when the final pileup distribution of the full dataset could not yet be known precisely. They thus use a comparatively wide frequency distribution of pileup events, designed to give the flexibility of reweighting the events to match the pileup distribution that would be determined for data. The latter is calculated from the total proton-proton inelastic cross section and the instantaneous luminosities of the individual bunch crossings [104].

4.2.4 Selection Results

The application of the triggers and the event selection yields a total of 171 121 events in the electron+jets channel, and 192 123 events with a muon in the final state. Using the calculated integrated luminosity of the dataset $\mathcal{L}_{\mathrm{int}} = 19.7\,\mathrm{fb}^{-1}$, the theoretically predicted cross sections of the individual processes σ_{eff}, and their selection efficiencies in the simulation, the per-process contributions to this event yield can be estimated:

$$N_{\mathrm{est}} = \frac{N_{\mathrm{sel}} \cdot \mathcal{L}_{\mathrm{int}} \cdot \sigma_{\mathrm{eff}}}{N_{\mathrm{prod}}} \tag{4.5}$$

In this formula N_{prod} and N_{sel} are the numbers of generated and selected simulated events of the process, which together define the selection efficiency of the process. A summary of the calculated event yields for the processes is given in Table 4.2.

For the actual analysis these simulation-based estimates are not considered to be accurate enough, especially with regard to the QCD multijet and W+jets processes; instead a template fit to the data is performed, which is described in Section 4.4.

Table 4.2: Predicted event yields for the selected dataset, corresponding to an integrated luminosity of $19.7\,\mathrm{fb}^{-1}$. The observed number of events in data is shown for comparison.

Process	Electron+jets	Muon+jets	Lepton+jets
$\mathrm{t\bar{t}}$	138 895	162 433	301 328
Single top (t)	1408	2397	3806
Single top (tW)	5561	6425	11 986
W+jets	12 613	14 658	27 271
Z+jets	2544	2103	4647
QCD multijet	4928	2495	7423
Total	165 949	190 511	356 461
Observed data	171 121	192 123	363 244

4.3 Data-Driven Modeling of QCD Multijet Production Processes

The modeling of QCD multijet production poses a significant challenge when relying on simulated samples; only a minuscule fraction of the produced events passes the event selection and thus is relevant to the analysis, as is explained in more detail in Section 4.1.2. Additionally, those few events represent tail regions of the kinematic distributions of the processes, which makes them very sensitive to even small amounts of mismodeling of the underlying distributions.

However, these issues can be avoided by modeling the multijet background contributions from the data themselves. For this purpose sideband regions are defined in such a way that they are enriched in multijet events. Two complementary strategies for the sideband definition are used, resulting in the construction of *anti-isolation* and *anti-ID* templates for the distributions that are needed in later analysis steps.

In the nominal event selection a significant suppression of the multijet events is achieved by requiring charged leptons to be isolated. Consequently one important strategy of obtaining a multijet-enriched sideband is to invert the isolation requirement, demanding the isolation of the lepton candidate to be in the range $0.2 < I^{\ell}_{\mathrm{rel}} < 0.5$ instead of $I^{\ell}_{\mathrm{rel}} < 0.1$ or $I^{\ell}_{\mathrm{rel}} < 0.12$. This leads to the construction of the *anti-isolation* template. In this definition, the lower bound of 0.2 is motivated by the desire to reduce the amount of signal events in the sideband region. Additionally, it needs to be considered that it is possible for one of these less well-isolated leptons to be part of a reconstructed jet. In order to avoid double-counting of the corresponding energy contributions, they are subtracted from the associated jet.

Because the muon trigger used in the regular event selection requires an isolated

Table 4.3: Trigger paths used for the QCD multijet template in the muon+jets channel, chosen for the absence of lepton isolation criteria.

Run range	Trigger
190 456 to 193 621	HLT_Mu24_eta2p1_CentralPFJet30_CentralPFJet25
193 834 to 203 742	HLT_Mu24_CentralPFJet30_CentralPFJet25
203 777 to 209 151	HLT_Mu18_CentralPFJet30_CentralPFJet25

muon, reducing the number of events that can pass the inverted isolation criterion, the triggers documented in Table 4.3 are used for the sideband region. The jet requirements of these triggers can be assumed to not introduce a significant bias, as the event selection requirement of four jets with at least 30 GeV is significantly harder to fulfill. For the electron channel the same trigger is used as in the regular event selection, since no other available trigger was found to provide better results.

In the case of the electron+jets channel it is possible to create an *anti-ID* template in addition to the anti-isolation one. Here the electron candidate is required to *not* pass either the conversion veto or the multivariate electron identification criterion. Any comparable sideband definition for the muon+jets channel suffers from a low number of selected events and a high signal contamination, restricting this approach to the electron+jets channel.

While the anti-isolation sideband is enriched in processes with a b or c quark decaying to a lepton, the anti-ID sideband shows a complementary bias, favoring for example processes involving photon conversions. As an illustration the fractions of processes have been determined in the few remaining events of the simulated samples: The processes with heavy quarks decaying to a lepton made up 56% of the events in the anti-isolation sideband, as compared to 10% in the anti-ID sideband and 27% in the signal region. One of the places where the benefit of this bias compensation of the two approaches is apparent is in the modeling of the pseudorapidity distribution of the charged leptons, which shows significantly larger width discrepancies when relying only on an anti-isolation template. An additional advantage of the introduction of the anti-ID sideband is that, in contrast to the anti-isolation sideband, it is not biased in the angular distributions between the electron and the jets.

In all sidebands the contributions of the $\mathrm{t\bar{t}}$ and W+jets processes are subtracted from the corresponding data templates in accordance with the fractions predicted by the simulated samples in the respective sidebands. This corresponds to subtractions of 6% and 9% in the anti-isolation templates for the electron+jet and muon+jets channels, respectively. In the anti-ID template of the electron channel the correction corresponds to 29% of the overall normalization; the higher signal contamination represents a drawback of this approach.

In the electron+jets channel the templates obtained via the two sidebands are scaled to the same normalization and added to obtain a merged template. In the muon+jets channel, which lacks a usable anti-ID template, the anti-isolation template is used by itself.

4.4 Background Estimation

The predicted event yields shown in Section 4.2.4 are subject to many uncertainties due to the limited accuracy of the simulated samples; for example, it is known that the fraction of events with heavy-flavor radiation in the simulated W+jets sample is smaller than the one observed in measurements. Similarly, the simulation cannot provide a reliable estimate for the normalization of the QCD multijet process.

For this reason a dedicated estimation of the process contributions is performed by a binned likelihood fit of the process templates to data distributions. The THETA framework [159] is used for the implementation of this fit. Even though this procedure determines the normalizations of both background and signal processes, it is commonly referred to as the *background estimation*.

The background estimation performed as part of this thesis relies on the variables $m_{\mathrm{T}}^{\mathrm{W}}$ and M_3. The shape differences of the different processes in these variables are demonstrated in Figure 4.6, which shows the respective normalized distributions; their features are explained in the following paragraphs.

The variable $m_{\mathrm{T}}^{\mathrm{W}}$ represents a calculation of the transverse mass of the leptonically decaying W boson from $E_{\mathrm{T}}^{\mathrm{miss}}$ and the p_{T} of the charged lepton, ignoring the small rest masses of the leptons:

$$m_{\mathrm{T}}^{\mathrm{W}} = \sqrt{2(E_{\mathrm{T}}^{\mathrm{miss}} p_{\mathrm{T}}^{\ell} - \vec{E}_{\mathrm{T}}^{\mathrm{miss}} \cdot \vec{p}_{\mathrm{T}}^{\ell})}\,. \tag{4.6}$$

If the given event contains a real W boson, the distribution of $m_{\mathrm{T}}^{\mathrm{W}}$ shows a peaking behavior corresponding to the Jacobian edge at values close to the invariant mass of the boson at about 80 GeV. This is the case for the signal, for single top quark production, and for W+jets production. The Z+jets and QCD multijet production processes, however, show simple distributions that decrease for higher values of $m_{\mathrm{T}}^{\mathrm{W}}$, allowing a separation from the other three processes.

The second variable, M_3, similarly corresponds to a simplified reconstruction of the invariant mass of a hadronically decaying top quark, using three of the reconstructed jets. Consequently this variable allows to discriminate the more strongly peaking processes with actual hadronically decaying top quarks, i. e. $\mathrm{t\bar{t}}$ and single top quark production, from the other ones. It exploits the fact that the top quarks are often produced with a significant amount of transverse momentum, separating the combination of the correct three jets from other combinations of three jets in the event. The variable thus is defined as the invariant mass of those three jets in the event which, summed vectorially, yield the highest transverse momentum.

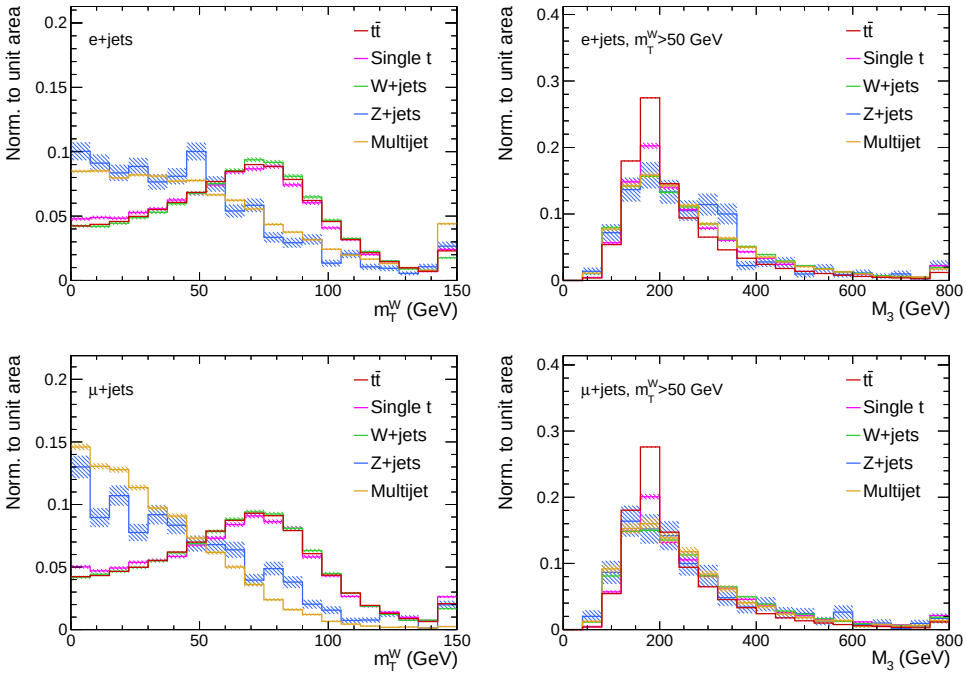

Figure 4.6: Shape comparisons of the $m_{\mathrm{T}}^{\mathrm{W}}$ and M_3 distributions for the processes involved in the background estimation. The electron+jets channel is shown in the upper row, whereas the corresponding distributions for the muon+jets channel are shown in the lower row. The distributions of M_3 have been derived from events with $m_{\mathrm{T}}^{\mathrm{W}} \geq 50\,\mathrm{GeV}$. The full $m_{\mathrm{T}}^{\mathrm{W}}$ distribution is shown, even though only bins with $m_{\mathrm{T}}^{\mathrm{W}} < 50\,\mathrm{GeV}$ enter the background estimation.

It needs to be noted that the separation power of these variables is not sufficient to determine all of the needed process normalizations accurately. For this reason the backgrounds of Z+jets and single top quark production are constrained to the corresponding predictions, as detailed below. These specific processes are chosen for the application of constraints because they not only have comparatively small expected yields in the selected samples, but in contrast to QCD multijet production they can also be considered to be well-modeled by the simulations.

As the event generation and selection procedures of the electron+jets and muon+jets channels differ significantly, most prominently due to the lepton efficiencies and different kinds of QCD multijet background processes, the background estimation is performed separately for the two channels.

Within each channel the samples are separated into those events with $m_{\mathrm{T}}^{\mathrm{W}} < 50\,\mathrm{GeV}$ and those with $m_{\mathrm{T}}^{\mathrm{W}} \geq 50\,\mathrm{GeV}$; the first group of events is used to perform a fit to the $m_{\mathrm{T}}^{\mathrm{W}}$ distribution itself, while the other group is fitted to the corresponding distribution of M_3. This separation of the events is performed to allow using both variables for the fit without using any event more than once; in the THETA fit framework this is necessary to obtain a correct calculation of the statistical uncertainties of the fit results. One possible way of circumventing this requirement would be to perform a two-dimensional fit, but in light of the statistical limitations of some of the process templates this has been decided against. The reason for using specifically the low-$m_{\mathrm{T}}^{\mathrm{W}}$ samples for the fit to $m_{\mathrm{T}}^{\mathrm{W}}$ lies in the significant shape differences of the processes in this region of the variable; the shape of M_3, on the other hand, behaves similarly regardless of which subsample is used.

The templates are normalized to the predictions obtained from simulated events, leaving the fitting procedure to determine a correction factor for the normalization of each process k:

$$\beta_k = \frac{N_k^{\mathrm{meas}}}{N_k^{\mathrm{pred}}} \tag{4.7}$$

The maximum likelihood procedure implemented in THETA and used to determine these factors relies on the MINUIT package [160]. It performs the minimization of the negative logarithm of a likelihood function, with the latter depending on the templates, the data, and the fit parameters β_k. Given an observed distribution d with n_i events in bin i and a total number of bins N_{bins}, the likelihood function is defined as

$$L(\beta_k; \Delta_k | d) = \prod_{i=1}^{N_{\mathrm{bins}}} P(n_i|\mu_i) \cdot G(\beta_k; \Delta_k)\,. \tag{4.8}$$

The first term of this equation,

$$P(n_i|\mu_i) = \frac{\mu_i^{n_i} \cdot e^{-\mu_i}}{n_i!}\,, \tag{4.9}$$

is the Poisson probability of observing n_i events if the Poisson mean is μ_i; the latter quantity is a function of the process normalizations that are to be determined

Table 4.4: Results of the background estimation together with the statistical uncertainties of the fit procedure. The uncertainties are correlated, as documented in Figure 4.9; this has been taken into account for the quoted uncertainties of the total background contributions. The last column represents the sum of the separate background estimations in the two channels.

Process	Electron+jets	Muon+jets	Lepton+jets
Single top (t+tW)	7016 ± 1328	7302 ± 1663	$14\,318 \pm 2128$
W+jets	$22\,508 \pm 1460$	$20\,522 \pm 1606$	$43\,030 \pm 2170$
Z+jets	2345 ± 510	2046 ± 415	4391 ± 658
QCD multijet	6136 ± 1201	4199 ± 588	$10\,335 \pm 1337$
Total background	$38\,005 \pm 1491$	$34\,096 \pm 1495$	$72\,074 \pm 2111$
$\mathrm{t\bar{t}}$	$133\,130 \pm 1521$	$158\,058 \pm 1538$	$291\,188 \pm 2163$
Observed data	171 121	192 123	363 244

by this fit. The second term in Equation (4.8) is a Gaussian constraint, which is used to constrain Z+jets and single top quark production to β values of 1.0 with uncertainties of 20%:

$$G(\beta_k; 0.2) = \frac{1}{\sqrt{2\pi \cdot (0.2)^2}}\, e^{-\frac{(\beta_k - 1.0)^2}{2 \cdot (0.2)^2}} \tag{4.10}$$

The width of 20% represents a conservatively estimated value, motivated by theory uncertainties on the cross sections and the precision of CMS measurements of related quantities. For the Z+jets process, the quoted uncertainties on the theoretical cross sections are negligibly small [147]; the constraint width is derived from remaining differences between measurements and simulations being on the order of 10% for both Z boson production in association with four jets [161] as well as for Z boson production with an associated b jet [162]. The single top quark process has theory uncertainties on the order of 8% [124], and both the t- and tW-channel measurements have precisions on the order of 10% [163, 164]. No strong dependence of the analysis results on the chosen constraint widths was found, which justifies the use of the conservatively rounded value of 20%.

All other process normalizations are free parameters of the fit, removing the need for a correct prediction of the event yields from the simulations.

The measured event yields can be found in Table 4.4. Comparing them to the predicted event yields of Table 4.2 it can be seen that, as expected and explained in earlier sections, the simulations perform comparatively well in predicting the signal event yield, but underestimate both the W+jets and the QCD multijet contributions. The obtained signal fractions are 78% in electron+jets and 82% in the muon+jets channel.

A comparison between the data distributions in the fit variables and the renormalized templates can be found in Figure 4.7. Figure 4.8 additionally shows

similar comparisons for the transverse momentum and pseudorapidity of the lepton. All distributions show good agreement between data and simulation. The small deviations in the charged lepton quantities are related to the modeling of the top p_{T} distribution, as discussed in Section 3.1.3, and of the QCD multijet background; they thus can be considered to be covered by the corresponding systematic uncertainties.

The correlation matrix for the fit parameters is documented in Figure 4.9. It is taken into account for the determination of the statistical uncertainties of the measurement in later analysis steps. Many of the strongest parameter correlations are related to the constrained backgrounds, demonstrating the need for these constraints.

4.5 Definition of a Fiducial Phase Space

Due to the restrictions imposed by the detector and the event selection, only a specific subset of events can be measured in the analysis. However, it is generally desirable to provide measurements that can be interpreted without intimate knowledge of the detector and the analysis procedure; this is necessary, for example, to allow for the calculation of theoretical predictions that can be compared to the measurement results. The most common method of accounting for this challenge is to perform a simulation-based extrapolation from the measured events to the full phase space of the analyzed process, e. g. of top quark pair production. This also is one of the approaches chosen for this thesis.

It needs to be understood, however, that this extrapolation is reliant on the correctness of the selection effects as they occur in the simulation – which also means that it relies on a correct description of the events that cannot be measured. An estimation of the associated uncertainties is difficult in the case of asymmetries corresponding to the SM predictions, which are not modeled perfectly by the simulation, and it is impossible to do in the general case where the asymmetry may be affected by any kind of unanticipated new physics contributions.

One may consider, for example, that new physics contributions typically take effect only at high energies. This means that they affect the selected events, which are comparatively energetic, more strongly than the events that do not pass the event selection. In this scenario the ratio between the two groups of events, which is needed for the extrapolation, will thus be different than the one obtained from a simulation based on the SM.

In order to produce results with a reduced dependence on the extrapolation, this thesis defines a *fiducial phase space* characterized by generator-level selection criteria that mimic the reconstruction-level criteria that are applied in the regular event selection of Section 4.2. Due to the qualitative similarity in the selection steps and thus the selected events, an extrapolation to this phase space is less reliant on assumptions about the behavior of the unmeasured events. Instead the

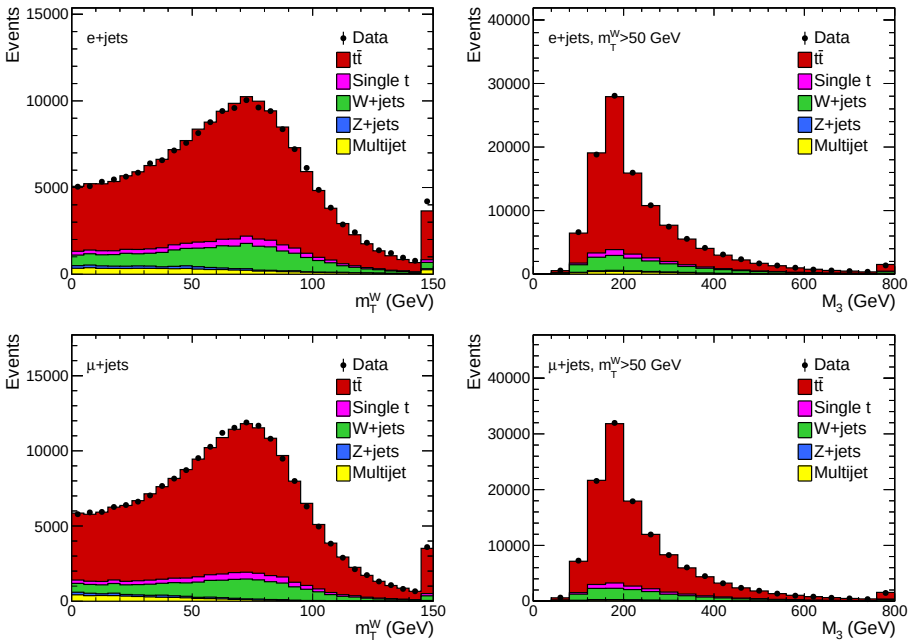

Figure 4.7: Comparison of data and templates in the variables $m_{\mathrm{T}}^{\mathrm{W}}$ and M_3 in the electron+jets channel (upper row) and in the muon+jets channel (lower row). All templates are normalized to the results of the background estimation.

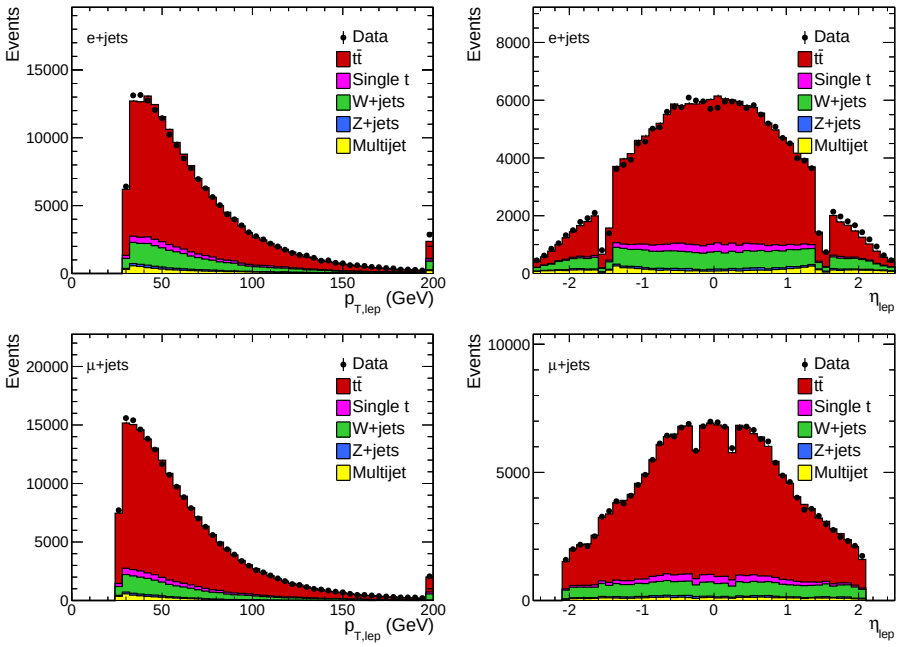

Figure 4.8: Comparison of data and templates in the transverse momentum and the pseudorapidity of the charged lepton in the electron+jets channel (upper row) and in the muon+jets channel (lower row). All templates are normalized to the results of the background estimation.

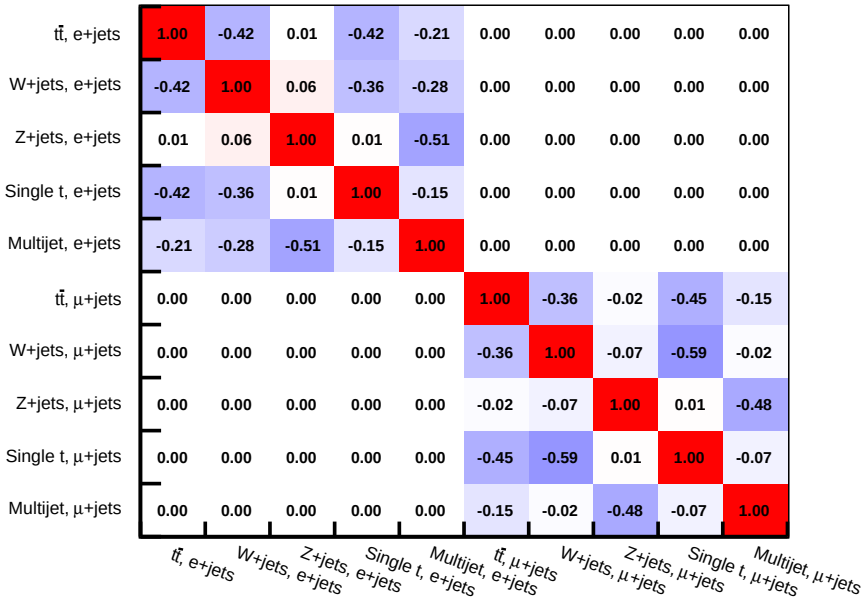

Figure 4.9: Correlation matrix for the fit parameters of the background estimation.

differences can be considered to be dominated by detector efficiencies and effects of statistical nature, both of which are comparatively well-modeled by simulations.

The applicability to only a constrained phase space makes it harder to interpret the results, however, so the direct comparison to theoretical calculations is of even higher importance than in the non-fiducial measurements. As a result the constraints under which those calculations can be performed are an important consideration when defining the details of the fiducial selection procedure.

Similar to how the reconstruction-level physical objects need to be defined for the regular event selection in Section 4.2.1, the corresponding generator-level objects must be defined for the fiducial selection.

Generator-level charged leptons are used as they appear in the final state of the hard interaction after the decay of the top quarks and W bosons. This definition corresponds to the status code "3" as defined by Pythia 6. It does not encompass an explicit correction for the energy loss due to the radiation of photons; such a correction constitutes a possible improvement, but it would require additional studies.

Instead of the jets clustered from reconstructed PF candidates, *generator jets* are used. They are clustered from the final generated particles of status code "1", that is, from those particles that remain after the hadronization and decay steps of the event generation. Just like the reconstruction-level jets they are formed using the anti-k_t algorithm with a resolution parameter of 0.5.

The advantage of using generator jets instead of generated partons lies in avoiding a dependence on the exact parton definition within the analysis. Due to different parton definitions being used in the simulations and in theoretical calculations, encompassing differing amounts of radiative effects, a reclustering of the partons with their radiations would have to performed in either case. As this would be complicated or even impossible to do correctly on the base of the available generator information, the use of generator jets is considered to be the superior solution.

It must be noted, however, that theoretical calculations typically do not encompass hadronization steps in such a way that jets are formed. In such calculations the criteria thus must be applied using the calculated partons instead of the generator jets outlined above. To improve the agreement between the two approaches, a clustering of the partons should be applied. Just like the clustering of the generator jets this should be done using the anti-k_t algorithm with a resolution parameter of 0.5. Studies comparing the results of the analysis using clustered generator partons and generator jets have shown that the differences between the two approaches are negligible in relation to the measurement resolution – indicating the validity of comparing the measurements based on generator jets to theory predictions based on clustered partons.

Using the generator-level objects defined above, the following selection criteria are applied to approximate those of the regular event selection:

Lepton selection: The event needs to contain exactly one electron with $p_{\mathrm{T}} > 30\,\mathrm{GeV}$ and $|\eta| < 2.5$, or exactly one muon with $p_{\mathrm{T}} > 26\,\mathrm{GeV}$ and $|\eta| < 2.1$.

Second-lepton veto: Any event that contains an additional electron with $p_{\mathrm{T}} > 20\,\mathrm{GeV}$, $|\eta| < 2.5$ or an additional muon with $p_{\mathrm{T}} > 10\,\mathrm{GeV}$, $|\eta| < 2.5$ is rejected.

Jet selection: At least four generator jets with $p_{\mathrm{T}} > 30\,\mathrm{GeV}$ and $|\eta| < 2.5$ are required for the event to be selected.

Lepton-jet separation: The event is discarded if any one of the jets as defined in the jet selection has only a small angular separation of $\Delta R < 0.4$ to the lepton. This criterion represents a coarse emulation of the lepton isolation criterion, which poses difficulties for the implementation in theoretical calculations.

In the simulated samples the fiducial region contains about 10% of the events of the full phase space. Roughly 50% of its events pass the main event selection of the analysis, while only 6% of the events of the full phase space fulfill those criteria. When judging these numbers, however, it must be kept in mind that the charge asymmetry behaves the same for all decay channels of the top quark pair system, even though both selections are aimed at the extraction of the lepton+jets channel. The magnitude of the 50% loss when applying the regular event selection on top of the fiducial selection can be understood by comparing the absolute sizes of the two phase phases, which also differ by roughly a factor of two. Most of this loss occurs due to the lepton trigger and identification requirements, which account for roughly 30%. The criteria on the number of jets and the b tagging correspond to remaining losses, contributing about 10% each.

A more intuitive demonstration of the benefits of the fiducial region can be found in Figure 4.10. It shows the generator-level values of the observables most relevant to this analysis in the full phase space, in the fiducial region, and in the phase space selected by the regular event selection. Compared to the full phase space, the fiducial phase space shows a behavior that is much more similar to that of the selected events. This corresponds to a reduced amount of physical difference that needs to be corrected for in the extrapolation to the given target phase space.

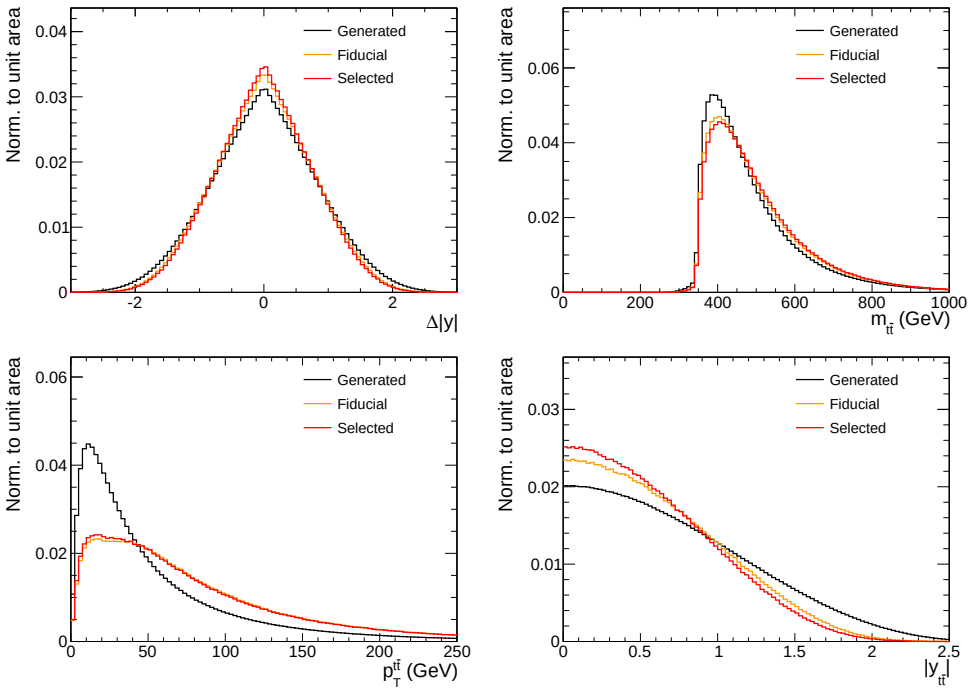

Figure 4.10: Demonstration of the distortions in the analysis observables $\Delta|y|$, $m_{t\bar{t}}$, $p_T^{t\bar{t}}$ and $|y_{t\bar{t}}|$ due to the regular and fiducial event selections. It can be seen that the fiducial region approximates the behavior of the regular event selection.

5 Measurement of the $\mathrm{t\bar{t}}$ Charge Asymmetry

The reconstruction detailed in Section 3.2 focuses on those particles that either result in a detector response themselves, or effect a shower that goes on to leave a detector response. For a particle like the top quark, which decays into other particles before it can cause either interaction, an additional reconstruction step is necessary. The detectable decay products of the top quarks need to be identified and combined to reconstruct the four-vectors of the top quarks themselves.

Using these four-vectors the relevant quantities for measurements of the charge asymmetry can be calculated at reconstruction level. A subtraction of the contributions from background processes needs to be performed to obtain a distribution that corresponds to a pure set of signal events.

The resulting background-subtracted spectra still are subject to sizable distortions from the unavoidable inefficiencies in the event selection and in the various reconstruction steps. For a meaningful comparison to theoretical predictions these distortions need to be corrected, which in this analysis is done using a regularized unfolding procedure.

The specific observables that need to be reconstructed and unfolded for the differential charge asymmetry measurements of this thesis are the following:

- The **sensitive variable** $\Delta|y|$.
- The **invariant mass** of the top quark pair $m_{\mathrm{t\bar{t}}}$.
- The **transverse momentum** of the top quark pair $p_{\mathrm{T}}^{\mathrm{t\bar{t}}}$.
- The absolute value of the **rapidity** of the top quark pair $|y_{\mathrm{t\bar{t}}}|$.

This chapter concerns itself with the analysis steps outlined above and the results of the measurement as a whole. After explanations of the top-quark-pair reconstruction and the background subtraction a detailed account of the unfolding procedure is given. It is followed by a description of the validation of this method, which is performed using pseudo experiments. The estimation of the systematic uncertainties of the measurement is described in Section 5.6, and finally the measurement results are presented in Section 5.7.

5.1 Reconstruction of $t\bar{t}$ Events

For the calculation of both the sensitive variable and the secondary variables in data a reconstruction of the four-vectors of the top quarks is necessary. For this, the reconstructed decay products of the top quarks need to be identified and their four-vectors need to be combined to yield the original top quark four-vectors. The reconstructed jets, leptons and missing transverse energy are the input for a procedure that builds various reconstruction hypotheses corresponding to different solutions of the problem of how the reconstructed objects relate to the particles occurring in the decay of the top quarks. In order to choose one of these hypotheses, a criterion is constructed that uses properties of the jets and the reconstructed particles to judge which hypothesis is most likely to be correct.

For the purpose of a more concise description of the procedure this section uses several abbreviations for the particles involved in the semileptonic decay process. The W bosons are abbreviated as $\mathrm{W_{had}}$ and $\mathrm{W_{lep}}$, indicating the hadronically and leptonically decaying bosons, respectively. Correspondingly, the two top quarks are labeled $\mathrm{t_{had}}$ or $\mathrm{t_{lep}}$ depending on the decay channel of their associated W bosons, and $\mathrm{b_{had}}$ and $\mathrm{b_{lep}}$ indicate the b quarks occurring in the decay of $\mathrm{t_{had}}$ or $\mathrm{t_{lep}}$.

5.1.1 Reconstruction of Possible Hypotheses

The charged lepton serves as a starting point for the event reconstruction, since the event selection ensures that there is always exactly one reconstructed charged lepton in the event. The lepton charge is reconstructed very reliably and thus can be used to identify whether the leptonically decaying top quark was a particle or an anti-particle.

The four-vector of the neutrino, on the other hand, requires a more sophisticated treatment. The missing transverse energy is used as an estimate of its transverse momentum. As it is known from other measurements that the neutrino rest masses are small enough to be negligible in the context of this analysis [20, 165], the mass of the reconstructed neutrinos is invariably set to zero. The z component of its momentum remains unknown, however, and needs to be calculated using additional assumptions.

In the event topologies that are of interest for this analysis the neutrino always occurs as a decay product of a leptonically decaying W boson. Because of this the following relation holds:

$$p_{\mathrm{W_{lep}}} = p_\ell + p_\nu \,, \tag{5.1}$$

with p_ℓ and p_ν being the four-momenta of the charged lepton and the neutrino, respectively.

With the assumption of an on-shell W boson the invariant mass of the boson can be fixed at $m_{\mathrm{W_{lep}}} = 80.4\,\mathrm{GeV}$, and a quadratic equation for the z component

of the neutrino momentum can be derived:

$$m_{\mathrm{W}}^2 = \left(E_\ell + \sqrt{(\vec{E}_{\mathrm{T}}^{\,\mathrm{miss}})^2 + p_{z,\nu}^2}\right)^2 - \left(\vec{p}_{\mathrm{T},\ell} + \vec{E}_{\mathrm{T}}^{\,\mathrm{miss}}\right)^2 - \left(p_{z,\ell} + p_{z,\nu}\right)^2 \tag{5.2}$$

Here E_ℓ and $\vec{p}_{\mathrm{T},\ell}$ denote the energy and the transverse momentum of the charged lepton, whereas $p_{z,\ell}$ and $p_{z,\nu}$ indicate the z components of the momenta of the charged lepton and the neutrino. The solution to this equation is given by

$$p_{z,\nu}^{\pm} = \frac{\mu\, p_{z,\ell}}{p_{\mathrm{T},\ell}^2} \pm \sqrt{\frac{\mu^2 p_{z,\ell}^2}{p_{\mathrm{T},\ell}^4} - \frac{E_\ell^2\, p_{\mathrm{T},\nu}^2 - \mu^2}{p_{\mathrm{T},\ell}^2}}\,, \tag{5.3}$$

where $p_{\mathrm{T},\nu}$ is the transverse momentum of the neutrino and the abbreviation μ is defined as

$$\mu = \frac{m_{\mathrm{W}}^2}{2} + p_{\mathrm{T},\ell} \cdot p_{\mathrm{T},\nu} \cdot \cos\Delta\phi\,, \tag{5.4}$$

with $\Delta\phi$ being the azimuthal angle between the charged lepton and the neutrino.

The radicand of Equation (5.3) in practice can take both positive and negative values. In the case of a positive radicand two real solutions for the z component can be calculated; they are both taken into account when assembling the list of possible reconstruction hypotheses. In about 30% of all cases the radicand takes negative values instead and thus requires a different treatment. It can be shown that this occurs whenever the reconstructed transverse mass of the W boson

$$m_{\mathrm{T,W}} = \sqrt{2\, p_{\mathrm{T},\ell}\, p_{\mathrm{T},\nu}\, (1 - \cos\Delta\phi)} \tag{5.5}$$

takes values that are larger than the value used for the constraint on its invariant mass. Usually these cases are not physical but have their origin in inaccuracies of the measurement of the missing transverse energy. In order to find a real solution for $p_{z,\nu}$ the transverse mass is assumed to equal 80.4 GeV, which via Equation (5.4) leads to a relation between $p_{x,\nu}$ and $p_{y,\nu}$. In a minimization procedure [166] a solution for the transverse momentum of the neutrino is found that satisfies this relation while deviating as little as possible from the measured components of the missing transverse energy. When the resulting transverse momentum is used Equation (5.3) yields a single solution for $p_{z,\nu}$.

With the leptons having been reconstructed only the four quarks occurring in the decays of top quarks and W bosons remain to be associated to the observed jets. In an event with N reconstructed jets there are $N \cdot (N-1) \cdot (N-2) \cdot (N-3)$ possible assignments. Due to all relevant quantities being invariant under exchange of the two light quarks occurring in the hadronic decay of the W boson, this number of combinations can be reduced by a factor of two.

The overall number of reconstruction hypotheses considering both the neutrino solutions and the jet-parton assignments thus can be calculated as

$$N_{\mathrm{hyp}} = N_{\mathrm{sol}}^{\nu} \cdot \frac{N \cdot (N-1) \cdot (N-2) \cdot (N-3)}{2}\,, \tag{5.6}$$

where N^{ν}_{sol} is the number of possible solutions for the z component of the neutrino four-vector. Assuming the most common cases of two neutrino solutions and 4 or 5 reconstructed jets the number of hypotheses takes values of 24 and 120, respectively.

Within a given hypothesis the hadronically decaying W boson can be reconstructed by adding the four-vectors of the two light quarks. The reconstructed neutrino four-vector is added to the four-vector of the charged lepton, yielding that of the leptonically decaying W boson. The top quark four-vectors, finally, are obtained by adding those of the corresponding W bosons and b quarks.

5.1.2 Choice of a Single Reconstruction Hypothesis

As only one of the hypotheses detailed above can be used for each event a criterion needs to be introduced that can decide which of the hypotheses is likely to be the one closest to the truth. This criterion need not rely on generator-level simulation lest it cannot be applied on data.

As a first step a discriminator d is defined that does use generator-level information to evaluate the agreement between generated and reconstructed particles. It is chosen to be the sum of the distances in the η-ϕ plane between the reconstructed and generated momentum vectors of the top quarks and the W bosons:

$$\begin{aligned} d = &\Delta R(p_{\mathrm{t}^{\mathrm{rec}}_{\mathrm{lep}}}, p_{\mathrm{t}^{\mathrm{gen}}_{\mathrm{lep}}}) + \Delta R(p_{\mathrm{t}^{\mathrm{rec}}_{\mathrm{had}}}, p_{\mathrm{t}^{\mathrm{gen}}_{\mathrm{had}}}) \\ &+ \Delta R(p_{\mathrm{W}^{\mathrm{rec}}_{\mathrm{lep}}}, p_{\mathrm{W}^{\mathrm{gen}}_{\mathrm{lep}}}) + \Delta R(p_{\mathrm{W}^{\mathrm{rec}}_{\mathrm{had}}}, p_{\mathrm{W}^{\mathrm{gen}}_{\mathrm{had}}}) \end{aligned} \tag{5.7}$$

For each event the hypothesis yielding the lowest value of d is declared the *best possible* (bp) hypothesis.

In the following a different discriminator ψ is constructed which aims to find the best possible hypothesis using reconstruction-level information only. It employs a likelihood-based approach, with the reconstructed masses and the b tagger discriminator values of the jets serving as inputs. Using the simulated signal sample likelihood terms are constructed that are proportional to the probability of a given hypothesis being the best possible one.

The reconstructed masses that are considered here are those of the two top quarks and of the hadronically decaying W boson. As can be seen in Figure 5.1, though, there is a correlation between the masses of the hadronically decaying top quark and of the hadronically decaying W boson; it stems from the fact that the latter is used in the reconstruction of the former. To avoid a negative impact on the reconstruction performance because of this correlation a linear decorrelation of all three masses is performed, yielding three new variables m_1, m_2 and m_3 as linear combinations of the original masses:

$$\begin{pmatrix} m_1 \\ m_2 \\ m_3 \end{pmatrix} = \begin{pmatrix} 1.00 & -0.06 & 0.00 \\ 0.05 & 0.94 & 0.34 \\ -0.02 & -0.34 & 0.94 \end{pmatrix} \begin{pmatrix} m_{\mathrm{t,lep}} \\ m_{\mathrm{t,had}} \\ m_{\mathrm{W,had}} \end{pmatrix} \tag{5.8}$$

Figure 5.1 demonstrates the reduced correlations after this procedure. The improvement in the reconstruction performance due to this procedure means that the best possible hypothesis is found in an additional 1% of the simulated events.

The terms entering the likelihood discriminator ψ are constructed separately for each of the decorrelated variables m_1 through m_3 by calculating the ratio of best possible hypotheses and all hypotheses as a function of the given variable. This ratio serves as a probability that the given hypothesis is the best possible one. The underlying distributions can be found in Figure 5.2.

The second piece of information going into ψ aside from the reconstructed masses is represented by the CSV b tagger discriminator values of the jets that are used for the hypothesis. Figure 5.3 shows the probability of a jet being assigned to a b quark in the best possible hypothesis as a function of the CSV discriminator value of the jet. Under the assumption of a flat prior this same distribution can be considered to be proportional to the probability of a hypothesis being the correct one if a jet of a given discriminator value has been assigned to one of the b quarks of the signature.

Similarly, the inverse of the probability at any given value of the discriminator is proportional to the hypothesis being the best possible one in case the jet has been assigned to one of the light quarks of the signature.

The final discriminant is obtained by combining the probabilities as functions of the decorrelated masses and the four terms relating to the b-tagger outputs:

$$\psi = \mathcal{L}(m_1)\mathcal{L}(m_2)\mathcal{L}(m_3)P_{\mathrm{b}}(x_{\mathrm{b,lep}})P_{\mathrm{b}}(x_{\mathrm{b,had}})(1 - P_{\mathrm{b}}(x_{\mathrm{q1}}))(1 - P_{\mathrm{b}}(x_{\mathrm{q2}}))\,, \tag{5.9}$$

where $x_{\mathrm{b,had}}$ and $x_{\mathrm{b,lep}}$ are the b-tagger outputs for the jets assigned to b quarks and x_{q1} and x_{q2} are those for the jets assigned to light quarks. The histograms describing the likelihoods are interpolated linearly for the evaluation of the individual terms. To achieve a higher degree of numerical stability the actual implementation of the criterion uses the logarithms of the probabilities instead of the probabilities themselves.

Choosing the hypothesis with the highest value of ψ yields the best possible hypothesis in about 33% of all simulated events passing the event selection. For reference: Even if there are only four reconstructed jets a random association is correct in only about 8% of all cases. The sign of the sensitive variable is reconstructed correctly in about 72% of the events. Among the subset of events for which the jets of the best possible hypothesis have an angular separation $\Delta R < 0.5$ to the generated quarks, the best possible hypothesis is found in 56% of the events; this shows that the comparatively low rate of 33% among all selected events in part is caused by the inefficiencies of earlier reconstruction steps.

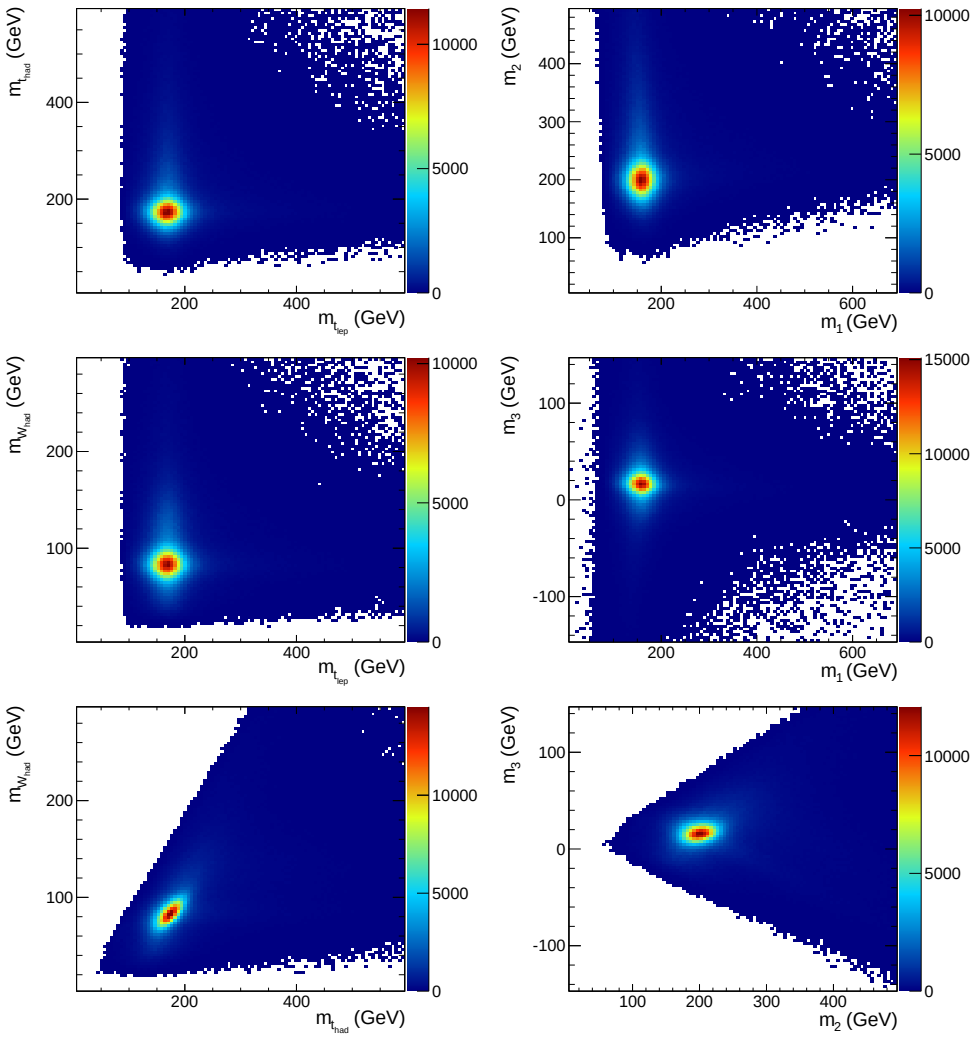

Figure 5.1: Correlation between the reconstructed mass variables before (left column) and after (right column) the linear decorrelation. The main correlation appears between $m_{\mathrm{t_{had}}}$ and $m_{\mathrm{W_{had}}}$ and is caused by the usage of the W boson for the reconstruction of the hadronically decaying top quark. The linearly decorrelated masses m_1, m_2 and m_3 show a reduced correlation.

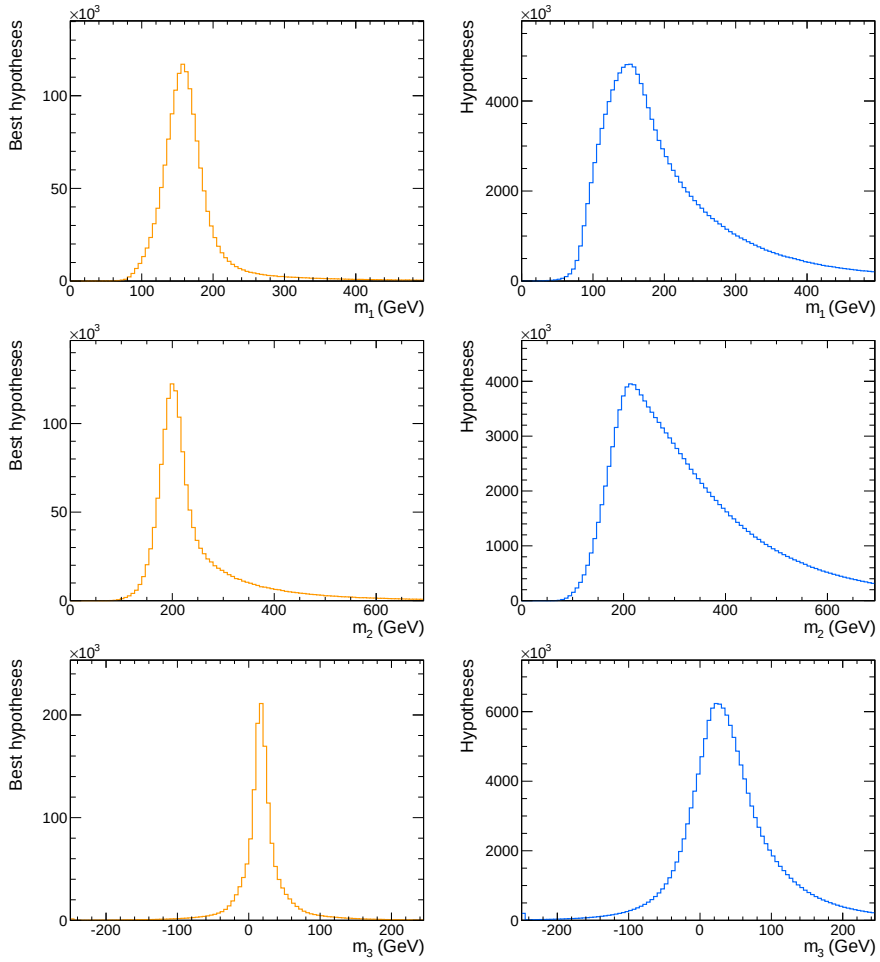

Figure 5.2: Distributions of the decorrelated masses m_1, m_2 and m_3 for the best possible hypotheses (left) and for all hypotheses (right).

Comparisons of the reconstructed masses, transverse momenta and rapidities in data and simulation can be found in Appendix A. Good agreement is found for these observables. Figures 5.4 and 5.5 in this section show the distributions of the sensitive and secondary variables, which are essential to the measurements that are performed in this thesis. No significant discrepancy is observed in the sensitive variable, yet the simulation fails to provide a perfect description of the secondary variables – as can be seen in Figure 5.5. The differences in $m_{\mathrm{t\bar{t}}}$ and $p_{\mathrm{T}}^{\mathrm{t\bar{t}}}$ are found to be covered by systematic uncertainties related to the modeling of the signal process. The difference in $y_{\mathrm{t\bar{t}}}$, on the other hand, has been studied using a reweighting of the simulated samples according to the results of a dedicated cross section analysis [167]; it has been found to not have a significant effect on the measured asymmetries.

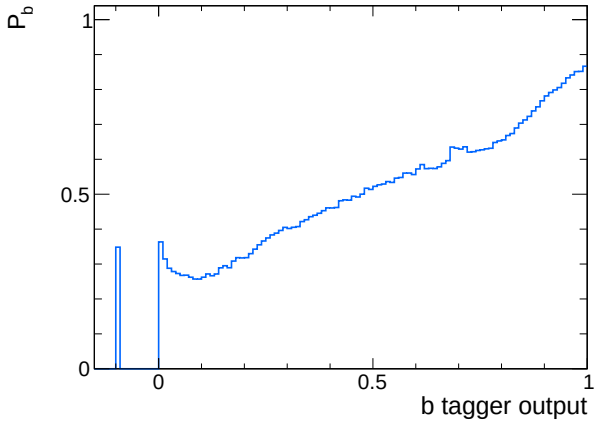

Figure 5.3: Probability distribution for a jet to be assigned to a b quark (instead of a light quark) in the best possible hypothesis as a function of the CSV discriminator value of the jet. The single bin below zero contains the information for all jets with a value smaller than zero.

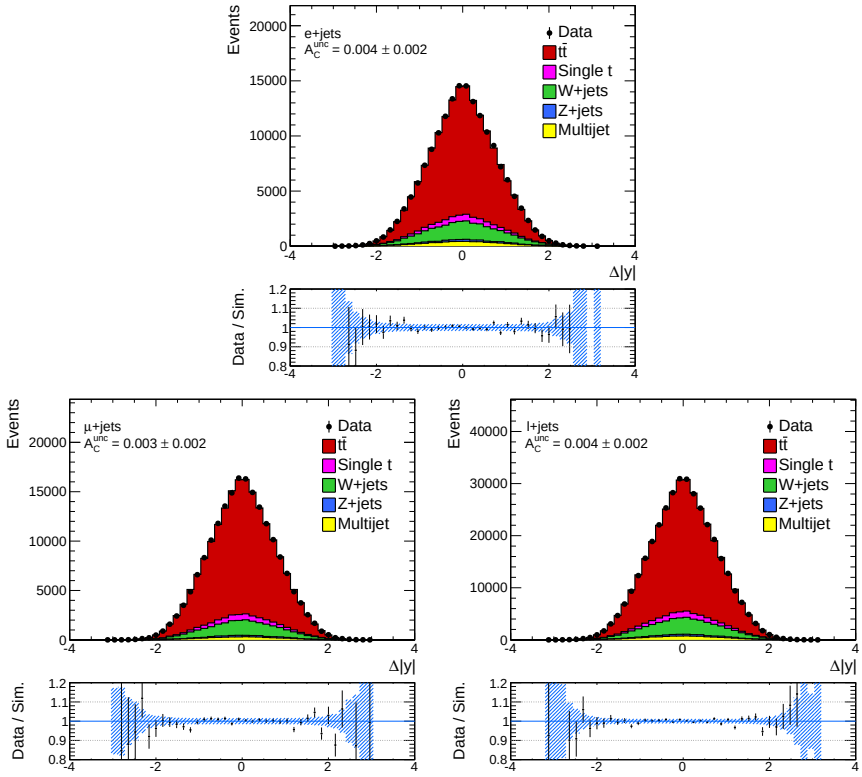

Figure 5.4: Distributions of $\Delta|y|$ for the electron+jets, muon+jets and combined lepton+jets channels. The error bands signify the statistical uncertainties of the simulation and the background normalization. For each channel the uncorrected asymmetries of the reconstructed data samples are shown. The simulation is normalized to the fit results.

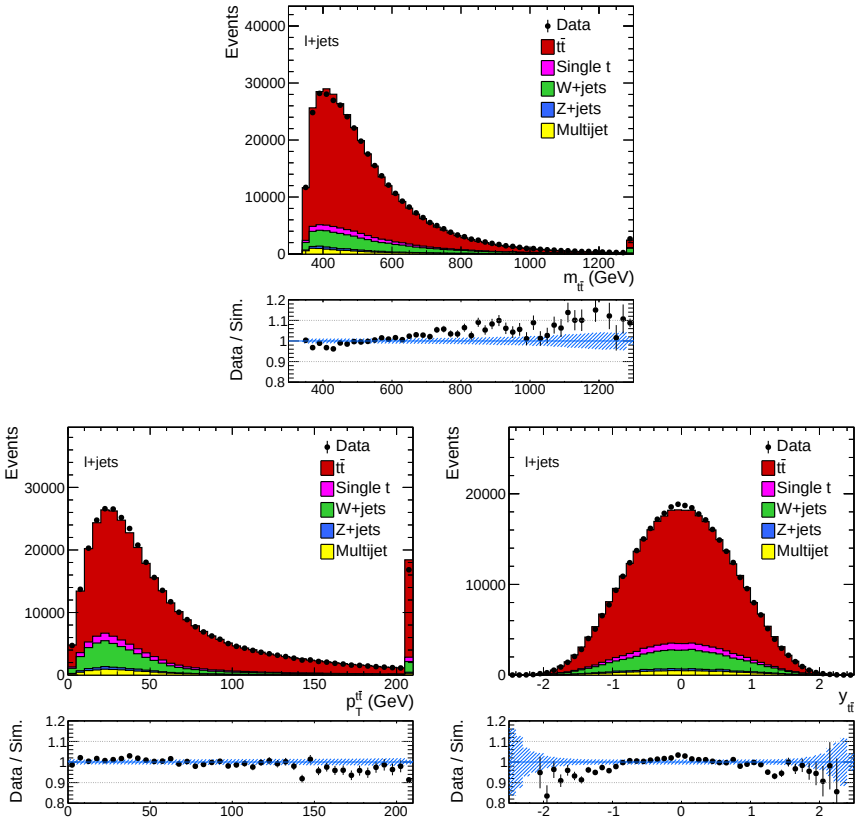

Figure 5.5: Distributions of the secondary variables $m_{\mathrm{t\bar{t}}}$, $p_{\mathrm{T}}^{\mathrm{t\bar{t}}}$ and $y_{\mathrm{t\bar{t}}}$ for the combined lepton+jets channel. The error bands signify the statistical uncertainties of the simulation and the background normalization. The simulation is normalized to the fit results of Section 4.4.

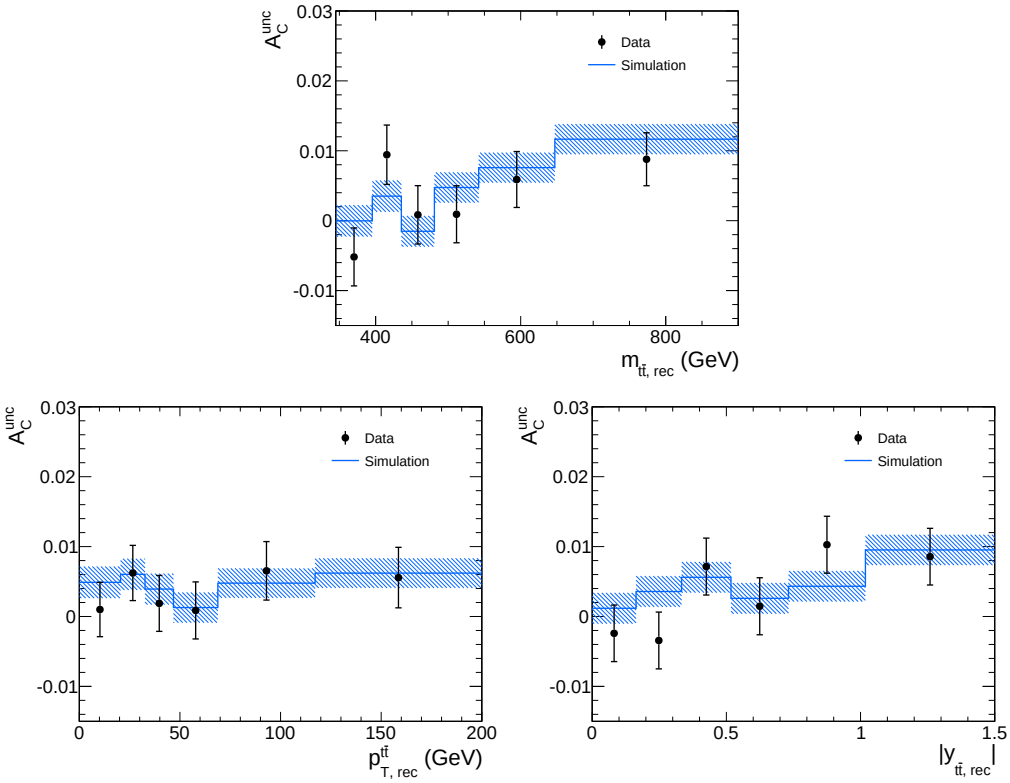

Figure 5.6: Results of the three differential measurements of the uncorrected charge asymmetry in the three secondary variables $m_{t\bar{t}}$, $p_T^{t\bar{t}}$ and $|y_{t\bar{t}}|$. The measurement is compared to the reconstructed asymmetries of the simulated samples, combined according to the results of the background estimation. All error bars correspond to statistical uncertainties.

5.2 The Need for Corrections to the Reconstructed Data

With the reconstruction of the $t\bar{t}$ system described in the previous section, uncorrected asymmetries can be calculated from the reconstructed data using Equation (1.10). This yields an inclusive asymmetry of $A_C^{unc} = 0.0036 \pm 0.0017$. The corresponding differential distributions, compared to the predictions from the simulated samples, are shown in Figure 5.6. The bin ranges that are used for these and other distributions of reconstruction-level asymmetries are detailed in Table 5.1 (c. f. Section 5.4.5 for an explanation of the binning choices in this analysis).

However, these comparisons suffer from the fact that the simulations are known to differ significantly from explicit calculations of the SM asymmetry; the reason for this is a lack of electro-weak corrections as well as a different choice of how the calculation is normalized, as detailed in Section 1.3.2. Furthermore, to compare any other theoretical calculation to the reconstructed data one would need to generate simulated events for the model and apply the detector simulation and

Table 5.1: Bin ranges of the three secondary variables ($m_{t\bar{t}}$, $p_T^{t\bar{t}}$ and $|y_{t\bar{t}}|$) that are used for differential measurements of the asymmetry in reconstructed variables.

	$m_{t\bar{t}}$ (GeV)	$p_T^{t\bar{t}}$ (GeV)	$\lvert y_{t\bar{t}}\rvert$
Bin 1	0 – 395	0 – 20.5	0 – 0.16
Bin 2	395 – 435	20.5 – 32.7	0.16 – 0.33
Bin 3	435 – 481	32.7 – 46.8	0.33 – 0.52
Bin 4	481 – 542	46.8 – 68.8	0.52 – 0.73
Bin 5	542 – 647	68.8 – 117	0.73 – 1.02
Bin 6	647 – ∞	117 – ∞	1.02 – ∞

event reconstruction, which in practice cannot be done by anybody but the analyst himself.

Because of this it is preferred to apply corrections to the reconstructed data to obtain values that can be compared to theoretical calculations. The corrections need to remove contributions from background processes, invert the effects of the detector resolution and the imperfect reconstruction, and account for the distorting effects of the event selection. Figure 5.7 shows a generator study of how the distortions due to reconstruction and event selection affect the variables that are most important for this analysis.

The following sections describe the individual correction steps that are applied in more detail.

5.3 Background Subtraction

In a first correction step the estimated background contributions are subtracted from the reconstructed data distributions. For this the fitted numbers of events and their uncertainties for the various background processes as given in Table 4.4 are used. As is documented in Figure 4.9, though, the background estimation suffers from non-negligible correlations between the individual process normalizations. To take into account not only the statistical uncertainties on the fit results but also the correlations between the fit parameters, a decorrelation of the contributions is performed. This is achieved by constructing new background templates as linear combinations of the original ones. The background templates $\vec{b_i}$ (where i represents the different background processes) are transformed into orthogonal templates $\vec{b'_j}$ with uncorrelated normalization uncertainties. For this purpose a matrix is constructed that contains the eigenvectors of the covariance matrix in its columns. It is used as a transformation matrix and applied to the vector of

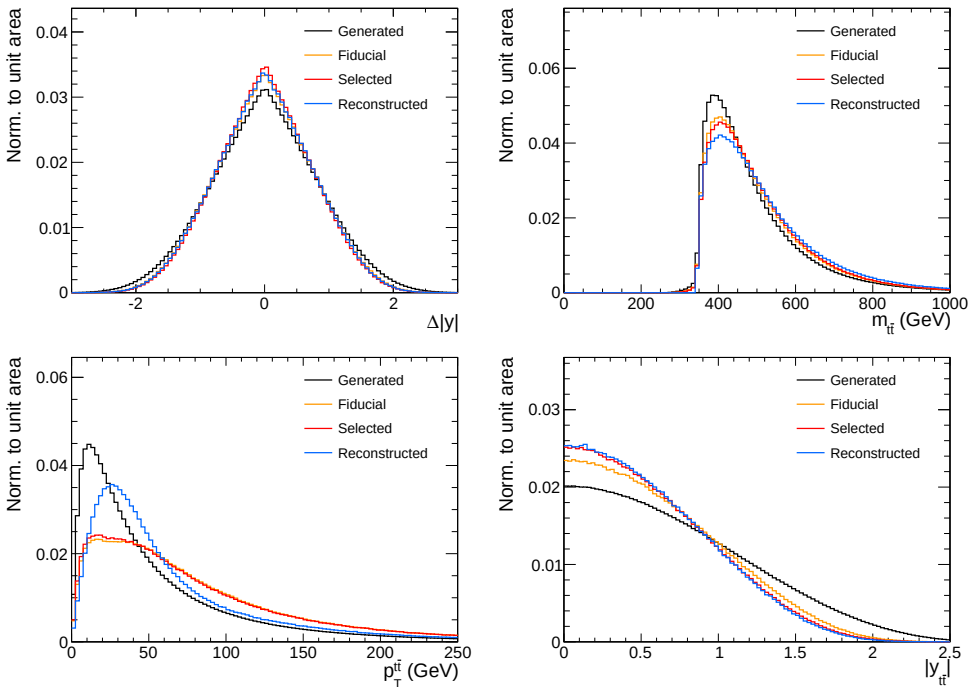

Figure 5.7: Demonstration of how the selected and reconstructed events are distorted in distributions of $\Delta|y|$, $m_{t\bar{t}}$, $p_T^{t\bar{t}}$ and $|y_{t\bar{t}}|$. The generated distributions of the $t\bar{t}$ signal sample before and after the event selection are compared to the reconstructed distributions. For reference the generated distribution in the fiducial phase space is shown as well.

background templates:

$$\vec{b_j'} = \sum_{i=1}^{N} v_{ji} \vec{b_i}\,, \tag{5.10}$$

where v_{ji} is the i^{th} element of the eigenvector $\vec{v_j}$ of the covariance matrix. It must be noted, though, that in general this transformation will change the normalizations of the individual background processes. The normalizations of the eigenvectors are free parameters and need to be adjusted in order to yield the same overall background distribution as before the decorrelation. Introducing a vector of normalization factors $\vec{s}$ for the individual eigenvectors, this requirement can be formulated as

$$\sum_{j=1}^{N} v_{ji} s_j = 1 \quad \forall \quad i\,. \tag{5.11}$$

Solving this system of equations leads to a single solution for each of the normalization factors, and the renormalized eigenvectors can then be employed to calculate the correct decorrelated background templates according to Equation (5.10). The covariance matrix of the decorrelated templates is by construction a diagonal matrix with the eigenvalues of the original covariance matrix in its diagonal ele-

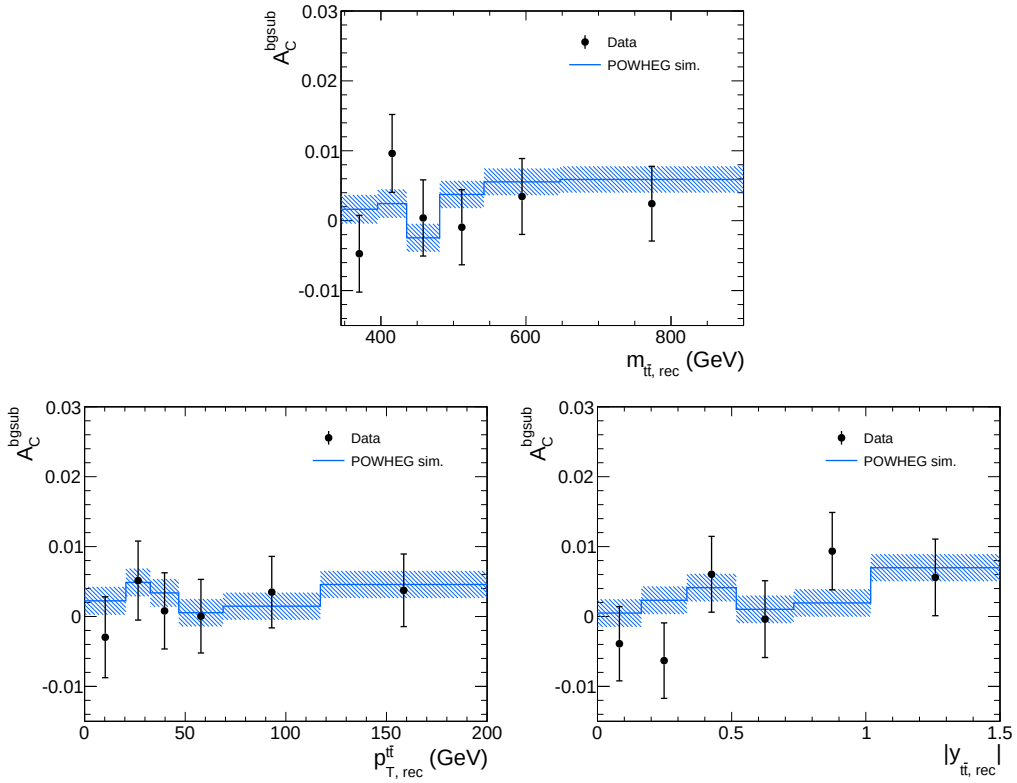

Figure 5.8: Results of the three differential measurements of the background-subtracted charge asymmetry in the three secondary variables $m_{t\bar{t}}$, $p_T^{t\bar{t}}$ and $|y_{t\bar{t}}|$. The measurement is compared to the reconstructed asymmetries observed in the simulated POWHEG signal sample. All error bars correspond to statistical uncertainties.

ments; these represent the squared normalization uncertainties of the decorrelated templates.

The orthogonal background templates are subtracted from the data, assuming Gaussian uncertainties on the background rates. It should be noted that the decorrelation of the templates does not affect the overall background distribution, but just the calculation of its aggregate statistical uncertainties.

After the background subtraction an inclusive asymmetry of $A_C^{\text{bgsub}} = 0.0008 \pm 0.0023$ is observed in data. Figure 5.8 shows the corresponding differential asymmetries in comparison to reconstruction-level asymmetries in the POWHEG simulation of $t\bar{t}$ events. Just like the uncorrected asymmetries these values show good agreement between prediction and data.

The underlying distributions of the sensitive variable within each bin of the secondary variables, with the backgrounds indicated but not yet subtracted, are

shown in Figures 5.9 to 5.11. The normalization deviations between simulation and data have the same origin as the shape deviations observed in the distributions of the secondary variables in Figure 5.5, and thus the same considerations apply.

It can be observed that the distribution of the sensitive variable progressively grows wider with increasing $m_{t\bar{t}}$. This has its origin in the declining importance of initial-state boosts relative to the kinetic energy within the $t\bar{t}$ system itself, with the boosts corresponding to a higher degree of correlation between the top quark flight directions.

A more complex behavior of the sensitive variable can be seen in the individual bins of $|y_{t\bar{t}}|$. Aside from the obvious widening of the sensitive variable for larger values of $|y_{t\bar{t}}|$ there are also some peaking structures within all bins except the lowest one. These structures are of a purely mathematical origin. It needs to be considered that while the sensitive variable is calculated as the difference of the top quark rapidities, $y_{t\bar{t}}$ takes values that are close to their average. A given minimum value of $|y_{t\bar{t}}|$, as it is required in all bins except the lowest one, can be achieved in two different ways: Either by rapidities of the same sign adding up to the needed value, or by rapidities of different signs having sufficiently different absolute values.

The prominent structures correspond to those points for which the difference in the absolute values of the rapidities is just large enough for the second class of events to reach the required value of $|y_{t\bar{t}}|$. In this case, with opposite signs of the rapidities, the absolute value of the sensitive variable is the same as the absolute value of the rapidity sum:

$$|\Delta\,|y|| = ||y_t| - |y_{\bar{t}}|| = |y_t + y_{\bar{t}}|$$

Thus for these events any upper or lower boundary on $|y_{t\bar{t}}|$ will also apply to the sensitive variable:

$$|y_{t\bar{t}}| \approx \left|\frac{y_t + y_{\bar{t}}}{2}\right| = \left|\frac{\Delta|y|}{2}\right|$$

This is why the peaking structures show up at values of the sensitive variable that are roughly twice as large as the respective upper or lower boundaries on $|y_{t\bar{t}}|$. While the lower boundary marks where this class of events enters the given bin of $|y_{t\bar{t}}|$, the upper boundary marks the start of the next bin and serves to reduce the tails of the distributions in all bins but the uppermost one.

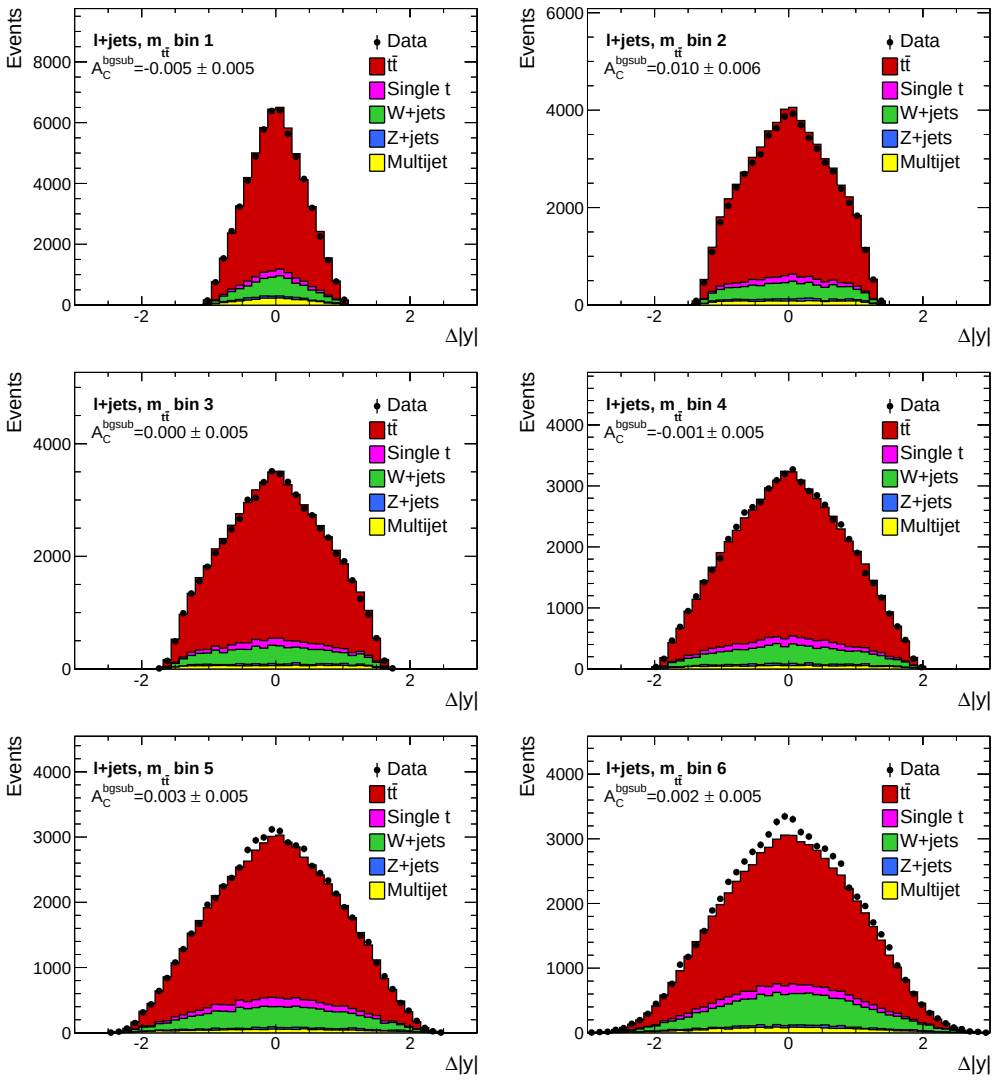

Figure 5.9: Reconstructed distributions of $\Delta|y|$ in six bins of the reconstructed $m_{\mathrm{t\bar{t}}}$. The background-subtracted asymmetry $A_{\mathrm{C}}^{\mathrm{bgsub}}$ is shown for each bin. The simulation is normalized to the fit results.

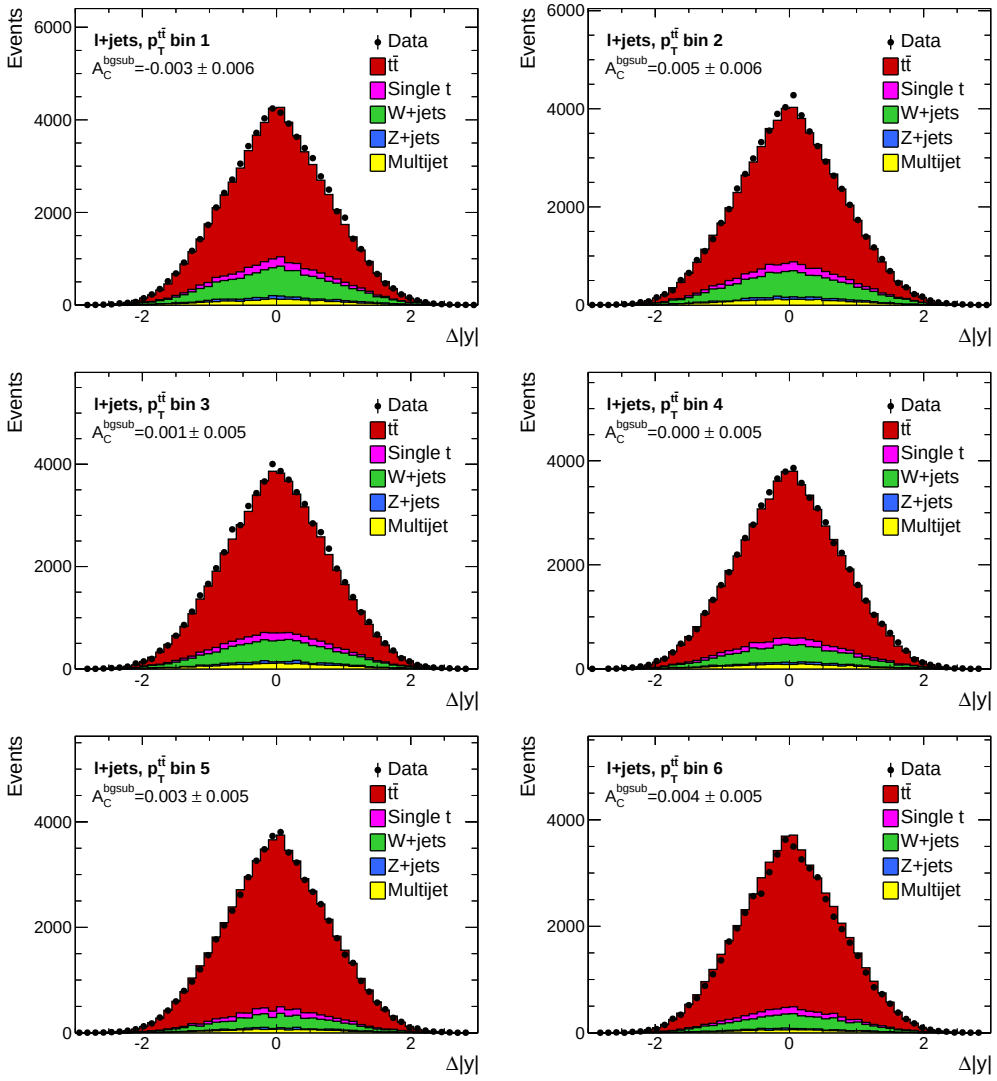

Figure 5.10: Reconstructed distributions of $\Delta|y|$ in six bins of the reconstructed $p_{\mathrm{T}}^{\mathrm{t\bar{t}}}$. The background-subtracted asymmetry $A_{\mathrm{C}}^{\mathrm{bgsub}}$ is shown for each bin. The simulation is normalized to the fit results.

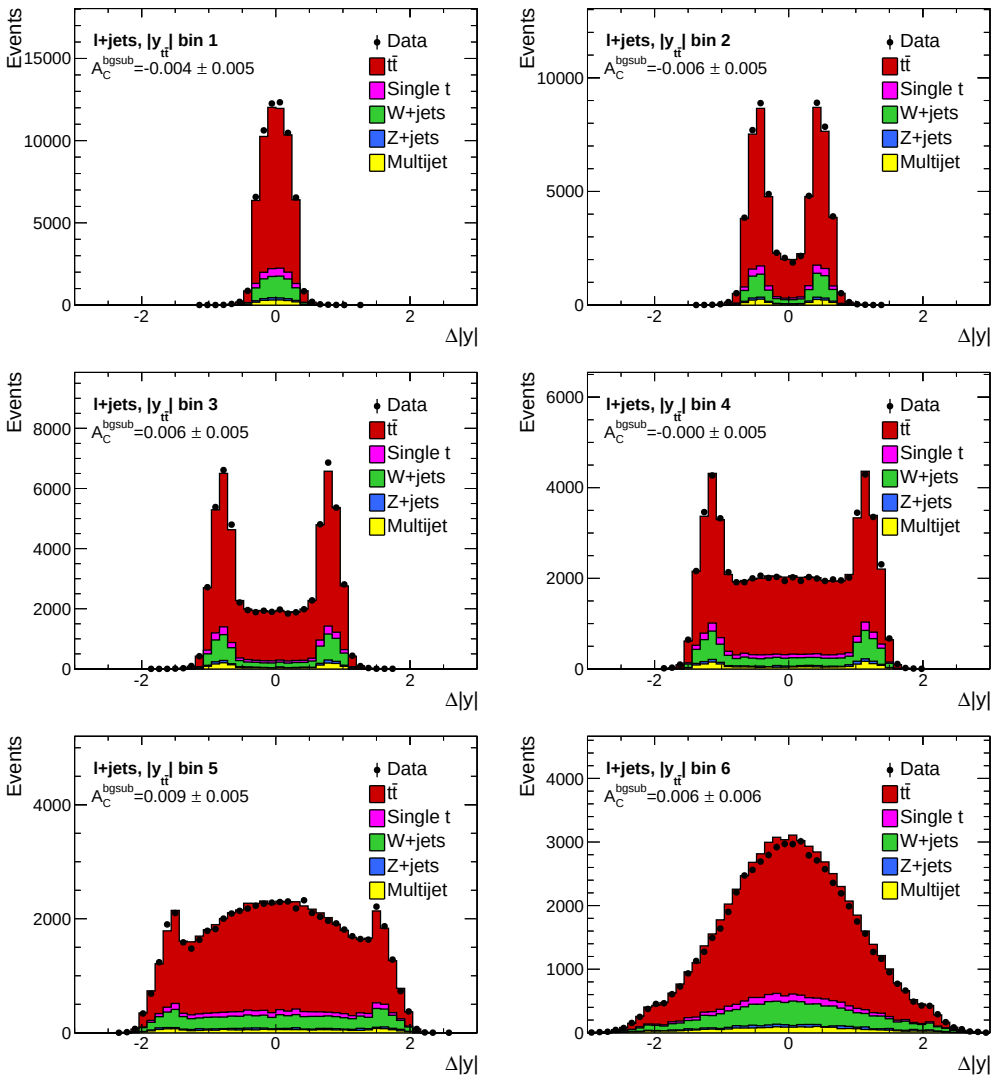

Figure 5.11: Reconstructed distributions of $\Delta|y|$ in six bins of the reconstructed $|y_{\mathrm{t\bar{t}}}|$. The background-subtracted asymmetry $A_{\mathrm{C}}^{\mathrm{bgsub}}$ is shown for each bin. The simulation is normalized to the fit results.

5.4 Regularized Unfolding

The distributions that are obtained after applying the background subtraction described in the previous section can be assumed to correspond to pure $t\bar{t}$ events. Due to the imperfect reconstruction of the $t\bar{t}$ system as well as the constraints imposed by the event selection, however, these distributions still are distorted relative to the true distributions of the full phase space of top quark pair production. A regularized unfolding procedure based on the TUnfold package [168, 169] is employed to correct the distortions and calculate distributions that can be compared to theoretical calculations.

5.4.1 Selection Effects

As indicated by the previously referenced Figure 5.7, the selection efficiency varies as a function of the variables that are most important to this analysis. This can be seen in greater detail in Figure 5.12, where the one- and two-dimensional selection efficiencies corresponding to the individual measurements of this analysis are shown. One effect that is clearly visible is the reduction of the selection efficiency in bins that correspond to higher average values of the top quark rapidities, like the outermost bins of the sensitive variable $\Delta|y|$ and the highest bins of $|y_{t\bar{t}}|$. This is a result of the limited angular range of the detector and the selection criteria that thus have been imposed on the pseudorapidities of the reconstructed objects. Another noteworthy effect is the reduction of the selection efficiency for events with lower energy content, as indicated by low values of $m_{t\bar{t}}$ or $p_{\mathrm{T}}^{t\bar{t}}$. The lower energy of the $t\bar{t}$ system corresponds to a lower energy of the produced jets and thus a lower chance for the event to pass the selection criteria on the reconstructed transverse momenta of the jets.

Similar to what was observed in Figure 5.11, the selection efficiency as a function of $|y_{t\bar{t}}|$ and $\Delta|y|$ behaves differently for bins in which $\Delta|y|$ is slightly larger than $|y_{t\bar{t}}|$. In this case the width of the phenomenon is reduced, though, as the bin sizes are smaller. The bins showing the effect are close to the boundary between events with same-sign rapidities and opposite-sign rapidities of the top quarks, i. e. one of the rapidities takes a value close to zero. This corresponds to a central position in the detector and thus means that the decay products of this quark have a high chance of remaining within the acceptance region of the analysis, yielding an improved selection efficiency.

The selection efficiency relative to the fiducial region, defined as the number of events selected in the event selection divided by the number of events in the fiducial region, can be seen in Figure 5.13. As the fiducial region is designed to emulate the reconstruction-level criteria imposed by the event selection, a more uniform distribution of selection efficiencies can be observed.

It should be noted that in the context of the fiducial measurements the term *selection efficiency* is not entirely accurate since the calculated values include the effect of events that are selected but not part of the fiducial region. The term

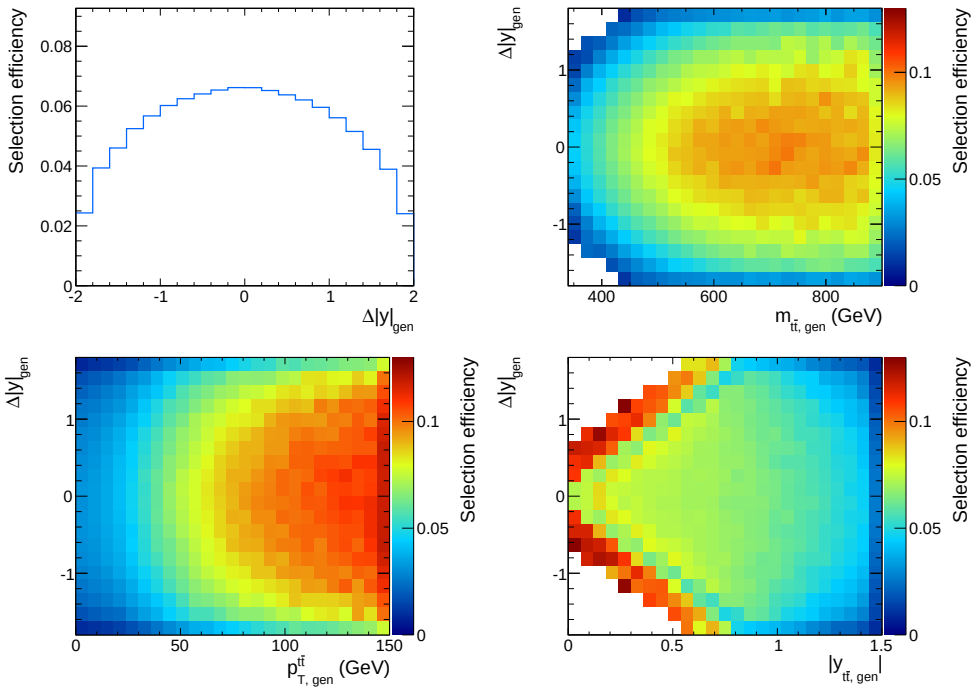

Figure 5.12: The dependence of the $t\bar{t}$ event selection efficiency on $\Delta|y|$ (top left) as well as its behavior as a two-dimensional function of $\Delta|y|$ and one of the secondary variables $m_{t\bar{t}}$, $p_T^{t\bar{t}}$ and $|y_{t\bar{t}}|$ (top right and bottom row). The outermost bins have been calculated including events beyond the axis ranges.

continues to be used, however, to avoid the introduction of additional complexity into the explanations of the method.

While Figures 5.12 and 5.13 are useful to gain an understanding of the effects at play, they are too finely-grained for the purposes of the unfolding method to be used. The distributions shown in Figures 5.14 and 5.15 are used instead. The reasoning behind these bin boundaries is detailed in Section 5.4.5.

5.4.2 Migration Effects

The reconstructed top quark four-vectors do not, in general, align perfectly with the true four-vectors. There are reasons for this in the identification criteria for physical objects interacting with the detector, in imprecisions in the measurements of the object energies and pseudorapidities, and finally in the reconstruction of the top quark pair outlined in Section 5.1. Some more specific examples are imperfections in the jet energy measurements, jets lost due to the selection criteria, and the selection of wrong reconstruction hypotheses.

All these effects result in a degraded resolution or even a bias of the reconstructed quantities. In order to understand and quantify the overall effects on the

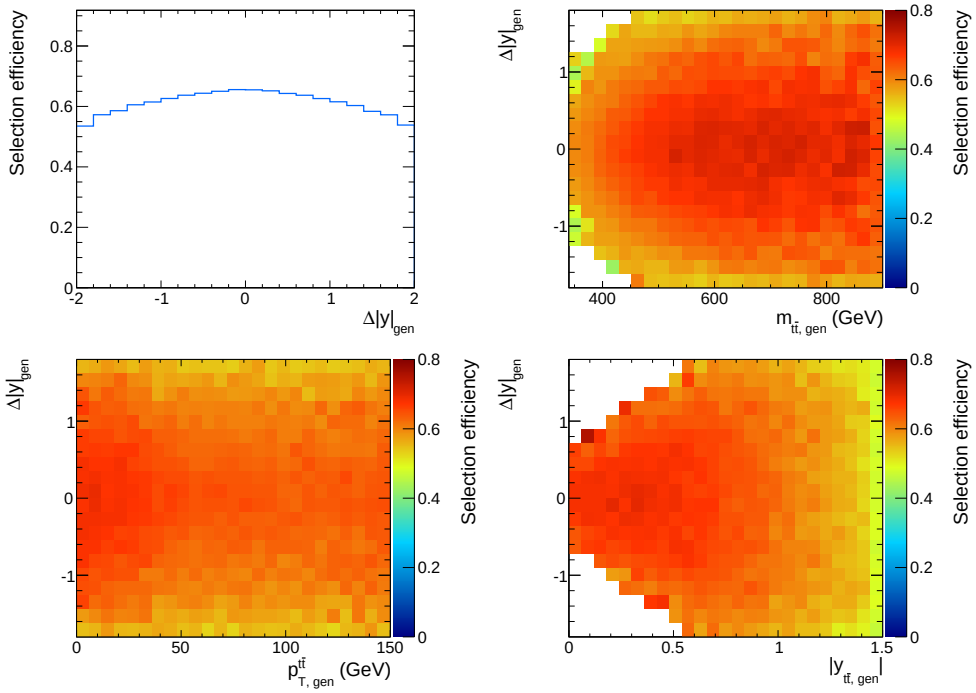

Figure 5.13: The dependence of the $t\bar{t}$ event selection efficiency relative to the fiducial phase space on $\Delta|y|$ (top left) as well as its behavior as a two-dimensional function of $\Delta|y|$ and one of the secondary variables $m_{t\bar{t}}$, $p_T^{t\bar{t}}$ and $|y_{t\bar{t}}|$ (top right and bottom row). The outermost bins have been calculated including events beyond the axis ranges.

reconstructed distributions, *migration matrices* are constructed using simulated samples. The matrices for the main observables of this analysis are shown in Figure 5.16.

In the case of a single observable, as in Figure 5.16(a), the migration matrix takes the form of a two-dimensional histogram with the true or generator-level values of the observable on the x-axis and the reconstructed values on the y-axis. In the case of an ideal reconstruction the matrix is diagonal, as off-diagonal elements represent misreconstructed events.

When two observables are measured at the same time the dimensionality increases and the matrices become four-dimensional. This has no profound impact on the mathematical foundations of the unfolding procedure. For the purposes of the visualization and the actual implementation, however, these four-dimensional matrices are transformed into two-dimensional matrices, as shown in Figures 5.16(b) to 5.16(d). After this transformation the axes repeatedly iterate through the indices of the sensitive variable bins – once for each bin of the secondary variable.

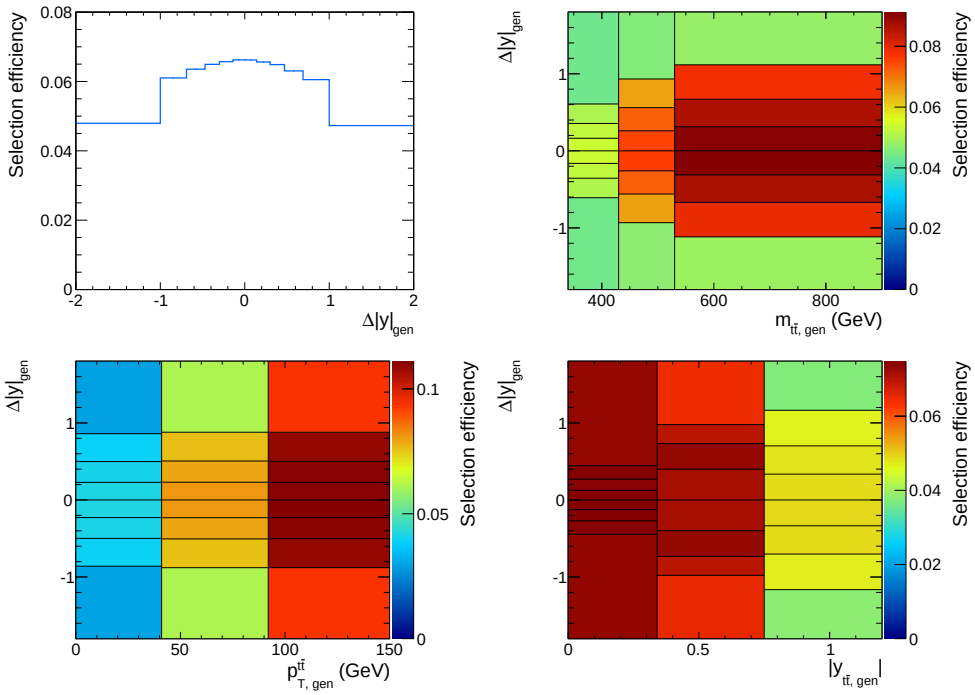

Figure 5.14: The dependence of the $t\bar{t}$ event selection efficiency on the sensitive variable (top left) as well as its behavior as a two-dimensional function of the sensitive variable and one of the three secondary variables $m_{t\bar{t}}$, $p_T^{t\bar{t}}$ and $|y_{t\bar{t}}|$ (top right and bottom row). The binning was chosen according to the reasoning given in Section 5.4.5.

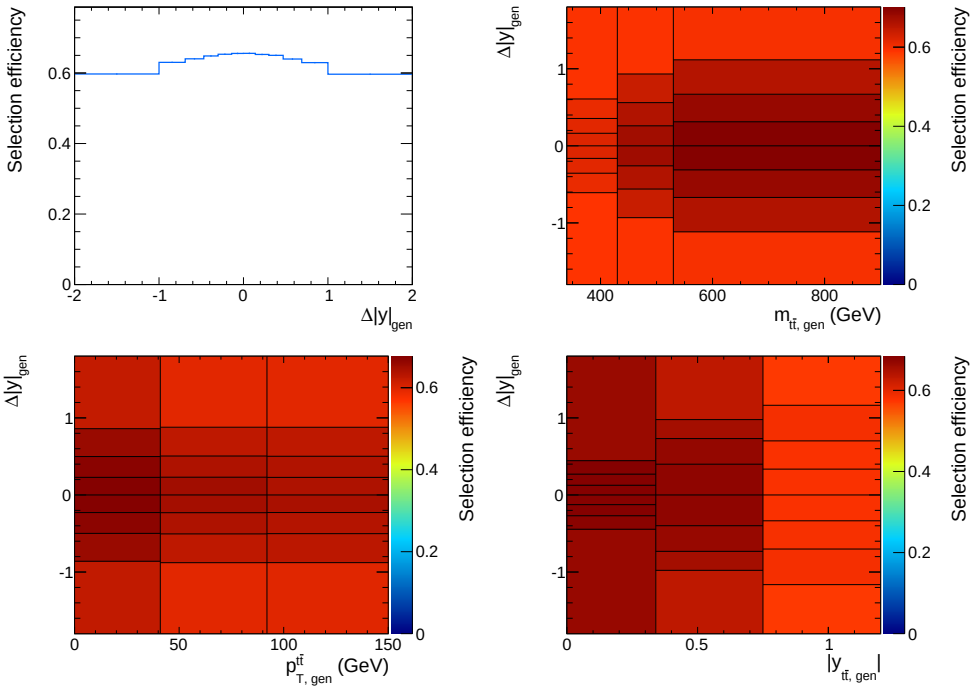

Figure 5.15: The dependence of the $\mathrm{t\bar{t}}$ event selection efficiency relative to the fiducial phase space on $\Delta|y|$ (top left) as well as its behavior as a two-dimensional function of $\Delta|y|$ and one of the three secondary variables $m_{\mathrm{t\bar{t}}}$, $p_{\mathrm{T}}^{\mathrm{t\bar{t}}}$ and $|y_{\mathrm{t\bar{t}}}|$ (top right and bottom row). The binning was chosen according to the reasoning given in Section 5.4.5.

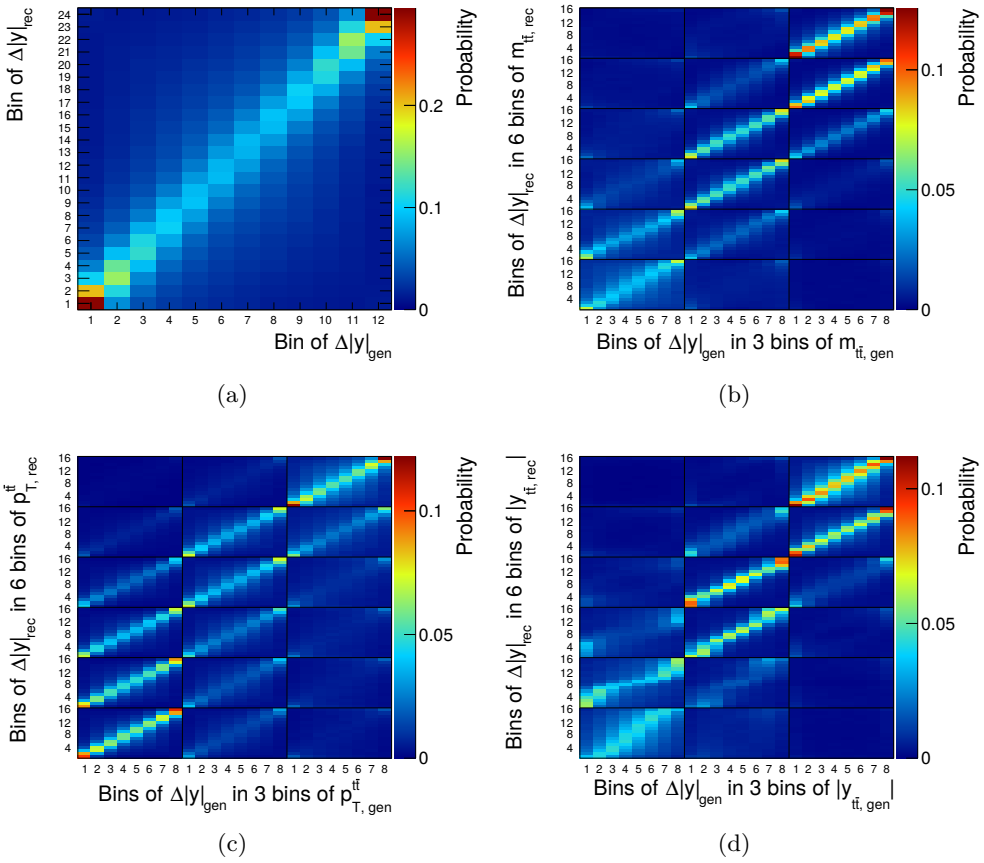

Figure 5.16: Migration matrices for the inclusive (top left) as well as the three-binned differential measurements (top right and bottom row). Each column of the matrices is normalized to unity to simplify interpretation: This way the individual entries correspond to the probability that a selected $t\bar{t}$ event with certain true values of the variables is found with specific reconstructed values of these same variables. These matrices equally apply to both the full and fiducial phase spaces.

5.4.3 Mathematical Foundation of the Unfolding Procedure

To correct for the distorting effects described above the TUnfold package [168] is used, which implements a regularized unfolding method [169].

For this purpose the distortion of the true spectrum $\vec{x}$ into the measured spectrum $\vec{w}$ is modeled as a transformation using a transition matrix A:

$$\vec{w} = A\vec{x} \tag{5.12}$$

This transition matrix is the product of the migration matrix and a diagonal matrix that contains the selection efficiencies for the individual bins. As such, it encompasses both the migration effects and the selection effects described above.

The same formula holds for multi-dimensional unfolding since the assignment of bin contents to vector elements can be chosen arbitrarily, disregarding the original geometry of the distributions.

The goal of the unfolding procedure is the inversion of Equation (5.12), allowing the calculation of the true spectrum $\vec{x}$ when given the reconstructed spectrum $\vec{w}$. One way of finding the exact solution is to transform the equation into a least-squares problem while taking into account the covariance matrix V_w of the measured distribution; the corresponding least-squares term F_{LS} can be written as

$$F_{\mathrm{LS}}(\vec{x}) = (A\vec{x} - \vec{w})^{\mathrm{T}}\, V_w^{-1}\, (A\vec{x} - \vec{w})\,. \tag{5.13}$$

While this yields an exact solution to the problem as described above, the application to a real measurement has additional requirements. The exact solution will induce a strong magnification of statistical fluctuations – because to the method they are indistinguishable from short-scale variations in the true spectrum that have been dampened by the measurement resolution. This magnification of the fluctuations induces strong negative correlations between neighboring elements of the solution vector. Such results are very hard to interpret and have only limited use for the calculation of derived quantities, even though they are not factually incorrect as long as the full covariance matrix is taken into account.

This problem can be compensated for by using a method that incorporates prior knowledge about the distribution to obtain non-exact but less correlated and physically more plausible solutions to Equation (5.12). To this end the least-squares problem introduced in Equation (5.13) is modified by two additional terms, yielding the final expression to be minimized:

$$F(\vec{x}, \kappa) = F_{\mathrm{LS}}(\vec{x}) + \tau \|L(\vec{x} - \vec{x}_{\mathrm{bias}})\|^2 + \kappa \left(N_{\mathrm{obs}} - \sum_{i=1}^{n} (A\vec{x})_i \right)^2 \tag{5.14}$$

The first new term, proportional to a regularization strength τ, comprises the regularization conditions that represent the prior knowledge on the distribution that is to be unfolded. If the true distribution can be assumed to be known in good approximation even before the measurement, as is the case for the measurements in this thesis, it is a sensible choice to regularize only the difference between the

unfolded data and the expected distribution. This allows to reduce the impact of the regularization on the large-scale structure of the physical distribution. It is for this purpose that the matrix encoding the regularization conditions, L, acts on the difference between the unfolded data $\vec{x}$ and a bias distribution $\vec{x}_{\text{bias}}$. The bias distribution is filled from the generator-level values of the simulated signal sample. Section 5.4.6 details the form and strength of the regularization conditions that have been chosen for this analysis.

The second auxiliary term, proportional to a Lagrangian multiplier κ, serves to ensure that the normalization of the result vector corresponds to the observed number of events on reconstruction level. This is achieved by applying the transition matrix to the solution vector and comparing the norm of the resulting vector to the number of data events N_{obs}. The main benefit of the introduction of this term is a better treatment of cases in which the uncertainties of the reconstructed data cannot be approximated to be Gaussian [170]. One important example of such a case are bins with low numbers of events, which have Poisson uncertainties that differ significantly from the Gaussian limit approached only for high numbers of events.

5.4.4 Statistical Covariance Matrices

The unfolding method minimizes Equation (5.14) and yields both a solution vector $\vec{x}$ and a statistical covariance matrix V_x for the individual elements of the solution vector. This covariance matrix includes the effects of the limited number of data events, the limited number of simulated events for the background subtraction, and the normalization uncertainties from the background estimation.

As a first step of its calculation, covariance matrices corresponding to the uncorrelated statistical bin-by-bin uncertainties of the templates and the correlated uncertainties of the overall template normalizations are added to the covariance matrix of the data. In a second step, this covariance matrix is transformed using a Jacobian matrix that is calculated for the analytical solution of the minimization problem given by Equation (5.14). The transformation yields the covariances of the unfolded values. A detailed account of these calculation steps can be found in reference [168].

However, the uncertainty due to the limited number of simulated signal events for the transition matrix needs to be estimated separately. It is an important effect; not only does it affect the statistical uncertainty of the main measurement, but it also reduces the accuracy in the determination of systematic uncertainties affecting the signal modeling. Due to their fine binning the transition matrices are the main components introducing this reliance on the number of simulated events.

Pseudo experiments are performed in order to study the corresponding statistical uncertainties affecting the measurement results. Within each experiment, the data are unfolded by a transition matrix with statistically varied elements. The unfolded bin contents or asymmetries are collected and used to calculate a covariance matrix

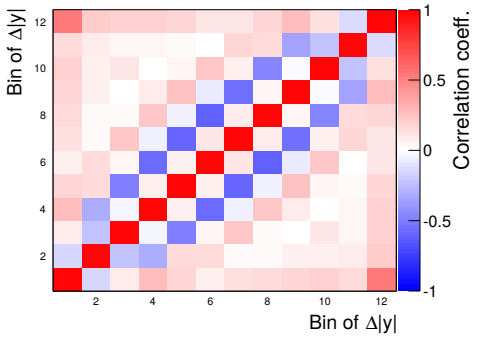

Figure 5.17: Statistical correlation matrix for the unfolded spectrum of the sensitive variable in the inclusive measurement in the full phase space.

using the formula

$$\mathrm{cov}(x, y) = \mathrm{E}[xy] - \mathrm{E}[x]\mathrm{E}[y]\,, \tag{5.15}$$

wherein x and y refer to individual elements whose covariance is to be determined, and E refers to the *expected value* of a given term. For this determination the average value of the given term can be used to represent its expected value.

As this analysis involves a partial symmetrization of the transition matrices, detailed in Section 5.4.7, each of the statistically varied transition matrices is resymmetrized before being applied to the data. Table 5.2 in that same section also gives an indication of how large the statistical uncertainties due to the transition matrix are.

As an example, the statistical correlation matrix for the bins of the sensitive variable in the inclusive measurement is shown in Figure 5.17. It can be seen that while the regularization does limit the negative correlations between nearest neighbors, such correlations as a result do occur between next-to-nearest neighbors. Avoiding this effect would require larger-scale regularization and thus not only an even more complicated method but also stronger regularization biases. Another significant feature of the correlation matrix is the large positive correlation coefficient for the outermost bins; studies have shown this to not be caused by the unfolding method but to be due to normalization variations in the background subtraction.

The covariance matrices described above apply either to the spectrum of the sensitive variable or, in the differential measurements of the asymmetry, to the combined spectrum of sensitive and secondary variables. Just as the asymmetries themselves are calculated from the spectra of the sensitive variable following Equation (1.10), the covariance matrices as well need to be transformed to yield the covariance matrices of the calculated asymmetries. For this purpose a propagation of the uncertainties in linear approximation is performed.

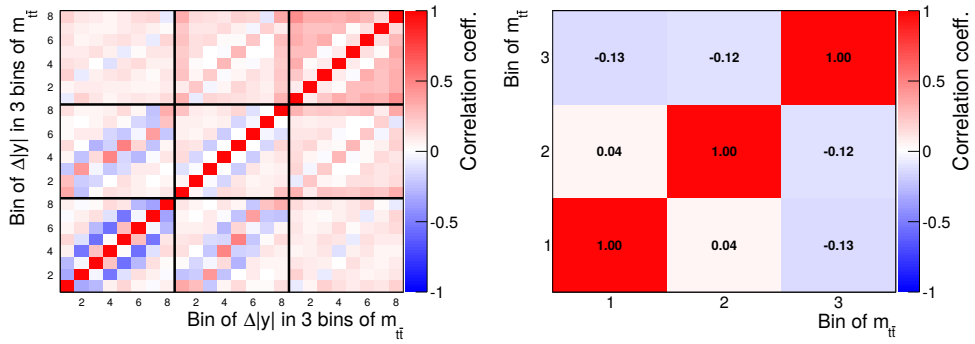

Figure 5.18: The statistical correlation matrix for the unfolded spectrum of the sensitive variable and a secondary variable (left) and the resulting correlation matrix of the calculated asymmetries (right).

As a first step the Jacobian matrix J of the calculated asymmetries as functions of the unfolded bins needs to be constructed; this is done by calculating the partial derivatives of the asymmetry formula given in Equation (1.10). It should be noted that only those partial derivatives can differ from zero in for which the given bins of the asymmetry distribution and the original unfolded distribution correspond to the same bin of the secondary variable distribution. Within any given bin i of the secondary variable the partial derivative of the asymmetry with regard to a bin j of the sensitive variable is given by

$$\frac{\partial A_{\mathrm{C},i}}{\partial N_{i,j^+}} = \frac{2N_i^-}{(N_i^+ + N_i^-)^2} \tag{5.16}$$

for bins j^+ corresponding to positive values of the sensitive variable and by

$$\frac{\partial A_{\mathrm{C},i}}{\partial N_{i,j^-}} = \frac{-2N_i^+}{(N_i^+ + N_i^-)^2} \tag{5.17}$$

for bins j^- corresponding to negative values of the sensitive variable. The Jacobian matrix is constructed using these partial derivatives, with each of the bins of the final asymmetry distribution corresponding to a row of the matrix, and each bin of the original unfolded spectrum corresponding to a column.

The covariance matrix of the asymmetries V_A then is obtained by transforming the covariance matrix of the sensitive and secondary variables using the Jacobian matrix:

$$V_A = JV_xJ^{\mathrm{T}}\,. \tag{5.18}$$

Figure 5.18 shows example correlation matrices for the input distribution and the results of this calculation. The full set of statistical correlation matrices can be found in Appendix B.

5.4.5 Choice of Binning

Several conditions should be considered when choosing the bins that are used in the context of an unfolding technique.

The resolution of the measured variables needs to be taken into account when deciding on the number of bins for the unfolded spectrum. A binning that is much finer than the measurement resolution will produce results that are strongly influenced by statistical fluctuations or by the regularization conditions. Additionally, the number of bins in the transition matrix grows quadratically with the chosen number of bins for the spectra themselves; this is important because the uncertainty due to the limited number of simulated events continues to be limiting factor in measurements of the charge asymmetry. A high number of bins in the transition matrix exacerbates this issue.

A binning that is too coarse, on the other hand, hides shape information that could have been unfolded successfully. It also has a higher dependency on the model assumptions introduced in the form of the simulated samples: While the selection efficiency or the migration behavior may vary strongly within a bin, the corresponding corrections can only be performed for the bin contents as a whole and thus rely on a correct prediction of the distribution of values within the bin.

Under these constraints it was chosen to use twelve bins for the unfolded distribution of the sensitive variable in the inclusive measurement. In the differential measurements this number is reduced to eight, accounting for the overall increase in bins due to the second variable that needs to be unfolded. The main measurements of the secondary variables use three bins, but an additional measurement in six bins of $m_{\mathrm{t\bar{t}}}$ is provided because of the high importance of the high-mass region for the search for new physics.

For the binning of the reconstructed values, which are the input to the unfolding method, it is recommended [169] to use a higher number of bins than what is used for the unfolded values. This protects against a loss of resolution due to the distortions introduced by the migration effects, as it allows for a more detailed modeling of their impact. Thus for this analysis it was chosen to use twice as many bins for each reconstructed variable distribution as compared to the corresponding unfolded variable distribution.

With the number of bins determined as described in the preceding paragraphs, the placement of the actual bin edges needs to be decided on. One reasonable criterion for measurements of very small asymmetries is to not introduce asymmetric behavior into the measurement method itself. As such, all bin edges used in this analysis are chosen to be symmetric around zero in the sensitive variable.

A second criterion is the minimization of distortions that may be introduced via the regularization conditions. The binning can be chosen in such a way that the resulting distributions have similar numbers of events within each bin,

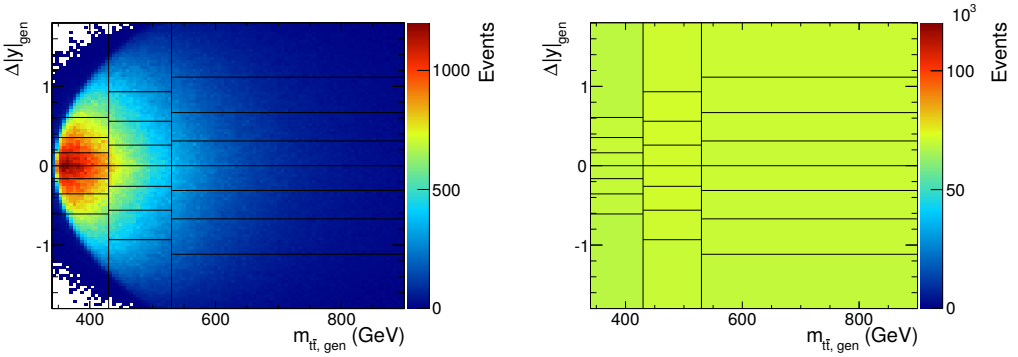

Figure 5.19: Two-dimensional spectrum of $\Delta|y|$ over $m_{t\bar{t}}$ in the selected events on generator level before (left) and after (right) optimization of the binning. For purposes of comparison the optimized bin edges are shown as black lines in both distributions.

as demonstrated in Figure 5.19. In this way the physical information of the expected distribution is moved into the binning itself, leaving only deviations from the expectation visible to the regularization. Advancements in the choice of regularization conditions, described in Section 5.4.6, have made this a less important issue than in previous iterations of the analysis.

A third criterion is the expected size of the uncertainties of the unfolded spectrum. A choice of bin edges that flattens the expected spectra, as outlined in the previous paragraph, yields the additional advantage that the resulting unfolded bins usually show comparable magnitudes of statistical uncertainties. This applies both to uncertainties stemming from the limited number of simulated events as well as to the uncertainties due to the limited number of data events.

Taking these considerations into account the binnings of reconstructed and parton-level values both are chosen to yield approximately flat distributions for the simulated signal events while still being exactly symmetrical around zero in the sensitive variable. For both binnings only those events that pass the event selection are used, as these are the events involved in the migration.

It must be noted that the measurement in six bins of $m_{t\bar{t}}$ is a special case. For this measurement the binning of $m_{t\bar{t}}$ has not been optimized in the way described above, but instead it is chosen to be directly comparable to the measurements done by the ATLAS collaboration. The main advantage of this bin choice is an increased granularity in the high-mass region. Disadvantages due to foregoing a part of the optimization have been compensated by a modified regularization procedure, described in Section 5.4.6, which ends up providing benefits to all of the differential measurements.

The full list of bin ranges can be found in Appendix C. By construction the criteria outlined above yield the same binning choices for the measurements in the full phase space and for the fiducial measurements.

Two significant criteria for the binning choice in an unfolding procedure are the *stability* and *purity* under the given migration effects. Under the given conditions, with twice as many reconstruction-level bins as parton-level bins, these criteria can be defined as follows. The stability quantifies what fraction of the events that are generated in a given bin is also reconstructed in the corresponding bins of the reconstruction-level spectrum. The purity, conversely, is the fraction of reconstructed events of a given bin grouping that also was generated in the corresponding bin of the parton-level binning.

The stability and purity of the individual bins is shown in Figure 5.20. The values are given with respect to the binnings used at parton-level. It can be seen that the individual bins of a given measurement do not differ widely in their purities and stabilities, which indicates that the binning choice is reasonably close to being optimal in terms of purity and stability.

5.4.6 Choice of Regularization Conditions

As described in Section 5.4.3, the regularization is introduced into the least-squares problem of the unfolding via a term

$$F_{\text{reg}}(\vec{x}) = \tau \|L(\vec{x} - \vec{x}_{\text{bias}})\|^2 \,. \tag{5.19}$$

The regularization thus is determined by the choice of a regularization matrix L that acts on the differences between the simulation and the unfolded data, hereafter referred to as $\vec{d} = \vec{x} - \vec{x}_{\text{bias}}$. Reflecting different possible priors the matrix can be constructed in many different ways, each of which results in a different bias of the result.

One example of a common choice is the use of a diagonal matrix, which has the effect that the overall normalization of $\vec{d}$ determines the size of the regularization term. In such a scheme any deviation from the expectation is reduced, resulting in a comparatively large model dependence of the unfolding relative to the amount of fluctuations that are suppressed.

The matrices used in this analysis are constructed according to a scheme that reduces this model dependence. For this it has to be understood that if one were to perform an interpolation of the measured discrete spectrum using cubic splines, for example, the fluctuations caused by statistical effects would result in large variations of the curvature of the interpolated curve. A sketch of this behavior is shown in Figure 5.21. The regularization can exploit this fact by suppressing solutions that yield large second derivatives of the spectrum $\vec{d}$, corresponding to the large curvatures. Compared to the example outlined above this has the advantage that effects that are linear in $\vec{d}$ can be measured without any distortion due to the regularization conditions.

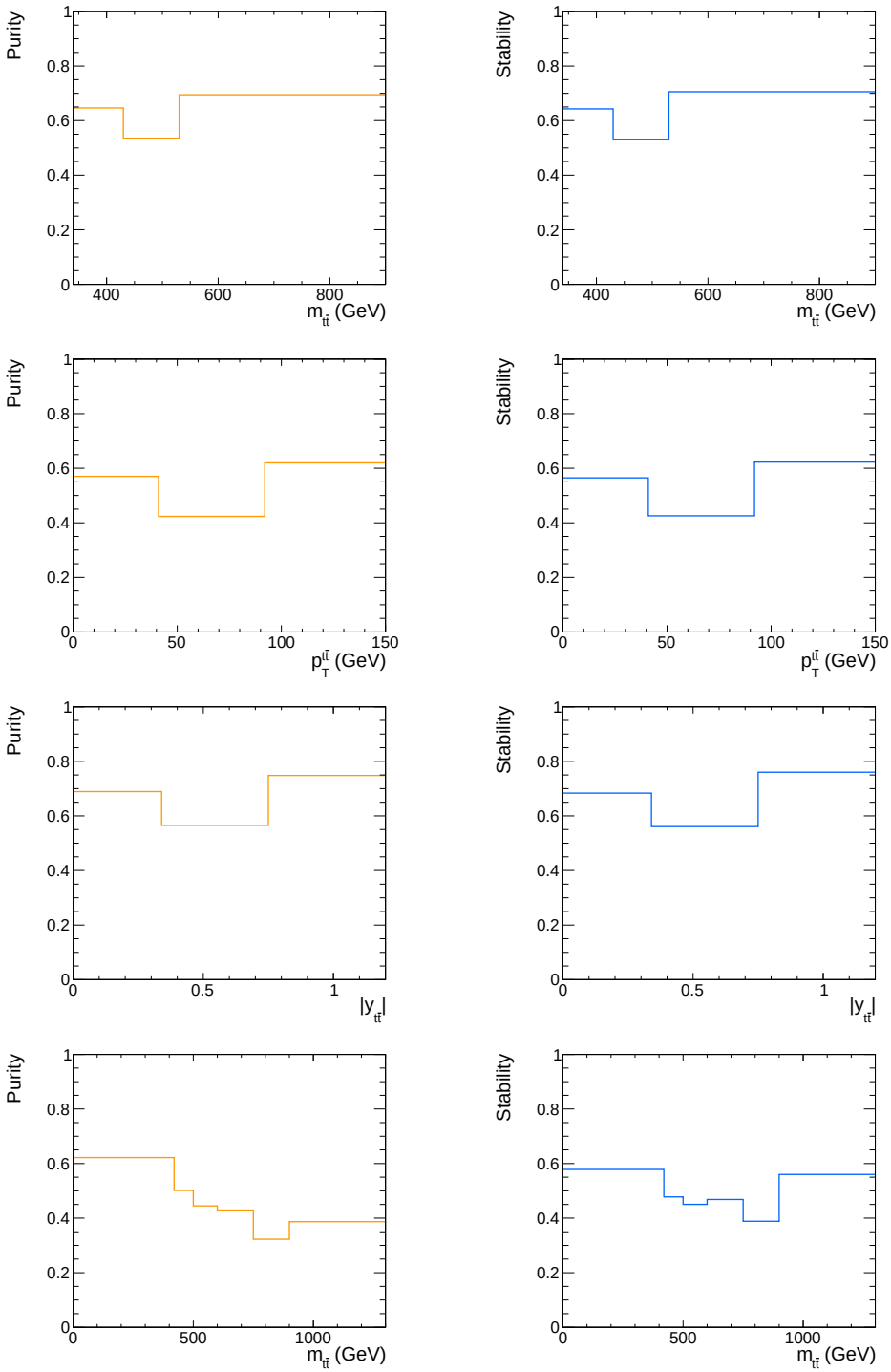

Figure 5.20: Purity (left) and stability (right) of the reconstruction of the secondary variable for the binnings used for the differential measurements of the charge asymmetry. The statistical uncertainties on these values are negligible.

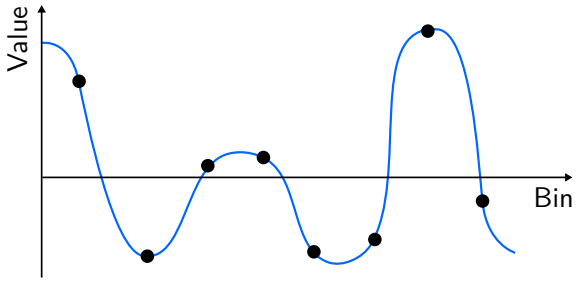

Figure 5.21: Sketch of the relation between statistical fluctuations of the measured values, shown as black dots, and the resulting interpretation in the form of a curved line. In this illustration the x-axis also represents the central value that would be measured at each point in the absence of statistical limitations.

To understand how the second derivative can be calculated for a discrete spectrum one needs to look at the central difference approximation of the second derivative of a continuous function:

$$f''(x) \approx \frac{f(x+\Delta x) - 2f(x) + f(x-\Delta x)}{\Delta x^2} \tag{5.20}$$

It represents an approximation of the second derivative of the function that is calculated using only three distinct values of the function from points close to the point of evaluation. This formula can be transferred to the discrete case by using the values of three neighboring bins i, j and k:

$$d_i - 2d_j + d_k \tag{5.21}$$

In this the distance Δx between evaluation points has been disregarded as it represents only a normalization factor. The matrix L, which can be understood as a coefficient matrix for $\vec{d}$, is then defined in such a way that terms corresponding to Equation (5.21) are introduced for every combination of three neighboring bins in the spectrum.

The outlined regularization terms work comparatively well when the binning is chosen in such a way that the unfolded distribution has similar amounts of events in each of its bins. However, biasing effects arise when the nominal bin contents themselves are expected to have a curving distribution. This is the case for the measurements in this thesis – either because the binning was not optimized to obtain an equal distribution, like in the six-binned measurement of $m_{t\bar{t}}$, or because the optimization has been done on the level of selected events instead of all events. Any unsimulated effect in the data that is roughly proportional to the expected contents of each bin will in this case lead to a curvature in $\vec{d}$. This curvature is reduced by the regularization and can lead to significant biases in the result. For the measurements in this thesis only small deviations from the simulation are to be measured and any effects can be assumed to be occurring on a large scale compared to the granularity of the binning. Under these conditions the scale of

deviations from the expectation in a bin can be assumed to be proportional to the bin contents, and the bias described above takes on an important role.

In order to reduce this bias the commonly used regularization terms of Equation (5.21) have been modified for this analysis. The underlying idea of the modification is to account for differing bin normalizations by rescaling the individual terms that are used to calculate the curvature. Each of the elements of $\vec{d}$ going into the curvature term is multiplied by the inverse of its nominal bin contents in the simulation:

$$c_i d_i - 2c_j d_j + c_k d_k \,, \tag{5.22}$$

wherein $c_i = 1/x_{i,\mathrm{sim}}$. These rescaled components then behave the same under the influence of effects that are proportional to the bin contents. Figure 5.22 shows the beneficial effect this has on the bias observed in linearity tests; the tests themselves are described in detail in Section 5.5.2.

As outlined in the previous section and demonstrated in Figure 5.19, among others, the binning schemes used in this analysis allow for different amounts of vertical overlap between horizontally neighboring bins. This increases the number of combinations of neighboring bins that need to be taken into account significantly. It also means that the regularization conditions need to be weighted differently to make sure that the curvature of directly neighboring bins has a bigger influence on the result than the curvature of bins that share only a very small part of their boundaries.

For this purpose each of the regularization conditions, as given in Equation (5.22), is weighted with an overall factor

$$w_{ijk} = \frac{o_{ij}}{h_j} \cdot \frac{o_{jk}}{h_j} \,, \tag{5.23}$$

where o_{ij} represents the amount of vertical overlap between the bins i and j, and h_j is the total height of the middle bin.

The outermost bins of the sensitive variable effectively have infinite height. A strict application of the scheme thus would yield weights of zero and disable regularization along the secondary variable. For this analysis instead it was chosen to treat them as if they extended to an arbitrary value of $+1.8$ or -1.8 instead of positive or negative infinity, restoring regularization along the secondary variable. There is no strong dependence of the results on the exact choice of this value, and consistency tests done using pseudo experiments (see Sections 5.5.1 and 5.5.2) show this to not introduce a significant bias into the measured asymmetries.

In summary, the individual regularization condition introduced by the matrix L for a given group of three bins is chosen to be

$$w_{ijk} \cdot \left(c_i d_i - 2c_j d_j + c_k d_k\right) \,. \tag{5.24}$$

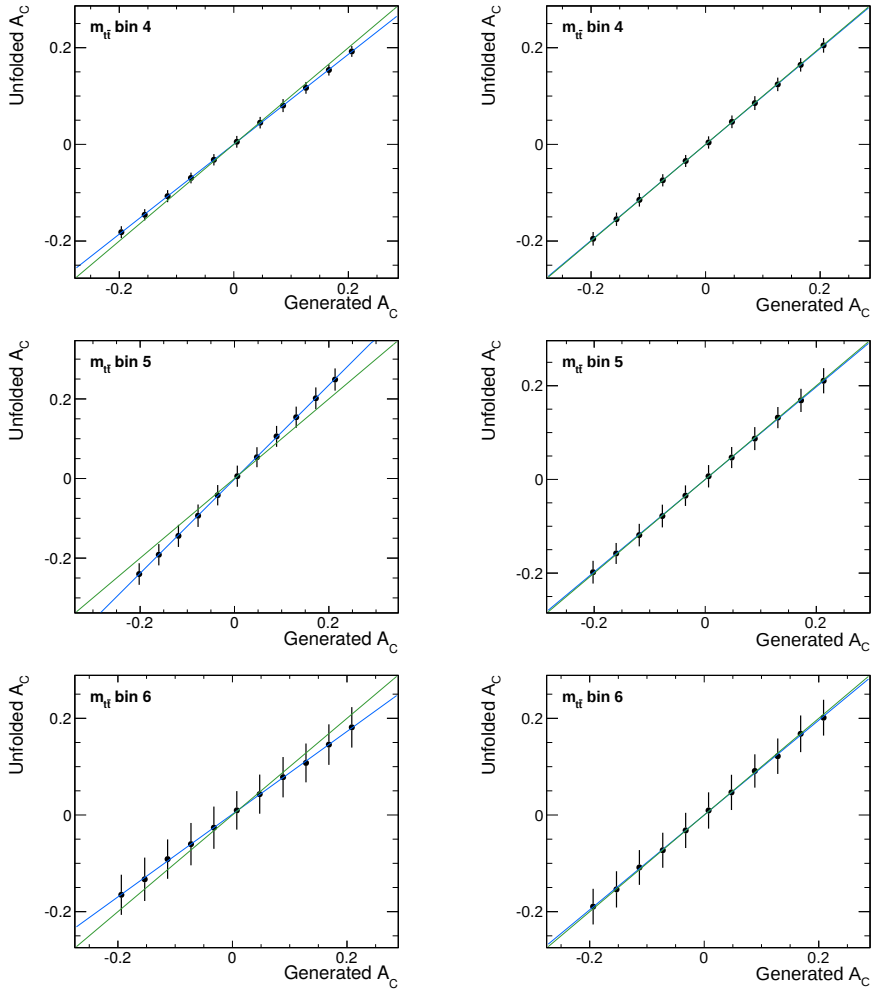

Figure 5.22: Some linearity tests in the fiducial phase space without (left column) and with (right column) compensation for differing expected bin contents, with all other optimizations being performed the same way. The points signify the measured asymmetries as a function of the generator-level asymmetry injected into the simulated samples. The result of a linear regression is drawn in blue, whereas the bisector is shown in green. In the ideal case both lines are identical. The shown error bars correspond to the uncertainty of an individual measurement. Linearity tests are described in more detail in Section 5.5.2

The overall strength of regularization and the relative strengths of the individual regularization conditions need further deliberation. For this it needs to be kept in mind that a lack of regularization results in negative correlations between the unfolded bins due to the magnification of the statistical fluctuations, whereas a regularization that is too strong overcompensates for this effect and introduces positive correlations between the unfolded bins. A minimization of the absolute values of the bin correlations thus is a good criterion to find a regularization strength that represents a sensible compromise between these two effects. This is referred to as the *minimization of the global correlations* [171] and represents an objective way of optimizing the regularization strengths.

The global correlation of the element i of $\vec{x}$ is defined [171] as

$$\rho_i = \sqrt{1 - \left[(V_x)_{ii} \cdot (V_x^{-1})_{ii}\right]^{-1}}. \tag{5.25}$$

It is a measure of the total amount of correlation between element i and all other elements of $\vec{x}$. The average of these ρ_i is calculated and the overall regularization strength is modified to find a minimum of the resulting value, as observed in pseudo experiments using the event yields determined in the background estimation in Section 4.4.

For most analyses the use of a single overall regularization strength yields sufficient results. In the context of the multidimensional distributions unfolded in this analysis, however, there is no good argument to be made why the regularization strength along the sensitive variable should be the same as the regularization strength along the secondary variable. Similarly, different regions of the secondary variable – like different bins of $m_{\mathrm{t\bar{t}}}$, for example – cannot be assumed to require the same regularization strengths. Finally, when the absolute bin contents differ widely between different regions of the spectrum, the optimal relative weight of the corresponding regularization conditions is not evident, either.

It is for this reason that in this analysis an approach has been chosen that employs a number of additional regularization strength parameters that apply only to specific subsets of the regularization conditions. These can be divided into two groups:

The first group consists of n parameters, with n being the number of bins in the unfolded spectrum of the secondary variable – i. e. 3 or 6 in the measurements of this analysis. Each of them modifies the strength of regularization along the sensitive variable within a given bin of the secondary variable.

The second group consists of $n - 2$ parameters. They control the strength of regularization along the secondary variable. Each parameter corresponds to one of the bins of the secondary variable that is used as central bin for the regularization conditions. As the two outermost bins of the spectrum never function as central bins they are not assigned dedicated parameters. This also means that for the unfolding of spectra with three bins only one parameter of this kind can be used.

To reduce the complexity of the technical implementation the optimization of these regularization parameters is performed one parameter at a time. In order to verify this approach a test has been performed where the order of determination of the parameters was reversed; the determined parameters have been found to remain stable under this reversal.

In the first steps the subset of parameters controlling the regularization along the sensitive variable is optimized. Each parameter is set to the value that minimizes the average global correlation of the unfolded bins, as defined above.

For the optimization of the parameters governing the regularization along the secondary variable, however, a slightly different method is used. Considering the fact that the differential measurements do not specifically aim to be measurements of the sensitive variable, but only need to unfold it to allow for the calculation of asymmetries, there is no reason to optimize the measurement for a minimal correlation between the unfolded bins along the secondary variable. What instead needs to be optimized is the correlation among the calculated asymmetries, which has been found to remain at finite negative values in the case of an optimization for the sensitive variable. For this purpose the covariance matrix of the unfolded spectrum V_x in Equation (5.25) is replaced by the covariance matrix of the asymmetries V_A, calculated as described in Section 5.4.4.

The reduction of correlations that is achieved by this method is demonstrated in Figure 5.23.

In summary it can be said that the introduction of the complex regularization scheme described in this section has helped to reduce the uncertainties in the asymmetries of the differential measurements, it has led to reduced correlations between the calculated asymmetries, and it has reduced the biases observed in linearity tests. Even though the scheme was developed for this measurement of the charge asymmetry in particular, the underlying ideas are applicable to other uses of regularized unfolding techniques and can be expected to yield improvements similar to the ones observed in this analysis.

5.4.7 Partial Symmetrization of the Transition Matrix

In this analysis an approximate symmetry of the transition matrices is exploited to reduce the statistical effects due to the limited number of simulated signal events, which have been described in Section 5.4.4.

For this it needs to be understood that $t\bar{t}$ production processes that involve only two gluons as incoming particles are inherently charge-symmetric. Similarly, detector effects to good approximation can be assumed to behave in a charge-symmetric way.

In the context of the sensitive variable charge-symmetric behavior means that positive and negative values of the variable need to occur at the same frequency. Transferring this to the migration matrix, it means that any migration from a value $\Delta|y|_{\text{gen}}$ to a value $\Delta|y|_{\text{rec}}$ needs to be just as frequent as migration from

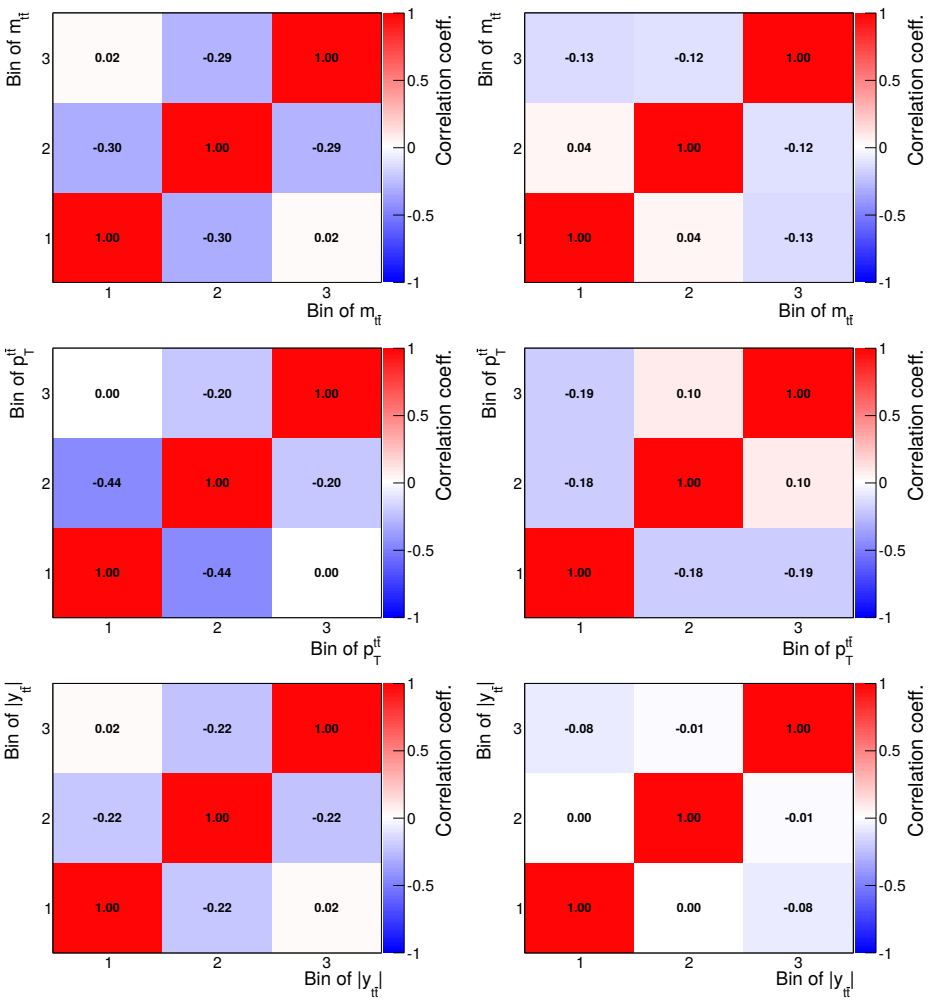

Figure 5.23: Statistical correlation matrices of the three-binned differential measurements in the full phase space without (left column) and with (right column) the optimization of the regularization conditions to the two-dimensional binning schemes. The new method yields a significant reduction of the correlations between neighboring bins.

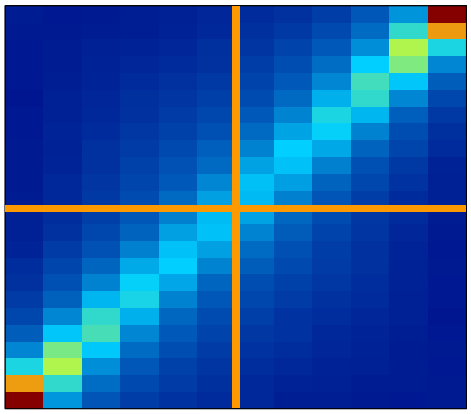

Figure 5.24: Illustration of the approximate symmetry that is exploited for an explicit symmetrization of the gluon-gluon channel. The migration matrix of the inclusive measurements is shown with two additional orange lines, indicating the two reflection axes that represent a central inversion symmetry in combination.

$-\Delta|y|_{\mathrm{gen}}$ to $-\Delta|y|_{\mathrm{rec}}$. An illustration of this symmetry for the case of the inclusive measurements is shown in Figure 5.24.

To exploit the symmetry the simulated events identified by the Monte Carlo generator to have occurred from gluon-gluon initial states are filled twice into the transition matrix, both for their actual values as well as for the charge-conjugated ones. An additional weight of 0.5 is applied in these cases to retain the normalization relative to the other production processes.

It should be noted that this method not only yields a factor of 2 in the number of simulated events of the dominant production processes, but it also explicitly suppresses asymmetric fluctuations in this symmetric component of the transition matrix.

A verification of the procedure has been performed using pseudo experiments. The underlying idea is to show the statistical compatibility between the two unfolded asymmetries with and without the application of the symmetrization procedure.

One starts with the assumption that asymmetric behavior in the gluon-gluon component of the transition matrix stems only from statistical effects. The symmetrized version of the transition matrix thus is taken as a baseline for the experiments, and each bin is varied statistically independently for each experiment. Due to the statistical variations asymmetric effects get introduced again, making this varied matrix an analogon to the original unsymmetrized transition matrix. This matrix is used to unfold the data; it is then resymmetrized and used to unfold the data a second time.

For each experiment the difference between the unfolded asymmetries is entered into a histogram. The resulting Gaussian distributions represent the expected statistical effects due to the symmetrization procedure. Using a χ^2 test to compare

Table 5.2: Statistical uncertainty due to the limited number of simulated events in the transition matrix, both before and after the application of the symmetrization of the events stemming from gluon-gluon production processes.

				$m_{\mathrm{t\bar{t}}}$		
	inclusive meas.			Bin 1	Bin 2	Bin 3
unsymmetrized	0.0024			0.0063	0.0032	0.0027
symmetrized	0.0014			0.0040	0.0020	0.0017
	$p_{\mathrm{T}}^{\mathrm{t\bar{t}}}$			$\lvert y_{\mathrm{t\bar{t}}} \rvert$		
	Bin 1	Bin 2	Bin 3	Bin 1	Bin 2	Bin 3
unsymmetrized	0.0036	0.0041	0.0051	0.0056	0.0028	0.0032
symmetrized	0.0022	0.0025	0.0036	0.0035	0.0017	0.0021

the standard deviations of these distributions to the actual shifts introduced by the symmetrization in the three-binned nominal measurements, it is found that the shifts are compatible with the hypothesis of purely statistical effects at a p-value of 88%.

Table 5.2 shows the effect of the symmetrization on the statistical uncertainty of the unfolded asymmetries that stems from the limited number of simulated signal events. The improvements are of the order of 30 to 40%.

5.5 Validation

5.5.1 Consistency Tests

With the unfolding method being a comparatively complex measurement method that can entail unintended biases, self-consistency tests are essential to ensure the validity of the method and to understand the biasing effects. They also allow to validate the behavior and size of statistical uncertainties.

In these tests the reconstruction-level distributions of the simulated samples and the data-driven templates are used to construct sets of pseudo data that derive their normalizations and compositions from what is observed in the background estimation on data, described in Section 4.4. The pseudo datasets then are subject to the same background subtraction and unfolding methods that are used in the measurements on data. The unfolded distributions and asymmetries resulting from these pseudo experiments can be compared to their generator-level equivalents, or the distribution of their values can be compared to the expected size of the statistical effects.

In a first step the normalizations of the individual processes are varied according to Gaussian probability distributions representing the statistical uncertainties

of the background estimation. The uncertainties due to the limited number of simulated events are accounted for by varying each bin of each template according to the statistical uncertainty on its content; here as well the Gaussian probability distribution is chosen as an approximation, because Poisson statistics do not apply to weighted events such as those making up the templates. Finally, in order to also simulate the Poisson statistics of the individual bins in the measured distributions, new distributions are constructed by randomly drawing the calculated numbers of events from the templates that were constructed in the previous step.

The off-diagonal elements of the covariance matrix of the background estimation have a comparatively small effect on the final uncertainties; because of this it has been considered acceptable to forgo the simulation of this effect for the pseudo experiments.

For each of the inclusive and differential measurements of this thesis 10,000 pseudo experiments are performed. The unfolded asymmetries are filled into histograms, and their mean value is compared to the true asymmetry of the simulated samples. The calculated statistical uncertainties of the asymmetries are filled into a different set of histograms, allowing to study the spread of the statistical uncertainty that is caused by the statistical effects themselves. Finally, the *pull* P is calculated and filled into a third set of histograms. It is defined as

$$P = \frac{A_{\mathrm{C}}^{\mathrm{true}} - A_{\mathrm{C}}^{\mathrm{corr}}}{\sigma_{\mathrm{calc}}}\,, \tag{5.26}$$

with the true and corrected asymmetries $A_{\mathrm{C}}^{\mathrm{true}}$ and $A_{\mathrm{C}}^{\mathrm{corr}}$ and the calculated statistical uncertainty σ_{calc}. The pull distribution allows to verify the calculation of the statistical uncertainty; if the uncertainty is calculated correctly the distribution is Gaussian and its standard deviation σ_{P} is close to 1.

Figures 5.25 to 5.27 show the distributions explained above for the inclusive measurement and the three-binned differential measurement of $m_{\mathrm{t\bar{t}}}$ in the full phase space of top quark pair production. The corresponding distributions for the remaining measurements of this thesis can be found in Appendix D. In all cases the distributions show a correct measurement of the central value of the asymmetry as well as a correct calculation of the statistical uncertainty.

5.5.2 Linearity Tests

The self-consistency tests presented in the previous section do not suffice to ensure the validity of the method in cases where the measured asymmetries differ from those in the simulated samples. This is a significant omission as standard model calculations yield considerably higher asymmetries than those simulated by the Monte Carlo generators, and many processes extending beyond the SM are known to lead to sizable changes in the charge asymmetry, as well.

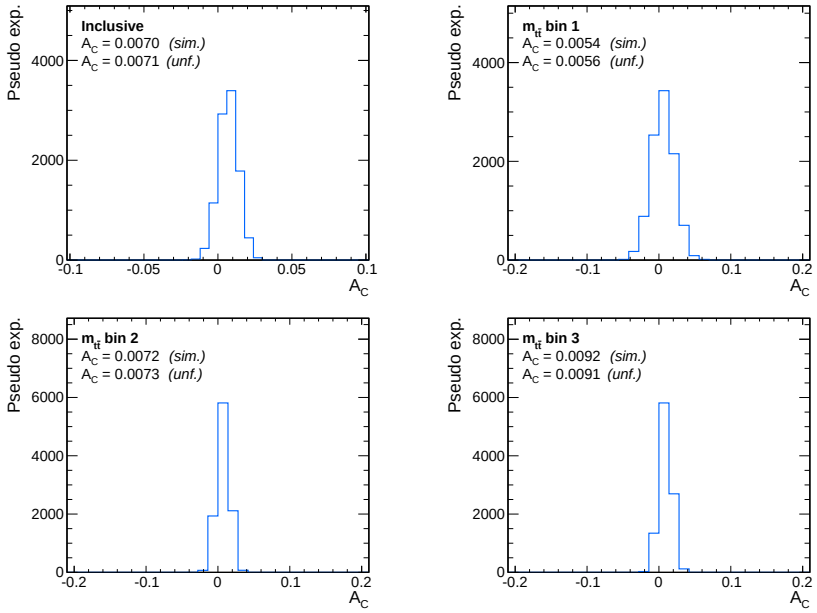

Figure 5.25: Distribution of the measured asymmetries in pseudo experiments corresponding to the inclusive measurement (top left) and the individual bins of a differential measurement in $m_{t\bar{t}}$ (top right, lower row) in the full phase space.

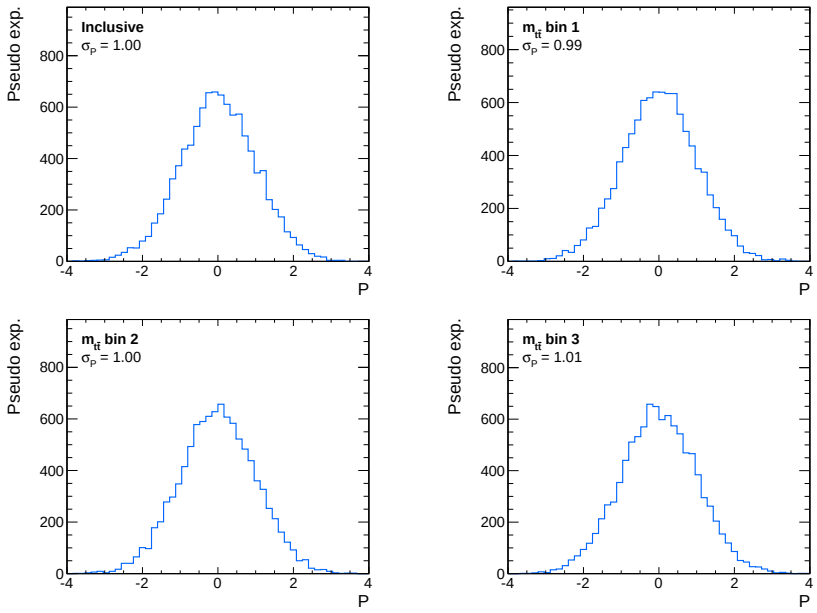

Figure 5.26: Pull distributions of the measured asymmetries in pseudo experiments corresponding to the inclusive measurement (top left) and the individual bins of a differential measurement in $m_{t\bar{t}}$ (top right, lower row) in the full phase space. σ_P signifies the standard deviation of the pull distribution.

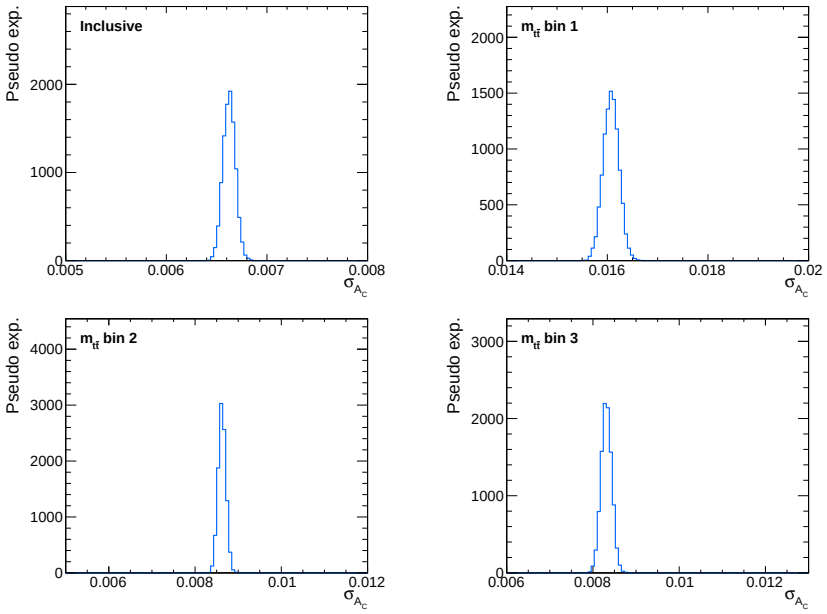

Figure 5.27: Distribution of the statistical uncertainties of the measured asymmetries in pseudo experiments corresponding to the inclusive measurement (top left) and the individual bins of a differential measurement in $m_{t\bar{t}}$ (top right, lower row) in the full phase space.

Linearity tests can be understood as self-consistency tests that are modified to perform a reweighting of the simulated signal samples, inducing different amounts of asymmetry in the samples. The method can be considered to pass the test only if the reweighted reconstruction-level asymmetries are unfolded to yield the values of the reweighted generator-level asymmetries.

The different asymmetries are induced by reweighting the events linearly as a function of the generated value of the sensitive variable. Thus the reweighting factors w are defined as

$$w = k \cdot \Delta|y| + 1\,. \tag{5.27}$$

In this k signifies the strength of the reweighting. For the tests performed in this thesis it is varied from -0.25 to $+0.25$, representing amounts of variation far beyond what is expected or observed in data.

It should be noted that the linear reweighting can only be considered a first-order approximation of any possible effects that could distort the distribution; if significant deviations from the expectation were observed, more finely adjusted tests ought to be performed to evaluate the given scenario. However, the results of this analysis do not indicate a need for such a procedure.

Figures 5.28 and 5.29 show the outcomes of these tests for the inclusive measurement and the three-binned differential measurement of $m_{t\bar{t}}$ in the full phase

space of top quark pair production. The corresponding figures for the remaining measurements of this thesis can be found in Appendix E.

In all cases it can be seen that the unfolded asymmetries can be described as linear functions of the generated asymmetries. While some of the functional relations show deviations from the ideal behavior, indicated by the bisector in green, the effects are small compared to the sizes of the uncertainties. For this evaluation it has to be understood that the reweighted asymmetries include much larger values than what is expected or actually observed in data; at the observed values the effect of the slope difference is small. Because the size and direction of the deviations depends on the exact nature of the performed reweighting, it cannot be accounted for by static correction factors. Instead an additional systematic uncertainty is assigned that covers both this effect and more complicated ones; this is described in Section 5.6.2.

Even though remaining regularization biases and statistical effects can play a role, the most significant part of the observed slope deviations has its origin in the extrapolation that is performed with the acceptance corrections. When the unmeasured phase space and the measured one behave differently under some effect, be it the explicit reweighting or the presence of new physics, their ratios change and the selection efficiencies determined in the nominal simulation do not represent the needed corrections perfectly anymore. This can be seen when comparing the linearity tests of the measurement in the full phase space with those in the fiducial phase space: Due to the reduced amount of extrapolation needed for the fiducial measurement its linearity tests show much smaller deviations from the bisector line. The corresponding figures for these tests can be found in Appendix E.

It should also be noted that, as explained and demonstrated in Section 5.4.6, a less optimized regularization scheme than the one developed in this thesis can lead to significantly bigger deviations.

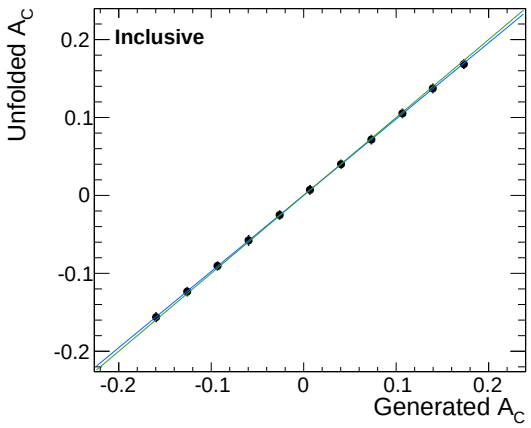

Figure 5.28: Linearity test: Mean of unfolded A_C in the full phase space as a function of the true simulated value. The error bars indicate the statistical uncertainty of a single measurement. The result of a linear regression is drawn in blue, whereas the bisector is shown in green.

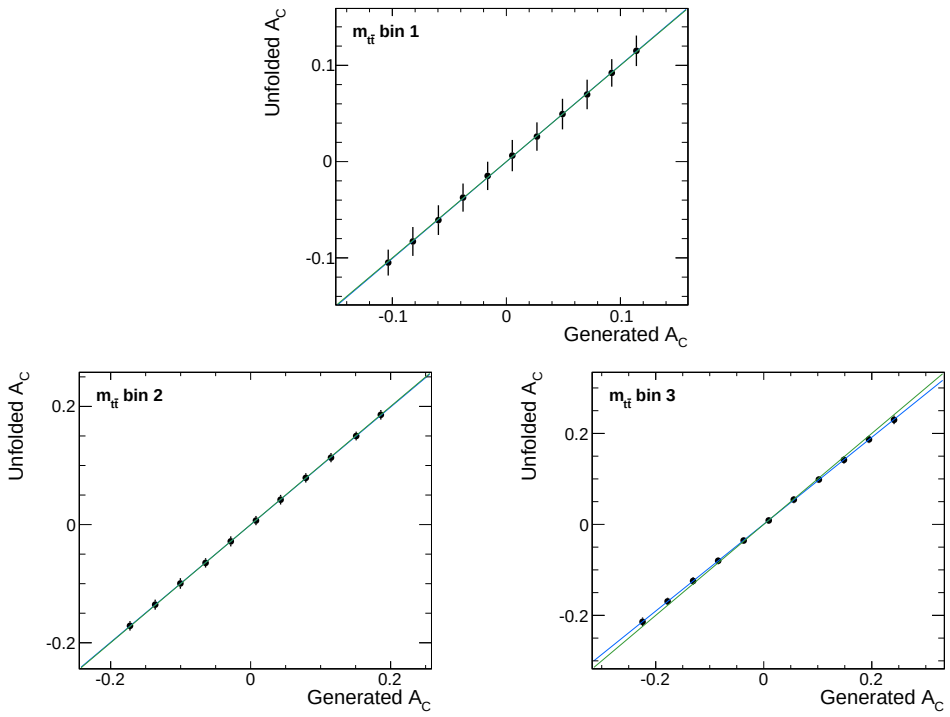

Figure 5.29: Linearity test: Mean of unfolded A_C in the full phase space as a function of the true simulated value in three bins of $m_{t\bar{t}}$. The error bars indicate the statistical uncertainty of a single measurement. The result of a linear regression is drawn in blue, whereas the bisector is shown in green.

5.6 Systematic Uncertainties

Beside the statistical uncertainties of the measurement described in some of the preceding sections the measurement also is subject to significant uncertainties due to systematic effects. While overall rate uncertainties do not have a strong influence on an observable that, like the charge asymmetry, is defined as a ratio, variations affecting the shapes of the distributions do have the potential to affect the charge asymmetry measurement.

Imprecisions in the simulation of the background processes affect the background estimation and the background subtraction.

Even though efforts have been made to achieve as low a model dependence as possible, the measurement also has a significant dependence on the correctness of the signal simulation. This dependence manifests at various points in the analysis.

The background estimation depends on a correct simulation of the variables $m_{\mathrm{T}}^{\mathrm{W}}$ and M3. A mismodeling results in wrong assumptions about the signal fraction and thus about both the correct normalizations of the background processes as well as the relative frequency of electron+jets and muon+jets signal events.

The reconstruction procedure has been optimized for the nominal signal sample; if the simulated input variables show deviations from the behavior in data, the reconstruction of data events will be of different precision than that of the simulated events. Such a worsened reconstruction performance changes the migration effects and thus the correctness of the migration matrix that has been obtained from simulation.

Finally, the regularization of the unfolded results suppresses deviations from the used simulated signal sample, introducing another dependency on its correctness.

In this analysis the systematic uncertainties are estimated by reperforming the measurement on data while using systematically shifted templates for the background estimation, the background subtraction, and the construction of the bias distribution and transition matrix used for the unfolding. The observed shifts in the measured distributions with regard to the nominal results then are taken to be a measure of the uncertainties due to the given systematic variation. Where two shifts of the same underlying uncertainty are available, the uncertainty generally is estimated as a normal distribution with a standard deviation that is defined by the larger of the two shifts.

The advantage of performing the estimation of systematic uncertainties in measurements on the actual data lies in the reduced model dependence of the resulting values; they are evaluated at the point in phase space indicated by data rather than at the point that is simulated by the chosen Monte Carlo generators.

5.6.1 Determination of Covariance Matrices

A proper evaluation of the differential distributions, such as a formal comparison with a given theory prediction, requires knowledge about the full covariance matrix

of the measured spectrum. The determination of the statistical covariance matrices of the asymmetries is discussed in Section 5.4.4, yet for the systematic uncertainties additional considerations need to be taken into account.

For a given set of variables the individual elements of a *statistical* covariance matrix are defined as

$$\mathrm{cov}(x, y) = \mathrm{E}\left[(x - \mathrm{E}[x]) \cdot (y - \mathrm{E}[y])\right] , \tag{5.28}$$

wherein x and y refer to individual elements of the set of variables and E refers to the *expected value* of a given term.

From this one can derive a definition of the covariance matrix for a systematic uncertainty that is described by n systematic shifts:

$$\mathrm{cov}(x, y) = \frac{1}{n} \sum_{i}^{n} \left[(x_i - x_{\mathrm{nom}}) \cdot (y_i - y_{\mathrm{nom}})\right] , \tag{5.29}$$

with x_i and y_i representing the values of variables x and y that are measured when the systematic shift i is applied, and x_{nom} and y_{nom} being the results of the nominal measurement. The choice of using the nominal values in place of the expected ones is motivated by the fact that they fulfill the same role: They represent those values that are considered to have the highest probability of being correct.

For a systematic uncertainty that is described by only a single shift with regard to the nominal values Equation (5.29) simplifies to

$$\mathrm{cov}(x, y) = (x_{\mathrm{sys}} - x_{\mathrm{nom}}) \cdot (y_{\mathrm{sys}} - y_{\mathrm{nom}}) , \tag{5.30}$$

with x_{sys} and y_{sys} referring to the values that are measured when the systematic shift is applied. From this form it can easily be seen that the calculated covariances correspond to one-sigma shifts if the systematic variation itself corresponds to a difference of one standard deviation. This is the case for the uncertainties considered in this thesis.

In the case of two shifts Equation (5.29) implies the calculation of the arithmetic mean of the absolute shifts with regard to the nominal results. This is a reasonable choice if the measurement results can be assumed to be linear functions of the size of the systematic shift. In this scenario any deviation between the two shifts is caused by purely statistical effects and the average value of the shifts is a good estimator of the correct uncertainty. However, the charge asymmetry itself is not linear in the variables used to calculate it, and additional nonlinear behavior can be introduced by the regularization of the unfolded results.

Thus for the case of two shifts a slightly more conservative approach has been chosen for some uncertainties of this analysis. For each variable the larger of the

observed shifts is determined separately; using the absolute values of these shifts, $\Delta x_{\max}$ and $\Delta y_{\max}$, the covariance is then defined as

$$\operatorname{cov}(x, y) = \Delta x_{\max} \cdot \Delta y_{\max} \cdot \operatorname{sign}\left((x_1 - x_2) \cdot (y_1 - y_2)\right) . \tag{5.31}$$

In this the sign of the covariance term is determined by whether the variables x and y move in the same direction or in opposite directions when changing from one systematic shift to the other. This procedure corresponds to a symmetrization of the largest observed shifts and thus constitutes a more conservative uncertainty estimate than the direct analog of statistical covariance definitions, described above.

Drawbacks that should be noted, however, are the nominal values not entering into the determination of the sign, and there not being a straightforward way of extending the method to a number of systematic shifts larger than two.

5.6.2 Individual Sources of Uncertainty

Jet Energy Scale (JES)

The energy correction factors that are applied to the reconstructed jets, as described in Section 3.2.6, are the results of measurements themselves [139] and thus are subject to many different uncertainties. For the estimation of the overall effects of these uncertainties separate correction factors have been provided that correspond to one-sigma variations of the underlying uncertainties. Just like the nominal factors their size depends on both η and p_{T} of the given jet, and their effects need to be propagated to the missing transverse momentum. In the determination of this uncertainty the varied correction factors are applied to the simulated samples. The corrections of the data sample remain the nominal ones.

Jet Energy Resolution (JER)

As explained in Section 3.2.6, measurements of the jet momenta have been found to have significantly worse resolution in data than in the simulated samples, motivating the introduction of an artificial smearing of the reconstructed jets in the simulation. The η-dependent uncertainties [140] of the underlying measured resolution ratios between data and simulation, shown in Table 5.3, are assumed to be fully correlated. For this reason the simulated samples are processed with parameter sets wherein all uncertainties have been varied by one standard deviation in the same direction.

Pileup

The measurement of the frequency distribution of pileup events in data that is the foundation for the reweighting of the simulated events, as described in Section 4.2.3, is subject to uncertainties as well. This is modeled as a 6% variation of the cross section that is assumed for the minimum bias events in the calculation of the

Table 5.3: Uncertainties of the jet p_T resolution ratios of data and MC simulation, adapted from [140]. The symbols σ(Data) and σ(Sim.) signify the jet p_T resolutions in data and in the simulation, respectively.

$\lvert\eta\rvert$ range	Uncertainty of σ(Data)/σ(Sim.)
0.0 - 0.5	0.026
0.5 - 1.1	0.028
1.1 - 1.7	0.029
1.7 - 2.3	0.046
2.3 - 2.8	0.062

pileup distribution. Thus the nominal cross section of 69 400 µb is varied to values of 73 564 or 65 236 µb, and the measurement is repeated with simulated samples that are reweighted to achieve the corresponding pileup distributions.

b-Tagging Uncertainty

The CSV b tagger is known to perform differently for simulated events and real data events. As described in Section 4.2.3, this is accounted for by a reweighting of the simulated events according to scale factors derived from dedicated measurements of the tagging performance. The uncertainties of these scale factors are given as functions of η and p_T of an individual jet and need to be propagated to the results of this analysis. This is done by performing eight different variations of the scale factors that contribute to this uncertainty, which can be understood as four groups of two opposing variations each. However, it also encompasses an additional ninth component resulting from the variation of the discriminator distribution used for the hypothesis selection in the reconstruction of the top quark pair system.

The scale factors are given separately for jets that are associated to light quarks or to heavy quarks in the simulation. Varying these two components up and down separately yields the first four components of the overall uncertainty. But as the dependency on η is much larger for this analysis than for most, additional variations of the scale factors are performed wherein the uncertainties are not treated as fully correlated shifts. Instead, a more conservative estimate is obtained by varying the scale factors of jets with $\eta < 0.8$ in the opposite direction from those with $\eta > 0.8$, which introduces more significant changes of the width of the pseudorapidity distributions. Doing this separately for jets associated to light and heavy quarks, the second set of four components of the uncertainty is obtained.

In the ninth scenario, finally, the effect of mismodeling of the discriminator distribution on the reconstruction performance is estimated. This is necessary as the discriminator values of the individual jets are used for the hypothesis selection in the reconstruction, as described in Section 5.1.2. Thus for this scenario the discriminator distribution of the signal simulation is reshaped to be closer to the one in data, and the effect on the measurement is taken to be the uncertainty. By comparing the selection efficiencies of the b-tag selection criterion with and

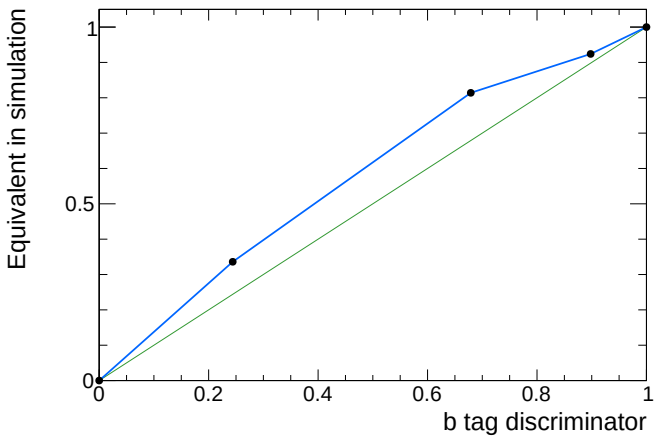

Figure 5.30: Interpolated points of the determined b-tag discriminator values in simulation (y-axis) that correspond to a given value in data (x-axis). For an easier interpretation the bisector line is shown as well.

without the scale factor, equivalent b-tag values can be found that reproduce the correct selection efficiencies without the application of scale factors. Interpolating linearly between the values for the three working points of the tagging algorithm and the values of 0 and 1 (which correspond to 100% and 0% selection efficiency, respectively, and thus necessarily are the same in every mapping), a function is obtained that allows to translate a b-tag value of the simulation into the b-tag value that corresponds to it in data. It is shown in Figure 5.30. For the estimation of the uncertainty the b-tag discriminator values of the jets in the signal simulation are transformed using this function before evaluating the likelihood terms that are used in the hypothesis selection.

Lepton Identification Efficiency

As detailed in Section 4.2.3, scale factors are applied to the simulated events to achieve the same lepton selection efficiencies as those observed in data. An overall variation of the uncertainties of these efficiencies does not have a significant effect on the measured asymmetries. It cannot be excluded, however, that the scale factors show slightly charge-asymmetric behavior within their uncertainties.

Variations of the overall ratio between positively and negatively charged leptons have a comparatively small effect on the charge asymmetry. This small effect has its origin in the differing reconstruction resolution for hadronically and leptonically decaying top quarks, which gets propagated to different resolutions for top quarks and top antiquarks if leptons of a specific charge are selected more frequently.

A larger effect occurs, though, if the widths of the pseudorapidity distributions differ for positively and negatively charged leptons. The overall uncertainty due to lepton identification efficiencies thus is estimated by reweighting the simulated events in such a way that a large width difference for differently charged leptons is

induced.

For one direction of the uncertainty events with positively charged leptons are weighted with

$$w_{\mathrm{pos}} = s_{\mathrm{nom}} - \sigma_- + \frac{|\eta_{\mathrm{lep}}|}{\eta_{\mathrm{max}}} \cdot (\sigma_+ + \sigma_-) \tag{5.32}$$

and negatively charged leptons are weighted with

$$w_{\mathrm{neg}} = s_{\mathrm{nom}} + \sigma_+ - \frac{|\eta_{\mathrm{lep}}|}{\eta_{\mathrm{max}}} \cdot (\sigma_+ + \sigma_-) \ . \tag{5.33}$$

In this, s_{nom} is the nominal lepton scale factor for a given lepton, σ_+ and σ_- are its asymmetric uncertainties, and η_{max} gives the maximum absolute values of the pseudorapidity allowed by the event selection for electrons or muons. It takes values of $\eta_{\mathrm{max,e}} = 2.5$ and $\eta_{\mathrm{max},\mu} = 2.1$, respectively. For the other direction of the uncertainty the formulas of Equations (5.32) and (5.33) are exchanged.

Taking Equation (5.32) as an example, the factors can be understood as a variation from the lower boundary of the allowed uncertainties $s_{\mathrm{nom}} - \sigma_-$ for central leptons to the upper boundary of the uncertainties $s_{\mathrm{nom}} + \sigma_+$ for leptons close to the largest allowed rapidity.

As the scale factor uncertainties of electrons and muons are largely uncorrelated they are varied separately and the covariance matrices are added to obtain the quoted uncertainties.

W+Jets Modeling

The W+jets process represents the most important background contribution. The dominant uncertainties in the modeling of this process lie in the renormalization and factorization scales as well as in the fraction of heavy-flavor quarks among the originating partons of the produced jets. However, no simulated samples of sufficient size have been available for the estimation of the scale dependence of this process, and the size of the uncertainty on the heavy-flavor fraction is not generally agreed upon. For this reason it was chosen to estimate the uncertainty of the W+jets modeling in this analysis by comparing the results obtained using the simulated samples to those obtained using a data-driven template.

This template is constructed similarly to the QCD multijet template in the main analysis. It is taken from a sideband in data where the requirement on the number of b-tagged jets is inverted, i. e. none of the jets passing the identification criteria is allowed to have a CSV discriminator value above the one corresponding to the medium working point of the tagging algorithm. The normalizations of the other processes in this template are estimated using the same procedure as the one described in Section 4.4, and they are subtracted from the template. For the modeling of the QCD multijet process in this sideband it is necessary to build new data-driven templates for this region, using the inverted criterion for the b tags. Apart from this there is no change with regard to the QCD multijet templates

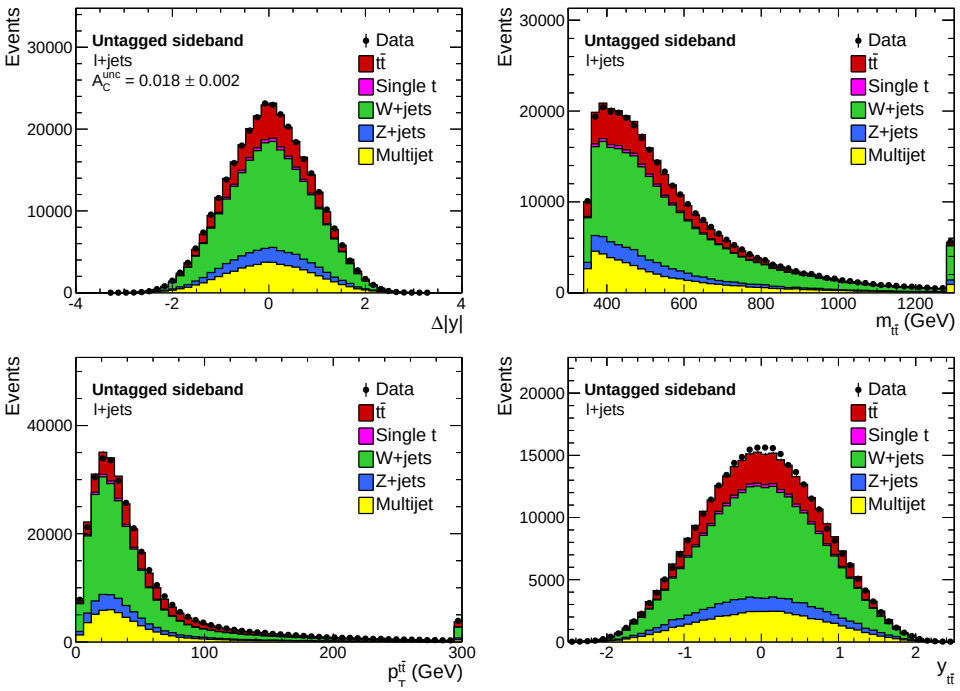

Figure 5.31: Distributions of $\Delta|y|$ and the secondary variables in the untagged sideband. The simulated distributions are normalized to the fit results obtained in the sideband itself.

used in the nominal measurement. The distributions of the sensitive and secondary variables in the sideband can be found in Figure 5.31.

To account for the difference between the signal region and the sideband region, the data-driven template is reweighted using correction factors derived from the simulation. These correction factors are calculated for a given distribution as the ratio between the simulated signal region and sideband region distributions of the process. The effect of these additional correction factors on the unfolded asymmetries has been found to be very small, indicating a low importance of the heavy-flavor fraction for this analysis.

QCD Multijet Modeling

As the QCD multijet templates are handled differently for the electron+jets and muon+jets channels, the systematic uncertainty also needs to be determined in different ways for the two of them.

In the case of the electron+jets channel the final template is constructed as the combination of templates from two different sideband regions. These two sidebands can be expected to be biased in different ways, and thus they are considered to be

sensible outer bounds for an uncertainty on the modeling of this process. Because of this the uncertainty in this channel is determined using the maximization of systematic shifts of Equation (5.31), with each of the original two templates used by themselves representing a systematic shift with regard to the nominal case.

In the muon+jets channels only a single sideband region has been found usable for the determination of a template. Because of this, a different approach has to be chosen for the estimation of the uncertainty. It also has to be considered that the exact composition of the QCD multijet contribution is hard to understand in the specific phase space selected by this analysis. This makes it hard to argue that any specific variation of the template is big enough to account for the full extent of conceivable mismodeling.

An underestimation of the uncertainties is to be avoided if at all possible, so a very conservative approach has been chosen for this contribution. In three scenarios the distributions obtained from the data-driven template are replaced by different ones, and the resulting covariance matrices are added. In the first two of these scenarios the distributions obtained from the $t\bar{t}$ simulation or from the W+jets simulation are used. The simulations of these two specific processes have been chosen because they are the only ones for which a high number of simulated events is available. In the final scenario the data-driven template itself is varied by changing the sign of the sensitive variable for all events, which as a result also inverts the asymmetries of the template. It can be assumed that the variations introduced by these very different distributions will be significantly larger than any systematic bias.

Biases of the Unfolding Method

As seen in the linearity tests of Section 5.5.2, the unfolding procedure can introduce biases of the measurement when the data deviate significantly from the simulation. As explained in that section, this can be either due to regularization biases or due to a shift in the needed acceptance corrections when the measured and unmeasured regions of phase space are not influenced in the exact same way.

However, biases can also be introduced in the correction of migration effects. As an example one can consider a case in which the asymmetry increases significantly as a function of the invariant mass of the top quark pair system. If one were to perform an inclusive charge asymmetry measurement of these data, the dependence on the mass would be invisible to the measurement. The high asymmetry would result in an enlarged number of events in the highest bin of the sensitive variable, but it would be unclear that the origin of this increase lies solely in the high-mass region. There is a problem to this that becomes apparent when considering that the reconstruction performance varies as a function of $m_{t\bar{t}}$. Due to the changed fraction of low-mass and high-mass events in the bin, the average reconstruction

Table 5.4: Comparison of generated and measured A_C values for the three reweighting scenarios used in the unfolding uncertainty for the inclusive measurement in the full phase space.

Scenario	A_C^{gen}	A_C^{meas}
Reweighted in $m_{t\bar{t}}$	0.0031	0.0040
Reweighted in $p_T^{t\bar{t}}$	−0.0001	0.0028
Reweighted in $\|y_{t\bar{t}}\|$	0.0018	−0.0006

performance in the bin is changed as well. Thus the migration matrix determined in simulation will be slightly inaccurate, introducing a bias into the measurement.

To estimate the magnitude of such effects it is tested how well the nominal unfolding procedure can determine the asymmetries of reweighted versions of the simulated sample. For this purpose pseudo datasets are constructed from the simulation similar to the ones in Section 5.5.1, but foregoing the statistical variation of the dataset.

The reweighting that is applied to the signal simulation is chosen in such a way that the asymmetry results of the three-binned differential measurements in data are approximated. As there are three such measurements – for $m_{t\bar{t}}$, $p_T^{t\bar{t}}$ and $|y_{t\bar{t}}|$ – three different reweighting scenarios are obtained. In each scenario the reweighting is performed according to Equation (5.27), like it is done for the linearity tests, but the strength k of the reweighting is varied depending on the generator-level bin of the secondary variable any given simulated event would fall into.

The unfolded asymmetries are compared to the reweighted generator-level ones, and the differences are used to construct one covariance matrix per reweighting scenario. For the final estimation of this uncertainty the three individual covariance matrices are averaged. This is a compromise between the very conservative possibility of adding all matrices – which yields higher uncertainties the more reweighting scenarios are used – and the use of an average of the differences themselves instead of an average of the covariances, which does not work well for the construction of covariance matrices and would also result in a less conservative estimate of the uncertainty.

Table 5.4 shows what kind of variations occur in the reweighted generator-level asymmetries and the corresponding unfolded asymmetries of the inclusive measurement. The tables for all other measurements can be found in Appendix F.

Event Generator

Due to the fact that the signal modeling enters into many parts of the analysis, as explained in the introduction to Section 5.6, a thorough estimation of uncertainties

related to the signal generator is needed. Instead of only performing variations on the parameters and processing of the POWHEG simulation, it thus has been chosen to also exchange the matrix element generator itself. For this uncertainty the nominal signal sample is replaced with a sample simulated by the leading-order generator MADGRAPH. This uncertainty thus also encompasses the difference between event generation according to leading order and next-to-leading order calculations.

In both cases PYTHIA is used for the parton shower and for hadronization. It should be noted, though, that the matching procedures between the matrix element generators and parton shower program vary significantly. Additionally, POWHEG simulates only up to one additional gluon radiation, whereas MADGRAPH simulates up to three. In both cases any further radiation is simulated by PYTHIA.

Parton Shower and Hadronization Modeling

The effects of the parton shower program can be seen most prominently in the spectra of additional gluon radiations, and in the constituents and energy distributions within the jets. While gluon radiation introduces negative contributions to the asymmetry, as explained in Section 1.3, the jet energy distributions affect the reconstruction performance and thus the correctness of the transition matrices.

To estimate the effect of variations in these parameters a different simulated signal sample is used and its results are compared to the nominal ones. In this sample the parton shower and hadronization are performed by HERWIG instead of PYTHIA. To avoid a double-counting of uncertainties the sample retains POWHEG as the matrix element generator.

Top Quark p_{T}-Reweighting

Differential cross-section measurements [167] have shown that the p_{T} spectrum of the top quarks in $\mathrm{t\bar{t}}$ events is significantly softer than the one generated by POWHEG or MADGRAPH. This observation is also supported by theory calculations of the spectrum [124]. As is described in more detail in Section 3.1.3, the simulated signal events are reweighted according to scale factors derived from the measurements cited above.

As there is no consensus on the origin of the discrepancy between data and simulation, it is unclear whether this reweighting can account for the observed effect without introducing different kinds of mismodeling. Consequently, a conservative estimate of the corresponding uncertainty is introduced by performing the measurement with samples lacking the p_{T}-reweighting.

Factorization and Renormalization Scales μ_{F} and μ_{R}

Variations in the factorization and renormalization scale μ_{F} and μ_{R} can have a significant effect on the simulated samples. These effects are studied using dedicated

samples generated using values of μ_F and μ_R that are varied simultaneously by factors of 2 and 0.5 with respect to the nominal scales of the simulation.

Due to the unavailability of dedicated POWHEG samples with a sufficient number of simulated events this uncertainty is estimated using MADGRAPH. This has to be understood as a compromise since MADGRAPH, being a leading-order generator, can be expected to have a significantly larger scale dependence than the next-to-leading order generation of POWHEG. Nevertheless, a controlled overestimation of the uncertainty is considered to be preferable to the sizable statistical fluctuations introduced when using the small POWHEG samples.

The detector simulation of these samples is performed using the less precise FASTSIM package [122]. For this reason and as a further concession to the limited size of the samples the covariance matrix is estimated in a direct comparison of the shifted samples, halving the observed differences in the results. This allows to avoid the additional statistical effects that would be introduced by comparisons to the nominal sample.

The scale dependence of the W+jets background process is not estimated explicitly; it is considered to be covered by the more general systematic uncertainty on the W+jets modeling.

Parton Distribution Functions

The parton distribution functions (PDFs) used in the event generation can affect both the rates and the kinematic distributions of the samples. However, the rates of the more important processes are determined by the background estimation, and small variations in the loose constraints on the single-top and Z+jets processes do not have noticeable effects on the results. Disregarding the W+jets process, which is assigned a dedicated modeling uncertainty based on a template derived from data, the main effect of the PDFs thus is in variations of the kinematic distributions of the $t\bar{t}$ sample.

When varying to a different PDF configuration than the nominal CT10 PDF set [32] the events of the signal simulation are reweighted according to the following factors:

$$w_i = \frac{f_{\mathrm{sys,p_1}}(x_1, Q^2) \cdot f_{\mathrm{sys,p_2}}(x_2, Q^2)}{f_{\mathrm{nom,p_1}}(x_1, Q^2) \cdot f_{\mathrm{nom,p_2}}(x_2, Q^2)} \tag{5.34}$$

Herein $f_{\mathrm{nom,p}_i}$ and $f_{\mathrm{sys,p}_i}$ are the nominal and alternative PDF sets for a given type of initial-state parton p_i, each depending on the Bjorken scale variable x and the resolution scale Q^2.

Since the POWHEG generator does not save the resolution scale used to calculate a given event, an approximation of the scale has to be calculated from the information that is available on analysis level. This approximation takes the form

$$Q^2 = m_{\mathrm{t}}^2 + p_{\mathrm{T,t}}^2 + p_{\mathrm{T},\bar{\mathrm{t}}}^2 \,, \tag{5.35}$$

with $m_{\mathrm{t}} = 172.5\,\mathrm{GeV}$ being the top quark mass parameter of the simulation and $p_{\mathrm{T,t}}$ and $p_{\mathrm{T,\bar{t}}}$ being the generator-level transverse momenta of the top quarks. The approximation in this calculation is that POWHEG uses the Born momenta of the quarks, i. e. the momenta before any gluons are radiated, whereas the only available top momenta when performing the reweighting are already affected by radiation. However, it has been found that for the purposes of this analysis the effects of the PDF variations do not depend strongly on the used scale parameter. Therefore the approximation is considered to be sufficient.

The PDF uncertainty is estimated not only by varying the nominal CT10 PDFs within their uncertainties as given by a set of eigenvectors, but also by comparing them to the MSTW2008 [172] and NNPDF2.1 [173] PDF sets with their respective uncertainties. The most common method of combining all this information is to form the envelope of the result variations induced by all the PDFs and their uncertainties, but the requirement of building a covariance matrix for the uncertainty prohibits such a treatment. Since the uncertainty actually is very small compared to other uncertainties of this analysis, it was chosen to use a conservative approach wherein the covariance matrices of the variations of different eigenvectors are summed.

However, due to the many different shifts needed to estimate this uncertainty even slight fluctuations – such as the effects of a reweighting of the statistical fluctuations that are present in the original sample – can add up to sizable contributions. To avoid this the effects of individual components do not undergo the maximization described by Equation (5.31); instead the associated variations of a given eigenvector are compared directly against one another and the difference is halved.

A further complication to the determination of this uncertainty arises because the NNPDF PDF set needs to be treated differently from the others. The reason is that its uncertainties are not described by a set of eigenvectors but by a set of 100 random variations. Following the recommendations for this PDF set, the elements of the covariance matrix are calculated by determining the arithmetic mean of the covariance matrix elements obtained when comparing each of the 100 shifted results to the result obtained with the nominal NNPDF PDF set.

Finally, two additional covariance matrices are calculated for the differences between the nominal values of CT10 and the other two PDF sets.

5.6.3 Calculated Uncertainties and Correlations

The covariance matrices of the individual systematic uncertainties are added to obtain the overall covariance matrices for the systematic uncertainties of the results. The square roots of their diagonal elements represent the uncertainties of the individual asymmetries; Tables 5.5 to 5.8 show these values for the inclusive measurements as well as the three-binned differential measurements in $m_{\mathrm{t\bar{t}}}$ for both measured phase spaces. All tables for these and the other measurements can

Table 5.5: Systematic uncertainties in the inclusive measurement of A_C in the *full phase space*.

Systematic uncertainty	Uncertainty in A_C
JES	0.0018
JER	0.0003
Pileup	0.0006
b tagging	0.0008
Lepton efficiency	0.0009
W+jets	0.0007
QCD multijet	0.0009
Unfolding	0.0022
Generator	0.0005
Hadronization	0.0011
p_T reweighting	0.0002
μ_F and μ_R	0.0007
PDF	0.0003
Total	0.0037

be found in Appendix G.

It can be seen that the measurements in the two phase spaces have comparable uncertainties, yet some significant differences do occur. To understand these differences two effects need to be kept in mind.

The first effect is that the fiducial measurements involve a significantly smaller part of the phase space of $t\bar{t}$ production; systematic uncertainties that affect the measured and unmeasured parts in different ways thus have a reduced influence on the fiducial measurements. One noteworthy example of this is the uncertainty due to the unfolding procedure in the inclusive measurements. It is dominant in the full phase space measurement, but of much smaller importance for the corresponding measurement in the fiducial phase space.

The other effect has its origin in the fact that the acceptance corrections of the fiducial measurements cause a less pronounced enhancement of the outer bins of the sensitive variable, reducing their relative importance for the measured asymmetries; c. f. Figures 5.14 and 5.15 on pages 99 and 100. Thus all systematic uncertainties that do not behave in the same way for low and high values of $|\Delta|y||$ will not show the same behavior for the two phase spaces.

Figure 5.32 shows the correlation matrices of the unfolded bins of the sensitive variable in the inclusive measurements. The negative correlations between the outermost bins and all other bins can be understood as significant width differences of the distributions obtained with the systematic variations. Similarly there are

Table 5.6: Systematic uncertainties in the inclusive measurement of A_C in the *fiducial phase space*.

Systematic uncertainty	Uncertainty in A_C
JES	0.0020
JER	0.0003
Pileup	0.0006
b tagging	0.0009
Lepton efficiency	0.0009
W+jets	0.0005
QCD multijet	0.0010
Unfolding	0.0012
Generator	0.0002
Hadronization	0.0010
p_T reweighting	0.0000
μ_F and μ_R	0.0002
PDF	0.0002
Total	0.0031

Table 5.7: Systematic uncertainties in the differential measurement of A_C in three bins of $m_{\mathrm{t\bar{t}}}$ in the *full phase space*.

	Uncertainty in A_C ($m_{\mathrm{t\bar{t}}}$)		
Systematic uncertainty	Bin 1	Bin 2	Bin 3
JES	0.0063	0.0008	0.0023
JER	0.0010	0.0005	0.0018
Pileup	0.0027	0.0003	0.0004
b tagging	0.0004	0.0009	0.0007
Lepton efficiency	0.0007	0.0008	0.0014
W+jets	0.0010	0.0025	0.0015
QCD multijet	0.0013	0.0024	0.0020
Unfolding	0.0017	0.0011	0.0033
Generator	0.0043	0.0021	0.0024
Hadronization	0.0040	0.0035	0.0022
p_T reweighting	0.0003	0.0007	0.0013
μ_F and μ_R	0.0064	0.0041	0.0043
PDF	0.0009	0.0006	0.0006
Total	0.0115	0.0071	0.0077

Table 5.8: Systematic uncertainties in the differential measurement of A_C in three bins of $m_{t\bar{t}}$ in the *fiducial phase space*.

	Uncertainty in $A_C(m_{t\bar{t}})$		
Systematic uncertainty	Bin 1	Bin 2	Bin 3
JES	0.0066	0.0009	0.0019
JER	0.0012	0.0006	0.0016
Pileup	0.0027	0.0003	0.0004
b tagging	0.0004	0.0009	0.0006
Lepton efficiency	0.0007	0.0007	0.0011
W+jets	0.0010	0.0030	0.0006
QCD multijet	0.0017	0.0030	0.0017
Unfolding	0.0018	0.0014	0.0004
Generator	0.0058	0.0028	0.0013
Hadronization	0.0042	0.0041	0.0014
p_T reweighting	0.0002	0.0008	0.0014
μ_F and μ_R	0.0057	0.0034	0.0045
PDF	0.0009	0.0004	0.0004
Total	0.0120	0.0077	0.0061

strong correlations between bins with the same absolute values but opposite signs of the sensitive variable, resulting in a second diagonal line in addition to the one describing the self-correlations. This as well can be understood to be the result of overall width differences, with bins on both sides of zero varying in comparable ways when the distribution widens or narrows.

Figures 5.33 and 5.34 show the correlation matrices of the unfolded asymmetries in the differential measurements, calculated from the summed systematic covariance matrices. While it can be seen that there are some non-negligible correlations, it has to be kept in mind that many of the systematic variations are subject to statistical fluctuations, introducing fluctuations into the correlation matrices themselves. This is especially apparent in the matrices for the six-binned measurement in $m_{t\bar{t}}$. Nevertheless these matrices represent the best available knowledge on the systematic correlations of the measurements.

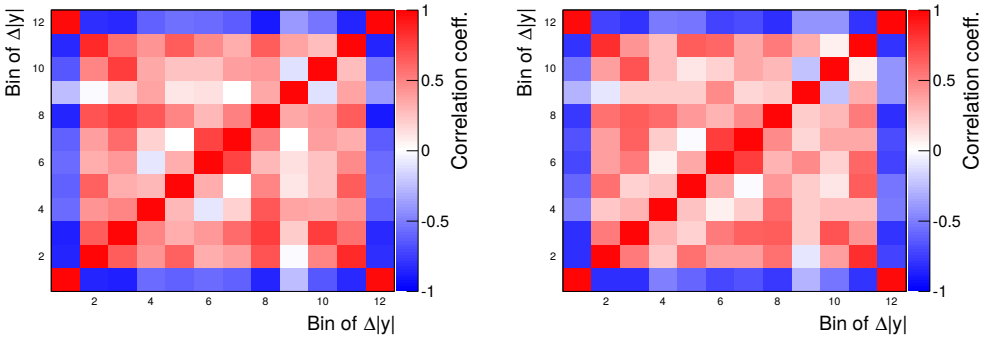

Figure 5.32: Covariance matrices of the unfolded bins of the sensitive variable in the inclusive measurement (a) in the full phase space and (b) in the fiducial phase space.

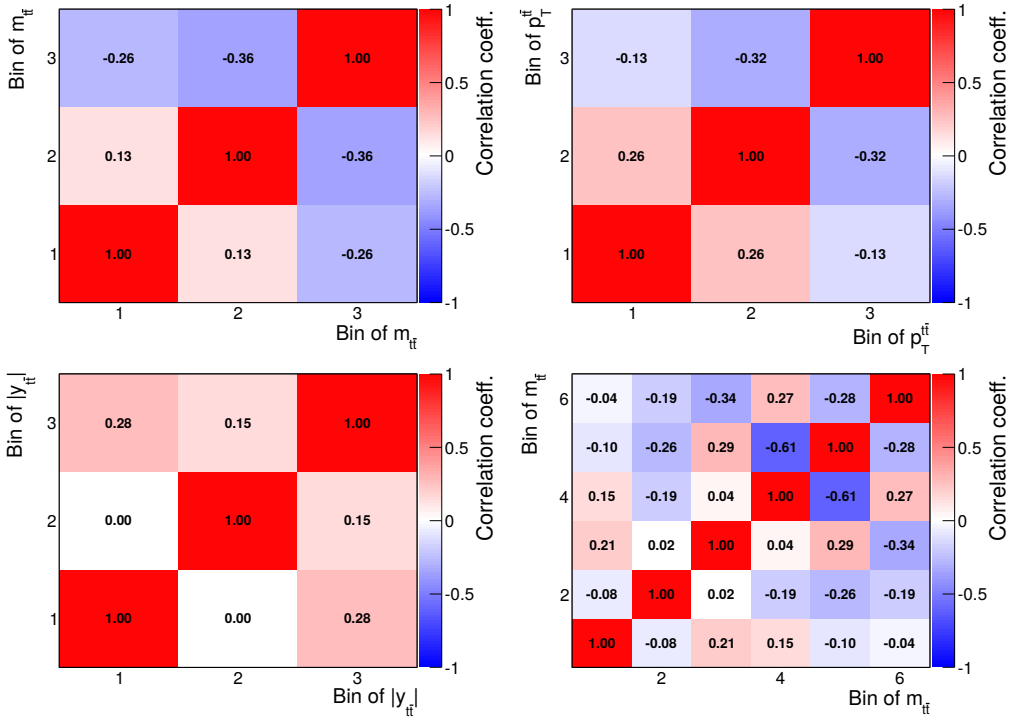

Figure 5.33: Covariance matrices of the unfolded asymmetries in the differential measurements in the *full phase space*.

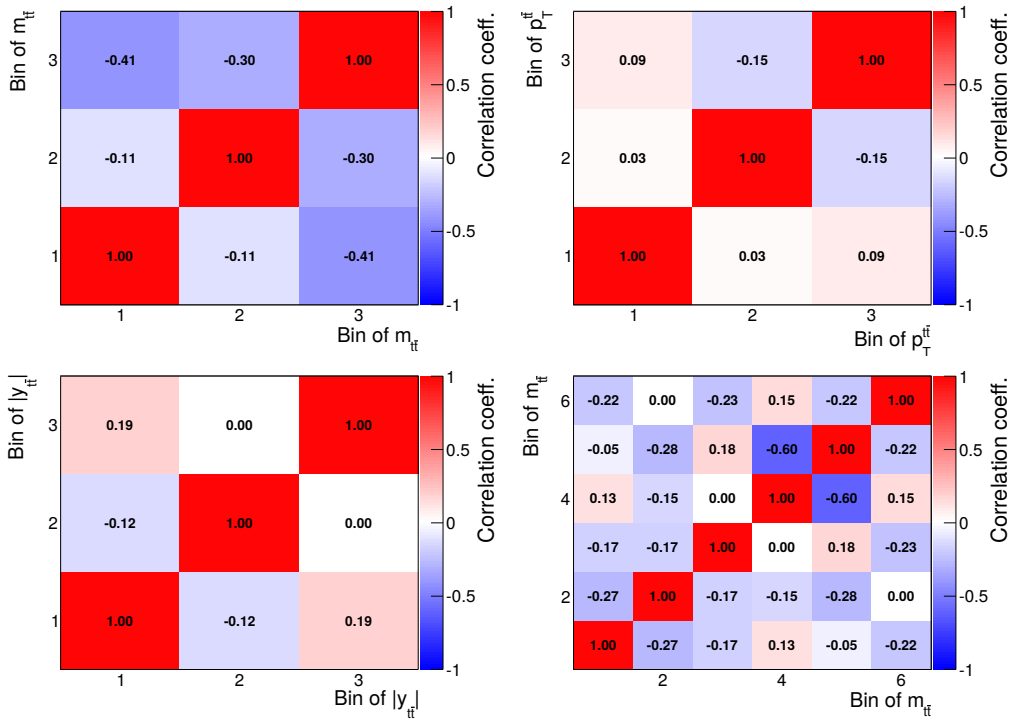

Figure 5.34: Covariance matrices of the unfolded asymmetries in the differential measurements in the *fiducial phase space*.

5.7 Results

The fully corrected charge asymmetry in the fiducial phase space is measured as

$$A_{\mathrm{C}}^{\mathrm{fid}} = -0.0035 \pm 0.0072 \text{ (stat.)} \pm 0.0031 \text{ (syst.)}\,, \tag{5.36}$$

whereas the corresponding measurement in the full phase space yields

$$A_{\mathrm{C}}^{\mathrm{full}} = 0.0010 \pm 0.0068 \text{ (stat.)} \pm 0.0037 \text{ (syst.)}\,. \tag{5.37}$$

Table 5.9 summarizes the values of the measured inclusive asymmetries in various stages of the analysis. It also compares the final measured asymmetries in the full and fiducial phase spaces to two different NLO calculations [43, 53] of the standard model asymmetry. Both these calculations encompass electroweak corrections, and in contrast to the POWHEG simulation they use the expanded scheme for the denominator of the charge asymmetry calculation (see Section 1.3.2). For both calculations the uncertainties are dominated by variations of the renormalization scales, which are varied from $m_{\mathrm{t}}/2$ to $2m_{\mathrm{t}}$.

Table 5.9: The measured inclusive asymmetry at the different stages of the analysis and the corresponding theoretical predictions for the SM.

	Asymmetry(A_{C})
Reconstructed	0.0036 ± 0.0017 (stat.)
Background-subtracted	0.0008 ± 0.0023 (stat.)
Corrected for migration effects	-0.0042 ± 0.0072 (stat.)
Fiducial phase space	-0.0035 ± 0.0072 (stat.) ± 0.0031 (syst.)
Prediction (Bernreuther, Si) [43]	0.0101 ± 0.0010
Full phase space	0.0010 ± 0.0068 (stat.) ± 0.0037 (syst.)
Prediction (Kühn, Rodrigo) [53]	0.0102 ± 0.0005
Prediction (Bernreuther, Si) [43]	0.0111 ± 0.0004

It can be seen that in contrast to the CDF measurements of the charge asymmetry at the Tevatron there is no hint of an enhanced charge asymmetry as compared to the standard model predictions. When also considering the combined charge asymmetry measurement in the full phase space [52] of the ATLAS and CMS collaborations at 7 TeV, which has a result of $0.005 \pm 0.007 \pm 0.006$, the measurements may in fact be seen as a hint towards slightly lower asymmetries than predicted by the current standard model calculations.

Figure 5.35 illustrates the unfolded distributions of the sensitive variable for the inclusive measurements of the charge asymmetry. Aside from the slight shift of the distribution corresponding to the differing asymmetries a good agreement

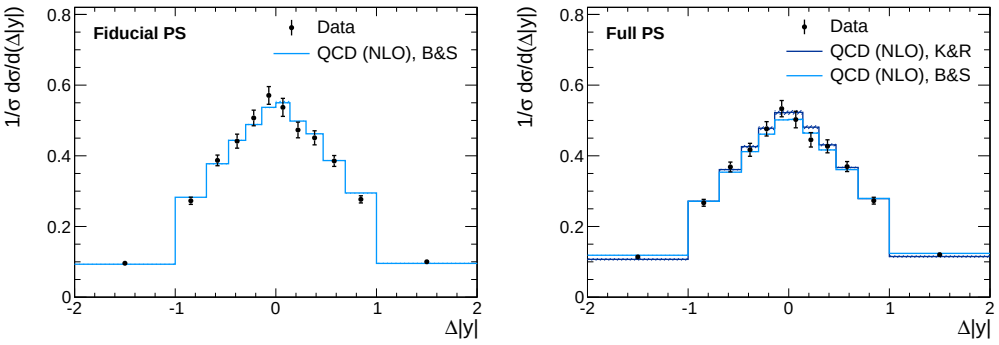

Figure 5.35: Unfolded inclusive $\Delta|y|$ distribution in the fiducial phase space (left) and in the full phase space (right). The measured values are compared to NLO calculations for the SM by Kühn and Rodrigo (K&R) [53] and Bernreuther and Si (B&S) [43].

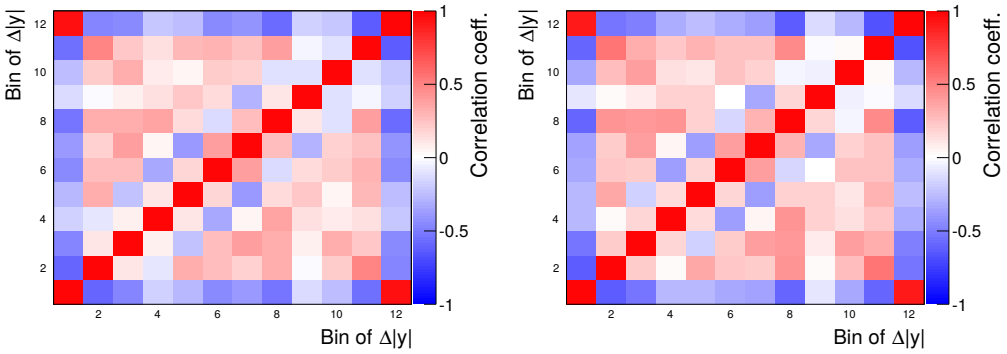

Figure 5.36: Correlation matrices for the unfolded inclusive $\Delta|y|$ distributions in the fiducial phase space (left) and in the full phase space (right).

between the measurement and the predictions is found. Figure 5.36 shows the correlation matrices for these distributions. Their features can be understood as a combination of the features of the statistical and systematic covariance matrices, which are discussed in Sections 5.4.4 and 5.6.3, respectively.

Figure 5.37 shows the results of the differential measurements in the fiducial phase space, and Figure 5.38 shows those for the full phase space; the corresponding correlation matrices are given in Figures 5.39 and 5.40. The numerical values of these results and the SM predictions can be found in Appendix H. The differential measurements give no indications of physics beyond the standard model.

In the full phase space the results are compared not only to standard model calculations but also to the predictions of an effective field theory [174, 175] introducing an effective axial-vector coupling of the gluon (EAG). This theory has been calculated for different scales of the new physics contributions; using scales on the order of 1.5 TeV the theory would be capable of explaining the high charge

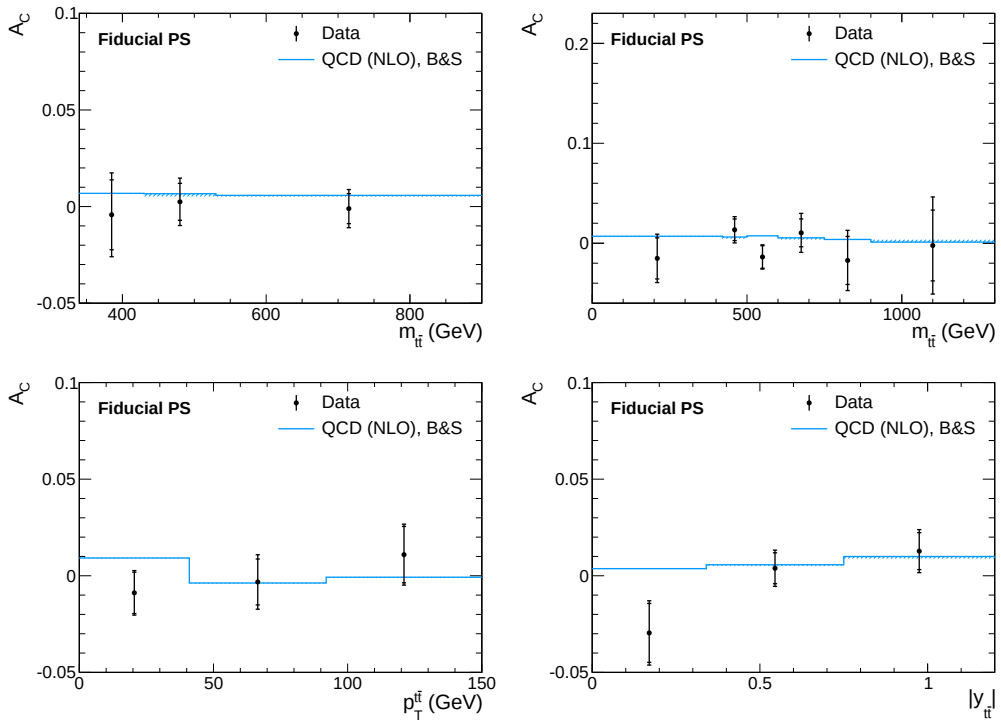

Figure 5.37: Corrected asymmetry in the *fiducial phase space* as a function of $m_{t\bar{t}}$ (upper left and upper right), $p_T^{t\bar{t}}$ (lower left), and $|y_{t\bar{t}}|$ (lower right). The former is shown in two different binnings. The measured values are compared to an NLO calculation for the SM by Bernreuther and Si (B&S) [43]. The inner bars indicate the statistical uncertainties while the outer bars represent the statistical and systematic uncertainties added in quadrature.

asymmetries measured by the CDF collaboration. Considering only those bins of the measurement that are most sensitive to the contributions of new physics, i. e. the highest bins of the measurements as functions of $m_{t\bar{t}}$, it can be determined that the results exclude new physics scales of up to 1.5 TeV for this model at two standard deviations.

At the time of writing, two other charge asymmetry analyses using 8 TeV data have been made public.

One of them is the competing analysis by an ATLAS group [176], which relies on a Bayesian unfolding technique and marginalizes many of its uncertainties. In comparison to the analysis presented in this thesis, less focus has been put on the independence from model assumptions, and a less conservative estimation of the systematic uncertainties has been performed. For these two reasons and because of the availability of larger simulated samples, the ATLAS analysis can quote slightly lower uncertainties in the inclusive measurement. The regularization technique developed for this analysis, however, allows for lower uncertainties in

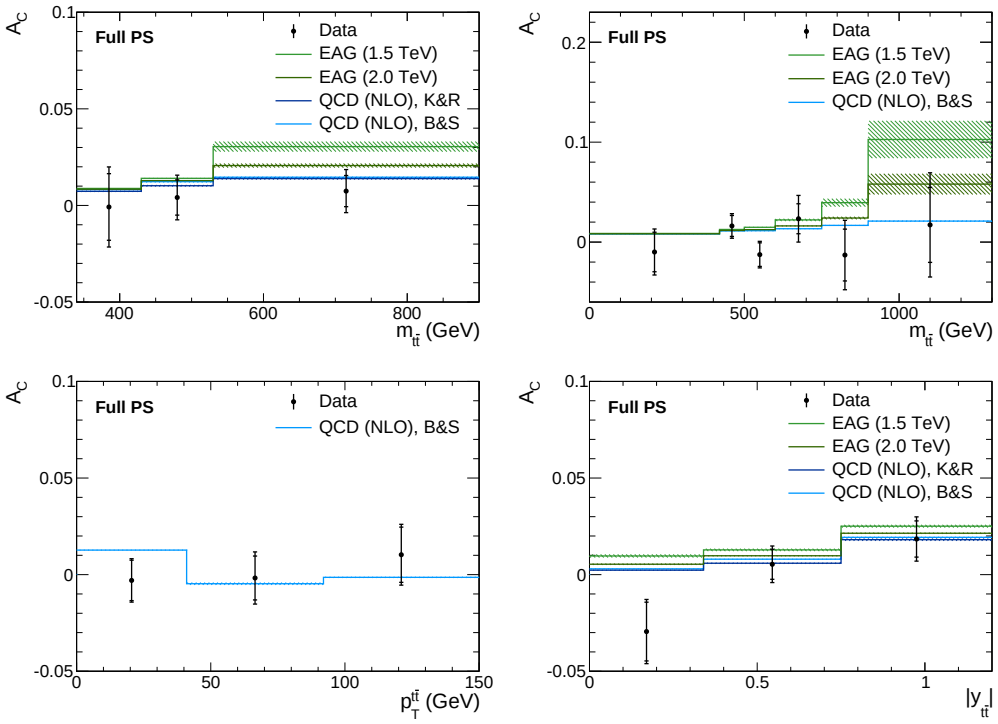

Figure 5.38: Corrected asymmetry in the *full phase space* as a function of $m_{\mathrm{t\bar{t}}}$ (upper left and upper right), $p_{\mathrm{T}}^{\mathrm{t\bar{t}}}$ (lower left), and $|y_{\mathrm{t\bar{t}}}|$ (lower right). The former is shown in two different binnings. The measured values are compared to NLO calculations for the SM by Kühn and Rodrigo (K&R) [53] and Bernreuther and Si (B&S) [43], as well as to the predictions of a model featuring an effective axial-vector coupling of the gluon (EAG) [174, 175]. The inner bars indicate the statistical uncertainties while the outer bars represent the statistical and systematic uncertainties added in quadrature.

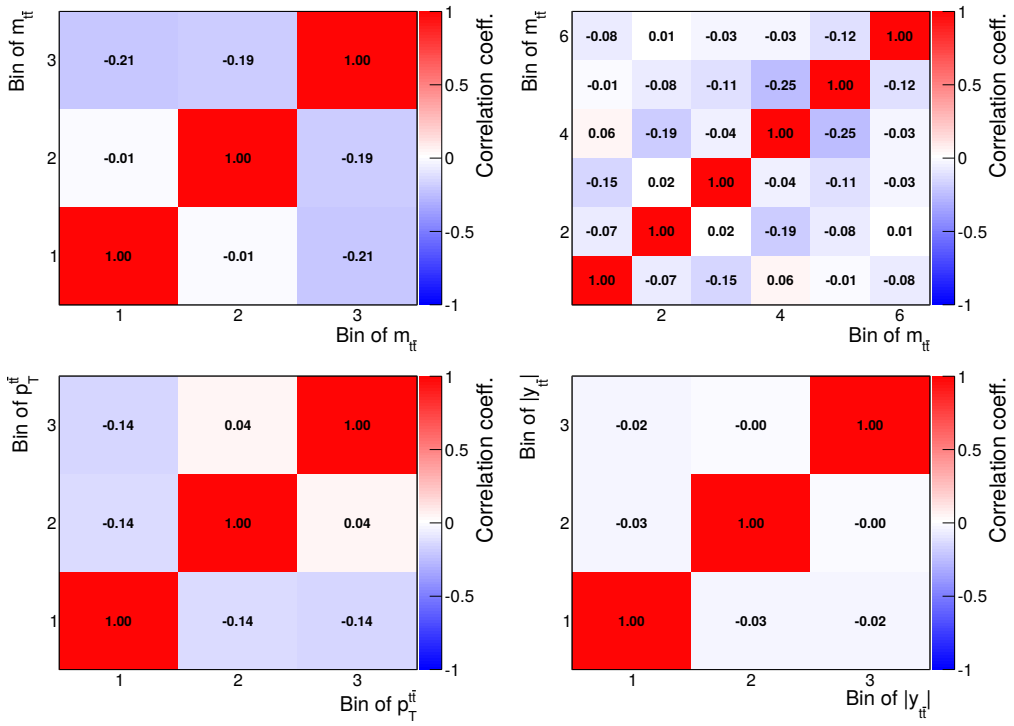

Figure 5.39: Correlation matrices for the differential measurements of the asymmetry as functions of $m_{t\bar{t}}$ (upper left and upper right), $p_T^{t\bar{t}}$ (lower left), and $|y_{t\bar{t}}|$ (lower right) in the *fiducial phase space*.

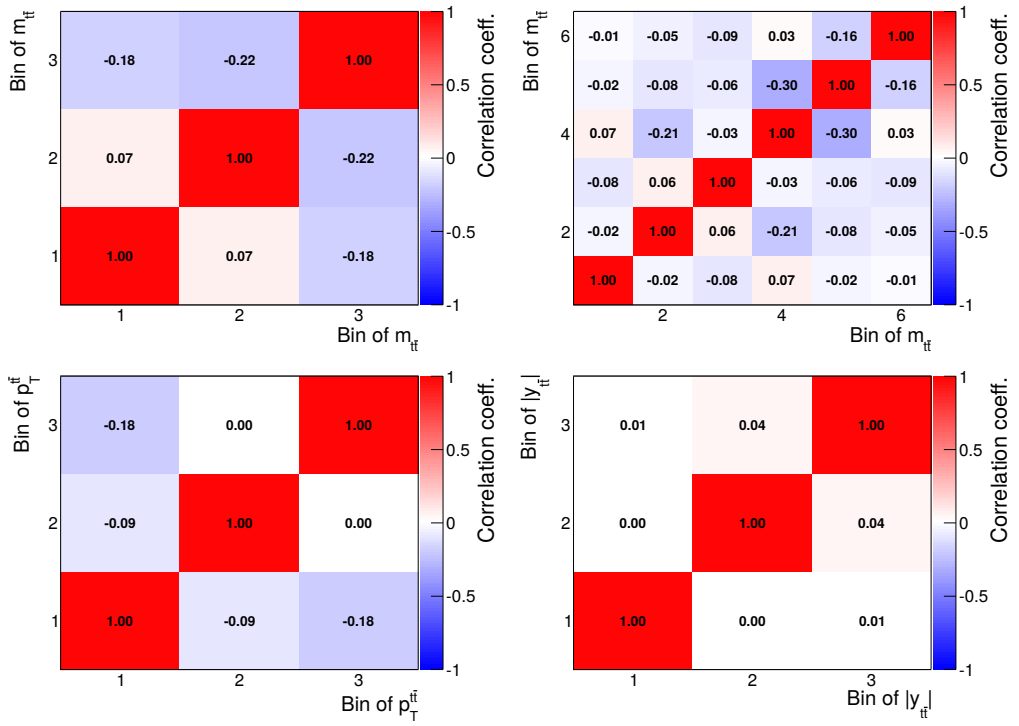

Figure 5.40: Correlation matrices for the differential measurements of the asymmetry as functions of $m_{t\bar{t}}$ (upper left and upper right), $p_T^{t\bar{t}}$ (lower left), and $|y_{t\bar{t}}|$ (lower right) in the *full phase space*.

the differential measurements while also having significantly smaller correlations between the individual values.

The other competing charge asymmetry analysis has been performed by a separate group within CMS [177] and can be considered to be the first application of a new measurement method for the charge asymmetry. This analysis relies on a purely mathematical separation of the simulated sensitive variable distribution into a symmetric and an anti-symmetric component, and it performs reconstruction-level fits relying on the two resulting templates. Due to the reliance on the correct modeling of the sensitive variable distribution in the simulation, this analysis can achieve a significant reduction of the statistical uncertainties. However, in addition to the intrinsically higher model dependence of this approach, a further drawback is that it has not yet been possible to extend the method to differential measurements.

Summing up, the analysis presented in this thesis compares favorably with competing analyses with regard to its attention to model independence and its precise differential measurements. Additionally, it is the only analysis providing a detailed measurement of the distribution of the sensitive variable itself, and it offers the first and only fiducial measurements of the charge asymmetry at the LHC.

Conclusion and Outlook

In this thesis several measurements of the $t\bar{t}$ charge asymmetry have been performed to obtain a better understanding of whether this observable is affected by new physics processes.

Corrections have been applied to obtain measured values both for the full phase space of top quark pair production, producing more generally comparable results, and for a reduced fiducial phase space, minimizing the dependence on standard model assumptions and the signal simulation.

In order to probe different components of the standard model charge asymmetry, as well as to enhance potential contributions due to physics beyond the standard model, the charge asymmetry has been measured differentially. These differential measurements have been performed as functions of the invariant mass, the transverse momentum, and the rapidity of the top quark pair system.

All results are found to be compatible with the standard model predictions, showing no indication for new physics contributions. Even the most significant deviations are of local significances that are smaller than two standard deviations, and they run counter to the predictions of the most promising models for new physics becoming visible in the charge asymmetry.

At the time of writing it has been roughly four years since the charge asymmetry in top quark pair production first received attention in the larger high-energy physics community due to the results obtained by the CDF and DØ collaborations. Due to improvements both in theory predictions and in the measurements at the Tevatron and at the LHC, among them notably the one documented in this thesis, the room for potential new physics contributions to this effect has shrunk significantly. To give an indication of the current status, a summary of the most relevant analyses of the inclusive charge asymmetries at the Tevatron and the LHC is shown in Figure 5.41.

Even though the original hints of BSM contributions could not be confirmed, the sensitivity of this observable to some otherwise elusive models warrants future measurements. One opportunity for this is presented by the 13 TeV operation of the LHC, which is just beginning at the time of writing and will greatly increase the general sensitivity to the effects of new heavy particles. For measurements of the charge asymmetry, however, the benefits provided by the larger numbers of $t\bar{t}$ events in those future runs are partially offset by a reduced fraction of charge-asymmetric production processes.

Due to these new conditions, different but related observables may become more interesting than the regular charge asymmetry. Prominent among them are the

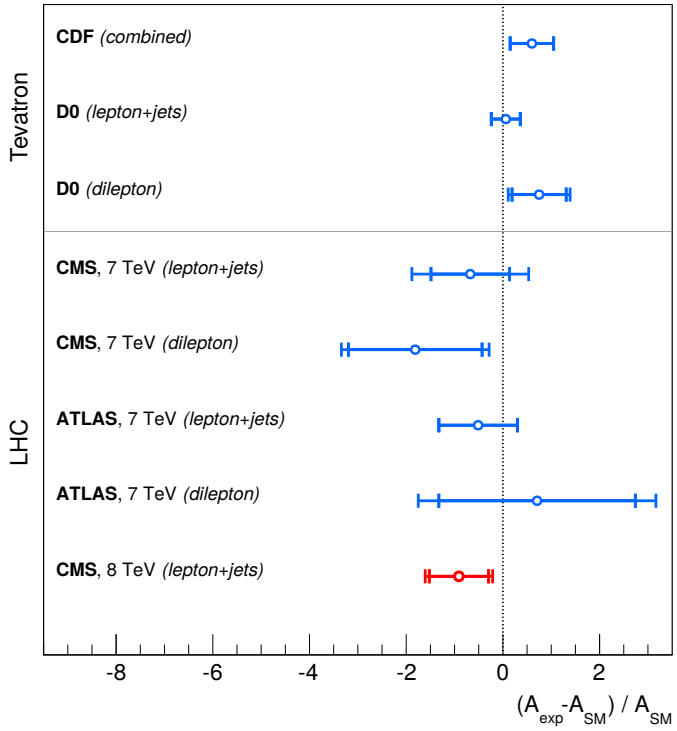

Figure 5.41: Summary of the most relevant measurements of the inclusive charge asymmetry at various experiments [48–51, 182–184] in relation to the respective theory predictions for the effect [43, 44]. The result of this thesis is shown in red.

incline and energy asymmetries [178], which explicitly consider the asymmetry in the presence of additional hard gluon radiation, as well as the so-called collider-independent asymmetries in the $u\bar{u}$ and $d\bar{d}$ initial states [59]. Similarly, with high integrated luminosities it may become viable to measure the charge asymmetry in $t\bar{t}\gamma$ events, which can give additional information on a possible cancellation between the asymmetries of the $u\bar{u}$ and $d\bar{d}$ initial states at the LHC [179].

Furthermore, partially complementary information can be provided by measurements of the azimuthal decorrelation of the top quarks [180] as well as by measurements of the lepton asymmetry in top quark pair production [181–183], with the latter also benefiting from better measurement resolutions than those achievable in analyses involving the reconstruction of the top quark four momenta.

Finally, if a lepton collider of sufficient energy should be built in the future, precision measurements of the charge asymmetry may yet again become one of the most promising tools to find hints of deviations from the standard model.

In light of these possibilities, it is assured that the charge asymmetry and related quantities will continue to hold the interest of the high-energy physics community for a long time.

Appendices

A Additional Reconstruction-Level Distributions

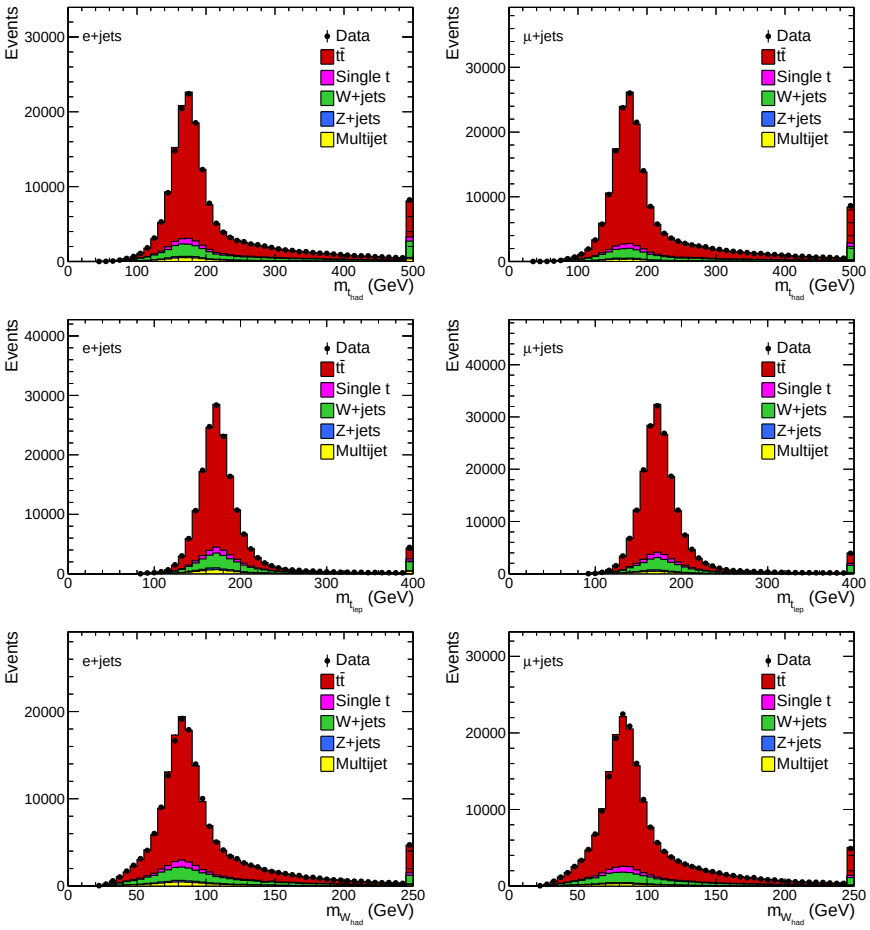

Figure A.1: Comparisons of data and simulation after reconstruction for the electron+jets (left column) and muon+jets (right column) channels. The distributions correspond to the masses of the hadronically decaying top quark, the leptonically decaying top quark and the hadronically decaying W boson. All templates are normalized to the results of the background estimation.

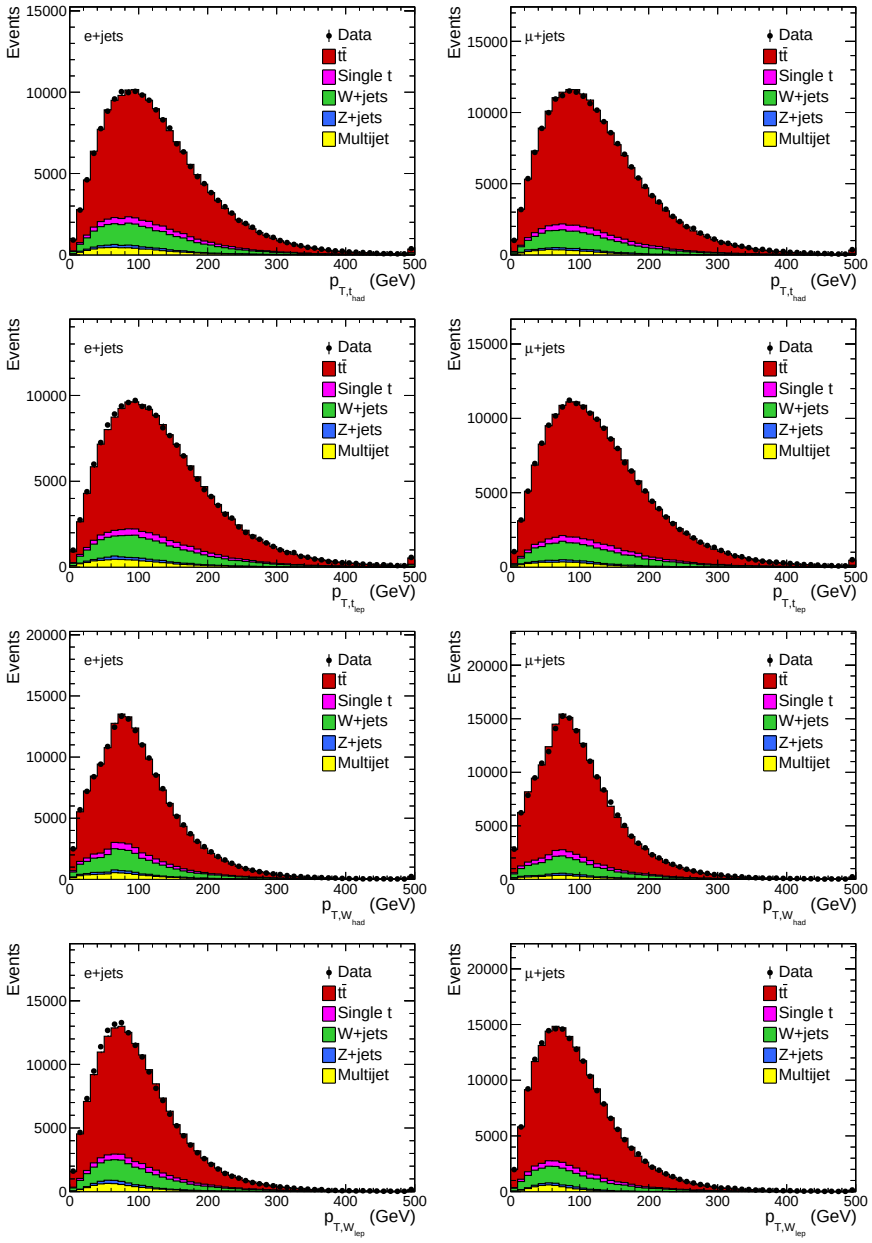

Figure A.2: Comparisons of data and simulation after reconstruction for the electron+jets (left column) and muon+jets (right column) channels. The distributions correspond to the transverse momenta of the hadronically and leptonically decaying top quarks, as well as of the hadronically and leptonically decaying W bosons. All templates are normalized to the results of the background estimation.

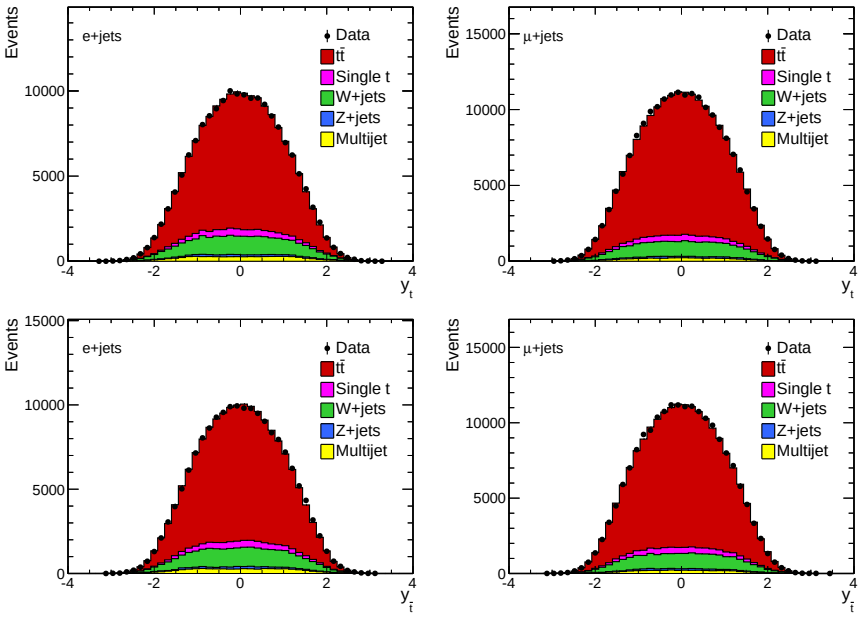

Figure A.3: Comparisons of data and simulation for the rapidity distributions of the reconstructed top quarks in the electron+jets (left column) and muon+jets (right column) channels. All templates are normalized to the results of the background estimation.

B Statistical Correlation Matrices

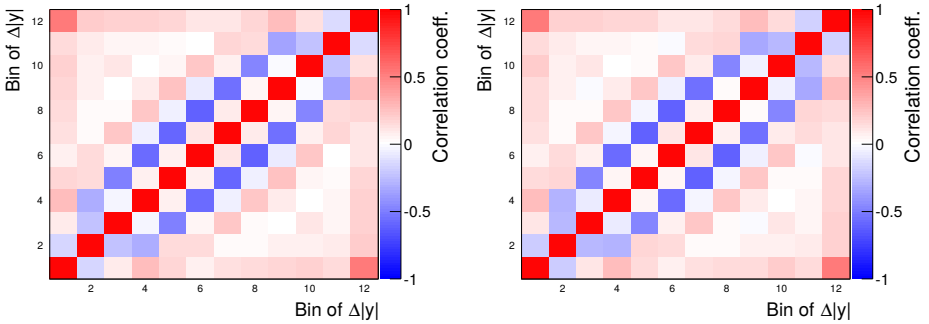

Figure B.1: Statistical correlation matrices of the inclusive measurements in the full phase space (left) and the fiducial phase space (right).

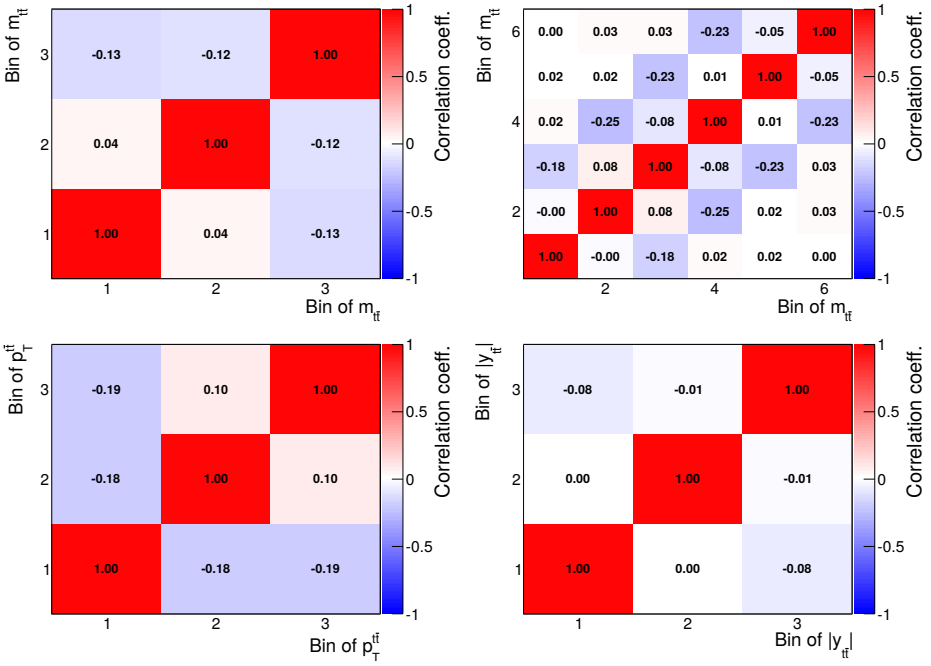

Figure B.2: Statistical correlation matrices of the differential measurements in the *full phase space*.

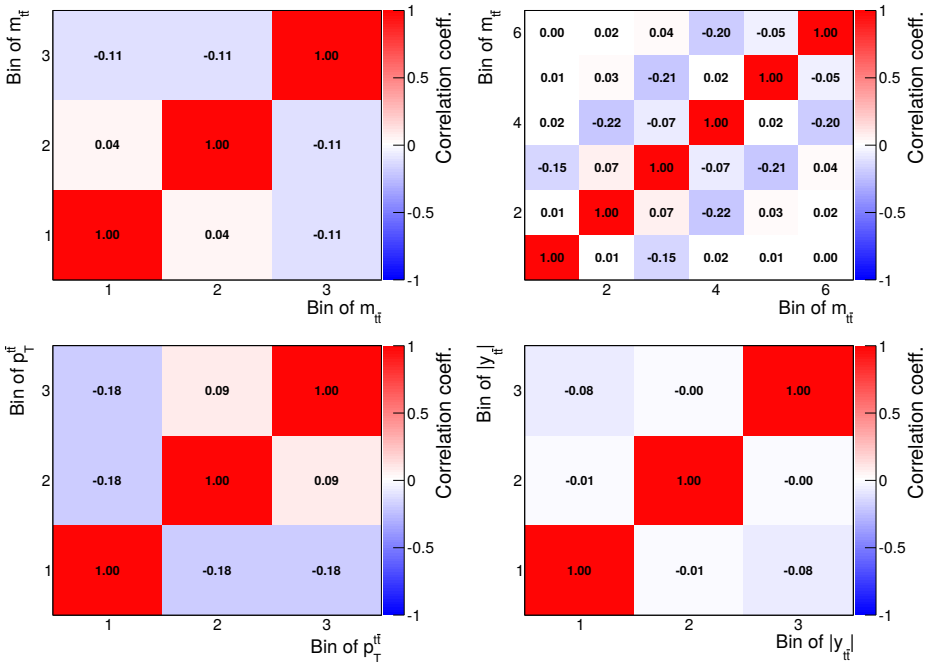

Figure B.3: Statistical correlation matrices of the differential measurements in the *fiducial phase space*.

C Bin Edges of the Measured Spectra

Table C.1: The bin ranges of the reconstructed $\Delta|y|$ distribution for the inclusive measurement.

Bin 1	$-\infty$, -1.27
Bin 2	-1.27, -1.01
Bin 3	-1.01, -0.83
Bin 4	-0.83, -0.70
Bin 5	-0.70, -0.58
Bin 6	-0.58, -0.48
Bin 7	-0.48, -0.38
Bin 8	-0.38, -0.30
Bin 9	-0.30, -0.22
Bin 10	-0.22, -0.14
Bin 11	-0.14, -0.07
Bin 12	-0.07, 0.00
Bin 13	0.00, 0.07
Bin 14	0.07, 0.14
Bin 15	0.14, 0.22
Bin 16	0.22, 0.30
Bin 17	0.30, 0.38
Bin 18	0.38, 0.48
Bin 19	0.48, 0.58
Bin 20	0.58, 0.70
Bin 21	0.70, 0.83
Bin 22	0.83, 1.01
Bin 23	1.01, 1.27
Bin 24	1.27, ∞

Table C.2: The bin ranges of the parton-level $\Delta|y|$ distribution for the inclusive measurement.

Bin 1	$-\infty$, -1.00
Bin 2	-1.00, -0.69
Bin 3	-0.69, -0.47
Bin 4	-0.47, -0.30
Bin 5	-0.30, -0.14
Bin 6	-0.14, 0.00
Bin 7	0.00, 0.14
Bin 8	0.14, 0.30
Bin 9	0.30, 0.47
Bin 10	0.47, 0.69
Bin 11	0.69, 1.00
Bin 12	1.00, ∞

Table C.3: The bin ranges of the reconstructed $\Delta|y|$ distributions for the three-binned differential measurements as functions of the three secondary variables $m_{t\bar{t}}$, $p_T^{t\bar{t}}$ and $|y_{t\bar{t}}|$.

		$m_{t\bar{t}}$ (GeV)					
		Bin 1 0 - 395	Bin 2 395 - 435	Bin 3 435 - 481	Bin 4 481 - 542	Bin 5 542 - 647	Bin 6 647 - ∞
$\Delta|y|$	Bin 1	$-\infty$, -0.65	$-\infty$, -0.95	$-\infty$, -1.14	$-\infty$, -1.28	$-\infty$, -1.40	$-\infty$, -1.49
	Bin 2	-0.65, -0.50	-0.95, -0.76	-1.14, -0.90	-1.28, -1.01	-1.40, -1.10	-1.49, -1.17
	Bin 3	-0.50, -0.39	-0.76, -0.60	-0.90, -0.71	-1.01, -0.79	-1.10, -0.86	-1.17, -0.92
	Bin 4	-0.39, -0.29	-0.60, -0.46	-0.71, -0.54	-0.79, -0.61	-0.86, -0.66	-0.92, -0.70
	Bin 5	-0.29, -0.21	-0.46, -0.33	-0.54, -0.39	-0.61, -0.44	-0.66, -0.48	-0.70, -0.51
	Bin 6	-0.21, -0.14	-0.33, -0.21	-0.39, -0.25	-0.44, -0.28	-0.48, -0.31	-0.51, -0.33
	Bin 7	-0.14, -0.07	-0.21, -0.10	-0.25, -0.12	-0.28, -0.14	-0.31, -0.15	-0.33, -0.16
	Bin 8	-0.07, 0.00	-0.10, 0.00	-0.12, 0.00	-0.14, 0.00	-0.15, 0.00	-0.16, 0.00
	Bin 9	0.00, 0.07	0.00, 0.10	0.00, 0.12	0.00, 0.14	0.00, 0.15	0.00, 0.16
	Bin 10	0.07, 0.14	0.10, 0.21	0.12, 0.25	0.14, 0.28	0.15, 0.31	0.16, 0.33
	Bin 11	0.14, 0.21	0.21, 0.33	0.25, 0.39	0.28, 0.44	0.31, 0.48	0.33, 0.51
	Bin 12	0.21, 0.29	0.33, 0.46	0.39, 0.54	0.44, 0.61	0.48, 0.66	0.51, 0.70
	Bin 13	0.29, 0.39	0.46, 0.60	0.54, 0.71	0.61, 0.79	0.66, 0.86	0.70, 0.92
	Bin 14	0.39, 0.50	0.60, 0.76	0.71, 0.90	0.79, 1.01	0.86, 1.10	0.92, 1.17
	Bin 15	0.50, 0.65	0.76, 0.95	0.90, 1.14	1.01, 1.28	1.10, 1.40	1.17, 1.49
	Bin 16	0.65, ∞	0.95, ∞	1.14, ∞	1.28, ∞	1.40, ∞	1.49, ∞
		$p_T^{t\bar{t}}$ (GeV)					
		Bin 1 0 - 20.5	Bin 2 20.5 - 32.7	Bin 3 32.7 - 46.8	Bin 4 46.8 - 68.8	Bin 5 68.8 - 117.2	Bin 6 117.2 - ∞
$\Delta|y|$	Bin 1	$-\infty$, -1.18	$-\infty$, -1.18	$-\infty$, -1.20	$-\infty$, -1.20	$-\infty$, -1.19	$-\infty$, -1.16
	Bin 2	-1.18, -0.89	-1.18, -0.89	-1.20, -0.90	-1.20, -0.90	-1.19, -0.90	-1.16, -0.88
	Bin 3	-0.89, -0.68	-0.89, -0.68	-0.90, -0.69	-0.90, -0.69	-0.90, -0.69	-0.88, -0.67
	Bin 4	-0.68, -0.51	-0.68, -0.51	-0.69, -0.52	-0.69, -0.52	-0.69, -0.52	-0.67, -0.50
	Bin 5	-0.51, -0.36	-0.51, -0.37	-0.52, -0.37	-0.52, -0.37	-0.52, -0.37	-0.50, -0.36
	Bin 6	-0.36, -0.23	-0.37, -0.23	-0.37, -0.24	-0.37, -0.24	-0.37, -0.24	-0.36, -0.23
	Bin 7	-0.23, -0.11	-0.23, -0.11	-0.24, -0.12	-0.24, -0.11	-0.24, -0.11	-0.23, -0.11
	Bin 8	-0.11, 0.00	-0.11, 0.00	-0.12, 0.00	-0.11, 0.00	-0.11, 0.00	-0.11, 0.00
	Bin 9	0.00, 0.11	0.00, 0.11	0.00, 0.12	0.00, 0.11	0.00, 0.11	0.00, 0.11
	Bin 10	0.11, 0.23	0.11, 0.23	0.12, 0.24	0.11, 0.24	0.11, 0.24	0.11, 0.23
	Bin 11	0.23, 0.36	0.23, 0.37	0.24, 0.37	0.24, 0.37	0.24, 0.37	0.23, 0.36
	Bin 12	0.36, 0.51	0.37, 0.51	0.37, 0.52	0.37, 0.52	0.37, 0.52	0.36, 0.50
	Bin 13	0.51, 0.68	0.51, 0.68	0.52, 0.69	0.52, 0.69	0.52, 0.69	0.50, 0.67
	Bin 14	0.68, 0.89	0.68, 0.89	0.69, 0.90	0.69, 0.90	0.69, 0.90	0.67, 0.88
	Bin 15	0.89, 1.18	0.89, 1.18	0.90, 1.20	0.90, 1.20	0.90, 1.19	0.88, 1.16
	Bin 16	1.18, ∞	1.18, ∞	1.20, ∞	1.20, ∞	1.19, ∞	1.16, ∞
		$|y_{t\bar{t}}|$					
		Bin 1 0 - 0.16	Bin 2 0.16 - 0.33	Bin 3 0.33 - 0.52	Bin 4 0.52 - 0.73	Bin 5 0.73 - 1.02	Bin 6 1.02 - ∞
$\Delta|y|$	Bin 1	$-\infty$, -0.30	$-\infty$, -0.62	$-\infty$, -0.95	$-\infty$, -1.28	$-\infty$, -1.57	$-\infty$, -1.45
	Bin 2	-0.30, -0.24	-0.62, -0.55	-0.95, -0.86	-1.28, -1.15	-1.57, -1.32	-1.45, -1.10
	Bin 3	-0.24, -0.19	-0.55, -0.49	-0.86, -0.78	-1.15, -1.05	-1.32, -1.04	-1.10, -0.85
	Bin 4	-0.19, -0.15	-0.49, -0.44	-0.78, -0.71	-1.05, -0.87	-1.04, -0.81	-0.85, -0.65
	Bin 5	-0.15, -0.11	-0.44, -0.39	-0.71, -0.62	-0.87, -0.64	-0.81, -0.59	-0.65, -0.47
	Bin 6	-0.11, -0.07	-0.39, -0.33	-0.62, -0.43	-0.64, -0.42	-0.59, -0.39	-0.47, -0.31
	Bin 7	-0.07, -0.04	-0.33, -0.20	-0.43, -0.22	-0.42, -0.21	-0.39, -0.19	-0.31, -0.16
	Bin 8	-0.04, 0.00	-0.20, 0.00	-0.22, 0.00	-0.21, 0.00	-0.19, 0.00	-0.16, 0.00
	Bin 9	0.00, 0.04	0.00, 0.20	0.00, 0.22	0.00, 0.21	0.00, 0.19	0.00, 0.16
	Bin 10	0.04, 0.07	0.20, 0.33	0.22, 0.43	0.21, 0.42	0.19, 0.39	0.16, 0.31
	Bin 11	0.07, 0.11	0.33, 0.39	0.43, 0.62	0.42, 0.64	0.39, 0.59	0.31, 0.47
	Bin 12	0.11, 0.15	0.39, 0.44	0.62, 0.71	0.64, 0.87	0.59, 0.81	0.47, 0.65
	Bin 13	0.15, 0.19	0.44, 0.49	0.71, 0.78	0.87, 1.05	0.81, 1.04	0.65, 0.85
	Bin 14	0.19, 0.24	0.49, 0.55	0.78, 0.86	1.05, 1.15	1.04, 1.32	0.85, 1.10
	Bin 15	0.24, 0.30	0.55, 0.62	0.86, 0.95	1.15, 1.28	1.32, 1.57	1.10, 1.45
	Bin 16	0.30, ∞	0.62, ∞	0.95, ∞	1.28, ∞	1.57, ∞	1.45, ∞

Table C.4: The bin ranges of the parton-level $\Delta|y|$ distributions for the three-binned differential measurements as functions of the three secondary variables $m_{\mathrm{t\bar{t}}}$, $p_{\mathrm{T}}^{\mathrm{t\bar{t}}}$ and $|y_{\mathrm{t\bar{t}}}|$.

		$m_{\mathrm{t\bar{t}}}$ (GeV)		
		Bin 1 0 - 430	Bin 2 420 - 530	Bin 3 530 - ∞
$\Delta\|y\|$	Bin 1	$-\infty$, -0.61	$-\infty$, -0.93	$-\infty$, -1.12
	Bin 2	-0.61, -0.36	-0.93, -0.56	-1.12, -0.67
	Bin 3	-0.36, -0.16	-0.56, -0.26	-0.67, -0.31
	Bin 4	-0.16, 0.00	-0.26, 0.00	-0.31, 0.00
	Bin 5	0.00, 0.16	0.00, 0.26	0.00, 0.31
	Bin 6	0.16, 0.36	0.26, 0.56	0.31, 0.67
	Bin 7	0.36, 0.61	0.56, 0.93	0.67, 1.12
	Bin 8	0.61, ∞	0.93, ∞	1.12, ∞
		$p_{\mathrm{T}}^{\mathrm{t\bar{t}}}$ (GeV)		
		Bin 1 0 - 41	Bin 2 41 - 92	Bin 3 92 - ∞
$\Delta\|y\|$	Bin 1	$-\infty$, -0.86	$-\infty$, -0.88	$-\infty$, -0.88
	Bin 2	-0.86, -0.50	-0.88, -0.51	-0.88, -0.50
	Bin 3	-0.50, -0.23	-0.51, -0.23	-0.50, -0.23
	Bin 4	-0.23, 0.00	-0.23, 0.00	-0.23, 0.00
	Bin 5	0.00, 0.23	0.00, 0.23	0.00, 0.23
	Bin 6	0.23, 0.50	0.23, 0.51	0.23, 0.50
	Bin 7	0.50, 0.86	0.51, 0.88	0.50, 0.88
	Bin 8	0.86, ∞	0.88, ∞	0.88, ∞
		$\|y_{\mathrm{t\bar{t}}}\|$		
		Bin 1 0 - 0.34	Bin 2 0.34 - 0.75	Bin 3 0.75 - ∞
$\Delta\|y\|$	Bin 1	$-\infty$, -0.44	$-\infty$, -0.98	$-\infty$, -1.16
	Bin 2	-0.44, -0.27	-0.98, -0.73	-1.16, -0.70
	Bin 3	-0.27, -0.13	-0.73, -0.40	-0.70, -0.34
	Bin 4	-0.13, 0.00	-0.40, 0.00	-0.34, 0.00
	Bin 5	0.00, 0.13	0.00, 0.40	0.00, 0.34
	Bin 6	0.13, 0.27	0.40, 0.73	0.34, 0.70
	Bin 7	0.27, 0.44	0.73, 0.98	0.70, 1.16
	Bin 8	0.44, ∞	0.98, ∞	1.16, ∞

Table C.5: The bin ranges of the reconstructed $\Delta|y|$ distributions for the six-binned differential measurement as a function of $m_{t\bar{t}}$.

		$m_{t\bar{t}}$ (GeV)					
		Bin 1 0 - 380	Bin 2 380 - 420	Bin 3 420 - 450	Bin 4 450 - 500	Bin 5 500 - 550	Bin 6 550 - 600
$\Delta\|y\|$	Bin 1	$-\infty$, -0.55	$-\infty$, -0.86	$-\infty$, -1.05	$-\infty$, -1.19	$-\infty$, -1.32	$-\infty$, -1.39
	Bin 2	-0.55, -0.43	-0.86, -0.69	-1.05, -0.84	-1.19, -0.94	-1.32, -1.03	-1.39, -1.09
	Bin 3	-0.43, -0.33	-0.69, -0.55	-0.84, -0.66	-0.94, -0.74	-1.03, -0.81	-1.09, -0.86
	Bin 4	-0.33, -0.26	-0.55, -0.42	-0.66, -0.50	-0.74, -0.57	-0.81, -0.62	-0.86, -0.66
	Bin 5	-0.26, -0.18	-0.42, -0.30	-0.50, -0.37	-0.57, -0.41	-0.62, -0.45	-0.66, -0.48
	Bin 6	-0.18, -0.12	-0.30, -0.19	-0.37, -0.24	-0.41, -0.26	-0.45, -0.29	-0.48, -0.31
	Bin 7	-0.12, -0.06	-0.19, -0.09	-0.24, -0.11	-0.26, -0.13	-0.29, -0.14	-0.31, -0.15
	Bin 8	-0.06, 0.00	-0.09, 0.00	-0.11, 0.00	-0.13, 0.00	-0.14, 0.00	-0.15, 0.00
	Bin 9	0.00, 0.06	0.00, 0.09	0.00, 0.11	0.00, 0.13	0.00, 0.14	0.00, 0.15
	Bin 10	0.06, 0.12	0.09, 0.19	0.11, 0.24	0.13, 0.26	0.14, 0.29	0.15, 0.31
	Bin 11	0.12, 0.18	0.19, 0.30	0.24, 0.37	0.26, 0.41	0.29, 0.45	0.31, 0.48
	Bin 12	0.18, 0.26	0.30, 0.42	0.37, 0.50	0.41, 0.57	0.45, 0.62	0.48, 0.66
	Bin 13	0.26, 0.33	0.42, 0.55	0.50, 0.66	0.57, 0.74	0.62, 0.81	0.66, 0.86
	Bin 14	0.33, 0.43	0.55, 0.69	0.66, 0.84	0.74, 0.94	0.81, 1.03	0.86, 1.09
	Bin 15	0.43, 0.55	0.69, 0.86	0.84, 1.05	0.94, 1.19	1.03, 1.32	1.09, 1.39
	Bin 16	0.55, ∞	0.86, ∞	1.05, ∞	1.19, ∞	1.32, ∞	1.39, ∞

		$m_{t\bar{t}}$ (GeV)					
		Bin 7 600 - 675	Bin 8 675 - 750	Bin 9 750 - 825	Bin 10 825 - 900	Bin 11 900 - 1050	Bin 12 1050 - ∞
$\Delta\|y\|$	Bin 1	$-\infty$, -1.45	$-\infty$, -1.49	$-\infty$, -1.52	$-\infty$, -1.52	$-\infty$, -1.53	$-\infty$, -1.44
	Bin 2	-1.45, -1.14	-1.49, -1.16	-1.52, -1.18	-1.52, -1.18	-1.53, -1.19	-1.44, -1.11
	Bin 3	-1.14, -0.89	-1.16, -0.92	-1.18, -0.93	-1.18, -0.94	-1.19, -0.93	-1.11, -0.86
	Bin 4	-0.89, -0.69	-0.92, -0.70	-0.93, -0.71	-0.94, -0.72	-0.93, -0.72	-0.86, -0.65
	Bin 5	-0.69, -0.50	-0.70, -0.51	-0.71, -0.52	-0.72, -0.52	-0.72, -0.52	-0.65, -0.47
	Bin 6	-0.50, -0.32	-0.51, -0.33	-0.52, -0.33	-0.52, -0.34	-0.52, -0.34	-0.47, -0.30
	Bin 7	-0.32, -0.16	-0.33, -0.16	-0.33, -0.16	-0.34, -0.16	-0.34, -0.17	-0.30, -0.15
	Bin 8	-0.16, 0.00	-0.16, 0.00	-0.16, 0.00	-0.16, 0.00	-0.17, 0.00	-0.15, 0.00
	Bin 9	0.00, 0.16	0.00, 0.16	0.00, 0.16	0.00, 0.16	0.00, 0.17	0.00, 0.15
	Bin 10	0.16, 0.32	0.16, 0.33	0.16, 0.33	0.16, 0.34	0.17, 0.34	0.15, 0.30
	Bin 11	0.32, 0.50	0.33, 0.51	0.33, 0.52	0.34, 0.52	0.34, 0.52	0.30, 0.47
	Bin 12	0.50, 0.69	0.51, 0.70	0.52, 0.71	0.52, 0.72	0.52, 0.72	0.47, 0.65
	Bin 13	0.69, 0.89	0.70, 0.92	0.71, 0.93	0.72, 0.94	0.72, 0.93	0.65, 0.86
	Bin 14	0.89, 1.14	0.92, 1.16	0.93, 1.18	0.94, 1.18	0.93, 1.19	0.86, 1.11
	Bin 15	1.14, 1.45	1.16, 1.49	1.18, 1.52	1.18, 1.52	1.19, 1.53	1.11, 1.44
	Bin 16	1.45, ∞	1.49, ∞	1.52, ∞	1.52, ∞	1.53, ∞	1.44, ∞

Table C.6: The bin ranges of the parton-level $\Delta|y|$ distributions for the six-binned differential measurement as a function of $m_{t\bar{t}}$.

		$m_{t\bar{t}}$ (GeV)					
		Bin 1 0 - 420	Bin 2 420 - 500	Bin 3 500 - 600	Bin 4 600 - 750	Bin 5 750 - 900	Bin 6 900 - ∞
$\Delta\|y\|$	Bin 1	$-\infty$, -0.58	$-\infty$, -0.89	$-\infty$, -1.05	$-\infty$, -1.14	$-\infty$, -1.17	$-\infty$, -1.14
	Bin 2	-0.58, -0.34	-0.89, -0.54	-1.05, -0.63	-1.14, -0.68	-1.17, -0.71	-1.14, -0.69
	Bin 3	-0.34, -0.16	-0.54, -0.25	-0.63, -0.29	-0.68, -0.32	-0.71, -0.33	-0.69, -0.33
	Bin 4	-0.16, 0.00	-0.25, 0.00	-0.29, 0.00	-0.32, 0.00	-0.33, 0.00	-0.33, 0.00
	Bin 5	0.00, 0.16	0.00, 0.25	0.00, 0.29	0.00, 0.32	0.00, 0.33	0.00, 0.33
	Bin 6	0.16, 0.34	0.25, 0.54	0.29, 0.63	0.32, 0.68	0.33, 0.71	0.33, 0.69
	Bin 7	0.34, 0.58	0.54, 0.89	0.63, 1.05	0.68, 1.14	0.71, 1.17	0.69, 1.14
	Bin 8	0.58, ∞	0.89, ∞	1.05, ∞	1.14, ∞	1.17, ∞	1.14, ∞

D Consistency Tests

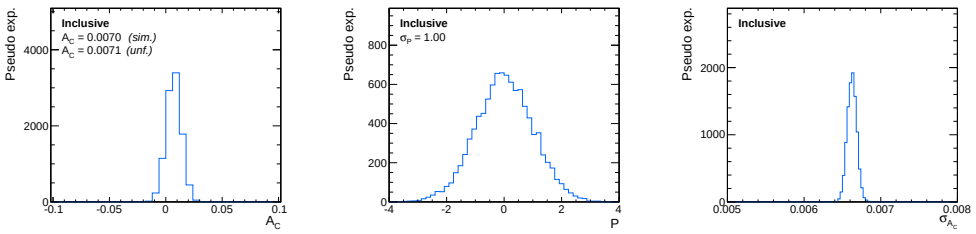

Figure D.1: Distribution of the measured asymmetries (left), the pull distribution (middle), and the distribution of the statistical uncertainties (right) of pseudo experiments corresponding to the inclusive measurement in the *full phase space*. σ_{P} signifies the standard deviation of the pull distribution.

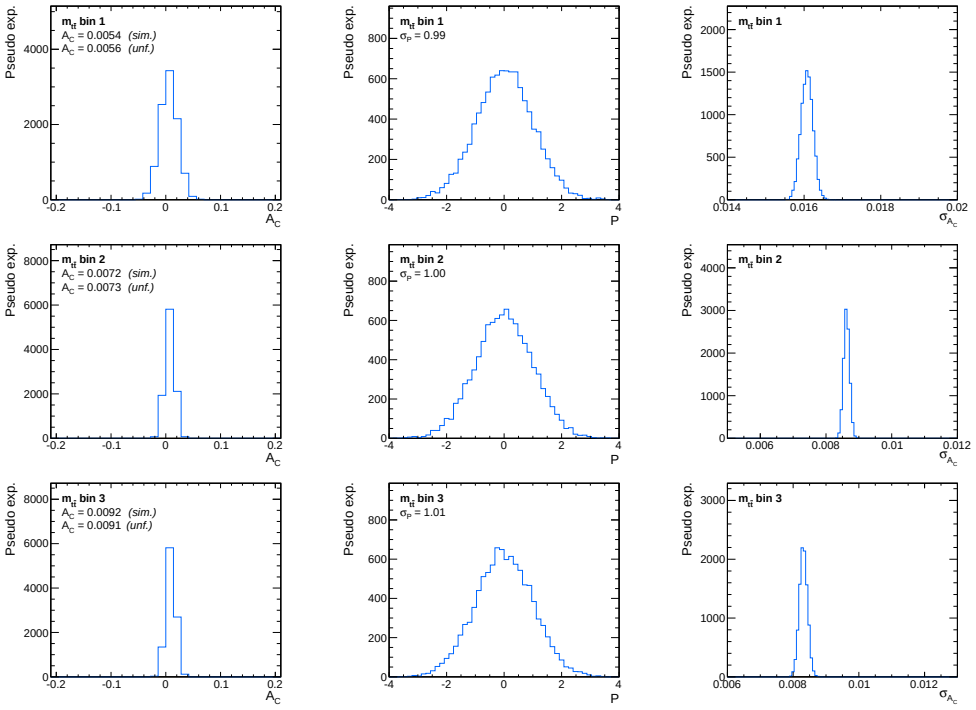

Figure D.2: Distribution of the measured asymmetries (left), the pull distributions (middle), and the distributions of the statistical uncertainties (right) of pseudo experiments corresponding to the differential measurement in three bins of $m_{\mathrm{t\bar{t}}}$ in the *full phase space*. σ_{P} signifies the standard deviation of the pull distribution.

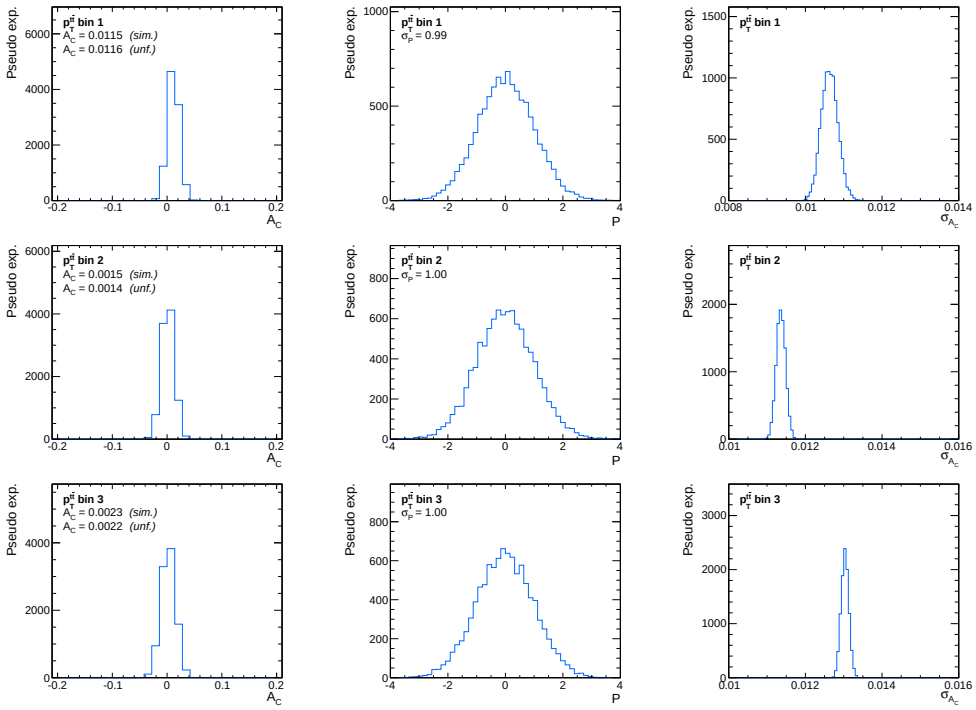

Figure D.3: Distribution of the measured asymmetries (left), the pull distributions (middle), and the distributions of the statistical uncertainties (right) of pseudo experiments corresponding to the differential measurement in three bins of $p_{\mathrm{T}}^{\mathrm{t\bar{t}}}$ in the *full phase space*. σ_{P} signifies the standard deviation of the pull distribution.

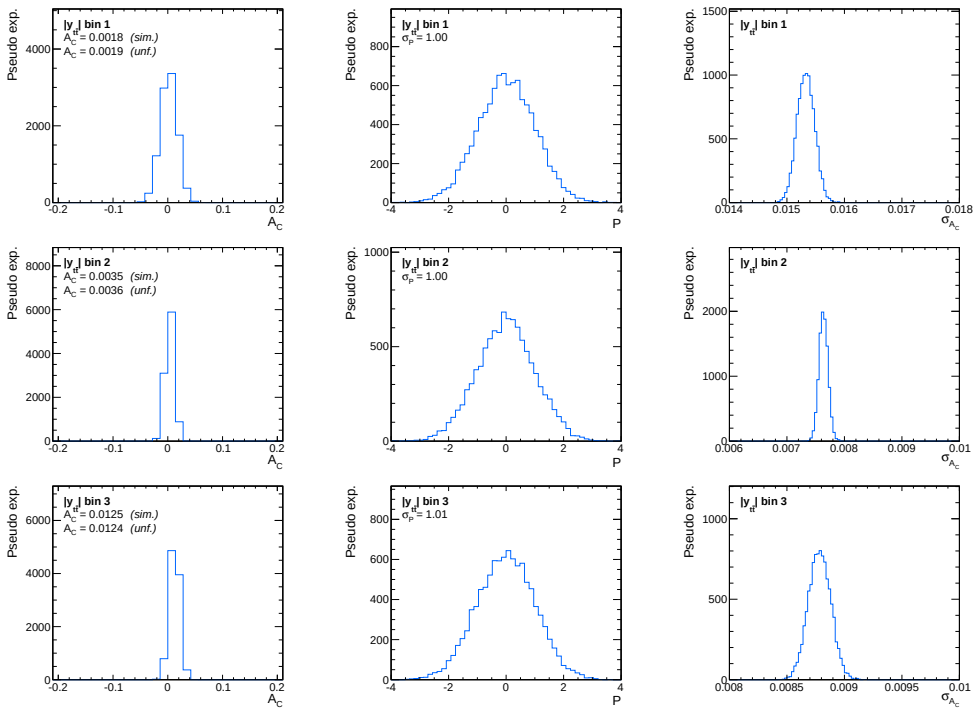

Figure D.4: Distribution of the measured asymmetries (left), the pull distributions (middle), and the distributions of the statistical uncertainties (right) of pseudo experiments corresponding to the differential measurement in three bins of $|y_{\mathrm{t\bar{t}}}|$ in the *full phase space*. σ_{P} signifies the standard deviation of the pull distribution.

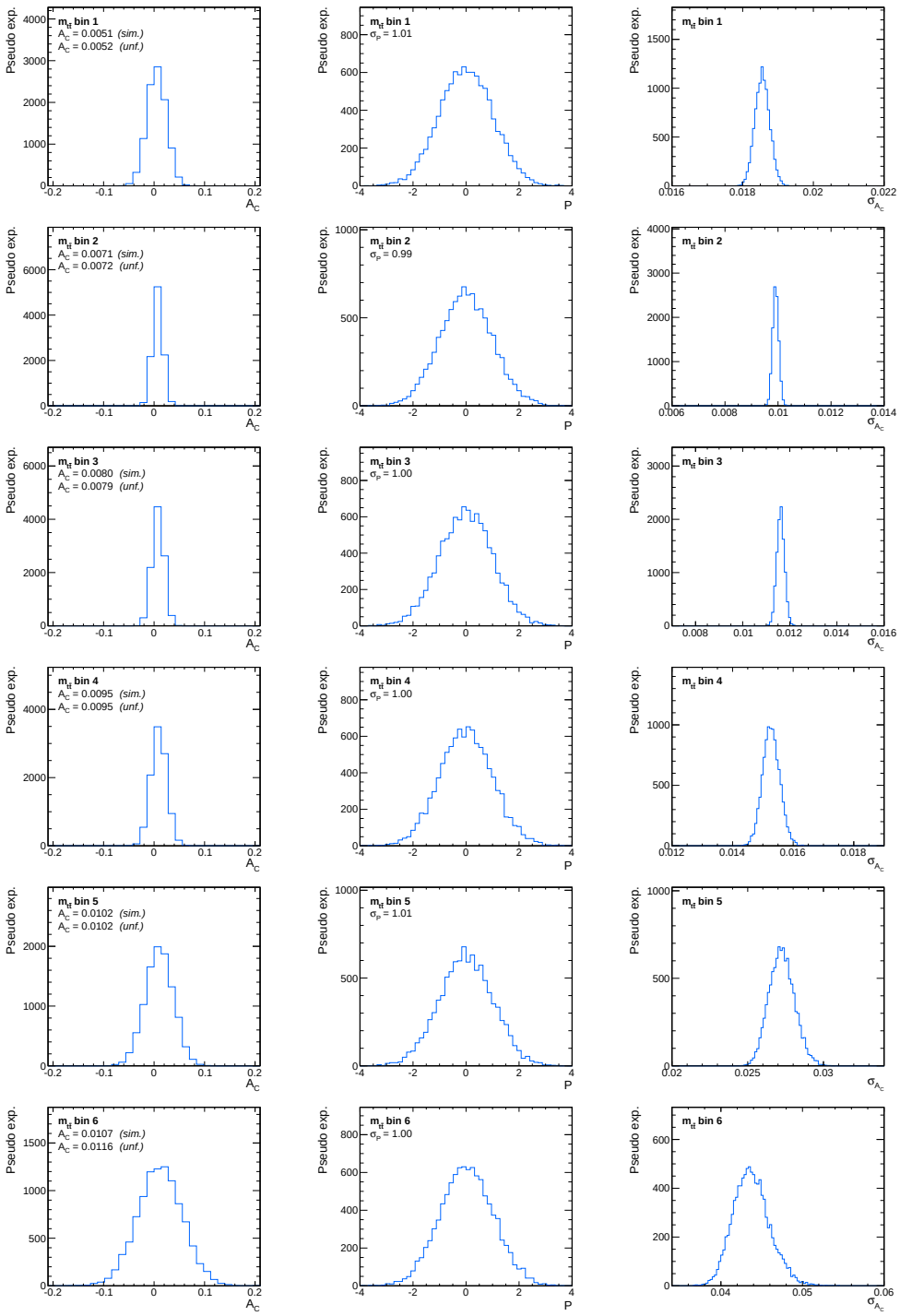

Figure D.5: Distribution of the measured asymmetries (left), the pull distributions (middle), and the distributions of the statistical uncertainties (right) of pseudo experiments corresponding to the differential measurement in six bins of $m_{\mathrm{t\bar{t}}}$ in the *full phase space*. σ_{P} signifies the standard deviation of the pull distribution.

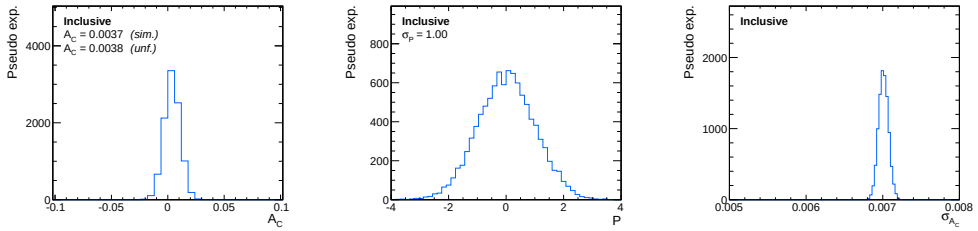

Figure D.6: Distribution of the measured asymmetries (left), the pull distribution (middle), and the distribution of the statistical uncertainties (right) of pseudo experiments corresponding to the inclusive measurement in the *fiducial phase space*. σ_P signifies the standard deviation of the pull distribution.

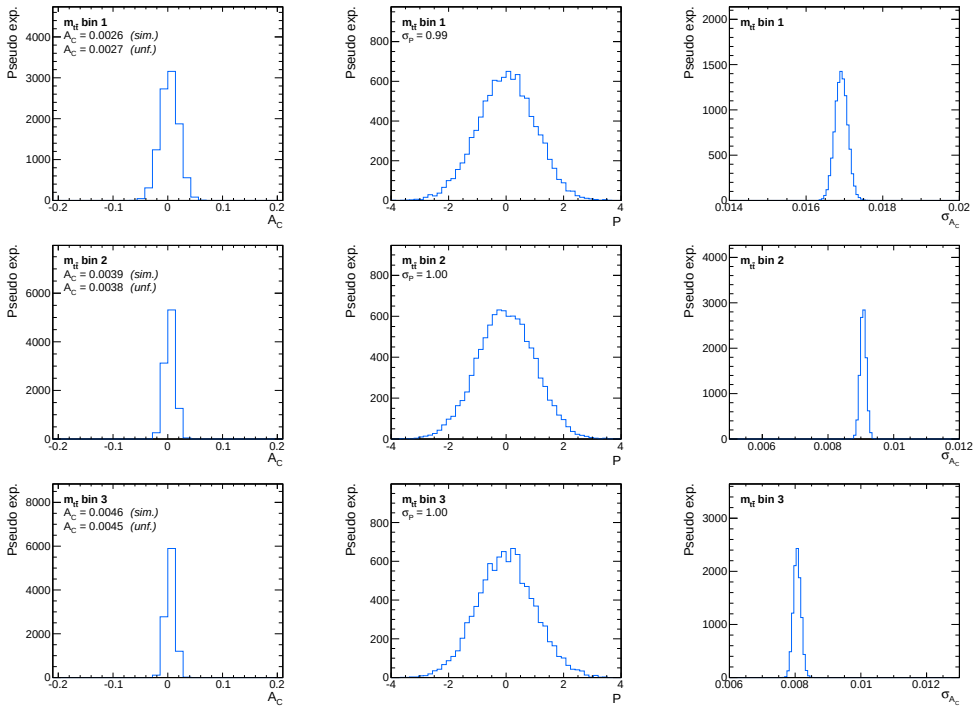

Figure D.7: Distribution of the measured asymmetries (left), the pull distributions (middle), and the distributions of the statistical uncertainties (right) of pseudo experiments corresponding to the differential measurement in three bins of $m_{t\bar{t}}$ in the *fiducial phase space*. σ_P signifies the standard deviation of the pull distribution.

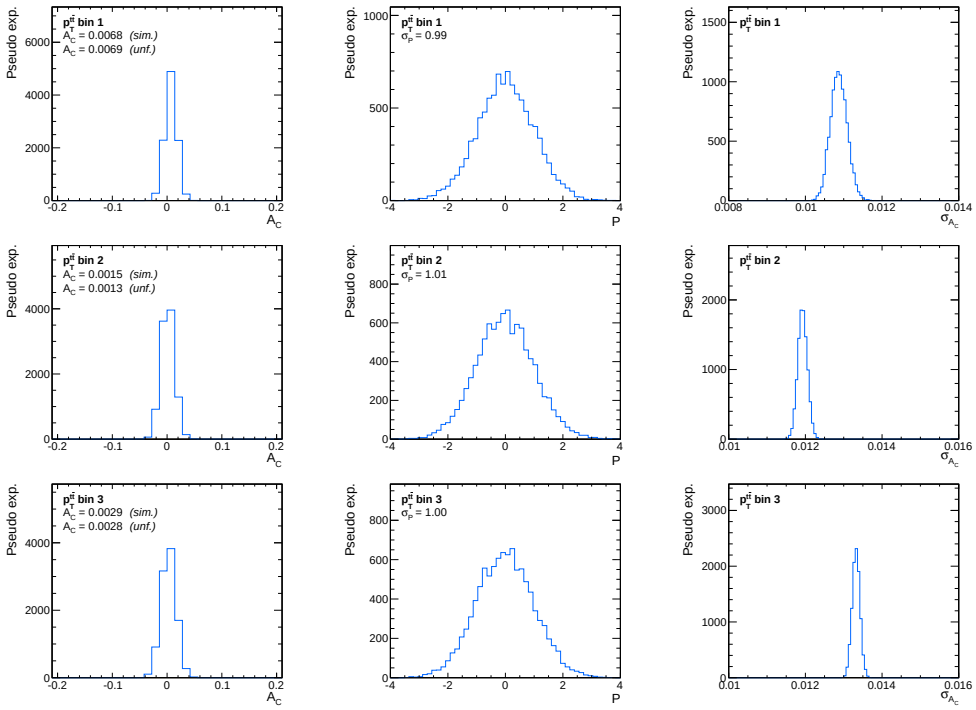

Figure D.8: Distribution of the measured asymmetries (left), the pull distributions (middle), and the distributions of the statistical uncertainties (right) of pseudo experiments corresponding to the differential measurement in three bins of $p_{\mathrm{T}}^{\mathrm{t\bar{t}}}$ in the *fiducial phase space*. σ_{P} signifies the standard deviation of the pull distribution.

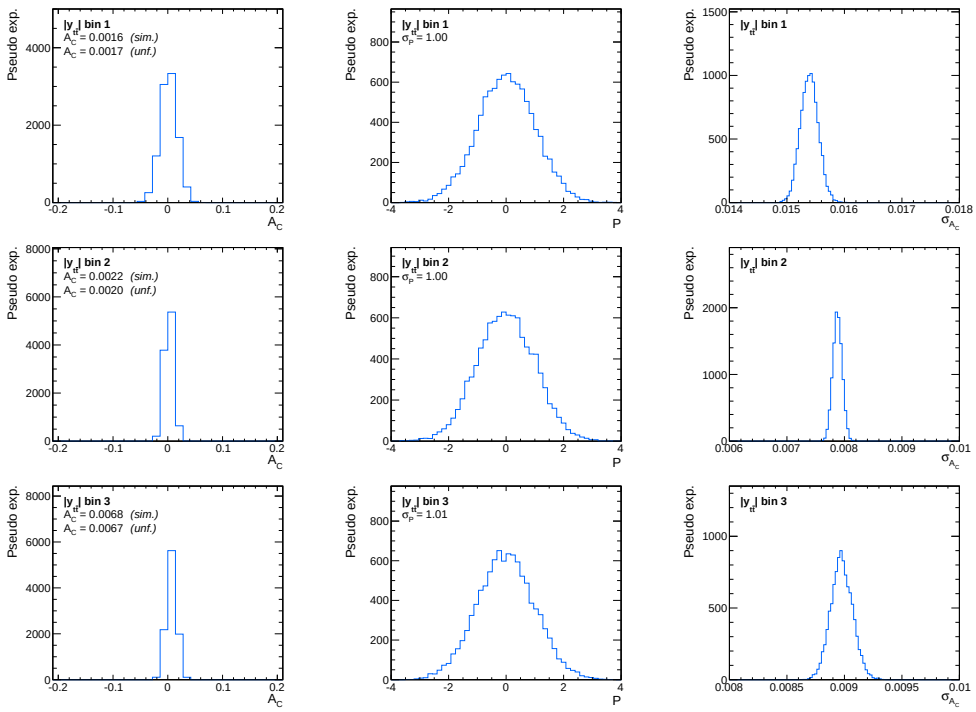

Figure D.9: Distribution of the measured asymmetries (left), the pull distributions (middle), and the distributions of the statistical uncertainties (right) of pseudo experiments corresponding to the differential measurement in three bins of $|y_{t\bar{t}}|$ in the *fiducial phase space*. σ_{P} signifies the standard deviation of the pull distribution.

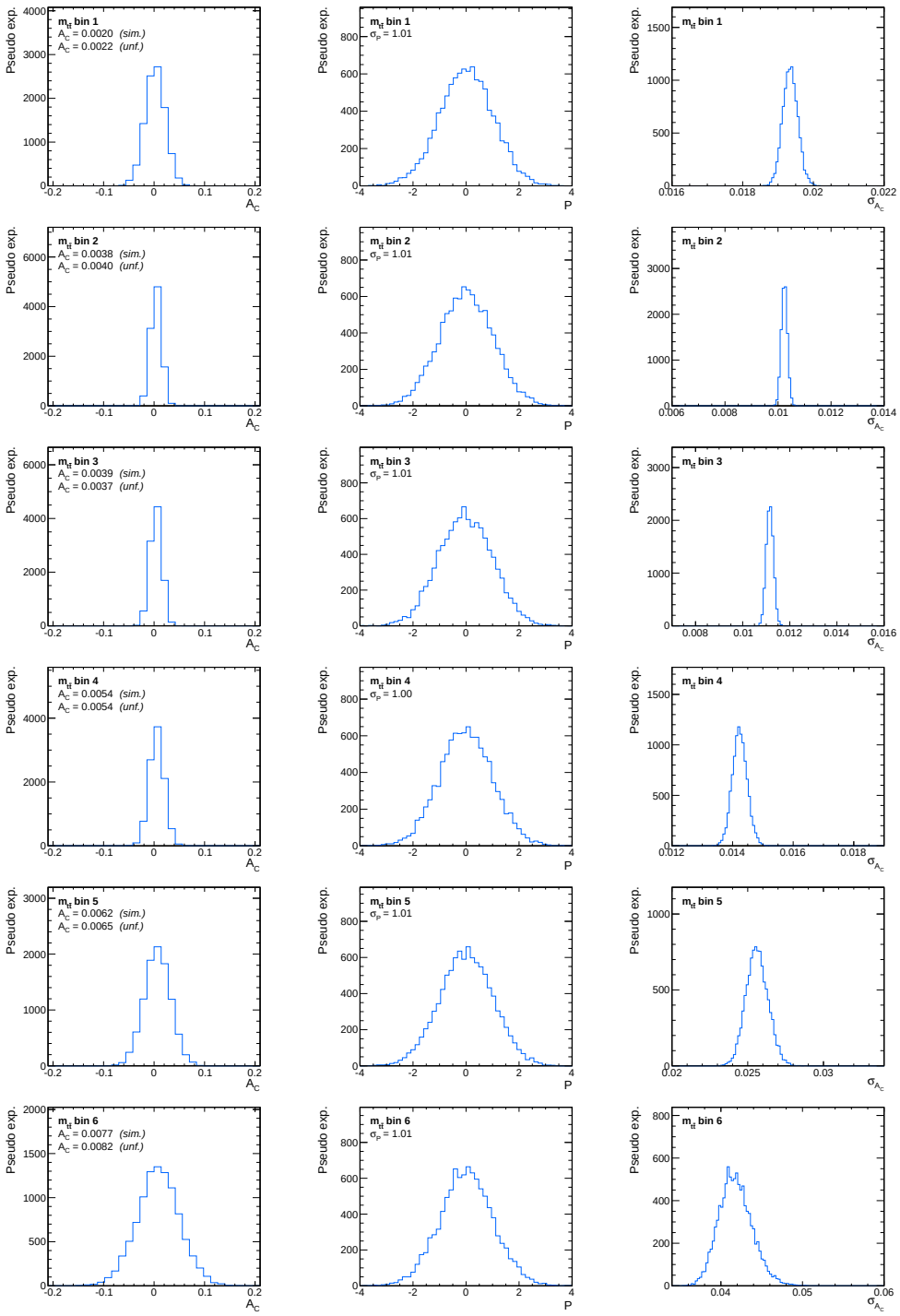

Figure D.10: Distribution of the measured asymmetries (left), the pull distributions (middle), and the distributions of the statistical uncertainties (right) of pseudo experiments corresponding to the differential measurement in six bins of $m_{t\bar{t}}$ in the *fiducial phase space*. σ_P signifies the standard deviation of the pull distribution.

E Linearity Tests

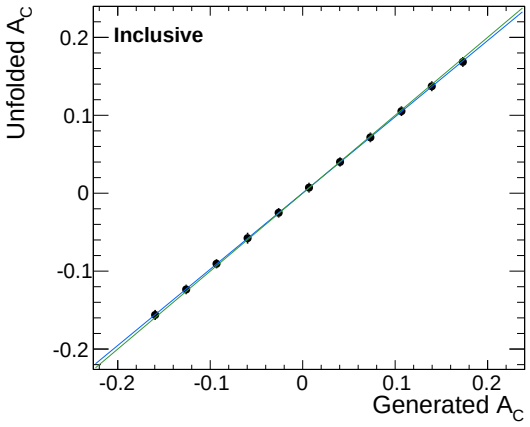

Figure E.1: Linearity test: Mean of unfolded A_C in the *full phase space* as a function of the true simulated value. The error bars indicate the statistical uncertainty of a single measurement. The result of a linear regression is drawn in blue, whereas the bisector is shown in green.

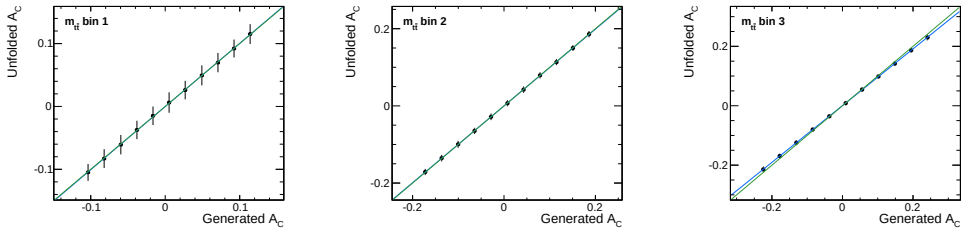

Figure E.2: Linearity test: Mean of unfolded A_C in the *full phase space* as a function of the true simulated value in three bins of $m_{t\bar{t}}$. The error bars indicate the statistical uncertainty of a single measurement. The result of a linear regression is drawn in blue, whereas the bisector is shown in green.

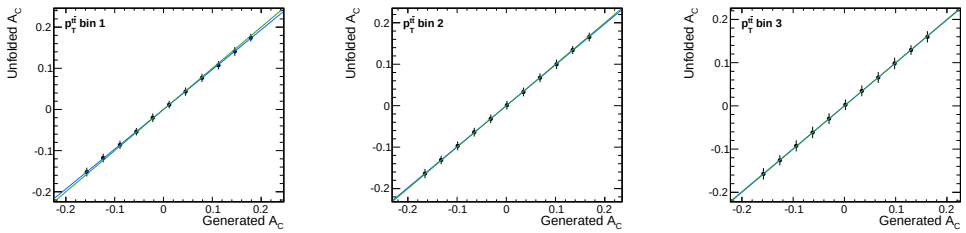

Figure E.3: Linearity test: Mean of unfolded A_C in the *full phase space* as a function of the true simulated value in three bins of $p_T^{t\bar{t}}$. The error bars indicate the statistical uncertainty of a single measurement. The result of a linear regression is drawn in blue, whereas the bisector is shown in green.

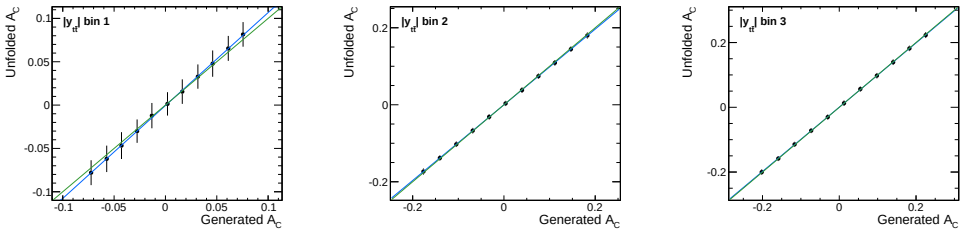

Figure E.4: Linearity test: Mean of unfolded A_{C} in the *full phase space* as a function of the true simulated value in three bins of $|y_{\mathrm{t\bar{t}}}|$. The error bars indicate the statistical uncertainty of a single measurement. The result of a linear regression is drawn in blue, whereas the bisector is shown in green.

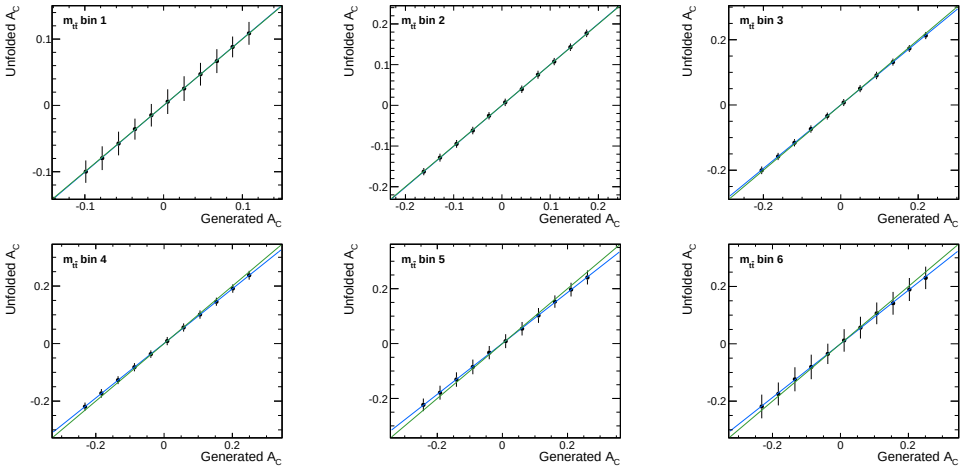

Figure E.5: Linearity test: Mean of unfolded A_{C} in the *full phase space* as a function of the true simulated value in six bins of $m_{\mathrm{t\bar{t}}}$. The error bars indicate the statistical uncertainty of a single measurement. The result of a linear regression is drawn in blue, whereas the bisector is shown in green.

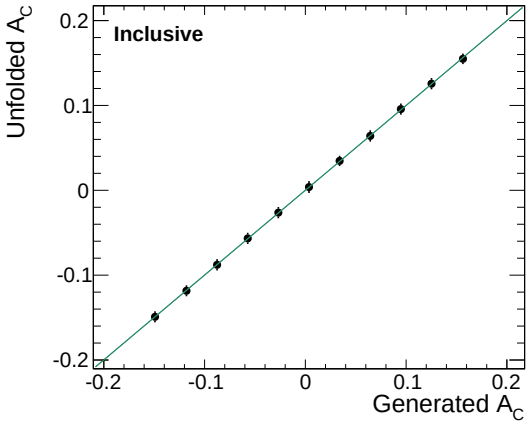

Figure E.6: Linearity test: Mean of unfolded A_C in the *fiducial phase space* as a function of the true simulated value. The error bars indicate the statistical uncertainty of a single measurement. The result of a linear regression is drawn in blue, whereas the bisector is shown in green.

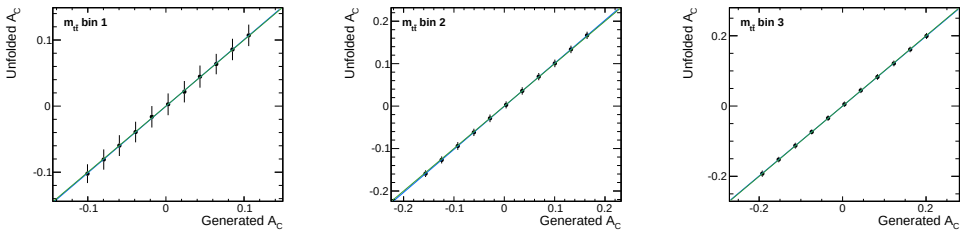

Figure E.7: Linearity test: Mean of unfolded A_C in the *fiducial phase space* as a function of the true simulated value in three bins of $m_{t\bar{t}}$. The error bars indicate the statistical uncertainty of a single measurement. The result of a linear regression is drawn in blue, whereas the bisector is shown in green.

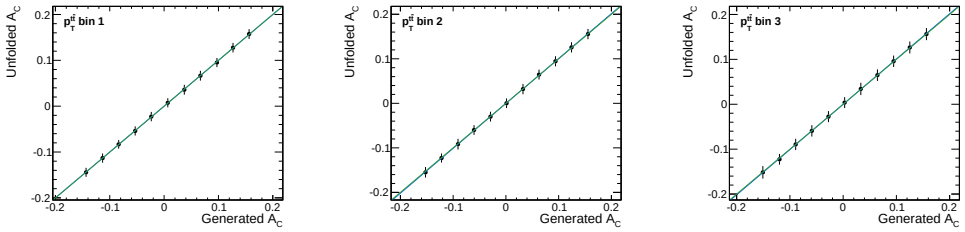

Figure E.8: Linearity test: Mean of unfolded A_C in the *fiducial phase space* as a function of the true simulated value in three bins of $p_T^{t\bar{t}}$. The error bars indicate the statistical uncertainty of a single measurement. The result of a linear regression is drawn in blue, whereas the bisector is shown in green.

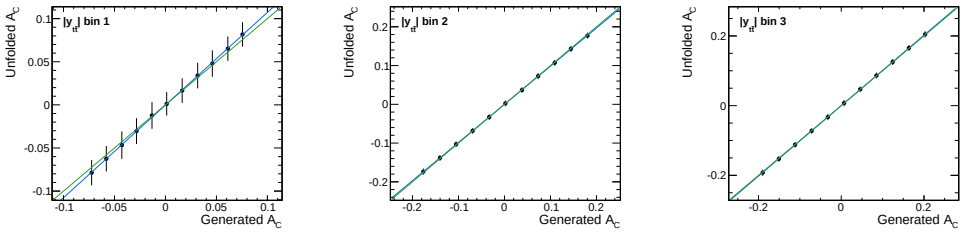

Figure E.9: Linearity test: Mean of unfolded A_{C} in the *fiducial phase space* as a function of the true simulated value in three bins of $|y_{\mathrm{t\bar{t}}}|$. The error bars indicate the statistical uncertainty of a single measurement. The result of a linear regression is drawn in blue, whereas the bisector is shown in green.

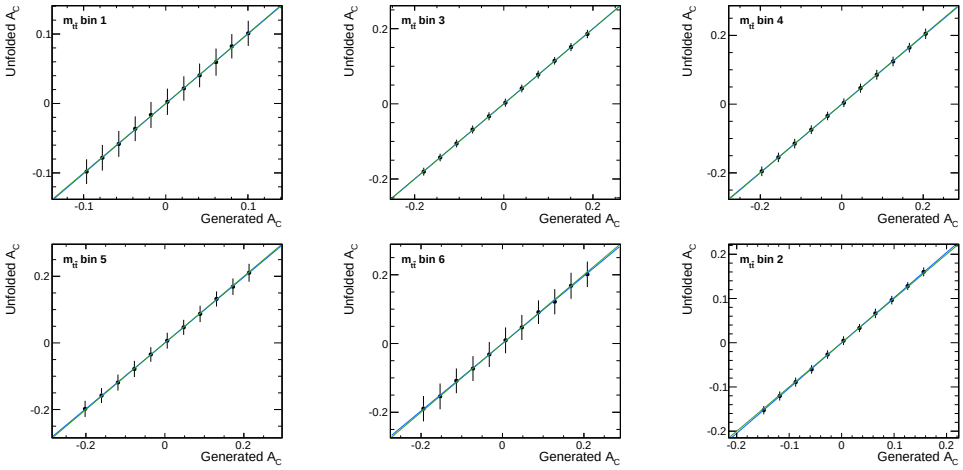

Figure E.10: Linearity test: Mean of unfolded A_{C} in the *fiducial phase space* as a function of the true simulated value in six bins of $m_{\mathrm{t\bar{t}}}$. The error bars indicate the statistical uncertainty of a single measurement. The result of a linear regression is drawn in blue, whereas the bisector is shown in green.

F Reweighted Aymmetries for the Unfolding Uncertainty

Table F.1: Comparison of generated and measured A_C values for the three reweighting scenarios used in the unfolding systematic for the inclusive measurement in the *full phase space*.

Scenario	A_C^{gen}	A_C^{meas}
Reweighted in $m_{t\bar{t}}$	0.0031	0.0040
Reweighted in $p_T^{t\bar{t}}$	−0.0001	0.0028
Reweighted in $\lvert y_{t\bar{t}}\rvert$	0.0018	−0.0006

Table F.2: Comparison of generated and measured A_C values for the three reweighting scenarios used in the unfolding systematic for the differential measurements in 3 bins in the *full phase space*.

	$m_{t\bar{t}}$ bin 1		$m_{t\bar{t}}$ bin 2		$m_{t\bar{t}}$ bin 3	
Scenario	A_C^{gen}	A_C^{meas}	A_C^{gen}	A_C^{meas}	A_C^{gen}	A_C^{meas}
Reweighted in $m_{t\bar{t}}$	−0.0008	−0.0006	0.0041	0.0038	0.0074	0.0076
Reweighted in $p_T^{t\bar{t}}$	0.0002	0.0006	−0.0008	0.0011	0.0002	0.0058
Reweighted in $\lvert y_{t\bar{t}}\rvert$	0.0007	−0.0021	0.0021	0.0017	0.0030	0.0024

	$p_T^{t\bar{t}}$ bin 1		$p_T^{t\bar{t}}$ bin 2		$p_T^{t\bar{t}}$ bin 3	
Scenario	A_C^{gen}	A_C^{meas}	A_C^{gen}	A_C^{meas}	A_C^{gen}	A_C^{meas}
Reweighted in $m_{t\bar{t}}$	0.0073	0.0080	−0.0023	−0.0016	−0.0012	−0.0002
Reweighted in $p_T^{t\bar{t}}$	−0.0030	−0.0024	−0.0017	−0.0017	0.0103	0.0101
Reweighted in $\lvert y_{t\bar{t}}\rvert$	0.0068	0.0045	−0.0039	−0.0061	−0.0042	−0.0073

	$\lvert y_{t\bar{t}}\rvert$ bin 1		$\lvert y_{t\bar{t}}\rvert$ bin 2		$\lvert y_{t\bar{t}}\rvert$ bin 3	
Scenario	A_C^{gen}	A_C^{meas}	A_C^{gen}	A_C^{meas}	A_C^{gen}	A_C^{meas}
Reweighted in $m_{t\bar{t}}$	−0.0001	0.0003	−0.0007	0.0000	0.0075	0.0084
Reweighted in $p_T^{t\bar{t}}$	−0.0010	−0.0002	−0.0037	−0.0012	0.0028	0.0070
Reweighted in $\lvert y_{t\bar{t}}\rvert$	−0.0295	−0.0259	0.0054	0.0014	0.0184	0.0197

Table F.3: Comparison of generated and measured A_C values for the three reweighting scenarios used in the unfolding systematic for the differential measurement in 6 bins of $m_{t\bar{t}}$ in the *full phase space*.

	$m_{t\bar{t}}$ bin 1		$m_{t\bar{t}}$ bin 2		$m_{t\bar{t}}$ bin 3	
Scenario	A_C^{gen}	A_C^{meas}	A_C^{gen}	A_C^{meas}	A_C^{gen}	A_C^{meas}
Reweighted in $m_{t\bar{t}}$	−0.0007	−0.0010	0.0033	0.0032	0.0056	0.0061
Reweighted in $p_T^{t\bar{t}}$	0.0002	0.0006	−0.0005	0.0013	−0.0010	0.0027
Reweighted in $\lvert y_{t\bar{t}}\rvert$	0.0006	−0.0023	0.0020	0.0007	0.0026	0.0028

	$m_{t\bar{t}}$ bin 4		$m_{t\bar{t}}$ bin 5		$m_{t\bar{t}}$ bin 6	
Scenario	A_C^{gen}	A_C^{meas}	A_C^{gen}	A_C^{meas}	A_C^{gen}	A_C^{meas}
Reweighted in $m_{t\bar{t}}$	0.0077	0.0079	0.0083	0.0084	0.0089	0.0091
Reweighted in $p_T^{t\bar{t}}$	0.0002	0.0057	0.0014	0.0085	0.0033	0.0113
Reweighted in $\lvert y_{t\bar{t}}\rvert$	0.0035	0.0034	0.0030	0.0022	0.0009	−0.0011

Table F.4: Comparison of generated and measured A_C values for the three reweighting scenarios used in the unfolding systematic for the inclusive measurement in the *fiducial phase space*.

Scenario	A_C^{gen}	A_C^{meas}
Reweighted in $m_{t\bar{t}}$	0.0003	0.0007
Reweighted in $p_T^{t\bar{t}}$	0.0011	−0.0004
Reweighted in $\lvert y_{t\bar{t}}\rvert$	−0.0036	−0.0048

Table F.5: Comparison of generated and measured A_C values for the three reweighting scenarios used in the unfolding systematic for the differential measurements in 3 bins in the *fiducial phase space*.

	$m_{t\bar{t}}$ bin 1		$m_{t\bar{t}}$ bin 2		$m_{t\bar{t}}$ bin 3	
Scenario	A_C^{gen}	A_C^{meas}	A_C^{gen}	A_C^{meas}	A_C^{gen}	A_C^{meas}
Reweighted in $m_{t\bar{t}}$	−0.0032	−0.0031	0.0011	0.0008	0.0031	0.0032
Reweighted in $p_T^{t\bar{t}}$	0.0004	−0.0019	0.0008	−0.0017	0.0021	0.0015
Reweighted in $\lvert y_{t\bar{t}}\rvert$	−0.0032	−0.0053	−0.0031	−0.0032	−0.0044	−0.0048

	$p_T^{t\bar{t}}$ bin 1		$p_T^{t\bar{t}}$ bin 2		$p_T^{t\bar{t}}$ bin 3	
Scenario	A_C^{gen}	A_C^{meas}	A_C^{gen}	A_C^{meas}	A_C^{gen}	A_C^{meas}
Reweighted in $m_{t\bar{t}}$	0.0033	0.0035	−0.0020	−0.0015	−0.0003	0.0004
Reweighted in $p_T^{t\bar{t}}$	−0.0061	−0.0061	−0.0015	−0.0015	0.0106	0.0105
Reweighted in $\lvert y_{t\bar{t}}\rvert$	−0.0004	−0.0014	−0.0055	−0.0070	−0.0047	−0.0071

	$\lvert y_{t\bar{t}}\rvert$ bin 1		$\lvert y_{t\bar{t}}\rvert$ bin 2		$\lvert y_{t\bar{t}}\rvert$ bin 3	
Scenario	A_C^{gen}	A_C^{meas}	A_C^{gen}	A_C^{meas}	A_C^{gen}	A_C^{meas}
Reweighted in $m_{t\bar{t}}$	−0.0002	0.0000	−0.0017	−0.0014	0.0024	0.0028
Reweighted in $p_T^{t\bar{t}}$	0.0003	−0.0005	−0.0010	−0.0025	0.0035	0.0016
Reweighted in $\lvert y_{t\bar{t}}\rvert$	−0.0299	−0.0264	0.0040	0.0003	0.0123	0.0136

Table F.6: Comparison of generated and measured A_C values for the three reweighting scenarios used in the unfolding systematic for the differential measurement in 6 bins of $m_{t\bar{t}}$ in the *fiducial phase space*.

	$m_{t\bar{t}}$ bin 1		$m_{t\bar{t}}$ bin 2		$m_{t\bar{t}}$ bin 3	
Scenario	A_C^{gen}	A_C^{meas}	A_C^{gen}	A_C^{meas}	A_C^{gen}	A_C^{meas}
Reweighted in $m_{t\bar{t}}$	−0.0036	−0.0039	0.0004	0.0003	0.0019	0.0022
Reweighted in $p_T^{t\bar{t}}$	−0.0001	−0.0023	0.0008	−0.0014	0.0008	−0.0008
Reweighted in $\lvert y_{t\bar{t}}\rvert$	−0.0037	−0.0059	−0.0030	−0.0040	−0.0037	−0.0035

	$m_{t\bar{t}}$ bin 4		$m_{t\bar{t}}$ bin 5		$m_{t\bar{t}}$ bin 6	
Scenario	A_C^{gen}	A_C^{meas}	A_C^{gen}	A_C^{meas}	A_C^{gen}	A_C^{meas}
Reweighted in $m_{t\bar{t}}$	0.0039	0.0040	0.0046	0.0046	0.0062	0.0062
Reweighted in $p_T^{t\bar{t}}$	0.0028	0.0019	0.0044	0.0043	0.0073	0.0079
Reweighted in $\lvert y_{t\bar{t}}\rvert$	−0.0035	−0.0034	−0.0045	−0.0048	−0.0061	−0.0071

G Systematic Uncertainties

Table G.1: Systematic uncertainties in the inclusive measurement of A_C in the *full phase space*.

Systematic uncertainty	Uncertainty in A_C
JES	0.0018
JER	0.0003
Pileup	0.0006
b tagging	0.0008
Lepton efficiency	0.0009
W+jets	0.0007
QCD multijet	0.0009
Unfolding	0.0022
Generator	0.0005
Hadronization	0.0011
p_T reweighting	0.0002
μ_F and μ_R	0.0007
PDF	0.0003
Total	0.0037

Table G.2: Systematic uncertainties in the differential measurement of A_C in three bins of $m_{t\bar{t}}$ in the *full phase space*.

	Uncertainty in $A_C(m_{t\bar{t}})$		
Systematic uncertainty	Bin 1	Bin 2	Bin 3
JES	0.0063	0.0008	0.0023
JER	0.0010	0.0005	0.0018
Pileup	0.0027	0.0003	0.0004
b tagging	0.0004	0.0009	0.0007
Lepton efficiency	0.0007	0.0008	0.0014
W+jets	0.0010	0.0025	0.0015
QCD multijet	0.0013	0.0024	0.0020
Unfolding	0.0017	0.0011	0.0033
Generator	0.0043	0.0021	0.0024
Hadronization	0.0040	0.0035	0.0022
p_T reweighting	0.0003	0.0007	0.0013
μ_F and μ_R	0.0064	0.0041	0.0043
PDF	0.0009	0.0006	0.0006
Total	0.0115	0.0071	0.0077

Table G.3: Systematic uncertainties in the differential measurement of A_C in three bins of $p_T^{t\bar{t}}$ in the *full phase space*.

	Uncertainty in $A_C(p_T^{t\bar{t}})$		
Systematic uncertainty	Bin 1	Bin 2	Bin 3
JES	0.0013	0.0036	0.0027
JER	0.0012	0.0018	0.0011
Pileup	0.0017	0.0004	0.0003
b tagging	0.0012	0.0005	0.0014
Lepton efficiency	0.0008	0.0009	0.0010
W+jets	0.0005	0.0010	0.0022
QCD multijet	0.0012	0.0011	0.0014
Unfolding	0.0014	0.0013	0.0019
Generator	0.0012	0.0030	0.0032
Hadronization	0.0009	0.0040	0.0027
p_T reweighting	0.0001	0.0003	0.0015
μ_F and μ_R	0.0014	0.0025	0.0009
PDF	0.0006	0.0007	0.0012
Total	0.0041	0.0073	0.0066

Table G.4: Systematic uncertainties in the differential measurement of A_C in three bins of $|y_{t\bar{t}}|$ in the *full phase space*.

	Uncertainty in $A_C(\lvert y_{t\bar{t}}\rvert)$		
Systematic uncertainty	Bin 1	Bin 2	Bin 3
JES	0.0046	0.0017	0.0012
JER	0.0020	0.0005	0.0010
Pileup	0.0014	0.0004	0.0011
b tagging	0.0005	0.0002	0.0032
Lepton efficiency	0.0005	0.0006	0.0017
W+jets	0.0020	0.0012	0.0005
QCD multijet	0.0013	0.0019	0.0028
Unfolding	0.0021	0.0028	0.0026
Generator	0.0012	0.0007	0.0007
Hadronization	0.0008	0.0029	0.0029
p_T reweighting	0.0009	0.0007	0.0005
μ_F and μ_R	0.0020	0.0017	0.0012
PDF	0.0004	0.0004	0.0012
Total	0.0067	0.0054	0.0066

Table G.5: Systematic uncertainties in the differential measurement of A_C in six bins of $m_{t\bar{t}}$ in the *full phase space*.

	Uncertainty in $A_C(m_{t\bar{t}})$		
Systematic uncertainty	Bin 1	Bin 2	Bin 3
JES	0.0071	0.0009	0.0027
JER	0.0037	0.0013	0.0003
Pileup	0.0029	0.0006	0.0005
b tagging	0.0005	0.0007	0.0006
Lepton efficiency	0.0009	0.0008	0.0009
W+jets	0.0009	0.0017	0.0009
QCD multijet	0.0017	0.0018	0.0009
Unfolding	0.0017	0.0013	0.0021
Generator	0.0015	0.0027	0.0027
Hadronization	0.0054	0.0036	0.0031
p_T reweighting	0.0012	0.0005	0.0010
μ_F and μ_R	0.0052	0.0029	0.0016
PDF	0.0009	0.0005	0.0012
Total	0.0118	0.0064	0.0061
	Bin 4	Bin 5	Bin 6
JES	0.0103	0.0131	0.0038
JER	0.0058	0.0039	0.0044
Pileup	0.0007	0.0023	0.0071
b tagging	0.0039	0.0037	0.0028
Lepton efficiency	0.0013	0.0018	0.0027
W+jets	0.0050	0.0045	0.0181
QCD multijet	0.0031	0.0061	0.0105
Unfolding	0.0032	0.0041	0.0047
Generator	0.0030	0.0112	0.0211
Hadronization	0.0060	0.0078	0.0057
p_T reweighting	0.0003	0.0051	0.0045
μ_F and μ_R	0.0084	0.0011	0.0139
PDF	0.0016	0.0062	0.0079
Total	0.0179	0.0231	0.0362

Table G.6: Systematic uncertainties in the inclusive measurement of A_C in the *fiducial phase space*.

Systematic uncertainty	Uncertainty in A_C
JES	0.0020
JER	0.0003
Pileup	0.0006
b tagging	0.0009
Lepton efficiency	0.0009
W+jets	0.0005
QCD multijet	0.0010
Unfolding	0.0012
Generator	0.0002
Hadronization	0.0010
p_T reweighting	0.0000
μ_F and μ_R	0.0002
PDF	0.0002
Total	0.0031

Table G.7: Systematic uncertainties in the differential measurement of A_C in three bins of $m_{t\bar{t}}$ in the *fiducial phase space*.

	Uncertainty in $A_C(m_{t\bar{t}})$		
Systematic uncertainty	Bin 1	Bin 2	Bin 3
JES	0.0066	0.0009	0.0019
JER	0.0012	0.0006	0.0016
Pileup	0.0027	0.0003	0.0004
b tagging	0.0004	0.0009	0.0006
Lepton efficiency	0.0007	0.0007	0.0011
W+jets	0.0010	0.0030	0.0006
QCD multijet	0.0017	0.0030	0.0017
Unfolding	0.0018	0.0014	0.0004
Generator	0.0058	0.0028	0.0013
Hadronization	0.0042	0.0041	0.0014
p_T reweighting	0.0002	0.0008	0.0014
μ_F and μ_R	0.0057	0.0034	0.0045
PDF	0.0009	0.0004	0.0004
Total	0.0120	0.0077	0.0061

Table G.8: Systematic uncertainties in the differential measurement of A_C in three bins of $p_T^{t\bar{t}}$ in the *fiducial phase space*.

	Uncertainty in $A_C(p_T^{t\bar{t}})$		
Systematic uncertainty	Bin 1	Bin 2	Bin 3
JES	0.0016	0.0039	0.0028
JER	0.0012	0.0019	0.0011
Pileup	0.0021	0.0004	0.0002
b tagging	0.0013	0.0006	0.0015
Lepton efficiency	0.0008	0.0009	0.0009
W+jets	0.0003	0.0008	0.0024
QCD multijet	0.0008	0.0010	0.0013
Unfolding	0.0006	0.0009	0.0015
Generator	0.0008	0.0027	0.0021
Hadronization	0.0012	0.0046	0.0027
p_T reweighting	0.0000	0.0008	0.0010
μ_F and μ_R	0.0021	0.0024	0.0011
PDF	0.0006	0.0005	0.0008
Total	0.0043	0.0076	0.006

Table G.9: Systematic uncertainties in the differential measurement of A_C in three bins of $|y_{t\bar{t}}|$ in the *fiducial phase space*.

	Uncertainty in $A_C(\lvert y_{t\bar{t}}\rvert)$		
Systematic uncertainty	Bin 1	Bin 2	Bin 3
JES	0.0047	0.0018	0.0015
JER	0.0020	0.0005	0.0008
Pileup	0.0013	0.0003	0.0012
b tagging	0.0005	0.0002	0.0033
Lepton efficiency	0.0005	0.0006	0.0016
W+jets	0.0020	0.0012	0.0012
QCD multijet	0.0013	0.0020	0.0026
Unfolding	0.0021	0.0023	0.0013
Generator	0.0012	0.0013	0.0008
Hadronization	0.0007	0.0024	0.0007
p_T reweighting	0.0011	0.0008	0.0008
μ_F and μ_R	0.0020	0.0011	0.0008
PDF	0.0004	0.0006	0.0014
Total	0.0067	0.0049	0.0057

Table G.10: Systematic uncertainties in the differential measurement of A_C in six bins of $m_{t\bar{t}}$ in the *fiducial phase space*.

	Uncertainty in $A_C(m_{t\bar{t}})$		
Systematic uncertainty	Bin 1	Bin 2	Bin 3
JES	0.0074	0.0008	0.0027
JER	0.0039	0.0015	0.0003
Pileup	0.0030	0.0007	0.0004
b tagging	0.0005	0.0006	0.0007
Lepton efficiency	0.0009	0.0008	0.0007
W+jets	0.0005	0.0022	0.0007
QCD multijet	0.0015	0.0021	0.0009
Unfolding	0.0018	0.0014	0.0010
Generator	0.0039	0.0034	0.0023
Hadronization	0.0066	0.0042	0.0013
p_T reweighting	0.0011	0.0007	0.0011
μ_F and μ_R	0.0043	0.0033	0.0006
PDF	0.0008	0.0002	0.0009
Total	0.0128	0.0075	0.0045
	Bin 4	Bin 5	Bin 6
JES	0.0080	0.0112	0.0033
JER	0.0051	0.0038	0.0041
Pileup	0.0007	0.0017	0.0055
b tagging	0.0035	0.0038	0.0027
Lepton efficiency	0.0011	0.0015	0.0025
W+jets	0.0045	0.0017	0.0107
QCD multijet	0.0020	0.0044	0.0112
Unfolding	0.0005	0.0002	0.0006
Generator	0.0014	0.0083	0.0207
Hadronization	0.0037	0.0070	0.0135
p_T reweighting	0.0017	0.0025	0.0059
μ_F and μ_R	0.0062	0.0022	0.0117
PDF	0.0010	0.0047	0.0038
Total	0.0137	0.0182	0.0333

H Results of the Differential Measurements

Table H.1: The corrected asymmetry values in the *full phase space* in three bins of the secondary variables $m_{t\bar{t}}$, $p_T^{t\bar{t}}$, and $|y_{t\bar{t}}|$, along with the SM theory predictions by Kühn and Rodrigo (K&R) [53] and Bernreuther and Si (B&S) [43]. The quoted measurement uncertainties are, in order, the statistical and systematic uncertainties.

		A_C in bin 1	A_C in bin 2	A_C in bin 3
$m_{t\bar{t}}$	Measured	$-0.0008 \pm 0.0172 \pm 0.0115$	$0.0041 \pm 0.0091 \pm 0.0071$	$0.0074 \pm 0.0081 \pm 0.0077$
	SM (K&R)	0.0073 ± 0.0003	0.0102 ± 0.0004	0.0139 ± 0.0005
	SM (B&S)	0.0082 ± 0.0004	0.0123 ± 0.0003	0.0146 ± 0.0003
$p_T^{t\bar{t}}$	Measured	$-0.0030 \pm 0.0105 \pm 0.0041$	$-0.0017 \pm 0.0113 \pm 0.0073$	$0.0103 \pm 0.0143 \pm 0.0066$
	SM (B&S)	0.0127 ± 0.0006	-0.0047 ± 0.0003	-0.0014 ± 0.0002
$y_{t\bar{t}}$	Measured	$-0.0295 \pm 0.0152 \pm 0.0067$	$0.0054 \pm 0.0078 \pm 0.0054$	$0.0184 \pm 0.0094 \pm 0.0066$
	SM (K&R)	0.0023 ± 0.0002	0.0059 ± 0.0003	0.0181 ± 0.0006
	SM (B&S)	0.0030 ± 0.0002	0.0080 ± 0.0003	0.0193 ± 0.0005

Table H.2: The corrected asymmetry values in the *fiducial phase space* in three bins of the secondary variables $m_{t\bar{t}}$, $p_T^{t\bar{t}}$, and $|y_{t\bar{t}}|$, along with the SM theory predictions by Bernreuther and Si (B&S) [43]. The quoted measurement uncertainties are, in order, the statistical and systematic uncertainties.

		A_C in bin 1	A_C in bin 2	A_C in bin 3
$m_{t\bar{t}}$	Measured	$-0.0043 \pm 0.0181 \pm 0.0120$	$0.0025 \pm 0.0095 \pm 0.0077$	$-0.0011 \pm 0.0078 \pm 0.0061$
	SM (B&S)	$0.0068^{+0.0000}_{-0.0014}$	$0.0067^{+0.0000}_{-0.0006}$	$0.0058^{+0.0002}_{-0.0004}$
$p_T^{t\bar{t}}$	Measured	$-0.0088 \pm 0.0107 \pm 0.0043$	$-0.0032 \pm 0.0119 \pm 0.0076$	$0.0109 \pm 0.0146 \pm 0.0060$
	SM (B&S)	$0.0092^{+0.0000}_{-0.0003}$	$-0.0037^{+0.0001}_{-0.0003}$	$-0.0008^{+0.0000}_{-0.0014}$
$y_{t\bar{t}}$	Measured	$-0.0296 \pm 0.0152 \pm 0.0067$	$0.0039 \pm 0.0080 \pm 0.0049$	$0.0127 \pm 0.0096 \pm 0.0057$
	SM (B&S)	$0.0037^{+0.0000}_{-0.0006}$	$0.0057^{+0.0000}_{-0.0010}$	$0.0100^{+0.0000}_{-0.0012}$

Table H.3: The corrected asymmetry values in the *full phase space* in six bins of $m_{\mathrm{t\bar{t}}}$, along with the SM theory predictions by Bernreuther and Si (B&S) [43]. The quoted measurement uncertainties are, in order, the statistical and systematic uncertainties.

		A_C in bin 1	A_C in bin 2	A_C in bin 3
$m_{\mathrm{t\bar{t}}}$	Measured	$-0.0099 \pm 0.0198 \pm 0.0118$	$0.0161 \pm 0.0105 \pm 0.0064$	$-0.0125 \pm 0.0118 \pm 0.0061$
	SM (B&S)	0.0081 ± 0.0004	0.0112 ± 0.0005	0.0114 ± 0.0004
		A_C in bin 4	A_C in bin 5	A_C in bin 6
$m_{\mathrm{t\bar{t}}}$	Measured	$0.0233 \pm 0.0150 \pm 0.0179$	$-0.0129 \pm 0.0259 \pm 0.0231$	$0.0172 \pm 0.0375 \pm 0.0362$
	SM (B&S)	0.0134 ± 0.0004	0.0167 ± 0.0006	0.0210 ± 0.0003

Table H.4: The corrected asymmetry values in the *fiducial phase space* in six bins of $m_{\mathrm{t\bar{t}}}$, along with the SM theory predictions by Bernreuther and Si (B&S) [43]. The quoted measurement uncertainties are, in order, the statistical and systematic uncertainties.

		A_C in bin 1	A_C in bin 2	A_C in bin 3
$m_{\mathrm{t\bar{t}}}$	Measured	$-0.0152 \pm 0.0205 \pm 0.0128$	$0.0134 \pm 0.0108 \pm 0.0075$	$-0.0137 \pm 0.0113 \pm 0.0045$
	SM (B&S)	$0.0070^{+0.0000}_{-0.0016}$	$0.0062^{+0.0002}_{-0.0000}$	$0.0074^{+0.0000}_{-0.0017}$
		A_C in bin 4	A_C in bin 5	A_C in bin 6
$m_{\mathrm{t\bar{t}}}$	Measured	$0.0103 \pm 0.0139 \pm 0.0137$	$-0.0172 \pm 0.0240 \pm 0.0182$	$-0.0023 \pm 0.0354 \pm 0.0333$
	SM (B&S)	$0.0054^{+0.0002}_{-0.0002}$	$0.0038^{+0.0024}_{-0.0000}$	$0.0011^{+0.0010}_{-0.0011}$

Bibliography

[1] *S. L. Glashow*, "Partial-symmetries of weak interactions", Nucl. Phys. 22 (1961) 579 – 588.

[2] *A. Salam and J. Ward*, "Electromagnetic and weak interactions", Phys. Lett. 13 (1964) 168 – 171.

[3] *M. Gell-Mann*, "A schematic model of baryons and mesons", Phys. Lett. 8 (1964) 214 – 215.

[4] *S. Weinberg*, "A Model of Leptons", Phys. Rev. Lett. 19 (1967) 1264–1266.

[5] *S. L. Glashow, J. Iliopoulos, and L. Maiani*, "Weak Interactions with Lepton-Hadron Symmetry", Phys. Rev. D 2 (1970) 1285–1292.

[6] *H. Georgi and S. L. Glashow*, "Unified Weak and Electromagnetic Interactions without Neutral Currents", Phys. Rev. Lett. 28 (1972) 1494–1497.

[7] *G. 't Hooft*, "Renormalizable Lagrangians for Massive Yang-Mills Fields", Nucl. Phys. B 35 (1971) 167 – 188.

[8] *G. 't Hooft and M. Veltman*, "Regularization and Renormalization of Gauge Fields", Nucl. Phys. B 44 (1972) 189 – 213.

[9] *D. J. Gross and F. Wilczek*, "Ultraviolet Behavior of Non-Abelian Gauge Theories", Phys. Rev. Lett. 30 (1973) 1343–1346.

[10] *H. D. Politzer*, "Reliable Perturbative Results for Strong Interactions?", Phys. Rev. Lett. 30 (1973) 1346–1349.

[11] *E598 Collaboration*, "Experimental Observation of a Heavy Particle J", Phys. Rev. Lett. 33 (1974) 1404–1406.

[12] *SLAC-SP-017 Collaboration*, "Discovery of a Narrow Resonance in e+ e- Annihilation", Phys. Rev. Lett. 33 (1974) 1406–1408.

[13] *S. W. Herb et al.*, "Observation of a Dimuon Resonance at 9.5 GeV in 400-GeV Proton-Nucleus Collisions", Phys. Rev. Lett. 39 (1977) 252–255.

[14] *CDF Collaboration*, "Observation of Top Quark Production in $\overline{p}p$ Collisions with the Collider Detector at Fermilab", Phys. Rev. Lett. 74 (1995) 2626–2631.

[15] *DØ Collaboration*, "Observation of the Top Quark", Phys. Rev. Lett. 74 (1995) 2632–2637.

[16] *K. Kodama et al.*, "Observation of Tau Neutrino Interactions", Phys. Lett. B 504 (2001) 218 – 224.

[17] *CMS Collaboration*, "Observation of a new boson at a mass of 125 GeV with the CMS experiment at the LHC", Phys. Lett. B 716 (2012) 30–61.

[18] *ATLAS Collaboration*, "Observation of a new particle in the search for the Standard Model Higgs boson with the ATLAS detector at the LHC", Phys. Lett. B 716 (2012) 1–29.

[19] *N. Jarosik, C. Bennett, J. Dunkley, B. Gold, M. Greason, et al.*, "Seven-Year Wilkinson Microwave Anisotropy Probe (WMAP) Observations: Sky Maps, Systematic Errors, and Basic Results", Astrophys. J. Suppl. 192 (2011) 14.

[20] *Planck Collaboration*, "Planck 2015 results. I. Overview of products and scientific results", arXiv:1502.01582 [astro-ph.CO], 2015.

[21] *G. Altarelli*, "The Standard Model of Particle Physics", arXiv:hep-ph/0510281 [hep-ph], 2005.

[22] *M. Kobayashi and T. Maskawa*, "CP Violation in the Renormalizable Theory of Weak Interaction", Prog. Theor. Phys. 49 (1973) 652–657.

[23] *ATLAS, CDF, CMS, DØ Collaboration*, "First combination of Tevatron and LHC measurements of the top-quark mass", arXiv:1403.4427 [hep-ex], 2014.

[24] *B. Lillie, L. Randall, and L.-T. Wang*, "The Bulk RS KK-gluon at the LHC", JHEP 09 (2007) 074.

[25] *Y. Tang*, "Vacuum Stability in the Standard Model", Mod. Phys. Lett. A 28 (2013) 1330002.

[26] *F. Bezrukov and M. Shaposhnikov*, "Higgs inflation at the critical point", Phys. Lett. B 734 (2014) 249–254.

[27] *Particle Data Group Collaboration*, "Review of Particle Physics", Chin. Phys. C 38 (2014) 090001.

[28] *J. R. Incandela, A. Quadt, W. Wagner, and D. Wicke*, "Status and Prospects of Top-Quark Physics", Prog. Part. Nucl. Phys. 63 (2009) 239–292.

[29] *K. Kröninger, A. B. Meyer, and P. Uwer*, "Top-Quark Physics at the LHC", The Large Hadron Collider: Harvest of Run 1 (2015) 259–300.

[30] *DØ Collaboration*, "Observation of Single Top-Quark Production", Phys. Rev. Lett. 103 (2009) 092001.

[31] *CDF Collaboration*, "Observation of Electroweak Single Top-Quark Production", Phys. Rev. Lett. 103 (2009) 092002.

[32] *H.-L. Lai, M. Guzzi, J. Huston, Z. Li, P. M. Nadolsky, et al.*, "New parton distributions for collider physics", Phys. Rev. D 82 (2010) 074024.

[33] "CT10 global analysis - Additional figures and results", `http://hep.pa.msu.edu/cteq/public/ct10/figs/` (August, 2015).

[34] *M. Czakon and A. Mitov*, "Top++: A Program for the Calculation of the Top-Pair Cross-Section at Hadron Colliders", Comput. Phys. Commun. 185 (2014) 2930.

[35] *J. H. Kühn and G. Rodrigo*, "Charge Asymmetry in Hadroproduction of Heavy Quarks", Phys. Rev. Lett. 81 (1998) 49–52.

[36] *J. H. Kühn and G. Rodrigo*, "Charge Asymmetry of Heavy Quarks at Hadron Colliders", Phys. Rev. D 59 (1999) 054017.

[37] *CDF Collaboration*, "Study of the Top Quark Production Asymmetry and Its Mass and Rapidity Dependence in the Full Run II Tevatron Dataset", CDF-Note-10807, `http://www-cdf.fnal.gov/physics/new/top/2012/LepJet_AFB_Winter2012/CDF10807.pdf`, 2012.

[38] *DØ Collaboration*, "Forward-Backward Asymmetry in Top Quark-Antiquark Production", Phys. Rev. D 84 (2011) 112005.

[39] *B. Gripaios, A. Papaefstathiou, and B. Webber*, "Probing the Colour Structure of the Top Quark Forward-Backward Asymmetry", JHEP 1311 (2013) 105.

[40] *J. H. Kühn and G. Rodrigo*, "Forward-backward and charge asymmetries at Tevatron and the LHC", `arXiv:1411.4675 [hep-ph]`, 2014.

[41] *CMS Collaboration*, "Measurement of the charge asymmetry in top-quark pair production in proton-proton collisions at $\sqrt{s} = 7$ TeV", Phys. Lett. B 709 (2012) 28–49.

[42] *CMS Collaboration*, "Measurement of the charge asymmetry in top quark pair production with the CMS experiment", CMS-PAS-TOP-10-010, `http://cds.cern.ch/record/1335714`, 2011.

[43] *W. Bernreuther and Z.-G. Si*, "Top quark and leptonic charge asymmetries for the Tevatron and LHC", Phys. Rev. D 86 (2012) 034026.

[44] *N. Kidonakis*, "The top quark forward-backward asymmetry at approximate N^3LO", Phys. Rev. D 91 (2015) 071502.

[45] *M. Czakon, P. Fiedler, and A. Mitov*, "Resolving the Tevatron Top Quark Forward-Backward Asymmetry Puzzle: Fully Differential Next-to-Next-to-Leading-Order Calculation", Phys. Rev. Lett. 115 (2015) 052001.

[46] *S.-Q. Wang, X.-G. Wu, Z.-G. Si, and S. J. Brodsky*, "Application of the Principle of Maximum Conformality to the Top-Quark Charge Asymmetry at the LHC", Phys. Rev. D 90 (2014) 114034.

[47] *CDF Collaboration*, "Forward-Backward Asymmetry in Top-Quark Production in $p\bar{p}$ Collisions at $\sqrt{s} = 1.96$ TeV", Phys. Rev. Lett. 101 (2008) 202001.

[48] *CDF Collaboration*, "Measurement of the top quark forward-backward production asymmetry and its dependence on event kinematic properties", Phys. Rev. D 87 (2013) 092002.

[49] *DØ Collaboration*, "Measurement of the forward-backward asymmetry in top quark-antiquark production in $p\bar{p}$ collisions using the lepton+jets channel", Phys. Rev. D 90 (2014) 072011.

[50] *CMS Collaboration*, "Inclusive and differential measurements of the $t\bar{t}$ charge asymmetry in proton-proton collisions at 7 TeV", Phys. Lett. B 717 (2012) 129–150.

[51] *ATLAS Collaboration*, "Measurement of the top quark pair production charge asymmetry in proton-proton collisions at $\sqrt{s} = 7$ TeV using the ATLAS detector", JHEP 1402 (2014) 107.

[52] *ATLAS and CMS Collaborations*, "Combination of ATLAS and CMS $t\bar{t}$ charge asymmetry measurements using LHC proton-proton collisions at 7 TeV", ATLAS-CONF-2014-012, ATLAS-COM-CONF-2014-014, CMS-PAS-TOP-14-006, `http://cds.cern.ch/record/1670517`, 2014.

[53] *J. H. Kühn and G. Rodrigo*, "Charge asymmetries of top quarks at hadron colliders revisited", JHEP 01 (2012) 063.

[54] *E. Alvarez*, "Improving top quark induced charge asymmetries at the LHC using $t\bar{t}$ transverse momentum", Phys. Rev. D 85 (2012) 094026.

[55] *J. Aguilar-Saavedra*, "Overview of models for the $t\bar{t}$ asymmetry", Nuovo Cim. C035N3 (2012) 167–172, `arXiv:1202.2382 [hep-ph]`.

[56] *S. Frixione, P. Nason, and C. Oleari*, "Matching NLO QCD Computations with Parton Shower Simulations: The POWHEG Method", JHEP 0711 (2007) 070.

[57] *S. Alioli, P. Nason, C. Oleari, and E. Re*, "A General Framework for Implementing NLO Calculations in Shower Monte Carlo Programs: The POWHEGBOX", JHEP 1006 (2010) 043.

[58] *J. Aguilar-Saavedra, D. Amidei, A. Juste, and M. Perez-Victoria*, "Asymmetries in top quark pair production at hadron colliders", arXiv:1406.1798 [hep-ph], 2014.

[59] *J. Aguilar-Saavedra and M. Perez-Victoria*, "$t\bar{t}$ charge asymmetry, family and friends", J. Phys. Conf. Ser. 447 (2013) 012015.

[60] *J. Aguilar-Saavedra and M. Perez-Victoria*, "Simple models for the top asymmetry: Constraints and predictions", JHEP 1109 (2011) 097.

[61] *J. F. Kamenik, J. Shu, and J. Zupan*, "Review of New Physics Effects in $t\bar{t}$ Production", Eur. Phys. J. C 72 (2012) 2102.

[62] *B. Grinstein, A. L. Kagan, M. Trott, and J. Zupan*, "Forward-backward asymmetry in $t\bar{t}$ production from flavour symmetries", Phys. Rev. Lett. 107 (2011) 012002.

[63] *B. Allanach and K. Sridhar*, "R-Parity Violating Supersymmetry Explanation for Large t tbar Forward-Backward Asymmetry", Phys. Rev. D 86 (2012) 075016.

[64] *P. Ferrario and G. Rodrigo*, "Massive color-octet bosons and the charge asymmetries of top quarks at hadron colliders", Phys. Rev. D 78 (2008) 094018.

[65] *A. Djouadi, G. Moreau, F. Richard, and R. K. Singh*, "The Forward-backward asymmetry of top quark production at the Tevatron in warped extra dimensional models", Phys. Rev. D 82 (2010) 071702.

[66] *K. Cheung, W.-Y. Keung, and T.-C. Yuan*, "Top Quark Forward-Backward Asymmetry", Phys. Lett. B 682 (2009) 287–290.

[67] *S. Jung, H. Murayama, A. Pierce, and J. D. Wells*, "Top quark forward-backward asymmetry from new t-channel physics", Phys. Rev. D 81 (2010) 015004.

[68] *A. E. Nelson, T. Okui, and T. S. Roy*, "A unified, flavor symmetric explanation for the $t\bar{t}$ asymmetry and Wjj excess at CDF", Phys. Rev. D 84 (2011) 094007.

[69] *J. Shu, T. M. Tait, and K. Wang*, "Explorations of the Top Quark Forward-Backward Asymmetry at the Tevatron", Phys. Rev. D 81 (2010) 034012.

[70] *J. Aguilar-Saavedra and M. Perez-Victoria*, "Asymmetries in $t\bar{t}$ production: LHC versus Tevatron", Phys. Rev. D 84 (2011) 115013.

[71] *J. Aguilar-Saavedra and M. Pérez-Victoria*, "Shaping the top asymmetry", Phys. Lett. B 705 (2011) 228 – 234.

[72] *CMS Collaboration*, "CMS Physics Technical Design Report Volume I: Detector Performance and Software", CERN-LHCC-2006-01, `https://cds.cern.ch/record/922757`, 2006.

[73] *CMS Collaboration*, "The CMS Experiment at the CERN LHC", JINST 3 (2008) S08004.

[74] *L. Evans and P. Bryant*, "LHC Machine", JINST 3 (2008) S08001.

[75] *CERN AC Team*, "The four main LHC experiments", CERN-AC-9906026, `http://cds.cern.ch/record/40525`, 1999.

[76] *J. Gruschke*, "Observation of Top Quarks and First Measurement of the $t\bar{t}$ Production Cross Section at a Centre-Of-Mass Energy of 7 TeV with the CMS Experiment at the LHC", PhD Thesis, Karlsruhe Institute of Technology, CERN-THESIS-2011-030 (2011).

[77] *G. Aad et al.*, "The ATLAS Experiment at the LHC", JINST 3 (2008) S08003.

[78] *K. Aamodt et al.*, "The ALICE Experiment at the LHC", JINST 3 (2008) S08002.

[79] *A. A. Alves et al.*, "The LHCb Detector at the LHC", JINST 3 (2008) S08005.

[80] *C. E. Hill and M. O'Neill*, "The High Voltage System for the High Intensity CERN Proton Source", CERN-PS-98-035-HP(1998).

[81] *C. E. Hill, A. M. Lombardi, E. Tanke, and M. Vretenar*, "Present Performance of the CERN Proton Linac", CERN-PS-98-045-HP(1998).

[82] *K. Schindl*, "The PS Booster as Pre-Injector for LHC", Part. Accel. 58 (1997) 63–78.

[83] *R. Cappi*, "The PS in the LHC Injector Chain", Part. Accel. 58 (1997) 79–89.

[84] *T. Linnecar*, "Preparing the SPS for LHC", Part. Accel. 58 (1997) 91–101.

[85] *CMS Collaboration*, "CMS Luminosity Collision Data", `https://twiki.cern.ch/twiki/bin/view/CMSPublic/LumiPublicResults` (May, 2015).

[86] *CMS Collaboration*, "Detector Drawings", CMS-PHO-GEN-2012-002, http://cds.cern.ch/record/1433717, 2012.

[87] *CMS Collaboration*, "The CMS tracker system project: Technical Design Report", CERN-LHCC-98-006, http://cds.cern.ch/record/368412, 1997.

[88] *CMS Collaboration*, "The CMS tracker: addendum to the Technical Design Report", CERN-LHCC-2000-016, http://cds.cern.ch/record/490194, 2000.

[89] *CMS Collaboration*, "The CMS Electromagnetic Calorimeter Project: Technical Design Report", CERN-LHCC-97-033, http://cds.cern.ch/record/349375, 1997.

[90] *CMS Collaboration*, "Changes to the CMS ECAL Electronics: Addendum to the Technical Design Report", CERN-LHCC-2002-027, http://cds.cern.ch/record/581342, 2002.

[91] *CMS Collaboration*, "The CMS Hadronic Calorimeter Project: Technical Design Report", CERN-LHCC-97-031, http://cds.cern.ch/record/357153, 1997.

[92] *CMS Collaboration*, "The CMS Muon Project: Technical Design Report", CERN-LHCC-97-032, http://cds.cern.ch/record/343814, 1997.

[93] *CMS Collaboration*, "The TriDAS Project Technical Design Report, Volume 1: The Trigger Systems", CERN-LHCC-2000-038, https://cds.cern.ch/record/706847, 2000.

[94] *CMS Collaboration*, "The TriDAS Project Technical Design Report, Volume 2: Data Acquisition and High-Level Trigger", CERN-LHCC-2002-026, https://cds.cern.ch/record/578006, 2002.

[95] *WLCG Collaboration*, "LHC Computing Grid: Technical Design Report", CERN-LHCC-2002-024, https://cds.cern.ch/record/840543, 2005.

[96] *M. A. Dobbs et al.*, "Les Houches guidebook to Monte Carlo generators for hadron collider physics", arXiv:hep-ph/0403045 [hep-ph], 2004.

[97] *V. N. Gribov and L. N. Lipatov*, "Deep Inelastic ep Scattering in Perturbation Theory", Sov. J. Nucl. Phys. 15 (1972) 438–450.

[98] *G. Altarelli and G. Parisi*, "Asymptotic Freedom in Parton Language", Nucl. Phys. B 126 (1977) 298.

[99] *Y. L. Dokshitzer*, "Calculation of the Structure Functions for Deep Inelastic Scattering and e^+e^- Annihilation by Perturbation Theory in Quantum Chromodynamics", Sov. Phys. JETP 46 (1977) 641–653.

[100] *V. Sudakov*, "Vertex parts at very high energies in quantum electrodynamics", Sov. Phys. JETP 3 (1956) 65–71.

[101] *B. Andersson, G. Gustafson, G. Ingelman, and T. Sjöstrand*, "Parton Fragmentation and String Dynamics", Phys. Rept. 97 (1983) 31–145.

[102] *B. R. Webber*, "A QCD Model for Jet Fragmentation Including Soft Gluon Interference", Nucl. Phys. B 238 (1984) 492.

[103] *G. Corcella, I. Knowles, G. Marchesini, S. Moretti, K. Odagiri, et al.*, "HERWIG 6: An Event generator for hadron emission reactions with interfering gluons (including supersymmetric processes)", JHEP 0101 (2001) 010.

[104] *CMS Collaboration*, "Utilities for Accessing Pileup Information for Data", `https://twiki.cern.ch/twiki/bin/view/CMS/PileupJSONFileforData` (June, 2015).

[105] *T. Stelzer and W. F. Long*, "Automatic Generation of Tree Level Helicity Amplitudes", Comput. Phys. Commun. 81 (1994) 357–371.

[106] *F. Maltoni and T. Stelzer*, "MadEvent: Automatic event generation with MadGraph", JHEP 0302 (2003) 027.

[107] *J. Alwall, P. Demin, S. de Visscher, R. Frederix, M. Herquet, et al.*, "MadGraph/MadEvent v4: The New Web Generation", JHEP 09 (2007) 028.

[108] *J. Alwall, M. Herquet, F. Maltoni, O. Mattelaer, and T. Stelzer*, "MadGraph 5 : Going Beyond", JHEP 06 (2011) 128.

[109] *M. L. Mangano, M. Moretti, F. Piccinini, R. Pittau, and A. D. Polosa*, "ALPGEN, a generator for hard multiparton processes in hadronic collisions", JHEP 07 (2003) 001.

[110] *S. Catani, F. Krauss, R. Kühn, and B. R. Webber*, "QCD Matrix Elements + Parton Showers", JHEP 11 (2001) 063.

[111] *F. Krauss*, "Matrix Elements and Parton Showers in Hadronic Interactions", JHEP 08 (2002) 015.

[112] *M. L. Mangano, M. Moretti, F. Piccinini, and M. Treccani*, "Matching matrix elements and shower evolution for top-quark production in hadronic collisions", JHEP 0701 (2007) 013.

[113] *S. Frixione and B. R. Webber*, "Matching NLO QCD computations and parton shower simulations", JHEP 06 (2002) 029.

[114] *S. Frixione, P. Nason, and B. R. Webber*, "Matching NLO QCD and parton showers in heavy flavor production", JHEP 08 (2003) 007.

[115] *R. Frederix and S. Frixione*, "Merging meets matching in MC@NLO", JHEP 12 (2012) 061.

[116] *J. Alwall, R. Frederix, S. Frixione, V. Hirschi, F. Maltoni, et al.*, "The automated computation of tree-level and next-to-leading order differential cross sections, and their matching to parton shower simulations", JHEP 1407 (2014) 079.

[117] *T. Sjostrand, S. Mrenna, and P. Z. Skands*, "PYTHIA 6.4 Physics and Manual", JHEP 05 (2006) 026.

[118] *P. Nason*, "A New Method for Combining NLO QCD with Shower Monte Carlo Algorithms", JHEP 11 (2004) 040.

[119] *P. Nason and B. Webber*, "Next-to-Leading-Order Event Generators", Ann. Rev. Nucl. Part. Sci. 62 (2012) 187–213.

[120] *S. Jadach, J. H. Kühn, and Z. Was*, "TAUOLA: A Library of Monte Carlo Programs to Simulate Decays of Polarized Tau Leptons", Comput. Phys. Commun. 64 (1990) 275–299.

[121] *GEANT4 Collaboration*, "GEANT4: A Simulation Toolkit", Nucl. Instrum. Meth. A506 (2003) 250–303.

[122] *CMS Collaboration*, "The fast simulation of the CMS detector at LHC", J. Phys. Conf. Ser. 331 (2011) 032049.

[123] *CMS Collaboration*, "Measurement of the differential cross section for top quark pair production in pp collisions at $\sqrt{s} = 8\,\text{TeV}$", arXiv:1505.04480 [hep-ex], 2015. Submitted to Eur. Phys. J. C.

[124] *N. Kidonakis*, "Differential and total cross sections for top pair and single top production", arXiv:1205.3453 [hep-ph], 2012.

[125] *CMS Collaboration*, "Particle-Flow Event Reconstruction in CMS and Performance for Jets, Taus, and MET", CMS-PAS-PFT-09-001, http://cds.cern.ch/record/1194487, 2009.

[126] *CMS Collaboration*, "Commissioning of the Particle-flow Event Reconstruction with the first LHC collisions recorded in the CMS detector", CMS-PAS-PFT-10-001, http://cds.cern.ch/record/1247373, 2010.

[127] *CMS Collaboration*, "Commissioning of the Particle-Flow reconstruction in Minimum-Bias and Jet Events from pp Collisions at 7 TeV", CMS-PAS-PFT-10-002, http://cds.cern.ch/record/1279341, 2010.

[128] *CMS Collaboration*, "Description and performance of track and primary-vertex reconstruction with the CMS tracker", JINST 9 (2014) P10009.

[129] *T. Speer et al.*, "Track Reconstruction in the CMS Tracker", Nucl. Instrum. Meth. A559 (2006) 143–147.

[130] *R. Frühwirth*, "Application of Kalman Filtering to Track and Vertex Fitting", Nucl. Instrum. Meth. A262 (1987) 444–450.

[131] *S. Baffioni et al.*, "Electron Reconstruction in CMS", Eur. Phys. J. C49 (2007) 1099–1116.

[132] *R. Frühwirth*, "Track Fitting with Non-Gaussian Noise", Comput. Phys. Commun. 100 (1997) 1–16.

[133] *W. Adam, R. Frühwirth, A. Strandlie, and T. Todorov*, "Reconstruction of Electrons with the Gaussian Sum Filter in the CMS Tracker at LHC", Journal of Physics G: Nuclear and Particle Physics 31 (2005) N9.

[134] *CMS Collaboration*, "Performance of CMS muon reconstruction in pp collision events at $\sqrt{s} = 7$ TeV", JINST 7 (2012) P10002.

[135] *S. Catani, Y. L. Dokshitzer, M. H. Seymour, and B. R. Webber*, "Longitudinally Invariant k_t Clustering Algorithms for Hadron Hadron Collisions", Nucl. Phys. B 406 (1993) 187–224.

[136] *Y. L. Dokshitzer, G. D. Leder, S. Moretti, and B. R. Webber*, "Better Jet Clustering Algorithms", JHEP 08 (1997) 001.

[137] *M. Wobisch and T. Wengler*, "Hadronization Corrections to Jet Cross-Sections in Deep Inelastic Scattering", `arXiv:hep-ph/9907280 [hep-ph]`, 1998.

[138] *M. Cacciari, G. P. Salam, and G. Soyez*, "The Anti-k_t Jet Clustering Algorithm", JHEP 04 (2008) 063.

[139] *CMS Collaboration*, "Determination of Jet Energy Calibration and Transverse Momentum Resolution in CMS", JINST 6 (2011) P11002.

[140] *K. Goebel, J. Haller, J. Ott, and H. Stadie*, "Jet Transverse Momentum Resolution Measurement using Dijet Events at $\sqrt{s} = 8$ TeV", internal CMS Analysis Note AN 2013/416, 2014.

[141] *DØ Collaboration*, "B Jet Identification", `http://www-d0.fnal.gov/Run2Physics/top/singletop_observation/b_tagging_graphic.png` (November, 2011).

[142] *CMS Collaboration*, "Identification of b-quark jets with the CMS experiment", JINST 8 (2013) P04013.

[143] *P. Van Mulders, A. Descroix, T. du Pree, G. Van Onsem, and J. Vizan*, "Implementation and training of the Combined Secondary Vertex MVA b-tagging algorithm in CMSSW", internal CMS Analysis Note AN 2012/441, 2013.

[144] *J. M. Campbell, J. Huston, and W. Stirling*, "Hard Interactions of Quarks and Gluons: A Primer for LHC Physics", Rept. Prog. Phys. 70 (2007) 89.

[145] *S. Drell and T.-M. Yan*, "Massive Lepton Pair Production in Hadron-Hadron Collisions at High-Energies", Phys. Rev. Lett. 25 (1970) 316–320.

[146] *M. Czakon, P. Fiedler, and A. Mitov*, "Total Top-Quark Pair-Production Cross Section at Hadron Colliders Through $O(\alpha_s^4)$", Phys. Rev. Lett. 110 (2013) 252004.

[147] *CMS Collaboration*, "Standard Model Cross Sections for CMS at 8 TeV", `https://twiki.cern.ch/twiki/bin/view/CMS/StandardModelCrossSectionsat8TeV?rev=30` (June, 2015). Internal.

[148] *Y. Li and F. Petriello*, "Combining QCD and electroweak corrections to dilepton production in FEWZ", Phys. Rev. D 86 (2012) 094034.

[149] *CMS Collaboration*, "MET Optional Filters", `https://twiki.cern.ch/twiki/bin/viewauth/CMS/MissingETOptionalFilters` (June, 2015).

[150] *CMS Collaboration*, "Anomalous HB/HE Noise at Startup: Characteristics and Rejection Algorithms", CMS Internal Note IN 2010/006, 2010.

[151] *CMS Collaboration*, "Effective Areas for the particle-based isolation for electrons", `https://twiki.cern.ch/twiki/bin/viewauth/CMS/EgammaEARhoCorrection` (May, 2015). Internal.

[152] *CMS Collaboration*, "Baseline muon selections for Run-I", `https://twiki.cern.ch/twiki/bin/view/CMSPublic/SWGuideMuonId` (May, 2015).

[153] *CMS Collaboration*, "Multivariate Electron Identification", `https://twiki.cern.ch/twiki/bin/view/CMS/MultivariateElectronIdentification` (June, 2015). Internal.

[154] *CMS Collaboration*, "Tools for Conversion Rejection (Electron ID) and Electron Vetoing (Photon ID)", `https://twiki.cern.ch/twiki/bin/view/CMS/ConversionTools` (June, 2015). Internal.

[155] *CMS Collaboration*, "Performance of b tagging at $\sqrt{s} = 8\,\text{TeV}$ in multijet, $\mathrm{t\bar{t}}$ and boosted topology events", CMS-PAS-BTV-13-001, `http://cds.cern.ch/record/1581306`, 2013.

[156] *CMS Collaboration*, "Re-weighting of events to account for BTag efficiency and mistag scale factors", https://twiki.cern.ch/twiki/bin/view/CMS/BTagWeight (May, 2015). Internal.

[157] *CMS Collaboration*, "Electron Efficiency for Top Quark Analysis", https://twiki.cern.ch/twiki/bin/view/CMS/KoPFAElectronTagAndProbe (May, 2015). Internal.

[158] *CMS Collaboration*, "Reference Muon ID and Isolation Efficiencies", https://twiki.cern.ch/twiki/bin/view/CMS/MuonReferenceEffs (May, 2015). Internal.

[159] "THETA - A Framework for Template Based Modelling and Inference", http://www.theta-framework.org.

[160] *F. James and M. Roos*, "Minuit: A System for Function Minimization and Analysis of the Parameter Errors and Correlations", Comput. Phys. Commun. 10 (1975) 343–367.

[161] *CMS Collaboration*, "Measurements of jet multiplicity and differential production cross sections of Z+jets events in proton-proton collisions at $\sqrt{s} = 7\,\text{TeV}$", Phys. Rev. D 91 (2015) 052008.

[162] *CMS Collaboration*, "Measurement of the production cross sections for a Z boson and one or more b jets in pp collisions at $\sqrt{s} = 7\,\text{TeV}$", JHEP 06 (2014) 120.

[163] *CMS Collaboration*, "Measurement of the t-channel single-top-quark production cross section and of the $|V_{\text{tb}}|$ CKM matrix element in pp collisions at $\sqrt{s} = 8\,\text{TeV}$", JHEP 06 (2014) 090.

[164] *CMS Collaboration*, "Observation of the associated production of a single top quark and a W boson in pp collisions at $\sqrt{s} = 8\,\text{TeV}$", Phys. Rev. Lett. 112 (2014) 231802.

[165] *A. Goobar, S. Hannestad, E. Mortsell, and H. Tu*, "The neutrino mass bound from WMAP 3 year data, the baryon acoustic peak, the SNLS supernovae and the Lyman-α forest", JCAP 0606 (2006) 019.

[166] *T. Chwalek*, "Measurement of the W-Boson Helicity-Fractions in Top-Quark Decays with the CDF II Experiment and Prospects for an Early $t\bar{t}$ Cross-Section Measurement with the CMS Experiment", PhD Thesis, Karlsruhe Institute of Technology, CERN-THESIS-2010-255 (2010).

[167] *CMS Collaboration*, "Measurement of differential top-quark pair production cross sections in the lepton+jets channel in pp collisions at 8 TeV", CMS-PAS-TOP-12-027, http://cds.cern.ch/record/1523611, 2013.

[168] *S. Schmitt*, "TUnfold: an algorithm for correcting migration effects in high energy physics", JINST 7 (2012) T10003.

[169] *V. Blobel*, "An Unfolding Method for High Energy Physics Experiments", arXiv:hep-ex/0208022 [hep-ph], 2002.

[170] *S. Baker and R. D. Cousins*, "Clarification of the Use of χ^2 and Likelihood Functions in Fits to Histograms", Nucl. Instrum. Meth. 221 (1984) 437–442.

[171] *V. Blobel*, "Unfolding – linear inverse problems", Notes for the Terascale Workshop on Unfolding and Data Correction at DESY, http://www.desy.de/~blobel/WorkshopMay10.pdf, 2010.

[172] *A. Martin, W. Stirling, R. Thorne, and G. Watt*, "Parton distributions for the LHC", Eur. Phys. J. C 63 (2009) 189–285.

[173] *R. D. Ball, V. Bertone, F. Cerutti, L. Del Debbio, S. Forte, et al.*, "Impact of Heavy Quark Masses on Parton Distributions and LHC Phenomenology", Nucl. Phys. B 849 (2011) 296–363.

[174] *E. Gabrielli, M. Raidal, and A. Racioppi*, "Implications of the effective axial-vector coupling of gluon on top-quark charge asymmetry at the LHC", Phys. Rev. D 85 (2012) 074021.

[175] *E. Gabrielli and M. Raidal*, "Effective axial-vector coupling of gluon as an explanation to the top quark asymmetry", Phys. Rev. D 84 (2011) 054017.

[176] *ATLAS Collaboration*, "Measurement of the charge asymmetry in top-quark pair production in the lepton-plus-jets final state in pp collision data at $\sqrt{s} = 8\,\text{TeV}$ with the ATLAS detector", arXiv:1509.02358 [hep-ex], 2015. Submitted to Eur. Phys. J. C.

[177] *CMS Collaboration*, "Measurement of the Charge Asymmetry in Top Quark Pair Production in pp Collisions at $\sqrt{s} = 8\,\text{TeV}$ using a Template Method", arXiv:1508.03862 [hep-ex], 2015. Submitted to Phys. Rev. D.

[178] *S. Berge and S. Westhoff*, "Top-Quark Charge Asymmetry Goes Forward: Two New Observables for Hadron Colliders", JHEP 07 (2013) 179.

[179] *J. A. Aguilar-Saavedra, E. Álvarez, A. Juste, and F. Rubbo*, "Shedding light on the $t\bar{t}$ asymmetry: the photon handle", JHEP 04 (2014) 188.

[180] *S. Choi and H. S. Lee*, "Azimuthal decorrelation in $t\bar{t}$ production at hadron colliders", Phys. Rev. D 87 (2013) 034012.

[181] *E. L. Berger*, "Top Quark Polarization and the Search for New Physics", arXiv:1301.5053 [hep-ph], 2013.

[182] *CMS Collaboration*, "Measurements of the $t\bar{t}$ charge asymmetry using the dilepton decay channel in pp collisions at $\sqrt{s} = 7\,\text{TeV}$", JHEP 04 (2014) 191.

[183] *ATLAS Collaboration*, "Measurement of the charge asymmetry in dileptonic decays of top quark pairs in pp collisions at $\sqrt{s} = 7\,\text{TeV}$ using the ATLAS detector", JHEP 05 (2015) 061.

[184] *D0 Collaboration*, "Simultaneous measurement of forward-backward asymmetry and top polarization in dilepton final states from $t\bar{t}$ production at the Tevatron", Phys. Rev. D 92 (2015) 052007.

Danksagung

Zunächst möchte ich meinem Doktorvater Prof. Dr. Thomas Müller dafür danken, dass er mir die Möglichkeit zur Promotion in seiner Arbeitsgruppe gegeben und mich von allen Sorgen hinsichtlich der Finanzierung meiner Arbeit befreit hat.

Meinem Korreferenten Prof. Dr. Ulrich Husemann möchte ich für die Übernahme eben dieses Amtes danken – sowie auch insbesondere für das bemerkenswert gründliche Korrekturlesen meiner Arbeit, das zu einigen sehr hilfreichen Verbesserungsvorschlägen geführt hat.

Ein ganz besonders großer Dank gebührt Dr. Thorsten Chwalek, der mich während der gesamten Arbeit betreut hat, der immer zur Stelle war, wenn es eine neue Problemstellung zu diskutieren galt, und der mich auch in Bezug auf organisatorische Aspekte der Arbeit immer unterstützt hat.

Überdies bin ich Dr. Jeannine Wagner-Kuhr und Dr. Jochen Ott zu großem Dank verpflichtet, da deren Hilfsbereitschaft und Expertise vor allem auch in der Anfangsphase meiner Promotion eine wichtige Unterstützung darstellten. Ebenso danke ich auch Dr. Matthias Mozer für das gründliche Korrekturlesen meiner Arbeit und für die Beantwortung einer Reihe von Fragen, die in meiner Prüfungsvorbereitung aufkamen.

Weiterhin möchte ich mich bei den restlichen Mitgliedern des Instituts für Experimentelle Kernphysik für die hervorragende Arbeitsatmosphäre und die stete Hilfsbereitschaft bedanken; diese gaben mir durchweg das Gefühl, im Institut von Freunden umgeben zu sein.

Schließlich gebührt meinen Eltern großer Dank dafür, dass sie mich während des Studiums und auch während der Arbeit selbst immer unterstützt haben und mir jenen bedingungslosen Rückhalt gaben, wie man ihn am Ende doch nur in der Familie erfährt.